



UNIVERSITÀ  
DEGLI STUDI  
DI BRESCIA


DOTTORATO DI RICERCA IN  
DIPARTIMENTO DI INGEGNERIA MECCANICA E INDUSTRIALE

ICAR/08 Scienza Delle Costruzioni

CICLO  
XXXIII

COMPLEMENTARY EXPERIMENTS, MODELLING, AND SIMULATIONS OF  
INNOVATIVE LI-ION BATTERIES

NOME DEL DOTTORANDO  
BUKET' BOZ

Firma..... 

NOME DEL RELATORE  
PROF. ALBERTO SALVADORI & PROF. JENNIFER L. SCHAEFER

Firma.....  Jennifer L. Schaefer

NOME DEL COORDINATORE DEL DOTTORATO  
PROF. LAURA ELENORA DEPERO

Firma..... 



## Sommario

Le prestazioni dell'elettrolita sono uno dei parametri più importanti nelle batterie agli ioni di litio. L'esafluorofosfato di litio ( $\text{LiPF}_6$ ) sciolto in un solvente organico liquido con additivi stabilizzanti è ancora la soluzione più diffusa grazie alla sua elevata conduttività ionica e compatibilità con diversi materiali per elettrodi. Nonostante i progressi nella progettazione dei materiali, ci sono ancora questioni irrisolte negli elettroliti liquidi, quali il basso numero di trasferimento ( $t_+$ ), infiammabilità, ecc. Il numero di trasferimento definisce il moto relativo dei cationi rispetto agli anioni all'interno di un campo elettrico. Vale uno per un elettrolita in cui solo gli ioni di litio sono mobili e zero per il caso opposto, in cui migrano solo gli anioni. L'elettrolita liquido convenzionale (cioè  $\text{LiPF}_6$ ) ha un numero di trasferimento inferiore a 0,5, perchè gli anioni voluminosi si muovono più velocemente degli ioni di litio a causa della solvatazione degli ioni di litio. Questo elevato movimento anionico provoca la formazione di gradienti di concentrazione all'interno di una cella elettrolitica, limitando la densità di energia e le velocità di carica. In questa dissertazione, viene studiata la fabbricazione di elettroliti gel polimerici reticolati con varie nanostrutture, contenenti sia sale libero che cariche legate tramite rigonfiamento degli ionomeri con soluzioni elettrolitiche liquide. Utilizzando l'elettrolita liquido in una rete polimerica, miriamo ad aumentare il numero di cariche all'interno del sistema per migliorare la conduttività ionica e il numero di trasferimento. Il sistema viene esaminato sia sperimentalmente che teoricamente. I modelli sono progettati e validati rispetto all'evidenza empirica degli esperimenti.

Nel Capitolo 1, viene discussa una panoramica completa della letteratura sugli elettroliti polimerici con proprietà di trasporto avanzate sia dal punto di vista sperimentale che di modellazione.

Nel secondo capitolo, le membrane di poli (etilenglicole) diacrilato (PEGDA) sono reticolate con diversi rapporti tra ossigeno e carica. È stato studiato l'impatto del diverso rapporto ossigeno / carica ( $\text{EO} = \text{Ch}$ ) sul numero di trasferimento e sulla conducibilità ionica in presenza di 1 M  $\text{LiPF}_6$  (EC-DEC 1: 1 v%). Si è scoperto che la conduttività ionica è fortemente influenzata dalla densità di carica della membrana, mentre il numero di trasferimento non varia con la composizione.

Le proprietà di trasporto sono state esaminate successivamente nei poli (glicole etilenico) dimetacrilato (PEGDMA) con membrane di vinil solfonato (VS) nel Capitolo 3. Si è scoperto che un elevato numero di trasferimento non è accompagnato da una diminuzione della conducibilità ionica totale. Inoltre, la struttura del polimero ha un grande impatto sulle proprietà di trasporto. In presenza di una struttura di nanopori nel polimero, l'elevata diffusività anionica non ha ridotto il numero di trasferimento a causa delle differenze nella dimensione molecolare.

Il Capitolo 4 si concentra sulla modellazione di elettroliti polimerici conduttori di ioni singoli (SIPE) sulla base del Capitolo 2. Per i SIPE viene fornita una struttura generale per il trasporto di massa accoppiato con reazioni chimiche. La conducibilità ionica nelle soluzioni organiche e l'associazione e la dissociazione dei cationi di litio vengono prese in considerazione per costruire il modello SIPE. La teoria costitutiva e la cinetica chimica sono state studiate per scrivere le equazioni che governano il problema multifisico. Il compromesso tra il numero di cariche e la diffusività è mostrato in termini di applicabilità del SIPE nelle batterie agli ioni di litio. Nell'ultimo capitolo è stato studiato un modello elettro-chemo-meccanico completamente accoppiato di batteria agli ioni di litio. La microstruttura dell'elettrodo è stata idealizzata come un mezzo trifase composto da particelle attive, particelle conduttive e elettrolita liquido convenzionale. Le leggi di equilibrio e le condizioni dell'interfaccia sono derivate per anodo, catodo, elettrolita e l'interfaccia tra anodo / elettrolita e catodo / elettrolita. Le relazioni costitutive, derivate da principi termodinamici, completano l'insieme delle equazioni di governo. Sono state prese in esame diverse forme dell'elettrodo, aumentando la superficie per l'intercalazione.

## Abstract

Electrolyte performance is one of the most essential parameters in lithium-ion batteries. Lithium hexafluorophosphate ( $\text{LiPF}_6$ ) dissolved in a liquid carbonate solvent with stabilizing additives is still the state of the art of electrolyte in current systems due to its high ionic conductivity and compatibility with several electrode materials. Despite progress on material design and fast charge and discharge capabilities, there are still issues with liquid electrolyte, namely, low transference number ( $t_+$ ), flammability, etc..  $t_+$  defines the relative motion of cations to anions within an electric field and equals unity for an electrolyte where only lithium ions are mobile and equals zero for the opposite case where only anions migrate. The conventional liquid electrolyte (i.e.,  $\text{LiPF}_6$ ) has a transference number below 0.5, in which the bulky anions move faster than lithium ions as a result of the large solvation shell of lithium ions. This high anion motion causes concentration gradients to form within a cell, limiting energy density and charge rates. In this dissertation, the fabrication of crosslinked polymer gel electrolytes with varied nanostructures, containing both free salt and bound charges via swelling of the network ionomers with liquid electrolyte solutions, are investigated. By utilizing the liquid electrolyte in a polymer network, we aim to increase the number of charges within the system to improve the ionic conductivity and transference number. The system is examined both experimentally and theoretically. The models are designed and validated against the empirical evidence from the experiments.

In Chapter 1, a comprehensive literature overview on polymer electrolytes with advanced transport properties from both experimental and modelling point of views is discussed.

In the second chapter, poly(ethylene glycol) diacrylate (PEGDA) membranes are crosslinked with varying ether oxygen to charge ratios. The impact of different ether oxygen to charge ratio ( $\text{EO}=\text{Ch}$ ) on transference number and ionic conductivity in the presence of 1 M  $\text{LiPF}_6$  (EC-DEC 1:1 v%) were investigated. It was found that ionic conductivity is highly influenced by the charge density of the membrane, whereas  $t_+$  does not vary with the composition. The free charges ultimately rule the transport properties in PEGDA membranes.

After these findings, the transport properties were examined in poly(ethylene glycol) dimethacrylate (PEGDMA) with vinyl sulfonate (VS) membranes in Chapter 3. It was found that the transference number and conductivity are not mutually exclusive and, for certain systems, an increase in the lithium transference number is not accompanied with a decrease in total ionic conductivity. Besides, the structure of the polymer has a great impact on the transport properties. In the presence of a nanoporous structure in the polymer, the high anion diffusivity did not reduce the transference number due to the molecular size differences.

Chapter 4 focuses on the modelling of single ion conducting polymer electrolytes (SIPes) based on Chapter 2. A general framework for coupled mass transport with chemical reactions is provided for SIPes. Ionic conductivity in carbonate based solutions and association and dissociation of lithium cations are taken into account to build the SIPE model. Constitutive theory and chemical kinetics were studied in order to write the governing equations for the multi-physics problem. The tradeoff between the number of charges and diffusivity is shown in terms of how this effects the SIPE's applicability to perform in lithium ion batteries.

In the last chapter, a fully coupled electro-chemo-mechanical lithium ion battery model was studied. The electrode microstructure was idealized here as a three-phase media made of active particles, conductive particles, and conventional liquid electrolyte. Balance laws and interface conditions are derived for anode, cathode, electrolyte and the interface between anode/electrolyte and cathode/electrolyte. Constitutive relations, derived from thermodynamic principles, complete the set of governing equations. Tailoring the electrode shape, by means of increasing the surface area for the intercalation was investigated.

## Table of Contents

|   |       |
|---|-------|
| Sommario.....   | iii   |
| Abstarct.....   | v     |
| List of Figures.....  | xi    |
| List of Tables.....   | xviii |
| Acknowledgement.....  | xx    |
| 1. Chapter 1- Introduction and State of Art.....                          | 1     |
| 1.1 Introduction .....  | 1     |
| 1.1.1 Electrochemical Transport Theory and Continuum Modelling.....       | 2     |
| 1.1.2 Organic-based Electrolytes with Enhanced Transport Properties ..... | 13    |
| 1.1.2.1 Solid-State Polymer Electrolytes .....                            | 14    |
| 1.1.2.2 Composite Polymer Electrolytes.....                               | 16    |
| 1.1.2.3 Gel Polymer Electrolytes .....                                    | 17    |
| 1.1.2.4 Polymer Electrolyte Applications on Lithium Metal Anode .....     | 22    |
| 1.2 Outline and Summary.....  | 24    |
| 2. Chapter 2- Investigation of Condensed Gel Polymer Electrolytes.....    | 25    |
| 2.1 Introduction .....  | 25    |
| 2.2 Experimental Section .....  | 26    |
| 2.2.1 Synthesis of Crosslinked Polymer Electrolyte (PEGDA-NaSS).....      | 26    |
| 2.2.2 Solvent and Salt Drying.....  | 28    |
| 2.2.3 Electrolyte Preparation .....                                       | 28    |
| 2.2.4 ICP-OES - Sample Preparation .....                                  | 29    |
| 2.2.5 ICP- OES – Standard Preparation .....                               | 29    |
| 2.2.6 ICP-OES – Measurement .....   | 30    |
| 2.2.7 Solvent and Electrolyte Uptake Test .....                           | 30    |
| 2.2.8 Conductivity Measurement.....                                       | 31    |
| 2.2.9 Lithium Symmetric Cells – Transference Number Measurement.....      | 31    |
| 2.2.10 Cathode Preparation – LiFePO <sub>4</sub> .....                    | 32    |
| 2.2.11 Li/LiFePO <sub>4</sub> Cells - Galvanostatic Cycling.....          | 32    |

|         |   |    |
|---------|---|----|
| 2.3     | Results and Discussion.....   | 33 |
| 2.3.1   | Polymer Synthesis and composition (PEGDA-SS).....   | 33 |
| 2.3.2   | Electrolyte Uptake Measurement.....   | 34 |
| 2.3.3   | ICP-OES Elemental Analysis.....   | 36 |
| 2.3.4   | Conductivity Measurement.....   | 40 |
| 2.3.5   | Transference Number Measurement- 1 M LIPF <sub>6</sub> (EC/DEC 1:1 v%).....               | 47 |
| 2.3.5.1 | Transference Number Measurement – EC/DEC (1:1 v%).....                                    | 55 |
| 2.3.6   | Full Cell Cycling Performance– Li metal/LiFePO <sub>4</sub> .....                         | 57 |
| 2.4     | Conclusion.....   | 64 |
| 3.      | Chapter 3- Investigation of Porous Polymer Electrolytes.....                              | 67 |
| 3.1     | Introduction.....   | 67 |
| 3.2     | Experimental Section – PEGDMA 750 g/mol-VS.....   | 68 |
| 3.2.1   | Vinyl Sulfonate Salt Preparation.....   | 68 |
| 3.2.2   | Water Content Measurement.....  | 69 |
| 3.2.3   | Synthesis of Crosslinked PEGDMA Membranes.....  | 69 |
| 3.2.3.1 | Transparent PEGDMA-VS-0.....  | 69 |
| 3.2.3.2 | Opaque PEGDMA-VS-0.....   | 70 |
| 3.2.3.3 | Opaque PEGDMA.....  | 72 |
| 3.2.4   | Ion Exchange.....   | 73 |
| 3.2.5   | Solvent and Salt Drying.....  | 73 |
| 3.2.6   | Electrolyte Preparation.....  | 74 |
| 3.2.7   | Solvent and Electrolyte Uptake Test.....  | 74 |
| 3.3     | Characterization.....   | 75 |
| 3.3.1   | Elemental Analysis – ICP-OES Inductively Coupled Plasma Atomic Emission Spectroscopy..... | 75 |
| 3.3.1.1 | Sample Preparation.....   | 75 |
| 3.3.1.2 | ICP- OES – Standard Preparation.....  | 75 |
| 3.3.1.3 | ICP-OES - Measurement.....  | 76 |
| 3.3.2   | Conductivity Measurement.....   | 76 |
| 3.3.3   | Fourier-Transform Infrared Spectroscopy (FTIR).....                                       | 77 |



|         |  |     |
|---------|--|-----|
| 3.3.4   | Scanning Electron Microscope (SEM) .....   | 77  |
| 3.3.5   | Lithium Symmetric Cells – Transference Number Measurement.....                                     | 77  |
| 3.3.6   | Cathode Preparation – LiFePO <sub>4</sub> .....  | 78  |
| 3.3.7   | Li/LiFePO <sub>4</sub> Cells - Galvanostatic Cycling .....   | 78  |
| 3.4     | Results and Discussion.....  | 79  |
| 3.4.1   | Polymer synthesis and composition (PEGDMA 750 mol/g-VS).....                                       | 79  |
| 3.4.2   | Electrolyte Uptake Measurement .....   | 80  |
| 3.4.3   | ICP-OES Elemental Analysis.....  | 80  |
| 3.4.4   | Scanning Electron Microscopy Images (SEM) .....  | 86  |
| 3.4.5   | Analysis Fourier-Transform Infrared Spectroscopy (FTIR) .....                                      | 87  |
| 3.4.6   | Conductivity Measurement.....  | 88  |
| 3.4.7   | Lithium Symmetric Cell- Impedance Measurement (Lithium Transference<br>Number).....                | 92  |
| 3.4.8   | Opaque and Transparent PEGDMA-VS with SO <sub>3</sub> – .....                                      | 102 |
| 3.4.8.1 | Ionic Conductivity Measurements .....  | 103 |
| 3.4.8.2 | Impedance Measurement – Li <sup>+</sup> Transference Number .....                                  | 104 |
| 3.4.9   | Full Cell Cycling Performance .....  | 106 |
| 3.5     | Summary and Outcomes .....   | 109 |
| 4.      | Chapter 4- Continuum Modelling of Single Ion Conducting Polymer Electrolytes                       | 111 |
| 4.1     | Introduction .....   | 111 |
| 4.1.1   | Single Ion Conducting Polymer Electrolyte Modeling .....   | 115 |
| 4.2     | 1 Dimensional Ionic Transport Continuum Model of Single Ion Conducting<br>Polymer Electrolyte..... | 117 |
| 4.2.1   | Single Ion Conducting Polymer Electrolyte Model Description.....                                   | 118 |
| 4.3     | Balance Laws .....   | 120 |
| 4.3.1   | Mass Balance.....  | 120 |
| 4.3.2   | Faraday’s Law .....  | 121 |
| 4.4     | Balance Equations of SIPE - Strong Forms .....   | 121 |
| 4.4.1   | Weak Forms of the Balance Equations.....   | 122 |

|         |   |     |
|---------|---|-----|
| 4.5     | Boundary and Initial Conditions, Modeling Assumption and Material Parameters .....  | 125 |
| 4.6     | Results and Discussion.....   | 127 |
| 4.7     | Summary and Outcomes .....  | 132 |
| 5.      | Chapter 5- The Influence of Electrode Morphology in the Electro-Chemo-Mechanical Response of Conventional Lithium-ion Batteries ..... | 134 |
| 5.1     | Introduction .....  | 134 |
| 5.2     | Mathematical Model .....  | 137 |
| 5.2.1   | Electrolyte Model .....   | 137 |
| 5.2.2   | Intercalating Electrodes .....  | 139 |
| 5.2.3   | Interface Conditions .....  | 140 |
| 5.2.4   | Material Parameters.....  | 142 |
| 5.2.5   | Geometry and Boundary Conditions .....  | 145 |
| 5.2.6   | Finite Element Implementation .....   | 148 |
| 5.2.7   | Non-Dimensional Governing Equations and Weak Forms .....  | 148 |
| 5.2.7.1 | Weak form.....  | 151 |
| 5.2.8   | Numerical Resolution.....   | 152 |
| 5.3     | Results and Discussion.....   | 154 |
| 5.3.1   | Electro-Chemo-Mechanical Response of the Planar Battery .....   | 154 |
| 5.3.2   | The impact of Cathode Morphology .....  | 157 |
| 5.3.3   | Changing the Morphology of Both Electrodes.....   | 159 |
| 5.4     | Conclusion.....   | 162 |
| 6.      | Summary and Outlook.....  | 163 |
| 7.      | References .....  | 166 |
| 8.      | Appendices .....  | 178 |
| 8.1     | Chapter-3.....  | 178 |
| 8.1.1   | The Principles of Electrochemical Impedance Spectroscopy.....   | 178 |
| 8.1.1.1 | The Basic Electrical Circuit Components .....   | 179 |

|  |     |
|--|-----|
| 8.1.2 Fitted Impedance Data.....               | 181 |
| 8.1.3 Liquid Electrolyte Characterization..... | 183 |

## List of Figures

|   |    |
|---|----|
| Figure 1.1: Sketch of conventional lithium-ion battery with lithium metal anode and LiFePO <sub>4</sub> porous cathode on discharge process.....  | 2  |
| Figure 1.2: Summary of Newman's and coworkers' study on the importance of transference number study.....  | 6  |
| Figure 1.3: McCloskey and coworker's modelling study with Newman's model on various transference number and ionic conductivity effect on concentration gradient are presented. ....   | 7  |
| Figure 1.4: Kim and colleagues illustrated the Li <sup>+</sup> and Li <sup>+</sup> clusters motions in PEO/LiTFSI electrolyte with regard to the schematic. ....  | 12 |
| Figure 1.5: The performance of SIPE BAB triblock copolymers results are depicted in A, B and C. A shows the capacities at different C-rates and temperatures. B presents the discharge profiles at 80°C at different C-rates with Li/LiFePO <sub>4</sub> configuration. C shows the C-rate performances at different temperatures. .... | 15 |
| Figure 1.6: Zhang and colleagues' study on SIPE full cell cycling performance with Li/LiFePO <sub>4</sub> .....   | 19 |
| Figure 1.7: Various GPE LiBs full cell performances.....  | 20 |
| Figure 2.1: Schematic of crosslinked PEGDA-SS membrane in 1 M LiPF <sub>6</sub> .....   | 26 |
| Figure 2.2 : ICP-OES standards preparation process for the calibration.....   | 30 |
| Figure 2.3: A sketch of coin cell assembly.....   | 33 |
| Figure 2.4: Structural schematics of the components of PEGDA-SS and film fabrication.....   | 34 |
| Figure 2.5: PEGDA-SS EO=Li 6,8,12 and 20 dry state (only 0.5 M LiCl ionic exchange).....  | 36 |
| Figure 2.6: Lithium concentration of GPE-6,8,12, 20 swelled in 1 M LiPF <sub>6</sub> (EC/DEC 1:1 v%)......  | 38 |
| Figure 2.7: Lithium concentration of GPE-6,8,12 and 20 in 1 M LiTFSI (DOL-DME 1:1 v%)......   | 39 |
| Figure 2.8: A) Ionic conductivity of each PEGDA 700 g/mol-SS membrane swelled to equilibrium in DOL-DME (1:1 v%) B) Ionic conductivity of each PEGDA 700 g/mol-SS membrane swelled to equilibrium in EC-DEC (1:1 v%).....   | 42 |

|  |    |
|--|----|
| Figure 2.9: A) Ionic conductivity of each PEGDA 700 g/mol-SS membrane swelled to equilibrium in 1 M LiTFSI (DOL-DME 1:1 v%) B) Ionic conductivity of each PEGDA 700 g/mol-SS membrane swelled to equilibrium in 1 M LiPF <sub>6</sub> (EC/DEC 1:1 v%) .....  | 43 |
| Figure 2.10: Ionic conductivity of 1 M LiPF <sub>6</sub> (EC-DEC 1:1 v%) .....   | 45 |
| Figure 2.11: Li metal/Gel Polymer Electrolyte/Li metal symmetric cell configuration for impedance measurement. ....  | 48 |
| Figure 2.12: a) Impedance response pre and post hold of Li symmetric cells with GPE-6 in 1 M LiPF <sub>6</sub> (EC/DEC 1:1 v%) b) Polarization curve - GPE-6 in 1 M LiPF <sub>6</sub> (EC/DEC 1:1 v%) .....  | 49 |
| Figure 2.13: a) Impedance response pre and post hold of Li symmetric cells with GPE-8 in 1 M LiPF <sub>6</sub> (EC/DEC 1:1 v%) b) Polarization curve - GPE-8 in 1 M LiPF <sub>6</sub> (EC/DEC 1:1 v%) .....  | 51 |
| Figure 2.14: a) Impedance response pre- and post-hold of Li symmetric cells with GPE-12 in 1 M LiPF <sub>6</sub> (EC/DEC 1:1 v%) b) Polarization curve - GPE-12 in 1 M LiPF <sub>6</sub> (EC/DEC 1:1 v%) .....   | 52 |
| Figure 2.15: a) Impedance response pre- and post-hold of Li symmetric cells with GPE-20 in 1 M LiPF <sub>6</sub> (EC/DEC 1:1 v%) b) Polarization curve - GPE-20 in 1 M LiPF <sub>6</sub> (EC/DEC 1:1 v%) .....   | 54 |
| Figure 2.16: a) Impedance response pre and post hold of Li symmetric cells with SIPE-8 in EC/DEC (1:1 v%) b) Polarization curve - SIPE-8 in EC/DEC (1:1 v%) .....  | 56 |
| Figure 2.17: Lithium metal/Gel Polymer Electrolyte/Lithium metal full cell configuration .....   | 58 |
| Figure 2.18: Charge and discharge profile of Li/GPE-12/LiCoO <sub>2</sub> at 0.1 C-rate .....  | 58 |
| Figure 2.19: a) GPE-12 after failure of the Li/LiCoO <sub>2</sub> , the carbon decomposition is seen clearly around the edges of the polymer membrane. b) The darken lithium metal surface which shows the unstable SEI formation. Correspondingly, LiFePO <sub>4</sub> is chosen for the rest of the study..... | 59 |
| Figure 2.20: Li/GPE-12/LiFePO <sub>4</sub> full cycling performance, including C-rate test from 0.1C – 5 C. 200 cycles are completed with 0.1 C-rate. ....   | 60 |
| Figure 2.21: Li/GPE-20/LiFePO <sub>4</sub> full cycling performance, including C-rate test from 0.1C – 5 C, 200 cycle is completed at 0.1 C-rate. ....   | 61 |

|   |    |
|---|----|
| Figure 2.22: Li/GPE-6/LiFePO <sub>4</sub> full cycling performance, including C-rate test from 0.1C – 0.3 C, 95 cycle is completed at 0.1 C-rate. ....  | 62 |
| Figure 2.23: Li/GPE-8/LiFePO <sub>4</sub> full cycling performance at C-rate 0.1 .....  | 63 |
| Figure 2.24: Skecth of high and low charge density membranes' (GPE-6 and GPE-20) dry and electrolyte (1 M LiPF <sub>6</sub> ) swollen states .....  | 65 |
| Figure 3.1: Vinyl sulfonate salt preparation set-up.....  | 68 |
| Figure 3.2: O-PEGDMA-VS-0 membrane preparation process in five steps.....   | 72 |
| Figure 3.3: ICP-OES standards preparation process for the calibration.....  | 76 |
| Figure 3.4: A) T-PEGDMA-VS-0 membrane B) O-PEGDMA-VS-0 membrane.....  | 79 |
| Figure 3.5: Dry (0.5 M LiCl ionic exchange solution) and 1 M LiPF <sub>6</sub> (EC-DEC 1:1 v%) swelled T-PEGDMA-VS-0 crosslinked membranes .....  | 81 |
| Figure 3.6: 1 M LiPF <sub>6</sub> (EC-DEC 1:1 v%) electrolyte swelled and dry O-PEGDMA-VS-0 crosslinked membranes.....  | 83 |
| Figure 3.7: a) SEM images of O-PEGDMA-VS-0. b) SEM images of T-PEGDMA-VS-0 .....  | 86 |
| Figure 3.8: Fourier transform infrared spectra of control PEGDMA and ionomer membranes created using our UV-cross-linking approach. A illustrates the opaque and transparent PEGDMA-VS-0 crosslinked membranes. B compares the pure PEGDMA membrane to transparent and opaque PEGDMA-VS-0.....      | 87 |
| Figure 3.9: Fourier transform infrared spectra (FTIR) of wet Opaque-PEGDMA-VS UV crosslinked membrane with open surface.....  | 88 |
| Figure 3.10: a) Conductivity of opaque and transparent PEGDMA-VS-0 swelled to equilibrium in DOL-DME (1:1 v%) b) Conductivity of opaque and transparent PEGDMA-VS-0 swelled to equilibrium in 1 M LiTFSI (DOL-DME 1:1 v %).....   | 89 |
| Figure 3.11: A) Conductivity of opaque and transparent PEGDMA-VS-0 swelled to equilibrium in EC-DEC solvent mixture (1:1 v %) B) Conductivity of opaque and transparent PEGDMA-VS-0 swelled to equilibrium in 1 M LiPF <sub>6</sub> (EC-DEC 1:1 v %) and 1 M LiPF <sub>6</sub> (EC-DEC 1:1 v%)..... | 90 |
| Figure 3.12: a) Impedance response pre- and post-potentiostatic hold of Li symmetric cells with O-PEGDMA-VS-0 in 1 M LiTFSI (DOL-DME 1:1 v%) b) Polarization curve – O-PEGDMA-VS-0 in 1 M LiTFSI (DOL-DME 1:1 v%).....  | 93 |

|   |     |
|---|-----|
| Figure 3.13: a) Impedance response pre and post hold of Li symmetric cells with T-PEGDMA-VS-0 in 1 M LiTFSI (DOL-DME 1:1 v%) b) Polarization curve – T-PEGDMA-VS-0 in 1 M LiTFSI (DOL-DME 1:1 v%) .....   | 94  |
| Figure 3.14: a) Impedance response pre and post hold of Li symmetric cells with O-PEGDMA-VS-0 in 1 M LiPF <sub>6</sub> (EC-DEC 1:1 v%) b) Polarization curve – O-PEGDMA-VS-0 in 1 M LiPF <sub>6</sub> (EC-DEC 1:1 v%) .....                             | 96  |
| Figure 3.15: a) Impedance response pre and post hold of Li symmetric cells with O-PEGDMA-VS-0 in 1 M LiPF <sub>6</sub> (EC-DEC 1:1 v%)- longer polarization b) Longer polarization curve – O-PEGDMA-VS-0 in 1 M LiPF <sub>6</sub> (EC-DEC 1:1 v%) ..... | 98  |
| Figure 3.16 : a) Impedance response pre and post hold of Li symmetric cells with thick O-PEGDMA-VS-0 in 1 M LiPF <sub>6</sub> (EC-DEC 1:1 v%) b) Polarization curve –thick O-PEGDMA-VS-0 in 1 M LiPF <sub>6</sub> (EC-DEC 1:1 v%) .....                 | 99  |
| Figure 3.17: a) Impedance response pre and post hold of Li symmetric cells with T-PEGDMA-VS-0 in 1 M LiPF <sub>6</sub> (EC-DEC 1:1 v%) b) Polarization curve – T-PEGDMA-VS-0 in 1 M LiPF <sub>6</sub> (EC-DEC 1:1 v%) .....                             | 101 |
| Figure 3.18: A) Conductivity of opaque (wet) and transparent PEGDMA-VS swelled to equilibrium in EC-DEC (1:1 v%) B) Conductivity of opaque (wet) and transparent PEGDMA-VS swelled to equilibrium in 1 M LiPF <sub>6</sub> (EC-DEC 1:1 v%) .....        | 103 |
| Figure 3.19: a) Impedance response pre and post hold of Li symmetric cells with wet opaque PEGDMA-VS in 1 M LiPF <sub>6</sub> (EC-DEC 1:1 v%) b) Polarization curve – Wet opaque PEGDMA-VS in 1 M LiPF <sub>6</sub> (EC-DEC 1:1 v%) .....               | 105 |
| Figure 3.20: Li/O-PEGDMA-VS-0-separator/LiCoO <sub>2</sub> full cycling performance, at 0.1 C-rate .....  | 106 |
| Figure 3.21: Li/O-PEGDMA-VS-0-separator/LiFePO <sub>4</sub> comparison Li/4xcelgrad/LiFePO <sub>4</sub> full cycling performance, at 0.1 C-rate. ....   | 107 |
| Figure 3.22: C-rate test performance of O-PEGDMA-VS-0 .....   | 108 |
| Figure 3.23: A sketch macroscopic and microscopic of O-PEGDMA-VS-0 membrane, swelled in 1 M LiPF <sub>6</sub> (EC-DEC 1:1 v%) .....   | 109 |
| Figure 4.1: A list of processes that take place in a battery during normal operation.....   | 113 |
| Figure 4.2: A list of models for the processes that take place in a battery during normal operation .....   | 113 |

|   |     |
|---|-----|
| Figure 4.3: A sketch of single ion conducting polymer electrolyte (SIPE).....   | 117 |
| Figure 4.4: Schematic representation of the planar Li/SIPE or GPE/LiFePO <sub>4</sub> the thickness and the domains. ....   | 118 |
| Figure 4.5: Lithium concentration and potential profile of GPE-6 with slow kinetics...  | 127 |
| Figure 4.6: Lithium concentration and potential profile of GPE-6 with $1.06 \times 10^{-9} \text{ m}^2/\text{s}$ with fast and slow reaction kinetics .....   | 128 |
| Figure 4.7: Lithium concentration and potential profiles of GPE-6 with 50 % dissociation .....  | 130 |
| Figure 4.8: Lithium concentration and potential profiles of GPE-6 with $1.06 \times 10^{-13} \text{ m}^2/\text{s}$ with fast and slow kinetics.....   | 131 |
| Figure 4.9: Lithium concentration and potential profiles of GPE-20 with infinitely fast and slow kinetics.....  | 132 |
| Figure 5.1: Schematic representation of a typical electrochemical cell and the characteristic microstructure of a porous electrode.....   | 135 |
| Figure 5.2: Schematic representation of the planar Li-ion batteries that is taken for full cell battery simulations. ....   | 143 |
| Figure 5.3: The schematic representation of modified electrode.....   | 146 |
| Figure 5.4: Computational domain adopted for the numerical simulations along with a schematic representation of the boundary conditions used.....   | 153 |
| Figure 5.5: Computational domain adopted for the numerical simulations along with a schematic representation of the boundary conditions used.....   | 154 |
| Figure 5.6: a) Simulated voltage profiles of the planar battery during constant-current-discharging at C-rates =1.0, 2.0, 4.0, and 8.0. In (b) is reported the ratio of extracted charge at the end of the extraction process over the theoretical capacity of the battery 64 mAh.. ..... | 154 |
| Figure 5.7: Lithium concentration (a) and hydrostatic pressure (b) in the planar battery as a function of x coordinate at time t=0, 2, 4, 6, 8, 12 minutes, and at the end of the process for 1.0 C-rate discharging. ....  | 156 |
| Figure 5.8: Comparison between the simulated volt- ages in the planar battery obtained though fully coupled chemo-mechanical analysis ( $\omega_{\text{Li}} = 0$ ), and by neglecting the mechanical effects ( $\omega_{\text{Li}} = 0$ ).....  | 157 |



|   |     |
|---|-----|
| Figure 5.9: Impact of cathode morphology on the simulated voltage for 1.0 (a) and 8.0 (b) C-rate discharging. ....  | 158 |
| Figure 5.10: Comparison between the lithium distribution in the battery at the end of 1.0 C-rate discharging for cathode morphologies $n = 1$ and $n = 10$ . ....         | 159 |
| Figure 5.11: Impact of battery morphology on the simulated voltage for 1.0 (a) and 8.0 (b) C-rate discharging. ....   | 161 |
| Figure 5.12: Comparison between the lithium distribution in the battery at the end of 8.0 C-rate discharging process for battery morphologies $n = 1$ and $n = 10$ . .... | 162 |

## List of Tables

|   |    |
|---|----|
| Table 2.1: Compositions, formulations, ether oxygen: charge ratio (EO=Ch), and charge density for studied SIPEs.....  | 28 |
| Table 2.2: 1 M LiPF <sub>6</sub> (EC-DEC 1:1 %) uptake data, by mass and volume, after four hours of swelling for studied SIPEs.....                          | 35 |
| Table 2.3: The number of charges in each PEGDA-SS membrane; dry and 1 M LiPF <sub>6</sub> (EC-DEC 1:1 v%) swelled state .....                                 | 37 |
| Table 2.4: The number of charges in each PEGDA-SS in 1 M LiTFSI (DOL-DME 1:1 v%) swelled state .....  | 39 |
| Table 2.5: Ionic conductivity of GPE-6,8,12 and 20 at 25°C in solvent mixtures and electrolytes .....   | 47 |
| Table 2.6: Extracted resistance and current values from impedance and polarization measurement – in 1 M LiPF <sub>6</sub> (EC/DEC 1:1 v%) swelled GPE-6.....  | 50 |
| Table 2.7: Extracted resistance and current values from impedance and polarization measurement in 1 M LiPF <sub>6</sub> (EC/DEC 1:1 v%) swelled GPE-8.....    | 51 |
| Table 2.8: Extracted resistance and current values from impedance and polarization measurement – in 1 M LiPF <sub>6</sub> (EC/DEC 1:1 v%) swelled GPE-12..... | 53 |
| Table 2.9: Extracted resistance and current values from impedance and polarization measurement – in 1 M LiPF <sub>6</sub> (EC/DEC 1:1 v%) swelled GPE-20..... | 54 |
| Table 2.10: Extracted resistance and current values from impedance and polarization measurement – in EC/DEC 1:1 v% swelled PEGDA-SS 8.....                    | 57 |
| Table 3.1: Compositions, formulations and charge density for studied polymer electrolytes.....  | 71 |
| Table 3.2: Compositions, formulations and charge density for studied PEGDMA membrane.....   | 73 |
| Table 3.3: 1 M LiPF <sub>6</sub> (EC-DEC 1:1 %) uptake data, by mass and volume, after four hours of swelling for studied SIPEs.....                          | 80 |
| Table 3.4: Elemental Analysis Results for O-PEGDMA-VS-0 and T-PEGDMA-VS-0 as dry (ionic exchange in 1 M LiCl) .....   | 82 |
| Table 3.5: Elemental Analysis Results for T-PEGDMA-VS-0 and O-PEGDMA-VS-0 in 1 M LiPF <sub>6</sub> (EC-DEC 1:1 v%).....                                       | 82 |

|  |     |
|--|-----|
| Table 3.6: Elemental Analysis Results for O-PEGDMA-VS-0 in 1 M LiTFSI (DOL-DME 1:1 v%) and 2 M LiOH .....  | 84  |
| Table 3.7: Elemental Analysis Results for T-PEGDMA-VS-0 and wet Opaque PEGDMA-VS as dry case .....   | 85  |
| Table 3.8: Ionic Conductivity of O-PEGDMA-VS-0 and T-PEGDMA-VS-0 at 25°C in solvent mixtures and electrolytes .....  | 92  |
| Table 3.9: Extracted resistance and current values from impedance and longer polarization measurement – 1 M LiTFSI (DOL-DME 1:1v%) swelled O-PEGDMA-VS-0 .....           | 94  |
| Table 3.10: Extracted resistance and current values from impedance and polarization measurement – 1 M LiTFSI (DOL-DME 1:1v%) swelled transparent PEGDMA-VS-0.            | 95  |
| Table 3.11: Extracted resistance and current values from impedance and polarization measurement – 1 M LiPF <sub>6</sub> (EC-DEC 1:1v%) swelled O-PEGDMA-VS-0.....        | 97  |
| Table 3.12: O-PEGDMA-VS-0 tLi + measurement results under the same conditions. .   | 98  |
| Table 3.13: Extracted resistance and current values from impedance and longer polarization measurement – 1 M LiPF <sub>6</sub> (EC-DEC 1:1v%) swelled O-PEGDMA-VS-0.     | 99  |
| Table 3.14: Extracted resistance and current values from impedance and polarization measurement – 1 M LiPF <sub>6</sub> (EC-DEC 1:1v%) swelled thick O-PEGDMA-VS-0.....  | 100 |
| Table 3.15: Extracted resistance and current values from impedance and polarization measurement – 1 M LiPF <sub>6</sub> (EC-DEC 1:1v%) swelled T-PEGDMA-VS-0 .....       | 102 |
| Table 3.16: Extracted resistance and current values from impedance and polarization measurement – 1 M LiPF <sub>6</sub> (EC-DEC 1:1v%) swelled wet opaque PEGDMA-VS..... | 105 |
| Table 4.1: Diffusion coefficients of GPE-6 and GPE-20 in EC-DEC (1:1 v%) solvent mixture .....   | 125 |
| Table 4.2: Reaction kinetics of GPE-6. ....  | 126 |
| Table 4.3: Reaction kinetics of GPE-20 .....   | 126 |
| Table 5.1: Material parameters of anode, cathode and the interfaces of anode/electrolyte and cathode/electrolyte .....   | 145 |

## Acknowledgement

I would like to first thank to my advisors, Prof. Alberto Salvadori and Prof. Jennifer L. Schaefer for their support, supervision and encouragement throughout my PhD and the opportunity they had given.

My sincere thanks to Prof. Alberto Salvadori to give me this unique opportunity. I am thankful his guidance and gratitude.

I would like to thank to the University of Brescia and Industrial and Mechanical Engineering Department to support me during my PhD.

I would like to express my sincere gratitude to Prof. Jennifer L. Schaefer, specifically that she welcomed me and made me feel like I am a part of the Schaefer Group. Her endless effort to make a better version of myself by teaching and guiding me brought me to where I am here now. Having her as my advisor made me believe as a woman, we can be strong in science.

I appreciate being part of University of Notre Dame and Chemical and Biomolecular Engineering Department for a year to accomplish my goals. I am very thankful for their full support during difficult times. I am also very thankful to Central for Environmental Science and Technology (CEST) and their members for all their help for my ICP experiments.

I sincerely thank my M4lab current and previous group members, both in the battery and mechanobiology team for their input on my modelling and theoretical studies. I could not have completed this work without all the discussions on partial differential equations and implementation. I am grateful for all the fun and your friendships. Additionally, I am so happy to work with an excellent master student Leonardo Della Vedova. I look forward to seeing where he will take this project.

Also, I would like to thank the Schaefer Group members for teaching me everything from scratch on how to work in the lab. The group has been a wonderful place to learn and grow every day. Especially, I want to thank my friend Hunter O. Ford, from my first day till the last, he was always there anytime I needed. It has been great to work and have fun at the same with you all.

Last but not least, my dearest friends for lifetime; Hazal Caglar, Pelin Tulpar, Maria Laura Tocci, Marco Faroni, Ipek Kuran, Tugce Ipek, Nazli Turan, Deniz Ocal, Danielle Smith, Sabrina Khan, Galiya Magazova, Duygu Saracoglu and all the countless people in my life, thank you all for being there for me anytime I needed despite the distance and standing with me throughout my PhD.

John R. Hoffman, he is the silver lining of my PhD. I would like to thank him for his support, help and his love. I imagine I would not have come this far without him. I look forward to our future together.

To the best brother, Anil Boz, I am thankful for him, his endless support and cheering me up always.

Lastly, to the best parents one can ask for, Saliha-Rahmi Boz. There are not enough words to express how thankful and grateful I am for you, your trust, endless support, encouragement and your help in many ways. I could not have done this without them.

# 1. Chapter 1- Introduction and State of Art

## 1.1 Introduction

The ability to convert chemical to electrical energy in closed electrochemical systems with high efficiency is the principal reason for rechargeable lithium batteries (LiBs) systems. Additionally, the high demand of LiBs powered devices in society such as pure electric, plug in hybrid electric vehicles (EV) and electronic devices requires the continued improvement of lithium-ion battery systems. In order to meet the global targets for reduction of greenhouse gases, significant growth in electric vehicles powered by Li-ion batteries has occurred recently. The sales number of electric vehicles in 2017 exceed for the first time one million cars per worldwide for the first time.<sup>1</sup> Nonetheless, the current devices and EVs have been suffering a few issues regarding their batteries: safety incidents, being heavy, and they take too long to charge. The scientific community have been trying to deal with all these problems both experimentally and theoretically.

Significant number of studies have aimed to increase energy density, along with higher charge and discharge rates in every component of the Li-ion battery. Tailoring the electrode thickness, Li rich transition metal oxides as cathode materials, application of different anodes (Li alloys or pure lithium metal) can be listed.<sup>2-4</sup>

A conventional lithium-ion battery consists of one anode, one cathode and a liquid electrolyte with a separator, which is a porous polyethylene or polypropylene material used to create ionic contact while maintaining electronic insulation between the two electrodes. A typical electrolyte for LiBs is made of a binary lithium salt and occasional additives dissolved in a solvent mixture based on carbonates.<sup>5</sup> The main advantage of commercial liquid electrolytes is high ionic conductivity (1-10 mS/cm) at ambient temperature. However, a majority fraction of this total ionic conductivity is the result of anion motion. As a result, concentration gradients form in the electrolyte in the presence of an electric field. The formation of the ion concentration gradients limits the practical charge/discharge rates as well as the active material utilization, particularly for thick, porous electrodes.

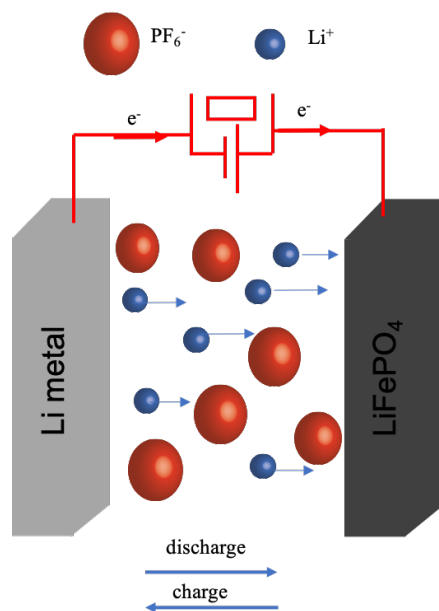


Figure 1.1: Sketch of conventional lithium-ion battery with lithium metal anode and  $\text{LiFePO}_4$  porous cathode on discharge process. Red spheres represent anions of the lithium salt. Blue spheres are Li cations.

The main focus of this study is to investigate electrolyte for enhanced ion transport properties, with the goal of mitigating the aforementioned limitations in charge/discharge rates and active material utilization. Polymer electrolytes with various transport properties, targeted high ionic conductivity and transference number are investigated both experimentally and theoretically for LiBs.

### 1.1.1 Electrochemical Transport Theory and Continuum Modelling

Computational modelling provides an opportunity to evaluate theory and predict the outcomes for developed systems with a wide range of timescale and length. There are several modelling methods which serve to comprehend different prospects of complex battery systems. For instance, density functional theory (DFT) calculations and molecular dynamics are being used to investigate main characteristics on the atomistic scale. Continuum level modelling is used to capture the macroscopic behaviors, such as; overall battery efficiency in terms of charge and discharge, as well as state of charge. Lately, Li and Monroe has published an excellent review on the methods for multiscale modelling for lithium ion batteries which can be described as a guideline between nanoscale and

macroscale approaches with respect to the thermodynamically rigorous multiphysics models.<sup>6</sup>

This section solely focuses on both continuum level model and experimental studies to understand the LiBs with different type polymer electrolytes and the advanced transport properties. There are excellent studies and reviews in literature in terms of atomistic scale modelling, which are addressed for the reader.<sup>7-9</sup>

The major lithium battery model was developed by Newman and co-workers. The evaluation of most applied battery model was started by considering dilute solution as an electrolyte and followed by moderately diluted solutions. Lastly, the model was formed as concentrated solution theory which is still widely applied for continuum LiBs.<sup>10, 11</sup>

In lithium ion battery modelling, the most common approach is known based on Newman's concentrated solution theory and electrochemical model for batteries.<sup>11,12, 13</sup> Herein, we explain the basis of the model due to the fact that it is used to investigate the polymer electrolyte behavior as well. Newman and Doyle's study in 1994 was the first of its kind in polymer electrolyte modelling, emphasizing the importance of transference number.

One of the significant parts of this study is to emphasize the importance of the transference number and conductivity on battery performance. It was depicted that unity transference number can improve the performance of the battery despite the lower conductivity of the electrolyte. The developed model was based on the concentrated solution theory which is the primary model for most of the current studies. The model based was developed first for infinite dilute solutions. Since this model was not enough to explain the complexity of electrolyte, in order moderately solution theory and as a last one concentrated solution theory were developed. Most of the current modelling researches are built on the Newman's model.<sup>10</sup>

In any battery, the system consists of ionic species or chemically distinct molecules. The concentration and velocity of species are  $c_k$  and  $v_k$  which from molar flux.  $\vec{N}_k = c_k v_k$   
The flux density of each dissolved species is given by;

$$\vec{N}_k = \underbrace{-z_k u_k F c_k \nabla \phi}_{\text{Migration}} - \underbrace{D_k \nabla c_k}_{\text{Diffusion}} + \underbrace{c_k v_k}_{\text{Convection}} \quad (\text{mol/cm}^2) \quad (1)$$



Charge per mole on a specie is defined  $z_k F$  in which charges of species are denoted with  $z_k$  and Faraday constant  $F$  are defined respectively. Therefore, the current in an electrolytic solution is due to the motion of charged species,

$$i = F \sum_k z_k N_k \quad (\text{A/cm}^2) \quad (2)$$

Material balance for every species can be written as,

$$\frac{\partial c_k}{\partial t} = - \vec{\nabla} \cdot \vec{N}_k \quad (3)$$

According to Poisson's equation, the excess charge produces the mean electric field which is written,

$$\vec{\nabla} \cdot (\epsilon \vec{E}) = \rho_e \quad (4)$$

In multicomponent systems, mechanical stress is taken into consideration and balance of momentum which relates the system to the action of stress and quasi static Lorentz body force,

$$\rho_e \vec{E};$$

$$\rho \frac{\partial v}{\partial t} = - \rho \vec{v} \cdot \vec{\nabla} \vec{v} - \vec{\nabla} \cdot \vec{\sigma} + \rho_e \vec{E} \quad (5)$$

In the large body of literature, continuum electrolyte models include the stress generation widely. Hofmann recently reported a study on electro-chemo-mechanical simulation for lithium ion battery. Phase field method was applied for the electro-chemical diffusion model for a lithium iron phosphate particle coupled with a small-strain elasto-plasticity model.<sup>14</sup>

In accordance with binary electrolyte modelling, Nernst-Planck dilute solution theory is the simplest model, ignoring finite volume occupied by the salt and any interaction between solute species. However, dilute solutions are adequate enough to represent real battery electrolytes. Hence, Newman's concentrated solution theory has been preferred to capture the realism in terms of ionic interactions. Newman and Chapman introduced the volume-average velocity as a reference convection to justify bulk convection induced by salt flux.<sup>15</sup>

$$\vec{v} = \bar{v}_e \left[ (1 - t_+^0) \frac{\vec{N}_+}{v_+} + t_+^0 \frac{\vec{N}_-}{v_+} \right] \bar{v}_0 \vec{N}_+ \quad (6)$$

Cation flux is written by,

$$\vec{N}_+ = -D\vec{\nabla}c_+ + \frac{\vec{\nabla}t_+^0}{Fz_+} + c\vec{v} \quad (7)$$

The transport properties play a crucial role in modelling. The cation transference number and ionic conductivity are the essential parameters. Li transference number in a binary salt electrolyte can be defined with the diffusivity of Li<sup>+</sup> and its counterion.<sup>10</sup> The definition of the Li<sup>+</sup> transference number in the dilute limit for a binary salt electrolyte in which both ions are univalent (a 1:1 electrolyte) relates the diffusion of Li<sup>+</sup> and its counterion through the following simple relationship,

$$t_+ = \frac{D_+}{D_+D_-} \quad (8)$$

Where  $t_+$  is the Li<sup>+</sup> transference number,  $D_+$  is the Li<sup>+</sup> diffusion coefficient,  $D_-$  is the anion diffusion coefficient. In accordance with equation (8), transference number is simply the fraction of total ionic conductivity which is carried by Li<sup>+</sup> in conventional liquid electrolyte. Ionic conductivity of any materials containing mobile ions can be described by equation (10),

$$\sigma_{total} = \sum n_j q_j \mu_j \quad (9)$$

' $n_j$ ,  $q_j$  and  $\mu_j$ ' represent the number of  $j$  ions in the material, the charge of an electron and the mobility of the ions in the electrolyte respectively. The ionic conductivity of binary electrolyte is the sum of the products of the terms in equation (9), for all effective ion species in the electrolyte.<sup>16</sup>

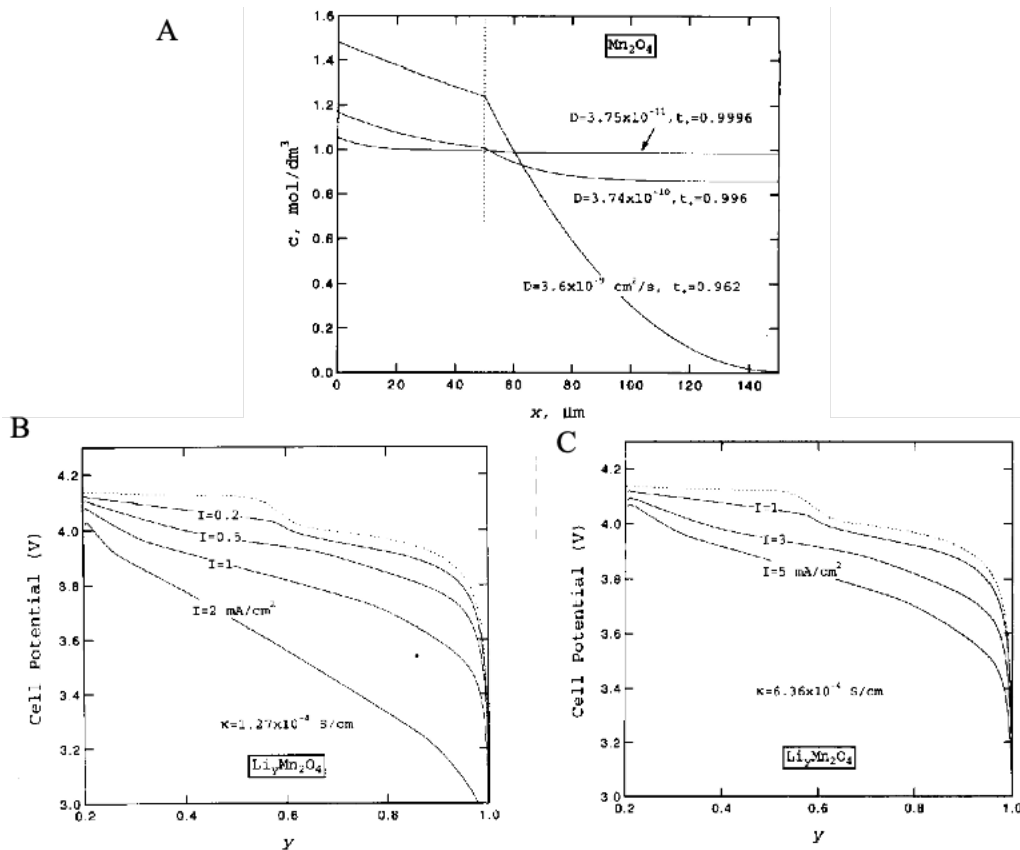


Figure 1.2: Summary of Newman's and coworkers' study on the importance of transference number study.<sup>11</sup> A depicts the effect of small variations transference number on concentration profile with galvanostatic process. B shows the potential profile with unity transference number at different currents densities. C presents the potential profile with one-fifth of the conductivity of in Figure with unity transference number.

The cation transference number is considerably lower than unity, approximately 0.3 or 0.4 in binary electrolyte systems. The cation transference number has a great impact on the battery performance. Within the battery operation anions tend to migrate in the opposite direction of lithium and accumulate at the electrode surface. Low transference numbers lead to severe concentration gradient occurrence in the electrolyte solution which limits the battery operating rate. Thus, it results in a concentration overpotential that restricts the operating voltage of the cell. Consequently, the battery faces the limited energy and power density. The importance of transference number has been raised by Newman and co-workers numerically.<sup>11</sup> In this study, the impact of conductivity and transference number on battery performance with lithium/polymer were investigated. It is concluded that even with the decreased on the conductivity, unity transference number improves the battery performance with respect to having larger energy densities and in terms of material

utilization. the importance of  $t_{Li^+}$  is demonstrated by keeping  $t_{Li^+}$  unity and decreased the ionic conductivity ten-fold, compared it with  $t_{Li^+}$  0.3 and high conductivity. The high  $t_{Li^+}$  with low conductivity performed better than the second case. Additionally, it is shown that at very low discharge rates, the concentration gradient is not large enough to cause depletion of electrolyte, high transference number does not have an impact on the system, whereas the high rates the improvement is seen.

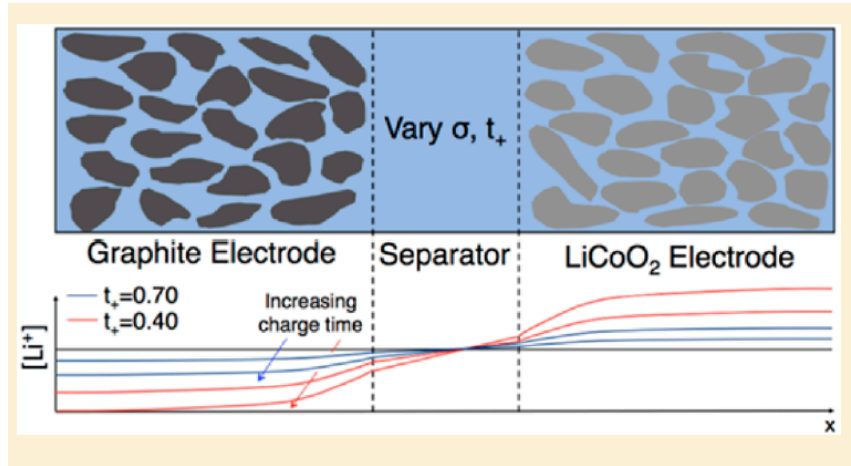


Figure 1.3: McCloskey and coworker's modelling study with Newman's model on various transference number and ionic conductivity effect on concentration gradient are presented.<sup>17</sup>

In mathematical modelling, the equation set up should be built properly to explain the physical meaning of the system. Nonetheless, the physical parameters of the applied model play a critical role to build realistic models. Hence, determining the transport properties is one of the crucial steps in numerical modelling. By its nature, experimental studies are the best way to validate system and obtain relevant transport properties, whereas optimizing the properties by the numerical studies and compared with the experimental data is more relevant for the sake of the study. In electrolyte literature, there are tremendous both experimental and theoretical studies about transport properties namely, ionic conductivity, transference number and diffusion coefficient etc. There are excellent studies which can be considered as guidelines. Liquid electrolyte has been investigated widely both experimentally and theoretically. Reimers studied the transport properties such, diffusion coefficient, transference number and salt activity of  $LiPF_6$  (PC/EC/DMC) at different temperature and different salt concentration due to the fact that  $LiPF_6$  is commonly used liquid electrolyte for commercial lithium ion batteries.<sup>18</sup> The prediction of

the cell performance at high currents was found challenging due to the strong concentration gradient and elevated temperature. Hence, diffusion coefficient and transference number were obtained experimentally. It was stated that  $\text{Li}^+$  transference number does not vary with the concentration whereas, diffusion coefficient and salt activity parameters are highly depending on the temperature and concentration of the electrolyte. The cells performance is a function of temperature. In 2017 Ehrl published a study on determining transference number in liquid binary electrolytes with  $\text{LiClO}_4$  (M) in (EC/DEC 50:50 % weight).<sup>19</sup> Theoretically, obtaining transference number by Sand equation was compared with Bruce Vincent and all the results were compared with experimental results.

Richardson and his colleagues recently published a detailed review on charge transport mechanisms in lithium ion batteries based on Newman's dilute and moderately concentrated solution theory.<sup>20</sup> In accordance with the simplicity and proven model, Newman's model has been widely used to compare experimental studies to theoretical studies.

With regard to features of concentrated solution theory, the Newman electrochemical model is also used for LiBs with polymer electrolytes with some modifications. Georén and Lindbergh published an innovative study on solid polymer electrolytes.<sup>21</sup> A macroscopic model, using concentrated solution theory was implemented to determine transport properties and thermodynamic activity factor, allowing concentration-dependent parameters. In the system copolymer of ethylene- and propylene oxide (EPO) mixture with 0.1 and 2 M LiTFSI salt were used to prepare the membrane. The characterization of the SPE was done experimentally and the numerical model was employed by using the experimentally obtained transport properties. The experimental and numerical results were fitted and compared with regard to constant properties and their concentration dependency. The multi-component diffusion equation by Maxwell–Stefan is employed to describe the transport. Overall, the numerical model was useful to test different theoretical cases; ideal versus nonideal electrolyte and locally constant properties versus concentration-dependent parameters. The model is capable of simulating electrochemical behavior of electrolyte and it can be easily adapted to study transport in gel polymer electrolyte systems

Danilov studied modelling of solid state lithium ion battery based on experimental data of thin film battery.<sup>22</sup> The detail model consisted of the charge transfer kinetics at the electrode and electrolyte interface, diffusion of lithium ion and migration and diffusion of ions in the electrolyte under different operating conditions. It was declared that the transport limitations in solid state electrolytes was related to the overpotential. The impact was much clearer with high current densities. The mathematical model was slightly different from the Newman's porous electrode theory. The reason why, the solid-state batteries are mostly made with thin film battery design.<sup>23, 24 25, 26</sup> Grazioli reported a solid state polymer electrolyte (SPE) model with a coupled ionic conduction and deformation model to enquire about the mechanical stress caused by ions' movement.<sup>27</sup> The model investigates the effect of polymer stiffness, thickness of SPE and internally induced stress under the battery operation. With regard to SPE modelling, the model is similar to Danilov's model, whereas the mechanical deformations are out of the scope of this study. However, there are excellent studies with thermo-chemo-mechanics couple SPE models.<sup>28,</sup><sup>29</sup> In 2019, Zhao published an extensive review on modelling of electro-chemo-mechanics in lithium ion batteries which includes solid electrolytes.<sup>30</sup> Furthermore, Faliya studied the charge distributions in solid state electrolytes.<sup>31</sup> As material, experimentally the most studied polymer for LIB system, PEO and lithium perchlorate (LiClO<sub>4</sub>) was chosen. The approach of the study is very different from the reported studies. Kelvin probe force microscopy (KPFM) with statistical analysis of noisy experimental data was used to measure and calculate the surface potential. Since the overpotential could be obtained by KPFM, the charge distribution was calculated by the Poisson equation under biased and unbiased conditions. Local charge oscillations inside the solid polymer were observed with respect to the oscillations in the potential. It was stated it is a relatively primary model but for the future references, it is planned to create a more efficient and reliable 3D model for hopping mechanism.

Solid polymer electrolytes are considered as an alternative for liquid electrolyte systems. However, at room temperature applications, the ionic conductivity of this type of materials is not high to maintain the cycling capability of the cell. Hence, gel polymer electrolyte has been introduced by adding a certain amount of a binary liquid electrolyte to polymer systems to increase the ionic conductivity.

One of the fundamental studies on gel polymer electrolyte system is done by Georén and Lindbergh on PC/LiClO<sub>4</sub>. This study is very unique due to the fact that it is one of the first and innovative papers on characterizing transport properties of gel polymer electrolyte for li-ion battery systems. In the study, specifically polymethylmethacrylate (PMMA) type monomer with propylene carbonate/lithium perchlorate salt solvent mixture were chosen because this system had been investigated experimentally before by several studies.<sup>32,33</sup> The mass transport was based on Maxwell- Stefan, multicomponent, mass transfer theory, electrochemically implemented by Newman's model. 0.1 and 2 M PC/LiClO<sub>4</sub> concentrations were characterized and modelled based on concentrated solution theory. The activity coefficients, and  $D_{jk}$  were utilized to be used in the following studies. Most of the studies focus solely either focus on the modelling or experimental approaches whereas, only a few studies have used the advantage of combining two different concepts. McCloskey and his colleagues' outstanding review is an outstanding example, which demonstrates significance of using two approaches.<sup>17</sup> More specifically, the group expressed the importance of high transference number especially with high c-rate applications such as electric vehicles (during acceleration) by using Newman's 1D battery model. A simple 1D model, the conventional lithium-ion battery configuration, a porous lithium graphite and lithium cobalt oxide LiC<sub>6</sub>/separator/LiCoO<sub>2</sub> with varying conductivity and transference number 1-10 mS/cm, 0.40 and 0.70, respectively. Taking into consideration the trade-off between conductivity and transference number, the outcomes were compared with the conventional liquid electrolyte (LiPF<sub>6</sub>). The impact of high transference number was observed at high current densities rather than lower in state of charge results. For instance, at 2 C-rate, 0.8 transference number with 50% lower conductivity of conventional liquid system had resulted in the same performance of liquid electrolyte. Therefore, it was concluded that the importance of  $t_+$  as well as maintaining high ionic conductivity. Beside their simulation work, it is an excellent review how to tailor polymer electrolytes to enhanced transport property polymer electrolytes.

Another important study on polymer electrolyte by means of continuum model and experimental work was done by Srinivasan group.<sup>34</sup> Instead of using only self-standing electrolyte, cathode particle LiFePO<sub>4</sub> was blended with poly(3-hexylthiophene)-bipoly(ethyleneoxide) (P3HT-PEO) copolymer, lithium bis

(trifluoromethanesulfonyl)imide (LiTFSI) lithium salt. As separator poly(styrene)-b poly(ethylene oxide) (PS-PEO) copolymer and LiTFSI was used for both experimental set-up and modelling. The fundamental focus of this study is to elaborate the nature of discharge process and state of charge of the electrode. Additionally, this model predicts the limiting factors of all type of solid state electrolytes. The mathematical model was based on Newman and co-workers' macro-homogeneous battery model. Ionic transport in copolymer binder and electrolyte were treated as in the solution phase of a porous electrode. Concentrated solution theory was used to describe the mass transport of salt in electrolyte and electrode. Butler Volmer kinetics were implemented to describe the rate of charge transfer. It was stated that electronic conductivity is depended on the potential. As a conclusion, full battery cell performance relies on the transport properties. For these type of complex electrolytes systems, the impact of ion clusters on the negative transference number is highly interesting research topic both experimentally and theoretically.<sup>35</sup>

<sup>36</sup>Electrophoretic NMR is powerful tool to determine the velocities of the ions under the applied electric field. Schönhoff and colleagues obtained with eNMR technique that  $\text{Li}^+$  drifts towards to positive electrode in complex ion clusters in lithium salt/ionic liquid mixtures at certain concentration and time range<sup>35</sup>. Balsara and Srinivasan have recently studied theoretically the negative transference number with poly(ethylene oxide)-based (PEO) and lithium bis(trifluoromethanesulfonyl) imide (LiTFSI) electrolytes. Based on Newman's concentrated solution theory, the effects of diffusion and migration driving forces on ion motion were examined. The negative transference number was observed at short time in regions far from the electrode surface. Evidently,  $\text{Li}^+$  moves in the same direction of TFSI. Thus, in this region, majority of the current is carried by the anions to compensate negative contribution of  $\text{Li}^+$  moving in the wrong direction.<sup>36</sup>



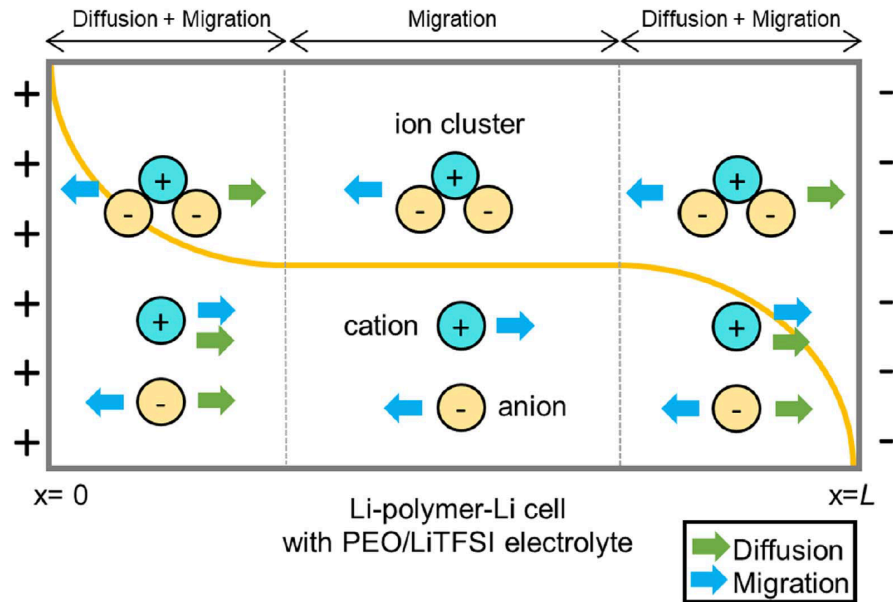


Figure 1.4: Kim and colleagues illustrated the  $\text{Li}^+$  and  $\text{Li}^+$  clusters motions in PEO/LiTFSI electrolyte with regard to the schematic. The occurrence of concentration gradient is depicted with orange line.<sup>36</sup>

Single ion conducting polymer electrolytes (SIPEs) by its definition have cation transference number of unity. Despite the large body of experimental studies, there are only a few studies regarding mathematical modelling. One of its kind, fully single ion conducting polymer electrolyte (SIPE) modelling study was published by Krewer's group in 2018.<sup>37</sup> In the study, pseudo-two-dimensional (P2D) model was used to compare the outcomes of SIPE and conventional binary electrolyte. The applied model was based Newman's work with some modifications.<sup>38</sup> At higher rates, it was reported that the potential losses in electrolyte region fairly less in SIPE case which led to higher energy than the liquid electrolyte case. In addition, the effect of the electrode thickness was investigated and resulted that SIPE are found to be suitable for thicker electrode designs. Guillon his colleagues modelled a garnet type electrolyte with high ionic conductivity based on experimental outcomes.<sup>39</sup> Jokar and his colleagues published a detailed review on Pseudo-two-Dimensional models of lithium-ion batteries. The review focused on the simplification of P2D model's equations to make it use in applications like Battery Management Systems. The study is very useful to comprehend the P2D approach in terms of how to modify the equation system by assumptions to each unique application.<sup>40</sup>

Even though, Newman's model has been employed extensively for continuum modeling studies, there are other approaches which have been used to improve the LiBs. In 2015 Salvadori and coworkers developed a novel approach for ionic transport in liquid electrolyte for lithium ion battery systems which is suitable to apply for multiscale modelling.<sup>41</sup> This model differs from the Newman's model in terms of implementing Maxwell's equations with Faraday's law of electrochemical charge transfer in order to overcome the non-constant electric field. By applying electroneutrality, the electric field becomes constant which contradicts Maxwell's equations. Since in Newman's model, electroneutrality is considered, this model does not allow scale transition. In contrast, Salvadori and coworkers' model directly allow to make the scale transition due to Maxwell's equations.

Multiscale modelling starts from atomistic scale, investigating the material properties and structure characteristics with molecular dynamics (MD) simulations and continues on macroscale modelling.<sup>42</sup> In nanometer scales, interface reactions between electrode and electrolyte take place and can be explained by continuum and MD simulations. In micrometer scale, each components of the battery are designed and modelled with respect to realistic scale. As the last scale, the whole battery system can be modelled in millimeters. Within the combination of four scales, more completed understanding of LiBs can be provided. In 2019, Franco and his colleagues published a comprehensive review on multiscale modelling.<sup>43</sup> The review consists of different types of multiscale modelling approaches and their tools and outcomes for the future of rechargeable battery systems. In terms of electrolyte modelling, atomistic scale modelling is important especially with polymer electrolytes. In literature, there are excellent studies on this topic, herein the reader is addressed to those studies due to the fact that this is not in the scope of this review.<sup>44</sup>

### **1.1.2 Organic-based Electrolytes with Enhanced Transport Properties**

The desire for high  $t_+$  and high conductivity have become the motivation for new design of electrolytes. Immobilizing the anions in a polymer backbone is one of the ways to mitigate anion diffusion and cause high  $t_+$ . With dry solid single ion conducting polymer

electrolytes, high  $t_+$  can be fulfilled, but these systems have shown to possess lower ionic conductivity.<sup>45</sup>

Besides from the organic based polymer electrolytes, there is a whole literature body on lithium inorganic electrolytes that are single ion conducting in nature. In order to keep the limited focus of the review, only organic-based electrolytes with high  $t_+$  are discussed here. Polymer electrolytes are thought to be advantageous to inorganic electrolytes on the basis of low density, flexibility, and potentially sustainability.

### 1.1.2.1 Solid-State Polymer Electrolytes

The chemistry and material properties of single-ion conducting polymer electrolytes (SIPes) have recently been reviewed by Armand and colleagues.<sup>46</sup> Here, we focus on the application of SIPes and other organic electrolytes with high lithium transference numbers in LiBs.

In 2013, Bouchet and Armand's group reported single-ion conductor, triblock copolymer polyanionic lithium 4-styrenesulphonyl(trifluoromethylsulphonyl)-poly(ethylene oxide) imide (P(STFSILi)-b-PEO-b-P(STFSILi))promising polymer electrolyte for lithium ion battery applications.<sup>47</sup> In this paper, the two different structure of PSTFSI blended with PEO were combined as single-ion BAB triblock copolymers. At 60°C, ionic conductivity measured as  $1.3 \times 10^{-5}$  S/cm which was relatively high and transference number of 0.85 was measured via electrochemical methods. The characterized SPE were assembled for a full cell cycling test to confirm the usefulness in the Li/LiFePO<sub>4</sub> configuration. At different temperatures (60,70 and 80°C) and rates, the battery showed an impressive performance for approximately 80 cycles without capacity fading. At 80 C and 2 C-rate, the discharge capacity was obtained as 138 mAh/g. Thus, this SPE study is one of milestone studies for SPE applications.

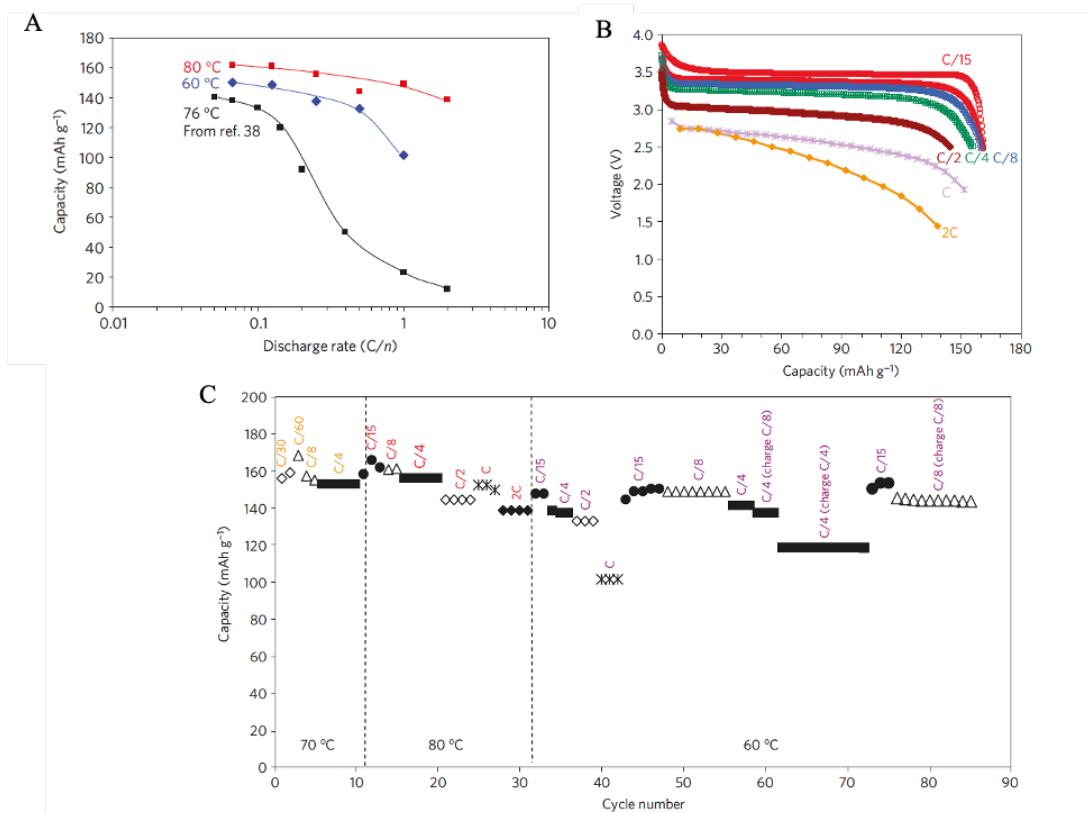


Figure 1.5: The performance of SIPE BAB triblock copolymers results are depicted in A, B and C. A shows the capacities at different C-rates and temperatures.<sup>47</sup> B presents the discharge profiles at 80 °C at different C-rates with Li/LiFePO<sub>4</sub> configuration. C shows the C-rate performances at different temperatures.

In 2016, Ma reported a single ion conducting polymer electrolyte composed of a polyanionic lithium salt, poly[(4-styrenesulfonyl) (trifluoromethyl(S- trifluoromethyl sulfonylimino) sulfonyl)imide] (PSsTFSI<sup>-</sup>) mixed with high-molecular-weight poly(ethylene oxide) (PEO).<sup>48</sup> The bound anionic groups on this polyanion have less binding energy to Li<sup>+</sup> than the PSTFSI. At 90 °C, ionic conductivity was 1.35x10<sup>-4</sup> S/cm and the transference number was almost akin to unity, 0.91. This solid SIPE is one of the highest performing reported in the literature until now. However, this study consists of only the synthesizing and the characterization of SIPE. The full cell cycling was not performed. The complex synthetic procedure to obtain the polyanion likely limits the practicality of this electrolyte.

Piszcz reported a novel single ion conducting polymer electrolyte with lithium poly[(trifluoromethyl)sulfonyl acrylamide (PA-LiTFSI) blended with PEO.<sup>49</sup> At 80 °C, ionic conductivity was measured as 1.77 × 10<sup>-5</sup> S/cm. Transference number was

measured as only 0.68; this result was explained by the authors as, even though anions were attached to polymer backbone, some ionic impurities were present. Besides, transference number measurement has been considered as a challenging technique where results may be impacted by interfacial chemistry.<sup>50</sup> A Li/PA-LITFSI/LiFePO<sub>4</sub> cell achieved 125-140 mAh/g over 5 cycles at 80°C and C/20. The over potential between charging and discharge potentials was extremely high, which was explained by the high resistivity of electrolyte and unstable SEI. The cell failed abruptly.

One of the novel and recent studies on SIPes was reported by Yuan.<sup>51</sup> Lithium poly [(cyano)(4-styrenesulfonyl) imide] (LiPCSI) was proposed as a solid polymer electrolyte for LIBs with various EO/Li<sup>+</sup> ratio. The highest ionic conductivity and transference number were obtained with PEO<sub>8</sub>-LiPCSI  $7.33 \times 10^{-5}$  S/cm at 60 °C and 0.84 respectively. Full cycling performance was reported with Li/PEO<sub>8</sub>-LiSCSI/LiFePO<sub>4</sub> configuration. The cell retained almost 100% capacity after the first couple cycles. The discharge capacity at 0.1 C-rate retained 120 mAh/g after 80 cycles. As a sign of low electrochemical stability, the over potential was compared between 1<sup>st</sup> and 80<sup>th</sup> cycle which varied among 0.06 and 0.1 V. In comparison, PEO<sub>8</sub>-LiClO<sub>4</sub> was resulted capacity fading and failure after the 12<sup>th</sup> cycle.

### 1.1.2.2 Composite Polymer Electrolytes

Composite polymer electrolytes wherein lithium-conducting inorganic electrolytes are mixed with polymer electrolytes are a growing area of research.<sup>52-56</sup> Li<sub>7</sub>La<sub>3</sub>Zr<sub>2</sub>O<sub>12</sub> structure, lithium thiophosphate glasses<sup>57, 58</sup>, Li<sub>2</sub>S-P<sub>2</sub>S<sub>5</sub> and NASICON type conductors, are some of the inorganic components that have been well-studied.<sup>59</sup> Overall, ionic conductivities at room temperature of these type electrolytes have been reported in the range of  $10^{-2}$  to  $10^{-4}$  S/cm, which is highly promising. Additionally, high Li<sup>+</sup> transference number seems to be achievable.<sup>60-62</sup> One of the recent studies has been published by Cai.<sup>63</sup> In the study, a composite solid-state polymer electrolyte was prepared which consisted of three dimensional Li<sub>6.4</sub>La<sub>3</sub>Zr<sub>2</sub>Al<sub>0.2</sub>O<sub>12</sub> (3D LLZAO) framework with conventional PEO/LiTFSI (T-LAPL). Transport properties, ionic conductivity and Li<sup>+</sup> transference number were acquired as  $2.51 \times 10^{-4}$  S/cm and 0.53 respectively. Even though the transport properties were not high as it was expected with regard to literature,

this ceramic blended electrolyte showed promising cycling performance with Li/T-LAPL/LiFePO<sub>4</sub> cell configuration. The initial discharge capacity was 165.9 mAh/g at 0.2C rate and the capacity remained 80% after 100 cycles. Similar material Li<sub>6.75</sub>La<sub>3</sub>Zr<sub>1.75</sub>Ta<sub>0.25</sub>O<sub>12</sub> (LLZTO) was used in Subramani's study.<sup>64</sup> Gel polymer electrolyte was prepared with poly (acrylonitrile-co-methyl acrylate) (P(AN-co-MA)) and 1 M LiPF<sub>6</sub>. The GPE was placed between synthesized LLZTO and LiFePO<sub>4</sub> cathode to facilitate the Li<sup>+</sup> movement. The ionic conductivity was measured for both GPE and LLZTO pellets  $1.9 \times 10^{-3}$  S/cm (20 °C) and  $2.5 \times 10^{-4}$  S/cm (25°C) respectively. Transference number of GPE was measured and calculated by Bruce-Vincent method as 0.67. Despite the presence of PF<sub>6</sub><sup>-</sup> anions in the system, the nitrile functionality in (P(AN-co-MA)) prevented the motions of anions. The full cell configuration Li|(Al/LLZTO/GPE)|LiFePO<sub>4</sub> was exhibited 94% capacity retention after 100 cycles. The high cell performance was explained by the capability of GPE to prevent the possible decomposition of solvent molecules and PF<sub>6</sub><sup>-</sup> anions at the interface at LLZTO and cathode. Besides improving the cycling performance, garnet type electrolytes are used as protective layer for lithium metal.<sup>65</sup>

### 1.1.2.3 Gel Polymer Electrolytes

As it was discussed previously, solid polymer electrolytes have resulted with lower ionic conductivity and been required to be operated at high temperatures for applicable lithium-ion battery systems. Beside the improvement of SPEs, solvent-polymer interaction and the solvent effect on the ion transport have gained prominence. Using the advantages of a single ion conducting polymer with the presence of different solvents or solvent mixtures have been applied at room temperature. One of the examples has been reported recently by Ford.<sup>66</sup> The crosslinked gel polymer electrolyte was based on poly(tetrahydrofuran) diacrylate (PTHF) with ionic monomer STFSI (styrene-SO<sub>2</sub>NSO<sub>2</sub>CF<sub>3</sub><sup>-</sup>). The comparison was done with poly(ethylene glycol)diacrylate (PEGDA) by having the same features. Ionic conductivity of PTHF and PEGDA crosslinked electrolytes in dry states at 25°C were  $3.1 \times 10^{-11}$  S/cm and  $4.6 \times 10^{-9}$  S/cm respectively. At 25°C, ionic conductivities were acquired for PTHF one in 1,3-dioxolane/dimethoxyethane (DOL-DME),  $2.7 \times 10^{-5}$  S/cm and in ethylene carbonate and

diethyl carbonate (EC-DEC)  $1.2 \times 10^{-4}$  S/cm. The improvement of the conductivity by addition of the solvent was substantial. Limiting current measurements were performed with PTHF membrane in EC/DEC and DOL/DME solvent mixtures. Despite the incompatibility of EC/DEC solvent mixture and lithium metal, the PTHF thick membrane achieved a limiting current density of 1 mA/cm<sup>2</sup>.

Different types of single ion conducting polymers have been developing to enhance the high transport properties.<sup>67</sup> Deng studied on SIPE based on sp<sup>3</sup> boron network.<sup>68</sup> At 25°C,  $1.47 \times 10^{-3}$  S cm<sup>-1</sup> ionic conductivity was achieved. The transference number was close to unity 0.89. Above all, the full cell cycling with Li/SIPE/LiFePO<sub>4</sub> delivered 124 mAh/g capacity with 1 C-rate after 500 cycles. Another boron containing a single ion conducting polymer electrolyte was reported by Chen.<sup>69</sup> In EC/DMC/LiClO<sub>4</sub> solvent solution poly (ethylene glycol) methyl ether methacrylate (PEGMA) with ABAPE was polymerized, ionic conductivity and transference number were acquired  $2.23 \times 10^{-3}$  S/cm and 0.71 respectively among the variations of weight percentages. The full cycling measurement was done with Li/SIPE/LiFePO<sub>4</sub> configuration and resulted approximately 130 mAh/g discharge capacity and 90% capacity retention after 100 cycles. Similar solvents are used for different SIPEs for LiBs.<sup>70, 71</sup>

Zhang investigated two different polymer matrixes as the backbone pentaerythritol tetrakis (2-mercaptoacetate) (PTMP) and pentaerythritol tetraacrylate (PETA) with lithium (4-styrenesulfonyl) (trifluoromethanesulfonyl) imide (-STFSI) ionic monomer.<sup>71</sup> The difference from the previous studies was the crosslinked SIPEs were not self-standing and instead polymer solutions were crosslinked on polypropylene (PP) nonwoven fabric. The ionic conductivity at room temperature was  $8.4 \times 10^{-4}$  S/cm, whereas the transference number was measured at 0.93 in the solvent mixture of ethylene carbonate-dimethylene carbonate (EC-DMC). Li/LiFePO<sub>4</sub> cells with this polymer electrolyte showed an excellent performance with 83% capacity retention after 400 cycles at 1 C. The performance was compared with a liquid electrolyte under the same conditions which resulted in 50% better capacity for 400 cycles.

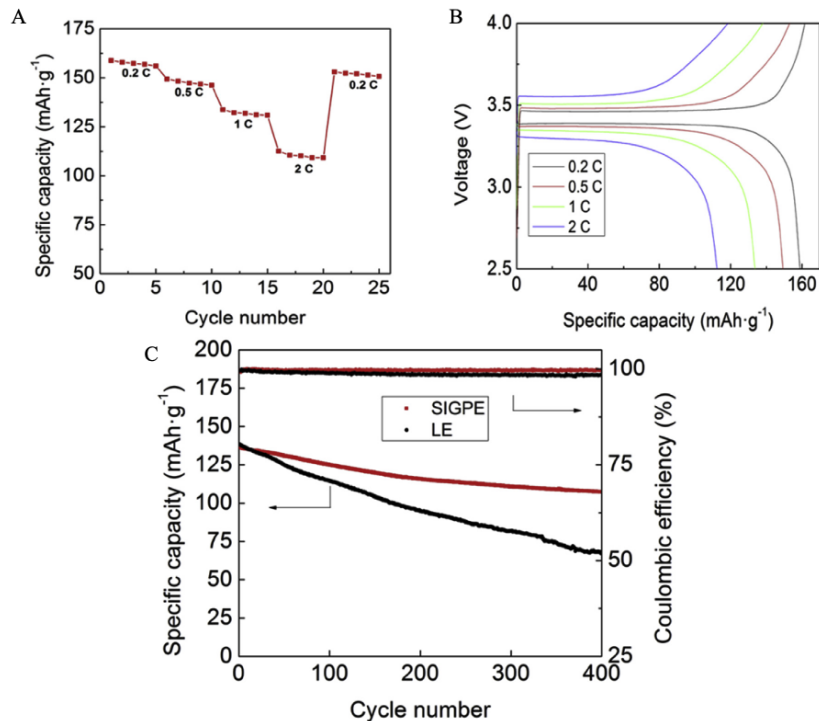


Figure 1.6: Zhang and colleagues' study on SIPE full cell cycling performance with Li/LiFePO<sub>4</sub>.<sup>71</sup> C shows the comparison between SIPE and liquid electrolyte after 400 cycles.

In order to overcome the low ionic conductivity problem, another solution is to use a liquid electrolyte in combination with a polymer matrix to yield a gel polymer electrolyte (GPE). However, the safety issues can be still questioned in terms of flammability, leakage etc. with the addition of solvents/electrolyte to the system.<sup>72</sup> In some of GPE studies states that the overall safety can be improved by decreasing the amount liquid electrolyte, in comparison to binary liquid electrolytes.<sup>73</sup> GPEs are not only having relatively high ionic conductivity but also better interfacial properties from the liquid phase. In addition, polymer in the electrolyte system can satisfy the desired mechanical properties. Figure 1.7 illustrates some of the high performance GPEs for various LiBs.



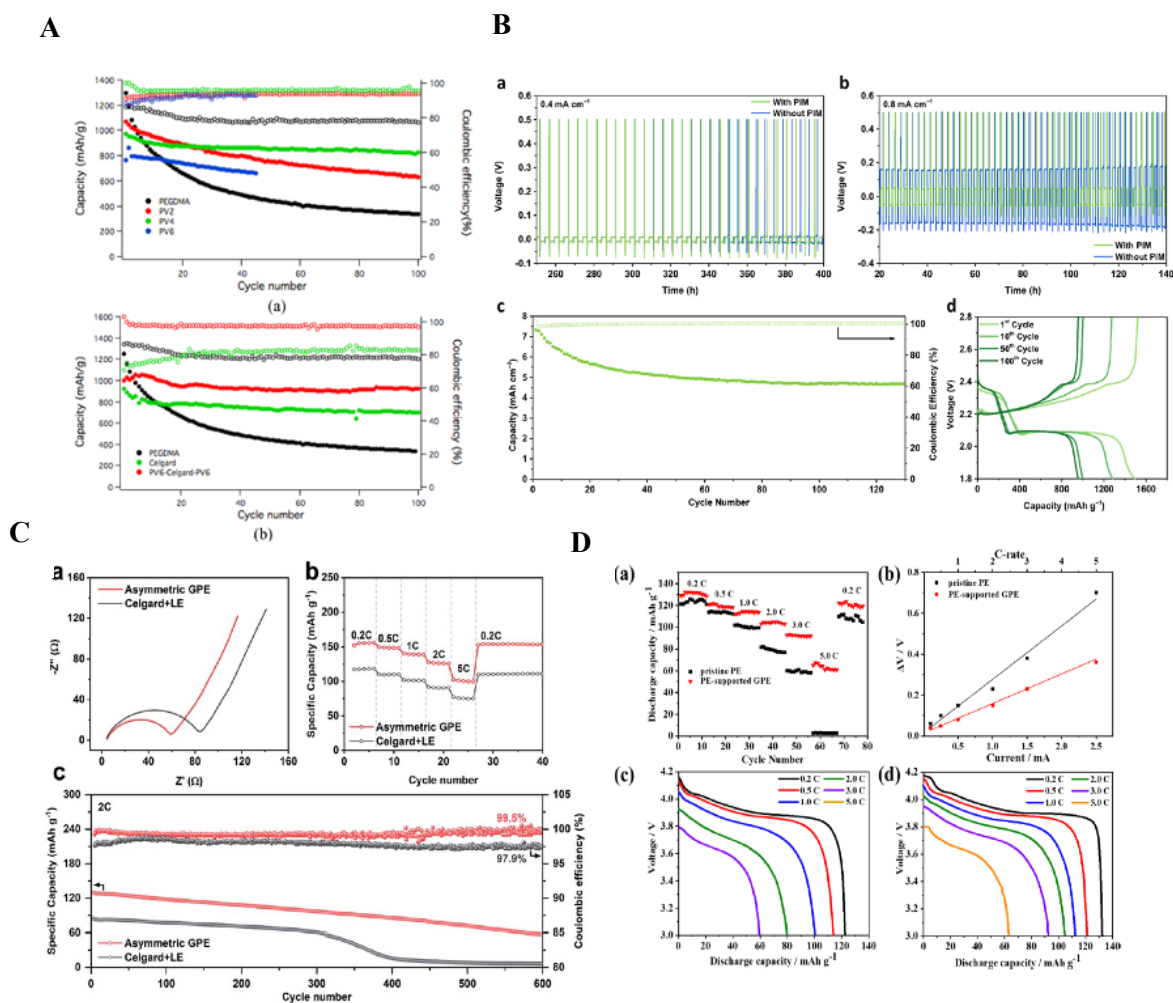


Figure 1.7: Various GPE LiBs full cell performances. A illustrates Archer's group study, GPE performance in Li-S battery.<sup>74</sup> The coulombic efficiency after 100 cycles is 98%. Under the same conditions, with celgard, the efficiency of the cell is 20%. B is the summary of Helm's group GPE's outstanding performance in Li-S cell.<sup>75</sup> C and D are the Li/LiFePO<sub>4</sub> cycling performances of GPEs in 1 M LiPF<sub>6</sub>.<sup>73, 76</sup>

Despite the listed advantages of GPEs, only few studies have been reported that have high  $t_{Li+}$  and high cyclability. Archer's groups' study, one of the most compelling GPE in the literature with  $1.14 \times 10^{-3}$  S/cm at 20 °C and exceedingly high  $t_{Li+}$ . The membrane was composed of crosslinker polyethylene glycol PEG containing SO<sub>3</sub><sup>-</sup> pendant with the addition of 1 M LiTFSI (DOL-DME).  $t_+$  of the system is reported as an impressive 0.96 which may be the highest transference number ever reported for a gel electrolyte containing free salt.<sup>74</sup> The high performance membrane was utilized in Li-S configuration. The Coulombic efficiency of the cell was obtained 98% for more than 100 cycles. Application of GPEs is promising for Li-S battery systems.<sup>77</sup> Following this, Wang reported polyethylene (PE) supported gel polymer electrolyte based on poly(ethylene glycol)

dimethacrylate (PEGDMA) with delocalized  $\text{SO}_3^-$ , using 1 M  $\text{LiPF}_6$  which has  $4.5 \times 10^{-4}$  S/cm at room temperature with  $0.72 t_+$ .<sup>76</sup> In conjunction with comparatively high transport properties, cycling performance for Li/GPE/ $\text{LiFePO}_4$  has improved significantly. Using additional  $\text{LiPF}_6$  in GPE has resulted high performance LiBs.<sup>73</sup> A comparative study between SIPEs and GPE based on a highly porous lithium sulfonated polyether ether ketone electrospun nanofiber membrane es-LiSPCE was published by He.<sup>78</sup> Besides the comparison, the porous structure of the polymer is of the striking point of the study. With regard to  $t_+$ , single ion conducting es-LiSPCE-ns resulted in a value of 0.89. es-LiSPCE-s gelled with 1 M  $\text{LiPF}_6$  showed slightly lower performance at 0.52 due to high mobility of  $\text{PF}_6^-$  anion. Room temperature measured conductivities for es-LiSPCE-ns and es-LiSPCE-s were  $1.45 \times 10^{-4}$  S/cm,  $2.53 \times 10^{-3}$  S/cm respectively. An outstanding cycling performance was achieved with es-LiSPCE-s at 6C over 600 cycles with 130.6 mAh/g in Li/ $\text{LiFePO}_4$  configuration.

Another common point of these reported studies is that GPEs are based on crosslinked polyethylene glycol PEG. However, there are other materials that can be used as a polymer backbone to make GPEs. For instance, Du described cellulose based gel polymer electrolyte with high transport properties, exhibiting a room temperature conductivity of  $6.34 \times 10^{-3}$  S/cm with a lithium transference number of 0.82. 1 M LiTFSI in DMSO was used as liquid electrolyte.<sup>79</sup> The full cell cycling was performed with Li/GPE/ $\text{LiNi}_{0.5}\text{Co}_{0.2}\text{Mn}_{0.3}\text{O}_2$  configuration and was resulted 122 mAh/g discharge capacity at 0.2C after 50 cycles. Recently, Kou reported high transference number gel polymer electrolyte by modifying widely used polymer backbone, P(VDF-HFP) with porous carbon nano powder.<sup>80</sup> Different weight ratios of porous carbon powder were doped in the P(VDF-HFP) matrix at 3% by weight, which resulted in a  $3.92 \times 10^{-3}$  S  $\text{cm}^{-1}$  ionic conductivity in the presence of 1 M  $\text{LiPF}_6$  (EC/DMC/EMC 1:1:1) liquid electrolyte. Even though, transference number was not reported, the full cycling Li/GPE/ $\text{LiCoO}_2$  was resulted with more than 90% columbic efficiency. PVDF-HFP has been an attractive material for GPE applications.<sup>73, 81, 82</sup>

Zhao studied a combined polymer backbone with PEG and cellulose as gel polymer electrolyte application.<sup>83</sup> Ionic conductivity was measured  $3.31 \times 10^{-3}$  S/cm and with 5% PEG in the polymer, transference number was 0.63. This study shows that sustainable and

different polymers can be modified with traditional and already proven polymer backbones to create better electrolytes in terms of transport properties for lithium-ion batteries.

Additionally, Kim and colleagues recently published a study on amine-functionalized boron nitride nanosheets as gel electrolyte for lithium ion battery systems with different cathodes.<sup>84</sup> At room temperature, ionic conductivity measured  $6.47 \times 10^{-4}$  S/cm,  $0.23 t_+$  with 1 M LiTFSI. In comparison to the similar examples, the transport properties are low, but it encourages using different materials to push forward the GPEs for Li-ion battery research area. Another significant point of this study is that some part of it was supported with finite element simulations. Therefore, it brings the importance of predicting performances of the systems with modelling. Up to now, some of the remarkable and recent experimental studies on gel polymer electrolytes have been mentioned.

#### **1.1.2.4 Polymer Electrolyte Applications on Lithium Metal Anode**

Lithium metal anode is highly beneficial for lithium ion battery systems due to its extremely high theoretical capacity (3860 mAh/g).<sup>85</sup> However, during the battery operation the capacity cannot be reached because of the unstable interface between electrolyte and the electrode which is caused by the very reactive nature of lithium metal. Therefore, the battery starts to face low Coulombic efficiency and lithium dendrite formation.

Lithium dendrites, uneven deposition of lithium on the lithium metal surface during the cell cycling is one of the challenges for usage of lithium in particle devices. The formation of lithium dendrites limits the battery lifetime and compromises the safety. The type of the electrolyte directly responsible for the nucleation of dendrites. There are several models to evaluate the dendrite nucleation. Chazalviel proposed a theory on lithium dendrite nucleation which was based on the existence of anions near the negative electrode surface.<sup>86</sup> Timescale for dendrite nucleation is based on anion depletion on the electrode surface. The growth of the dendrites is due to the velocity of anions which depends on the mobility ( $\mu$ ) and the electric field, ( $v_i = -\mu_i E$ ). In 1992, the theory was modified by taking into consideration the electro-convection during the electro-deposition and the experimentally, it was shown that the growth of the lithium dendrites was linked to the current densities. On the contrary, Newman and Monro's theory relied on the elasticity of separators.<sup>87</sup> The main point of the model is that using high mechanical strength materials

as a separator could eliminate the growth of lithium dendrites. The most recent theory is developed by Archer's group which developed Chazalviel's theory by taking into consideration the effect of partially fixed anions in a solid electrolyte.<sup>88</sup> There are excellent studies and reviews on specifically targeting the lithium dendrite formation which are suggested for reader's interests.<sup>89-91</sup> In consideration of all these models polymer electrolytes are suggested to reduce the formation of lithium dendrites on the lithium metal surface. In accordance with the theoretical studies, concentration gradients are one of the reasons for lithium dendrites. By restricting the anion motion and increasing the cation transference in the electrolyte could be a possible solution to prevent the dendrite nucleation.

In 2016 Tikekar's study covered the basic principles of designing electrolytes and interfaces for stable lithium metal batteries.<sup>92</sup> Lithium dendrite growing on the lithium metal surface was explained in detail and possible approaches were suggested, improving transport properties; cation transference number, high ionic conductivity and developing the mechanics of the electrolytes. Another method is to coat polymer on the lithium metal surface to suppress the dendrite formation as well as enhancing high transport properties. Until now, this application is limited to several studies. Archer's group reported nanometer thick artificially formed SEI by using lithiated ionomers on a lithium metal surface.<sup>93</sup> Depending on the thickness of the layer, S/cm ionic conductivity and 0.9  $\text{Li}^+$  transference number were obtained. Visual electrochemical deposition showed lithium dendrite suppression was observed as compared to pristine lithium. More recently, Helms group's nanoporous polymer film study has remarkable outcomes in terms of high transport properties and lithium metal surface coating application.<sup>75</sup> Despite the presence of free anions ( $-\text{TFSI}^-$ ) in the system, the lithium transference number obtained was 0.72. It was claimed that at polymer-electrolyte interface, counter ions from the electrolyte may be rejected due to their larger sizes. Hence,  $\text{Li}^+$  is the only one that can diffuse in the pore network. Even though controlling lithium dendrite formation is out of the scope of this paper, in terms of lithium surface coating, the study depicts very promising results.

## 1.2 Outline and Summary

High energy density and power density of battery is a highly desired goal of the future sustainable solution for transportation and energy solution. Study on high performance lithium-ion battery by means of high transport property electrolytes is summarized with the most recent and fundamental studies with regard to experimental and modelling approach.

Liquid, binary salt containing, electrolytes are still the state of the art in lithium-ion batteries due to its high concentration despite low transference number. However, the polymer based electrolyte studies have been investigated broadly and those could lead the future direction of electrolyte for lithium ion batteries. Polymer electrolytes with additives, tethered anions on the polymer backbone and dispersed in solvent mixture or dual ion electrolytes with proper polymer structure could be one of the driving features for electrolytes with enhanced transport properties.

Continuum lithium-ion battery models with focusing on the transport properties in electrolyte have been investigated broadly. The study reveals the progresses made since the pioneering publications and made clear that modelling has been becoming more accurate and predictive with the advanced techniques.

Improving the transport properties of the electrolyte has been an important research area for experimental studies. Herein, we specifically focus on the polymer electrolyte as single ion conducting polymer electrolytes or liquid electrolyte in polymer systems. However, there are other potential systems to lead high transference number such as, lithium ceramics<sup>94</sup>, liquid solutions; polyelectrolyte solutions<sup>95</sup>, solvent in salt systems<sup>96</sup>.

In this dissertation, we would like to focus on the importance of combining modelling and experimentally studies. In order to make accurate cell prediction, the transport properties  $\sigma$ ,  $D$ ,  $t_+$  must be known with high accuracy from experimental measurements. First, liquid electrolyte in polymer systems is going to be discussed in detail experimentally. Specified polymer backbones and ionomers with conventional liquid electrolyte are used in two chapters. The following chapter is SIPE modelling based on the experimental evidences with a set partial differential equations. As the last chapter, the impact of the electrode surface on the performance of the conventional lithium-ion battery is examined.

## 2. Chapter 2- Investigation of Condensed Gel Polymer Electrolytes

### 2.1 Introduction

In battery systems, the electrolyte is a crucial component in terms of transport of ions across the battery. In conventional lithium-ion batteries, there is a liquid electrolyte which consists of a binary salt dissolved in an organic carbonate mixture with an inert separator. Despite the severe side effects, such as concentration gradient formation which triggers lithium dendrite formation, conventional liquid electrolyte has still been used broadly in current devices. However, development of an advanced electrolyte is essential for next-generation systems with enhanced performance. Organic liquid electrolytes have low transference number,  $t_+$ , due to free anion mobility which leads to the formation of concentration gradients. The presence of a concentration gradient in an operating cell causes substantial polarization in cases of high charge and discharge rates and non-uniform lithium deposition on the electrode.<sup>97</sup> Therefore, single ion conducting polymer electrolytes (SIPES) in which anions are immobilized in the polymer backbone, permitting only cation mobility in the polymer matrix, are researched. These systems have a favorable high transference number, but they have lower ionic conductivity at room temperature ( $10^{-4}$  to  $10^{-5}$  S/cm). Herein, to increase the number of charges and mobility, a certain amount of conventional liquid electrolyte is introduced to the SIPE. Lithium salt can affect the polymer system in a different way such as dissociation and association degrees of the ions. We aim to investigate the impact of presence of both bonded charges and the free salt on the system.

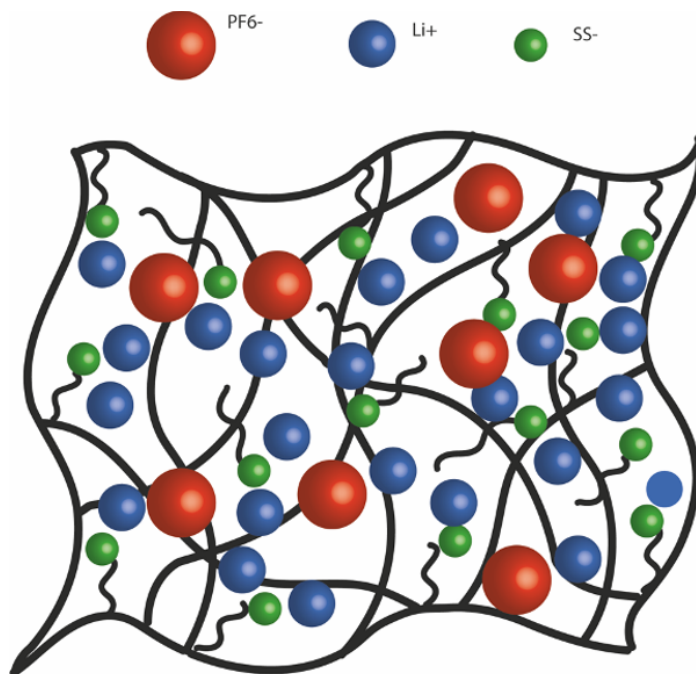


Figure 2.1: Schematic of crosslinked PEGDA-SS membrane in 1 M  $\text{LiPF}_6$ . The green spheres represent the bonded anions on the PEGDA backbone, the blue spheres are the lithium cations. The red spheres are the mobile  $\text{PF}_6^-$  anions.

In this chapter, the bonded charges on the polymer backbone and the impact of free charges from the liquid electrolyte were investigated. Poly(ethylene glycol) diacrylate (PEGDA) membranes are made with varying ether oxygen to charge ratios, with the impact of different ether oxygen to charge ratio (EO=Ch) ratio on transport properties being evaluated. Figure 2.1 shows a schematic of the ionic species in this type of gel polymer electrolyte with both bound and free anions and counter lithium cations.

## 2.2 Experimental Section

### 2.2.1 Synthesis of Crosslinked Polymer Electrolyte (PEGDA-NaSS)

The appropriate amount of the monomer 700 g/mol poly (ethylene glycol) diacrylate (PEGDA) was dissolved in dimethyl sulfoxide (DMSO, Sigma Aldrich). The exact mass varied with EO=Ch ratios and the values for each membrane are shown in Table 1. Sodium 4-vinylbenzenesulfonate (NaSS, Sigma Aldrich) was added into the solution in accordance with the relevant EO=Ch ratios. The solution was stirred until NaSS was

completely dissolved. To this monomer solution, the photoinitiator 2-hydroxy-4'-(2-hydroxyethoxy)-2-methyl propiophenone (Sigma-Aldrich) was added and dissolved. The monomer solution was sandwiched between two 1/4 in. thick borosilicate glass plates (McMaster Carr) separated by 200  $\mu\text{m}$  thick glass microscope slides (VWR), which were then placed in a UVC-515 Ultraviolet Multilinker 254 nm UV oven. The plates were flipped every two minutes to ensure both sides of the solution received equal UV radiation. The monomer solutions were photo-crosslinked for a total of 45 minutes. Afterwards, the polymer films were washed with DMSO to remove any unreacted material. The films were then placed in a stirred ion exchange solution of 0.5 M lithium chloride to achieve lithiated forms of the polymer. The ion exchange solution was replaced every 12 hours for 48 hours, after which free salt was washed from the films by repeating the same process but with deionized water that does not contain salt. The films were air dried for two days, brought into an argon filled glovebox ( $< 10$  ppm  $\text{O}_2$ ,  $< 0.1$  ppm water) and vacuum dried for 16 hours at  $80^\circ\text{C}$  to remove residual solvent. Ion exchange was confirmed stoichiometrically via inductively coupled plasma-optical emission spectroscopy (ICP-OES).



Table 2.1: Compositions, formulations, ether oxygen: charge ratio (EO=Ch), and charge density for studied SIPEs.

| Sample Name   | Crosslinker      | Crosslinker mass (g) | NaSS (g) | DMSO (g) | Photoinitiator (g) | EO=Ch | Charge Density (mol Ch/g dry polymer) |
|---------------|------------------|----------------------|----------|----------|--------------------|-------|---------------------------------------|
| PEGDA-control | PEGDA, 700 g/mol | 0.7500               | -        | 1.1121   | 0.0007             | -     | 0                                     |
| GPE-6         | PEGDA, 700 g/mol | 0.4582               | 0.2918   | 1.1121   | 0.0014             | 6     | 0.0019                                |
| GPE-8         | PEGDA, 700 g/mol | 0.5079               | 0.2421   | 1.1121   | 0.0013             | 8     | 0.0016                                |
| GPE-12        | PEGDA, 700 g/mol | 0.5696               | 0.1804   | 1.1121   | 0.0011             | 12    | 0.0012                                |
| GPE-20        | PEGDA, 700 g/mol | 0.6298               | 0.1202   | 1.1121   | 0.0010             | 20    | 0.0008                                |

### 2.2.2 Solvent and Salt Drying

Electrolyte salts, solvents including anhydrous 1,3-dioxolane (DOL) and anhydrous 1,2-dimethoxyethane (DME), and solvent mixtures that were used for electrolyte preparation, conductivity, transference number measurement and coin cell applications were obtained from Sigma Aldrich and were stored over 3 Å molecular sieves for at least four days before use to ensure low moisture content.

### 2.2.3 Electrolyte Preparation

1 M lithium bis(trifluoromethanesulfonyl)imide (LiTFSI) in a 1:1 volume DOL and DME mixture was prepared. In an argon filled glovebox, LiTFSI salt was dried under

vacuum at 120 °C for 12 hours. LiTFSI was added to the DOL-DME mixture and dissolved. The electrolyte was kept and used within an argon filled glovebox.

The second electrolyte, 1 M lithium hexafluorophosphate ( $\text{LiPF}_6$ ) in a 1:1 volume ethylene carbonate (EC) (Sigma Aldrich) and diethyl carbonate (DEC) (Sigma Aldrich) solvent mixture was prepared. The solvent mixture of EC-DEC (1:1 volume) was prepared in an argon filled glovebox and dried with 3 Å molecular sieves for two days. The water content in EC-DEC (1:1) solvent was measured via the Karl Fischer (KF) titration method (< 25 ppm).  $\text{LiPF}_6$  salt was added and dissolved in the EC-DEC mixture. For a portion of this study, a 1 M  $\text{LiPF}_6$  EC-DEC (50:50 volume) (Sigma Aldrich) solution was also used.

#### **2.2.4 ICP-OES - Sample Preparation**

To prepare samples for ICP-OES analysis, samples must be in either gas or liquid form in order to be processed efficiently in the plasma. In order to achieve this, both dry and swelled state polymers were digested in nitric acid. In accordance with prepared standards, the desired concentration of digested polymer was 1 ppm. In the case of 1 M LiTFSI (DOL-DME) or 1 M  $\text{LiPF}_6$  (EC-DEC) electrolyte swelled membranes, prior to the digestion process, the samples were wiped with a Kimwipe tissue to remove any excess electrolyte from the surface and were dried under vacuum at 80°C for 12 hours. Dry samples were weighed and taken out from the glovebox. The digestion process took place in the fume hood. Before starting the digestion, volumetric flasks, single neck round bottom flask, and disposable glass pipets were washed with 5% nitric acid ( $\text{HNO}_3$ ) and rinsed with deionized water three times to eliminate contamination. The polymer samples were put in the single neck round bottom flasks and 10 ml concentrated  $\text{HNO}_3$  was added. The flask was connected to condenser columns and placed within an oil bath. The digestion process took place for twelve hours at 250°C. The final digested solution was then transferred into 100 ml volumetric flasks and diluted with deionized water to 5%  $\text{HNO}_3$  and 95% water.

#### **2.2.5 ICP- OES – Standard Preparation**

Lithium standards for ICP-OES calibration were prepared in the range of 0.16 ppm, 0.4 ppm, 0.8 ppm, 1.6 ppm and 2 ppm. The volumetric pipets and volumetric flasks used in this process were washed with 5%  $\text{HNO}_3$  and rinsed with deionized water three times.

A 1000 ppm lithium standard was obtained from Sigma Aldrich and diluted with deionized water to 100 ml and 250 ml lithium standards in volumetric flasks. From the 100 ml lithium standard solution, 0.4 ppm and 2 ppm standards were made via dilution. From the 250 ml lithium standard solution, 0.16 ppm, 0.8 ppm and 1.6 ppm standards were prepared in the same manner.

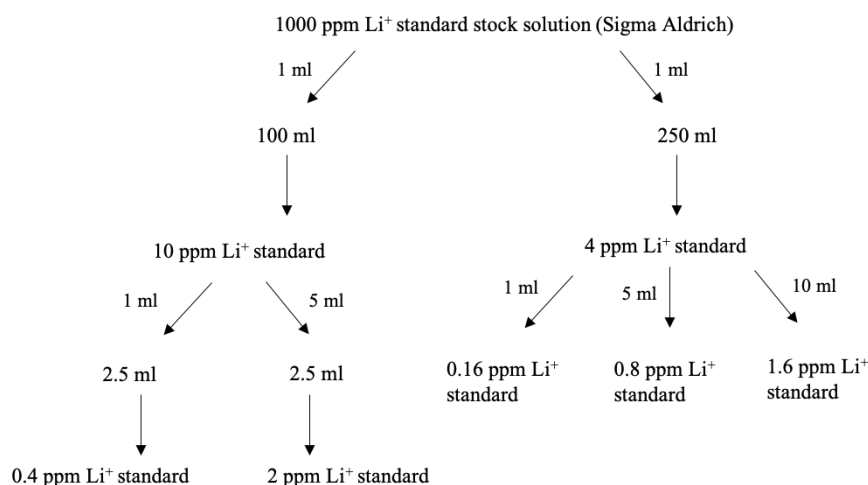


Figure 2.2 : ICP-OES standards preparation process for the calibration.

## 2.2.6 ICP-OES - Measurement

The prepared polymer samples and lithium standards were put in 15 ml sample tubes. The concentrations of lithium were measured using a Perkin Elmer Optima 800 ICP-OES. The lithium standard solutions and samples were placed in the sample holder. With regard to standards, first the calibration curve was prepared by the program itself and later on, the samples were measured one by one. Each sample measurement took approximately two minutes. The results were evaluated according to the intensity vs. concentration (ppm) calibration.

## 2.2.7 Solvent and Electrolyte Uptake Test

Uniform 1/2 in diameter samples of polymer were prepared in the dry state. The diameter and thickness of each polymer were measured and weighed in the dry state. From the previous report, the polymer samples which are swelled in electrolytes or solvents reach equilibrium in four hours.<sup>98</sup> In this study, the polymers were swelled in electrolytes or

solvents for twenty-four hours. Three samples each of GPE-6, 8, 12 and 20 were swelled in 1 M LiTFSI (DOL-DME 1:1 volume) or 1 M LiFF<sub>6</sub> (EC-DEC 1:1). Before the membranes were swelled in electrolyte, each sample was weighed, and the dimensions (thickness and diameter) were measured with a micrometer (Mitutoyo No. 293-349-30). Each of the samples were placed in a vial and covered with parafilm to limit the exposure to moisture. The polymers were soaked in the electrolyte for twenty-four hours. The excess electrolyte was removed from the polymer surface with a Kimwipe tissue and the dimensions (diameter, thickness) and mass uptake were measured.

### **2.2.8 Conductivity Measurement**

Each GPE sample was swelled in either 1 M LiTFSI (DOL-DME 1:1) or 1 M LiFF<sub>6</sub> (EC-DEC 1:1) electrolyte, as well as either DOL-DME or EC-DEC solvent mixture at least four hours prior to the conductivity measurement. The polymer membranes were removed from the electrolyte solution and the excess amount of electrolyte was removed with Kimwipe tissue prior to measurement of the thickness. The sample thickness is necessary information for using the Novocontrol Turnkey Broadband Dielectric Spectrometer. After that, the GPEs were rinsed with electrolyte or solvent and sandwiched between brass electrodes within the glovebox. The Novocontrol Turnkey Broadband Dielectric Spectrometer was used to measure conductivity over the temperature range of -20 °C to 85 °C from cold to hot at an increment of 15°C. The  $\sigma_{DC}$  was extracted as the region over which a plateau in the  $\sigma_{AC}$  vs frequency was observed.

### **2.2.9 Lithium Symmetric Cells – Transference Number Measurement**

In the glovebox, lithium metal (Alfa Aesar, 0.75 mm thick, 99.9 %) was polished to remove the oxide layer. Two 3/8 in. diameter lithium pieces were punched from this polished lithium metal. Beforehand, 1/2 in. diameter GPE films were swelled in 1M LiTFSI (DOL-DME 1:1) electrolyte for 24 hours. Within 2032 type coin cells (MTI Corp), the lithium metal was placed and wetted with 20  $\mu$ L of electrolyte. The swelled GPE was then inserted in between. Two stainless steel spacers (15.5 mm diameter x 0.2 mm thick) and one wave spring were used, and the coin cell was sealed with an electronic crimper. An

Ametek Princeton Applied Research Parstat MC was used for the impedance spectroscopy and evaluation of  $t_{Li+}$  measurements.

### **2.2.10 Cathode Preparation – LiFePO<sub>4</sub>**

Lithium iron phosphate (LiFePO<sub>4</sub>) powder (MTI Corporation) was mixed with Carbon Black (MTI Batch No. 0011512) and polyethylene oxide (PEO) (100K g/mol) at a mass ratio of 60:20:20. 300  $\mu$ L of acetonitrile (CH<sub>3</sub>CN) was added to the mixture and stirred overnight. The cathode slurry was spread onto aluminum foil and casted with a doctor blade at a thickness of 200  $\mu$ m. The cathode sheet was transferred into a glovebox and dried at 90°C under high vacuum for 12 hours to remove residual CH<sub>3</sub>CN and water. Upon completing the drying process, the prepared cathode sheet was punched into 3/8 in. circular pieces to be used in coin cell applications.

### **2.2.11 Li/LiFePO<sub>4</sub> Cells - Galvanostatic Cycling**

In the glovebox, lithium metal (Alfa Aesar, 0.75 mm thick, 99.9 %) was polished to remove the oxide layer. One 3/8 in. diameter lithium piece was punched from the polished lithium metal. With the same diameter punch, one piece of LiFePO<sub>4</sub> (thickness 50–60  $\mu$ m) was cut from the dried cathode sheet. A 1/2 in. diameter punch of polymer membrane was swelled in 1M LiTFSI (DOL-DME 1:1 v%) or 1 M LiPF<sub>6</sub> (EC-DEC 1:1 v%) electrolyte until it reached equilibrium. Inside 2032 type coin cells (MTI Corp), the LiFePO<sub>4</sub> cathode was wetted with 20  $\mu$ L electrolyte to increase the contact with the GPE film. Before placing the lithium metal, an additional 10  $\mu$ L electrolyte was added on the GPE film. Two stainless steel spacers (15.5 mm diameter x 0.2 mm thick) and one wave spring were used, and the coin cell was sealed with an electronic crimper. A Neware Battery Systems Battery Tester was used for galvanostatic cycling.

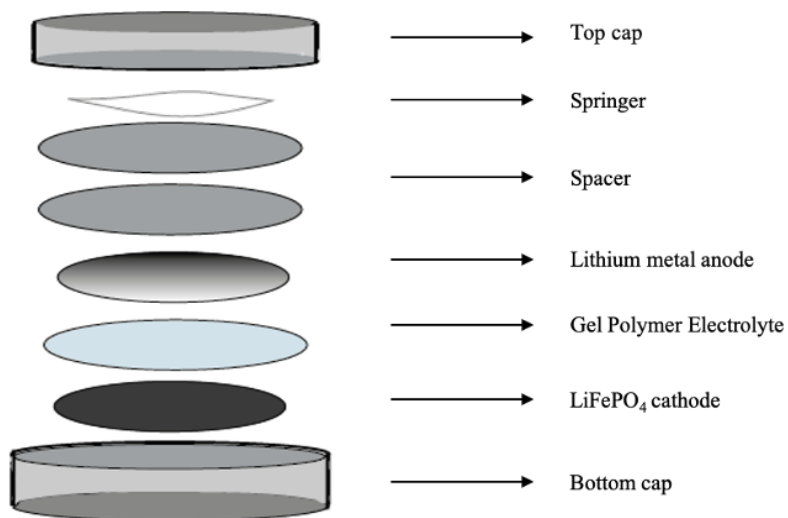


Figure 2.3: A sketch of coin cell assembly.

## 2.3 Results and Discussion

### 2.3.1 Polymer Synthesis and composition (PEGDA-SS)

The gel polymer electrolyte system under investigation was prepared with the crosslinker PEGDA-700 g/mol which contains one oxygen and two  $-CH_2-$  groups per repeat unit  $-(OCH_2CH_2)_n-$  and the sodium 4-vinylbenzenesulfonate (styrene sulfonate - SS) ionic monomer. Five different compositions of ether oxygen: charge ratio (EO=Ch) namely, 6, 8, 12 and 20 were prepared with PEGDA of molecular weight 700 g/mol with NaSS as the ionic unit. As a control membrane, pure PEGDA 700g/mol was prepared. The detailed composition of each sample is shown in Table 2.1. The molecular weight of crosslinker was held constant, while the ether oxygen: charge ratio was varied. The effects of this on the charge density in relation to the conductivity, transference number and cycling was investigated. For the following sections, PEGDA-SS EO=Ch (6, 8, 12 and 20) are hereby referred to as GPE-6, GPE-8, GPE-12 and GPE-20 respectively.

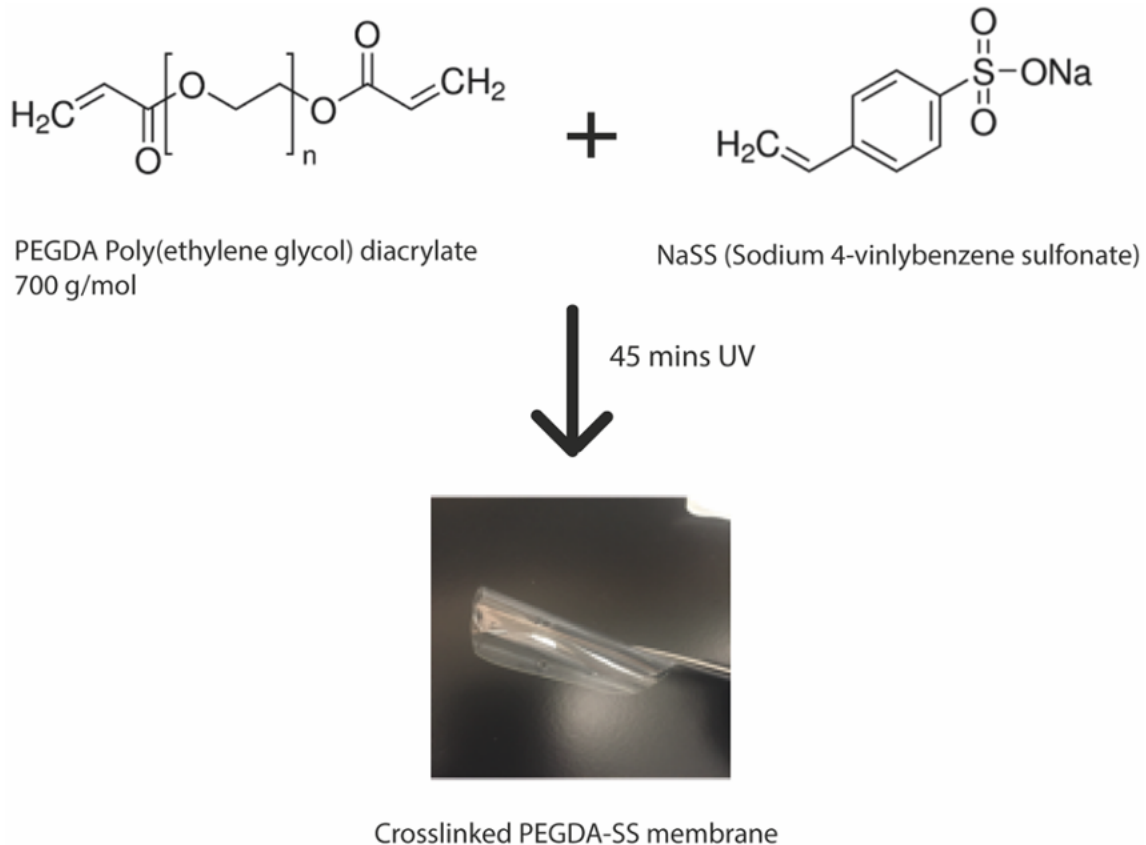


Figure 2.4: Structural schematics of the components of PEGDA-SS and film fabrication.

### 2.3.2 Electrolyte Uptake Measurement

In order to observe the swelling ratio of each GPE film, three samples of GPE-6, 8, 12, and 20 were swelled in 1 M LiTFSI (DOL-DME 1:1 volume) for 24 hours and isotropic expansion is assumed. Before swelling, each sample was weighed, and the thickness and diameter was measured. Upon reaching equilibrium, the masses of the swelled samples were recorded. The electrolyte uptake ratio was calculated using equation (1).

$$\% \text{ swelling ratio} = \frac{m_{\text{swelled}} - m_{\text{dry}}}{m_{\text{dry}}} \times 100 \quad (1)$$

Regarding the ether oxygen density, the variation on uptake is demonstrated on table 2.2. Electrolyte uptake capability of the polymers is dependent on the polymer characteristics, such as charge density, and can be varied regarding the solvent types. With varying charge densities, the swelling ratio can change dramatically. With higher charge densities, the electrolyte swelling ratio is lower in comparison to lower charge densities. Ionic monomers in polymer networks are able to create physical crosslinks through ionic

aggregation due to electrostatic attraction. In the case of high charge density polymer such as GPE-6, the ionic agglomeration is observed more clearly, and more physical crosslinks are formed. Whereas lower charge densities such GPE-20 results in few physical crosslinks so that, the solvent/electrolyte swelling ability increases.

Table 2.2: 1 M LiPF<sub>6</sub> (EC-DEC 1:1 %) uptake data, by mass and volume, after four hours of swelling for studied SIPEs.

\*Calculated by measuring change in thickness and diameter. \*\* calculated by measuring change in thickness and assuming isotropic expansion.

Table 2.2a: Mass and volume increase after 1 M LiPF<sub>6</sub> (EC-DEC 1:1 V%) swelling.

| <b>Sample</b> | <b>Mass Increase %*</b> | <b>Standard Deviation</b> | <b>Volume Increase %**</b> | <b>Standard Deviation</b> |
|---------------|-------------------------|---------------------------|----------------------------|---------------------------|
| GPE-6         | 15%                     | ±20                       | 9%                         | ±2                        |
| GPE-8         | 39%                     | ±5                        | 19%                        | ±1                        |
| GPE-12        | 144%                    | ±6                        | 143%                       | ±12                       |
| GPE-20        | 152%                    | ±17                       | 130%                       | ±4                        |

Table 2.2b: Mass and volume increase after 1 M LiPF<sub>6</sub> (EC-DEC 1:1 V%) swelling.

| <b>Sample</b> | <b>Mass Increase %*</b> | <b>Standard Deviation</b> | <b>Volume Increase %**</b> | <b>Standard Deviation</b> |
|---------------|-------------------------|---------------------------|----------------------------|---------------------------|
| GPE-6         | 65%                     | ±21                       | 60%                        | ±5                        |
| GPE-8         | 108%                    | ±8                        | 68%                        | ±5                        |
| GPE-12        | 107%                    | ±2                        | 64%                        | ±2                        |
| GPE-20        | 121%                    | ±7                        | 98%                        | ±5                        |

Dielectric constants of different solvents also impact the electrolyte swelling capability of the polymer which results in a variation of conductivity. The mass and volume increase of each GPE in 1 M LiPF<sub>6</sub> (EC-DEC 1:1 V%) and 1 M LiTFSI (DOL-DME 1:1v%) are depicted in Table 2.2a and 2.2b. The dielectric constant of DOL/DME (DOL  $\epsilon = 7.0$  and DME  $\epsilon = 7.3$  at 25°C)<sup>99</sup> solvent mixture is lower than the EC/DEC (EC at 40°C  $\epsilon = 90.3$ , EC is solid at room temperature, DEC  $\epsilon = 2.82$  at 25°C)<sup>100</sup>. Lower charge



density results in less physical crosslinks in polymer backbone hence, the uptake capability is higher for GPE-20. For better understanding, elemental analysis is pursued to compare between dry and swelled states of membranes.

### 2.3.3 ICP-OES Elemental Analysis

Elemental analysis for both dry and electrolyte swelled state is performed in this study for two main reasons. Firstly, after membrane synthesis, the ionic exchange between  $\text{Li}^+$  and  $\text{Na}^+$  needs to be confirmed and the amount of lithium in the membrane needs to be quantified. Secondly, after swelling in electrolyte, the excess amount of lithium in the polymer matrix, which was dissolved in the binary solvent mixture, is acquired. Thus, the quantity of  $\text{Li}^+$  in the gel polymer membrane is determined and the impact of salt ( $\text{LiPF}_6$  and  $\text{LiTFSI}$ ) on conductivity is presented in the next section.

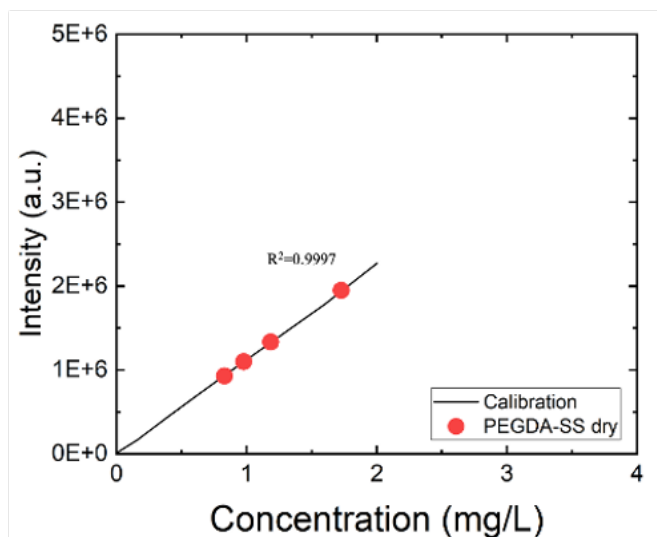


Figure 2.5: PEGDA-SS EO=Li 6,8,12 and 20 dry state (only 0.5 M  $\text{LiCl}$  ionic exchange).

Table 2.3: The number of charges in each PEGDA-SS membrane; dry and 1 M LiPF<sub>6</sub> (EC-DEC 1:1 v%) swelled state.

| Sample Name       | Estimated Concentration (mol/cm <sup>3</sup> ) | Bonded Charge (dry state) Concentration (mol/cm <sup>3</sup> ) | $\frac{C_{Li^+}^{measured}}{C_{Li^+}^{estimated}}$ | Bonded and Free Charges (1 M LiPF <sub>6</sub> swelled state) Concentration (mol/cm <sup>3</sup> ) | $\frac{C_{Li^+}^{measured}}{C_{Li^+}^{estimated}}$ |
|-------------------|--|--|--|--|--|
| GPE-6 (EO=Li 6)   | $2.5 \times 10^{-3}$                           | $2.6 \times 10^{-3}$   | 106%   | $1.9 \times 10^{-3}$   | 109%   |
| GPE-8 (EO=Li 8)   | $2.5 \times 10^{-3}$                           | $2.6 \times 10^{-3}$   | 104%   | $3.4 \times 10^{-3}$   | 152%   |
| GPE-12 (EO=Li 12) | $1.7 \times 10^{-3}$                           | $1.8 \times 10^{-3}$   | 101%   | $3.6 \times 10^{-3}$   | 252%   |
| GPE-20 (EO=Li 20) | $1.3 \times 10^{-3}$                           | $1.3 \times 10^{-3}$   | 95%  | $6.0 \times 10^{-3}$   | 356%   |

Figure 2.5 and 2.6 show the ICP-OES results for the dry and 1 M LiPF<sub>6</sub> swelled states of PEGDA-SS. Regarding the dry state, the ionic exchange is confirmed with the comparison between the estimated lithium concentration and measured lithium concentration for each sample which gives the bonded charges on PEGDA backbone. There is a small deviation  $\pm 5\%$  of the measurement. The comparison between the calculated value and the obtained value ratio should be 90-95% to confirm ionic exchange occurs. The values being greater than this is related to excess lithium on the membrane. Due to the high charge density, PEGDA-SS 6 has the highest lithium concentration compared to the other samples. The dense physical crosslinks yield a higher number of charges in the backbone. Whereas the EO=Li 20 has the lowest lithium concentration because of its low charge density. There are not enough physical crosslinks between the polymer and lithium cations to bond. On the other hand, electrolyte swelling changes the number charges in the membrane in a different way. Low charge density membranes are capable of swelling the liquid electrolyte more than high charge density membranes. Hence, the total number of charges increases largely. EO=Li 20 has  $6.05 \times 10^{-3}$  mol/cm<sup>3</sup> of Li<sup>+</sup>, which is dominated by the free charges from the liquid electrolyte. Free lithium cations are able to stay either on the polymer surface or in the polymer matrix. The exact

state in which these ions are associated cannot be obtained but within these results we are able to see how polymer chemistry plays a role in terms of gel electrolyte. GPE-12 which has in total  $3.6 \times 10^{-3} \text{ mol/cm}^3$  of  $\text{Li}^+$ ,  $1.8 \times 10^{-3} \text{ mol/cm}^3$  dwells bonded charges.

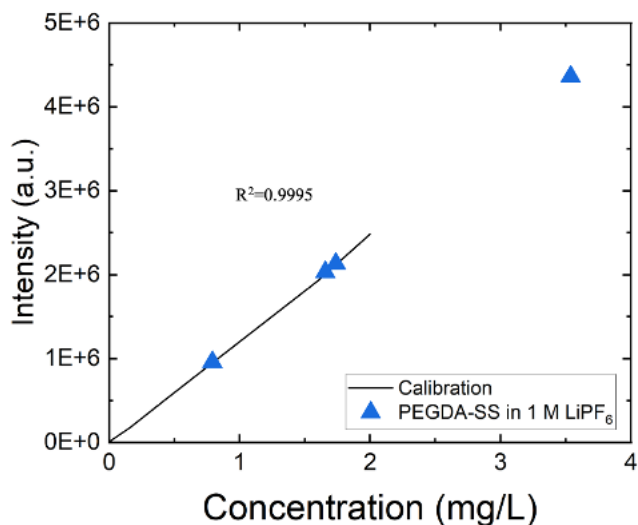


Figure 2.6: Lithium concentration of GPE-6,8,12, 20 swelled in 1 M  $\text{LiPF}_6$  (EC/DEC 1:1 v%).

Interestingly, after swelling in 1 M  $\text{LiPF}_6$ , the total number of charges in GPE-6 is lower than the dry, ionic case. With respect to the electrolyte swelling ratio, this membrane is not capable of swelling electrolyte. GPE-6 is very stiff material due to its high charge density. Therefore, the GPE cannot swell in electrolyte, which is clear from the electrolyte swelling ratio and ICP-OES outcomes. This brings the question; how does the liquid electrolyte effect the ion dissociation in the polymer? This topic is rather very complex and slightly out of scope of this study and is part of an ongoing work.

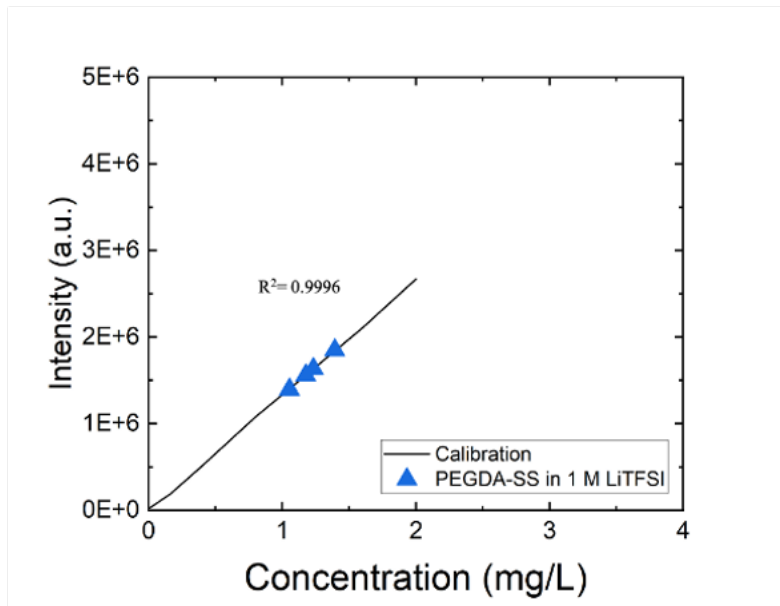


Figure 2.7: Lithium concentration of GPE-6,8,12 and 20 in 1 M LiTFSI (DOL-DME 1:1 v%).

Table 2.4: The number of charges in each PEGDA-SS in 1 M LiTFSI (DOL-DME 1:1 v%) swelled state.

| Sample Name       | Estimated Concentration (mol/cm <sup>3</sup> ) | Bonded and Free Charges (1 M LiTFSI swelled state) Concentration (mol/cm <sup>3</sup> ) | $\frac{C_{Li^+}^{measured}}{C_{Li^+}^{estimated}}$ |
|-------------------|--|---|--|
| GPE-6 (EO=Li 6)   | $2.5 \times 10^{-3}$                           | $3.2 \times 10^{-3}$  | 128%   |
| GPE-8 (EO=Li 8)   | $2.5 \times 10^{-3}$                           | $2.5 \times 10^{-3}$  | 100%   |
| GPE-12 (EO=Li 12) | $1.8 \times 10^{-3}$                           | $2.7 \times 10^{-3}$  | 150%   |
| GPE-20 (EO=Li 20) | $1.4 \times 10^{-3}$                           | $2.7 \times 10^{-3}$  | 192%   |

Table 2.4 summarizes the number of charges in each GPEs in 1 M LiTFSI (DOL-DME 1:1 v%). In comparison to LiPF<sub>6</sub> case, the number of charges is lower. The difference in dielectric constants of each solvent affects polymer solvent interaction. Overall, the

similar trend on increase on number of charges is observed with LiTFSI electrolyte case too.

### 2.3.4 Conductivity Measurement

Conductivity measurements were performed for each GPE for both solely solvent mixtures of DOL-DME (1:1 volume) and EC/DEC (1:1 v) as well as in 1 M LiTFSI (DOL-DME 1:1 v) and 1 M LiPF<sub>6</sub> (EC/DEC 1:1 v). The solvent mixture and electrolyte conductivities were measured to determine the effect of lithium salt on the gel electrolyte system. Without the presence of lithium salt, ionic conductivity is based only on the mobility of lithium cations and the number of those mobile lithium cations. The number of mobile lithium cations in the SIPE is expected to be affected by the dissociation reaction rate and the dielectric constant of the matrix and/or solvent. In a salt-doped electrolyte, it is widely known that the mobility of anions is higher than cations.<sup>101</sup> Hence, it can be said that the ionic conductivity of an electrolyte in the presence of lithium salt in the form of LiX, is mostly dominated by counterions whether the electrolyte is liquid or polymer electrolyte.

One of each GPEs were swelled in DOL-DME (1:1 volume) solvent mixture and 1 M LiTFSI (DOL-DME 1:1 volume) and conductivity was measured between -20 to 85 °C. The conductivity results are showed in Figure 2.8A and 2.8B.

Figure 2.8A depicts the ionic conductivity in the DOL-DME (1:1) solvent mixture. In this case, GPE-6, 8, 12, and 20 are considered as a single ion conducting polymer electrolyte (SIPE). Therefore, this shows only the lithium conductivity in pure solvent as a function of temperature. In polymer electrolytes with poly(ethylene oxide), the ion conduction mechanism is based on cation-ether oxygen interaction and their coupled motion with the segmental motion of PEO chain.<sup>102</sup> Moreover, ionic conductivity of SIPE varies with the charge density and lithium interaction between solvent molecules and polymer chains. As expected, the ionic conductivity of each case increases with respect to temperature elevation. The dissociation of ion pairs and the polymer segmental mobility both increase with increasing temperature, resulting in higher ionic conductivities.

At room temperature, the highest ionic density SIPE, EO-Ch 6, results in the lowest ionic conductivity,  $8.99 \times 10^{-8}$  S/cm. The high charge density polymers tend to have more ionic aggregation which leads to low cation dissociation and slower polymer segmental dynamics. In this case, the lithium cation is more coordinated with the bound anion(s) and has less interaction with the solvent molecules. Hence, the ionic conductivity is the lowest because of the fact that ions which are solely solvated by just the solvent molecules have higher mobility than the cations which are coordinated with the polymer chain.<sup>98</sup> A similar phenomena is observed with GPE-8 too, in which the ionic conductivity at room temperature is slightly higher than GPE-6, at  $3.02 \times 10^{-7}$  S/cm. In addition, the dielectric constant of the solvent mixture has an impact on ionic conductivity due to the solvation effect. Specifically, the dielectric constants of DOL and DME are  $\epsilon = 7.0$  and  $\epsilon = 7.3$  at 25°C are low in contrast to carbonate solvents. This influences the dissociation of counter ions (-SS) adversely and ensues the lower ionic conductivity.<sup>66</sup>

Low charge density electrolytes GPE-12 and 20 have one order magnitude higher ionic conductivities at 25°C,  $1.42 \times 10^{-6}$  and  $5.71 \times 10^{-7}$  S/cm. The ionic monomer -SS can create physical crosslinks through ionic agglomeration due to electrostatic attraction the bound charges within the polymer backbone. Low charge density compositions result in fewer physical crosslinks. Hence, lithium cations are able to coordinate with the solvent molecules rather than the polymer. Consequently, the mobility of lithium cations solvated with only the solvent is increased and high ionic conductivity is observed despite the low dielectric constant of DOL-DME (1:1 v) mixture.

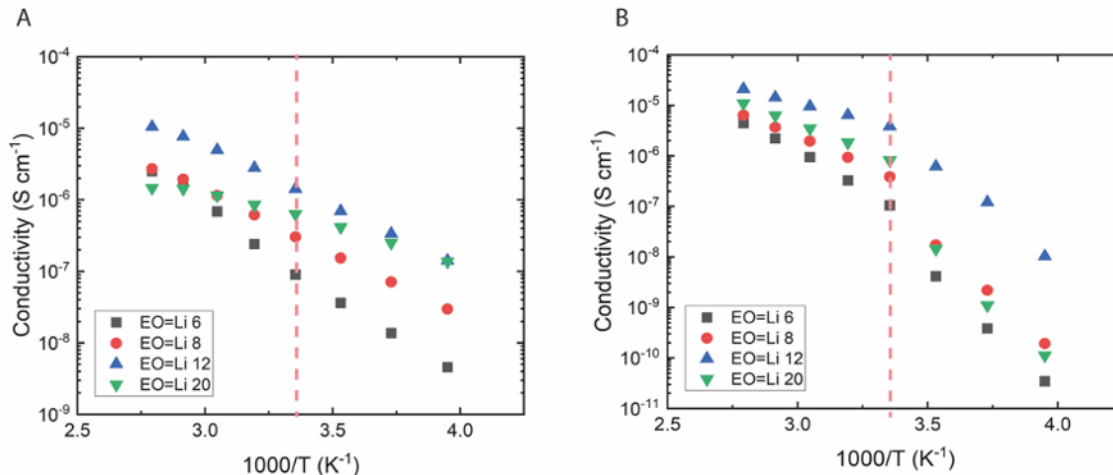


Figure 2.8: A) Ionic conductivity of each PEGDA 700 g/mol-SS membrane swelled to equilibrium in DOL-DME (1:1 v%) B) Ionic conductivity of each PEGDA 700 g/mol-SS membrane swelled to equilibrium in EC-DEC (1:1 v%).

The same experiment is done in EC/DEC (1:1) to compare the difference between two solvent mixtures. In Figure 2.8B, the ionic conductivities for GPE-6 ,8, 12 and 20 are presented. The general trend of the ionic conductivity is complementary to DOL-DME case. For this solvent mixture, the melting temperature of EC is approximately 20°C. Thus, data below 25°C shows lower ionic conductivity due to crystallization of the solvent.

GPE-6 again shows the lowest ionic conductivity at 25°C,  $1.05 \times 10^{-7}$  S/cm, which is one order magnitude lower than DOL-DME instance. Due to the high dielectric constant of EC (at 40°C,  $\epsilon = 90.3$ ), the ionic conductivities are slightly higher than DOL-DME case with the same composition of membranes. GPE-8 in EC/DEC (1:1 v) resulted in a conductivity of  $3.84 \times 10^{-7}$  S/cm at 25°C which is the same order of magnitude as the previous case. The high charge density of these GPE and the high dielectric constant of EC did not improve the ionic conductivity. Moreover, the lowest charge density membrane GPE-20 had an ionic conductivity at 25°C of  $8.16 \times 10^{-7}$  S/cm. The tendency of ionic conductivity decreasing until the melting point of EC (20°C) is approximately two order magnitude lower and almost the same as for each membrane expect for GPE-12 which is one order magnitude higher. This escalation trend continues after the melting point and GPE-12 achieved the highest ionic conductivity for each temperature. Herein, GPE-12 has the optimum charge density and the highest compatibility in carbonate based solutions among other GPEs. At 25°C, the ionic conductivity is  $3.81 \times 10^{-6}$  S/cm, which is

approximately two orders of magnitude higher than GPE-20. The differences in the conductivity can be related to differences in the dissociation of  $\text{Li}^+$  from the anion due to the interactions with the solvent molecules and/or polymer chains. Except for the different ratios of ether oxygen-cation in the polymers, the remaining conditions (experiment condition, the amount of solvent etc.) are constant. GPE-12 has shown the best performance in ionic conductivity for both solvent examples. It can be concluded that, for SIPE in solvent cases, charge density of the membrane plays a crucial role, and the dielectric constant of the solvents impacts the ionic conductivity for the same composition of membranes. The dissociation of anions in the membrane are related to those two important factors.

These ionic conductivities are low for SIPE applications in comparison to literature.<sup>66, 68</sup> Additionally, these SIPEs are found to be similar to Nafion® type membranes which consists of polytetrafluoroethylene (PTFE) backbone and pendent sulfonic acid groups.<sup>103, 104</sup> Two common solvent mixtures have been applied to increase the dissociation and directly improve ionic conductivity, whilst due to hard electrostatic nature of -SS, the desired, higher ionic conductivity cannot be obtained. Therefore, during the rest of the study, the effect of adding free lithium salt is examined.

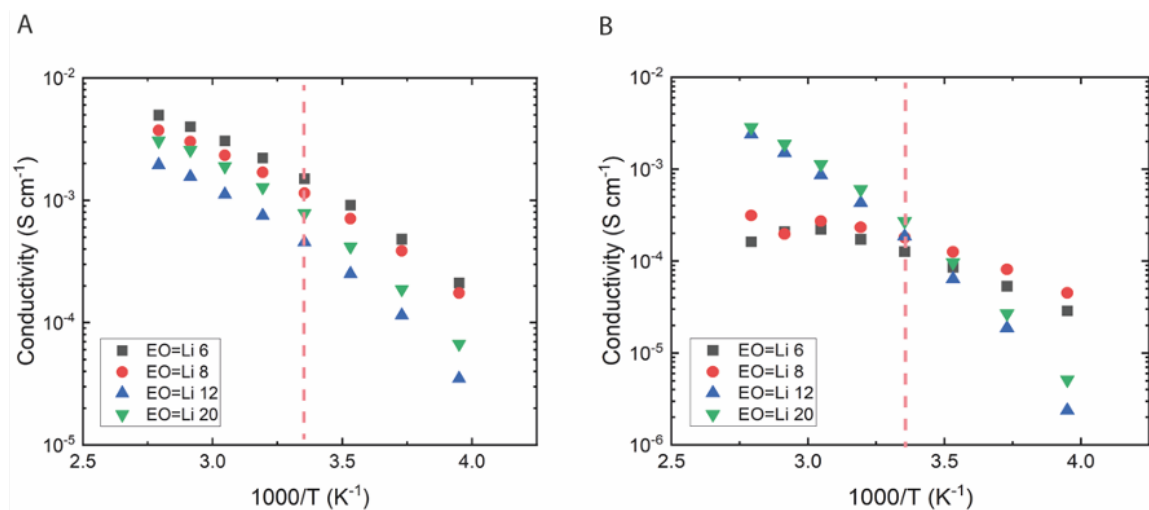


Figure 2.9: A) Ionic conductivity of each PEGDA 700 g/mol-SS membrane swelled to equilibrium in 1 M LiTFSI (DOL-DME 1:1 v%) B) Ionic conductivity of each PEGDA 700 g/mol-SS membrane swelled to equilibrium in 1 M LiPF<sub>6</sub> (EC/DEC 1:1 v%).

Figure 2.9 A demonstrates the ionic conductivity for GPE-6, 8, 12, and 20 in 1 M LiTFSI (DOL-DME 1:1 volume). The improvement in ionic conductivity is observed



clearly with the addition of 1 M LiTFSI salt in the solvent mixture. The two high charge density polymer electrolytes and two low charge density electrolytes behave in the same manner between the temperature range. At 25°C, the highest ionic conductivity is achieved by GPE-6, at  $1.5 \times 10^{-3}$  S/cm. It is followed by GPE-8 at  $1.15 \times 10^{-3}$  S/cm. Those ionic conductivities seem certainly promising considering the ionic conductivity of solely 1 M LiTFSI (DOL-DME 1:1 v). On the other hand, these results are inconsistent with the electrolyte uptake ratios. The GPE-6 and GPE-8 are very stiff materials due to the higher degree of physical crosslinking. Therefore, it is expected to be similar to previous cases, such as in only solvent. The high conductivity values may be explained due to possible excess liquid electrolyte on the membrane surface, which was present during assembly of the conductivity cells. GPE-6 and GPE-8 have very stiff nature due to their high charge density. Thus, liquid electrolyte on the membrane surface might have dominated the measurement. The results represent the total conductivity, it cannot be identified whether the lithium ions or anions are induced to this. 1 M LiTFSI is not the main electrolyte for LiB systems with LiFePO<sub>4</sub> or LiCoO<sub>2</sub> because of the fact that at higher potentials, such as higher than 3 V, the degradation and corrosion of current collector (aluminum) can be observed. However, it is an excellent electrolyte to compare with 1 M LiPF<sub>6</sub> (EC-DEC) due to the fact that 1 M LiTFSI (DOL-DME) is a common electrolyte especially for Li-sulfur batteries.

Lower charge density polymers GPE-12 and GPE-20 achieved conductivities of  $4.54 \times 10^{-4}$  S/cm and  $7.81 \times 10^{-4}$  S/cm at 25°C, respectively. For both of them, the addition of 1 M LiTFSI has improved the ionic conductivity two orders of magnitude. In terms of structure, GPE-12 and GPE-20 are softer than GPE-6 and 8. Therefore, the issues seen for the denser membranes did not occur for these polymers. In addition, the electrolyte uptake results support this argument.

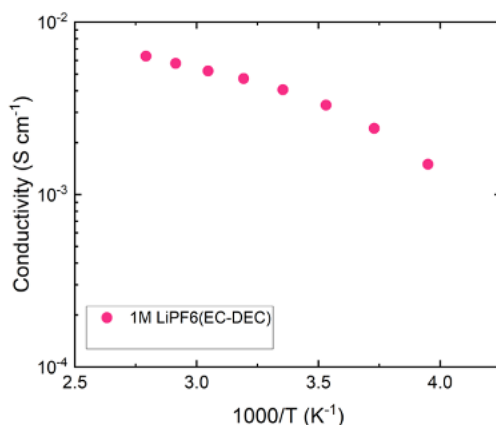


Figure 2.10: Ionic conductivity of 1 M LiPF<sub>6</sub> (EC-DEC 1:1 v%).

Figure 2.10 presents the ionic conductivity results in 1 M LiPF<sub>6</sub> (EC-DEC 1:1 volume). LiPF<sub>6</sub> is the most widely applied electrolyte for commercial LiBs. For all the GPEs, the ionic conductivity of the gels swelled with this electrolyte is highest in comparison to 1 M LiTFSI (DOL-DME 1:1 v) swelled and the pure solvent swelled gels. The fundamental reason is that ionic conductivity of the liquid LiPF<sub>6</sub>-based electrolyte at 25°C is noticeably higher than the LiTFSI-based electrolyte and pure solvents. Figure 2.10 depicts the ionic conductivity of 1 M LiPF<sub>6</sub> (EC-DEC 1:1 v.) at the same temperature range (-20 °C to 85 °C). The similar incremental trend with the temperature rise is observed in the liquid electrolyte case and as well as a lower ionic conductivity until EC's melting point. At 25°C, the ionic conductivity of 1 M LiPF<sub>6</sub> (EC-DEC 1:1 v%) was obtained as  $4.05 \times 10^{-3}$  S/cm. After measuring the conductivity of the 1 M LiPF<sub>6</sub> (EC-DEC 1:1 v%) liquid electrolytes, the GPEs' conductivities are measured to perceive the influence on the GPEs. Similar to the previous case, the ionic conductivity for all the membranes increased as temperature increased. The increment is much clearer with addition of salt due to the high dissociation of LiPF<sub>6</sub> in the solvent. One of the most striking features of Figure 2.9 B is the difference between the low and high charge density membranes. Between -20°C and 85°C the GPE-6 and GPE-8 results are very akin to each other at  $8.56 \times 10^{-5}$  S/cm and  $1.26 \times 10^{-4}$  S/cm respectively. Additionally, for each temperature, the difference in ionic conductivity is very small for GPE-6 and 8. The electrolyte uptake ratio of GPE-6 and GPE-8 which are stated in the previous section are low. These two membranes are not able to swell the electrolyte due to the high charge density. In the PEGDA backbone, the ionic

agglomeration is high and electrostatic attraction is high also. Therefore, those materials are stiffer due to more physical crosslinks and are not able to swell the electrolyte. However, the ionic conductivity has increased. It can be highlighted that the overall ionic conductivity is being measured. Since, it is a binary electrolyte,  $\text{PF}_6^-$  are participating in the overall conductivity, which is written in equation 2.

$$\sigma = \sum \eta_1 \mu_1 e_1 + \eta_2 \mu_2 e_2 + \eta_3 \mu_3 e_3 \quad (2)$$

$\eta$ ,  $e$  and  $\mu$  represent the number of ions in the material, the charge of an electron and the mobility of the ions in the electrolyte respectively. Number notations represent, free lithium ions from the lithium salt (1), lithium ions are paired with -SS anions (2) and free  $\text{PF}_6^-$  from lithium salt (3) respectively.

At 25°C, the ionic conductivity of GPE-6, 8, 12, and 20 are noticeably close to each other. However, lower charge density membranes, GPE-12 and GPE-20 have slightly higher values due to their electrolyte uptake capability. GPE-12 measured an ionic conductivity of  $1.85 \times 10^{-4}$  S/cm, with GPE-20 measuring  $2.71 \times 10^{-4}$  S/cm. With regard to the outcomes, addition of electrolyte to the polymer membrane increases the ionic conductivity. Hence, free ions dominate the ionic conductivity due to their mobility. Consequently, ionic conductivities at 25°C show that GPE-6, 8, 12, and 20 are all suitable to be used as an electrolyte for LiBs. However, another important transport property, cation transference number, is measured to evaluate the proportion of the total ionic conductivity that is due to lithium transport for battery applications. Table 2.5 summarizes the ionic conductivity of each GPEs at 25°C in all applied solvent mixtures and electrolytes.

Table 2.5: Ionic conductivity of GPE-6,8,12 and 20 at 25°C in solvent mixtures and electrolytes.

| Sample Name | DOL-DME (1:1 v%) (S/cm) | 1 M LiTFSI (DOL-DME 1:1 v%) (S/cm) | EC-DEC (1:1 v%) (S/cm) | 1 M LiPF <sub>6</sub> (EC-DEC 1:1 v%) (S/cm) |
|-------------|-------------------------|------------------------------------|------------------------|--|
| GPE-6       | $8.99 \times 10^{-8}$   | $1.50 \times 10^{-3}$              | $1.05 \times 10^{-7}$  | $8.56 \times 10^{-5}$                        |
| GPE-8       | $3.02 \times 10^{-7}$   | $1.15 \times 10^{-3}$              | $3.84 \times 10^{-7}$  | $1.26 \times 10^{-4}$                        |
| GPE-12      | $1.42 \times 10^{-6}$   | $4.54 \times 10^{-4}$              | $3.81 \times 10^{-6}$  | $1.85 \times 10^{-4}$                        |
| GPE-20      | $5.71 \times 10^{-7}$   | $7.81 \times 10^{-4}$              | $8.16 \times 10^{-7}$  | $2.71 \times 10^{-4}$                        |

### 2.3.5 Transference Number Measurement- 1 M LiPF<sub>6</sub> (EC/DEC 1:1 v%)

Transference number is one of the key parameters for battery performance which can be described as the fraction of ionic conductivity contributed by the lithium ion rather than its counter ion.<sup>10</sup> Measuring the transference number has been always challenging. Therefore, most of the studies have shown only the conductivity data which can be accessible easily with simple polarization techniques. In this study, the Bruce-Vincent method has been used to obtain the lithium transference number of all GPE systems. Bruce-Vincent method is based on a potentiostatic-polarization and is relevant for polymer electrolytes.<sup>105</sup> In 1987, this method was introduced by Peter G. Bruce and Colin A. Vincent. During the transference number measurement, applying a small constant potential ( $\leq 10\text{mV}$ ) on the symmetric cell, which consists of an electrolyte and two lithium electrodes results in a drop of the initial current value ( $I_0$ ) until a steady-state value ( $I_{ss}$ ) is reached. The initial current is a result of migration of all charged species. If no redox reaction occurs with the anion and the net anion flux is zero, the anion current will vanish in the steady-state and hence, the total current will represent the cations. Passivating layers at the electrodes enforce an additional contact resistance. The corresponding voltage drop has to be subtracted from the applied potential difference. The contact resistance is measured by an impedance measurement shortly before and after the potentiostatic-

polarization and the cation transference number is calculated by equation 3. The derivation of equation 3 is based on an ideal electrolyte which take explicit account of the concentration gradient and demonstrate the departure from a linear current-voltage relationship as the concentration gradient is increased.<sup>105, 106</sup> Additionally, Nernst-Einstein relationship obeys in this method.

$$t_+ = \frac{I_{ss}(\Delta V - I_0 R_0)}{I_0(\Delta V - I_{ss} R_{ss})} \quad (3)$$

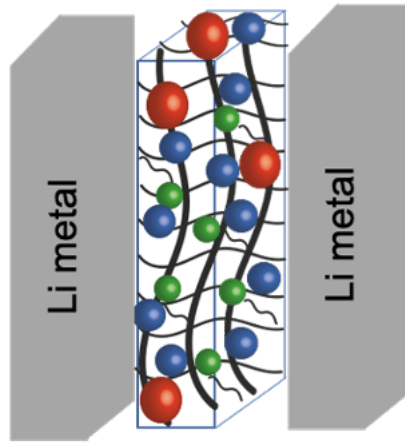


Figure 2.11: Li metal/Gel Polymer Electrolyte/Li metal symmetric cell configuration for impedance measurement.

In this study, the transference number is measured for all GPEs to understand the transport properties with regard to improving cycling performance. The  $t_+$  measurements are carried out in 1 M LiPF<sub>6</sub> (EC/DEC 1:1 v%) electrolyte and EC/DEC (1:1 v%) solvent mixture. The reason why 1 M LiTFSI (DOL/DME 1:1 v%) and DOL/DME solvent mixtures are not used for  $t_+$  measurement is that for the full battery cycling, at higher potentials, LiTFSI reacts with the aluminum current collector and degrades in the cell. Therefore, only LiPF<sub>6</sub> and its solvent mixture are tested with GPEs. Figure 2.11 presents the schematic of symmetric cell configuration.

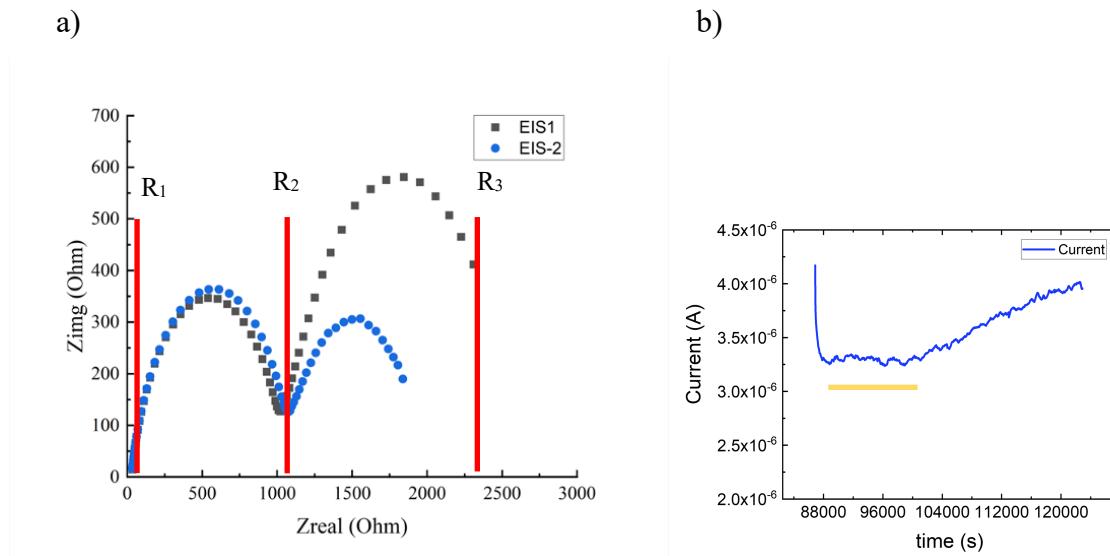


Figure 2.12: a) Impedance response pre and post hold of Li symmetric cells with GPE-6 in 1 M LiPF<sub>6</sub> (EC/DEC 1:1 v/v) b) Polarization curve - GPE-6 in 1 M LiPF<sub>6</sub> (EC/DEC 1:1 v/v).

Figure 2.12 represents the impedance response and polarization curve for Li/GPE-6/Li cell.  $R_1$  is the bulk electrolyte resistance which is 34 ohms.  $R_2$  is assigned as the charge transfer resistance. The last resistance  $R_3$  is open to discussion. Despite the fact that there is no clear evidence, this resistance might be related to a layer between polymer and lithium electrode. Ford also reported similar phenomenon on his SIPE study, and it was speculated that this small layer might have occurred due to some reaction between the gel electrolyte and the lithium surface.<sup>66</sup> This small region can be considered as an effective solid electrolyte interface (SEI). In the literature, under right conditions, this semi-circle type impedance can be modelled by R-Q component and finite distance Warburg diffusion impedance element.<sup>107</sup> This behavior is slightly different from semi-infinite 45° Warburg element which can be observed commonly on liquid electrolytes. The difference between two Warburg elements arises from the length scale of the layer and the time scale of the impedance measurement. The SEI investigation is out of the scope of this study. Hence, in order to fit a single R-Q element, the two semi circles are treated separately and two different  $t_+$  are calculated.

Table 2.6: Extracted resistance and current values from impedance and polarization measurement – in 1 M LiPF<sub>6</sub> (EC/DEC 1:1 v%) swelled GPE-6.

| Sample                  | R <sub>1</sub><br>(ohms) | R <sub>2</sub><br>(ohms) | R <sub>ss</sub> or R <sub>0</sub><br>(R <sub>2</sub> -R <sub>1</sub> )<br>(ohms) | I <sub>ss</sub> (A)     | I <sub>o</sub> (A)      |
|-------------------------|--------------------------|--------------------------|--|-------------------------|-------------------------|
| GPE-6 pre hold (EIS-1)  | 34                       | 1029                     | 995  | -                       | 4.17 × 10 <sup>-6</sup> |
| GPE-6 post hold (EIS-2) | 35                       | 1075                     | 1040   | 3.27 × 10 <sup>-6</sup> | -                       |

| Sample                  | R <sub>1</sub><br>(ohms) | R <sub>3</sub><br>(ohms) | R <sub>ss</sub> or R <sub>0</sub><br>(R <sub>3</sub> -R <sub>1</sub> )<br>(ohms) | I <sub>ss</sub> (A)     | I <sub>o</sub> (A)      |
|-------------------------|--------------------------|--------------------------|--|-------------------------|-------------------------|
| GPE-6 pre hold (EIS-1)  | 34                       | 2309                     | 2275   | -                       | 4.17 × 10 <sup>-6</sup> |
| GPE-6 post hold (EIS-2) | 35                       | 1838                     | 1803   | 3.27 × 10 <sup>-6</sup> | -                       |

The calculated transference numbers for GPE-6 in 1 M LiPF<sub>6</sub> (EC/DEC 1:1 v%) are certainly high in comparison to liquid electrolyte, achieving 0.77 and 0.75 for the first and second semi circles. The polarization is done at 10.12 mV. Table 2.6 shows the obtained results (after fitting on R-Q) for the first semi circle. The bulk resistance changes slightly after the polarization and a small increment is observed on the charge transfer resistance too. It can be seen that the resistances are noticeably high due to thickness of the polymer and the contact between lithium electrodes. High resistance is detected for SIPE cases in literature.<sup>108</sup> Additionally, having lower conductivity also causes a high resistance. 0.77  $t_{Li^+}$  is extremely high for gel polymer electrolyte applications. Generally, SIPEs result close to unity. In terms of transference number, it is a very promising result. However, as it was mentioned earlier, due to the rigid nature of GPE-6, it is not very applicable for practical applications. This result may not be reproduceable. The polarization curve does not look very stable as well. For the calculations, the average is taken which was

highlighted by yellow line. Speculatively, the increase is related to electrolyte decomposition and electrolyte reaction between lithium metal.

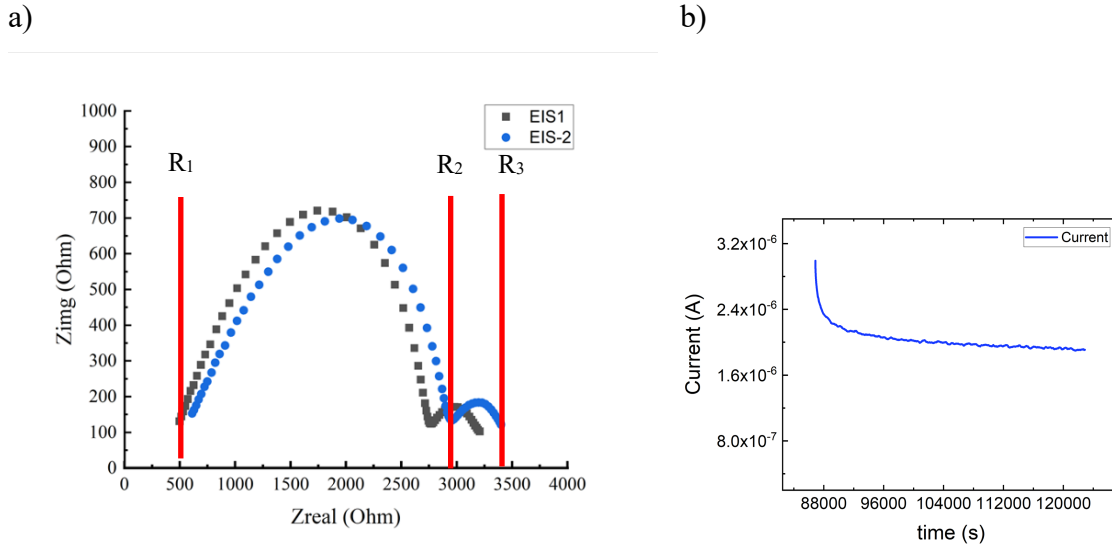


Figure 2.13: a) Impedance response pre and post hold of Li symmetric cells with GPE-8 in 1 M LiPF<sub>6</sub> (EC/DEC 1:1 v%) b) Polarization curve - GPE-8 in 1 M LiPF<sub>6</sub> (EC/DEC 1:1 v%).

The following measurements were done with Li/GPE-8/Li with 1 M LiPF<sub>6</sub> (EC/DEC 1:1 v%) cell configuration. Figure 2.13a and b depict the outcome for impedance response and the polarization curve through the experiments.

Table 2.7: Extracted resistance and current values from impedance and polarization measurement in 1 M LiPF<sub>6</sub> (EC/DEC 1:1 v%) swelled GPE-8.

| Sample                        | R <sub>1</sub><br>(ohms) | R <sub>2</sub><br>(ohms) | R <sub>ss</sub> or R <sub>0</sub><br>(R <sub>2</sub> -R <sub>1</sub> )<br>(ohms) | I <sub>ss</sub> (A)     | I <sub>0</sub> (A)      | t <sub>Li+</sub> |
|-------------------------------|--------------------------|--------------------------|--|-------------------------|-------------------------|------------------|
| GPE-8<br>pre hold<br>(EIS-1)  | 496.9                    | 2765.2                   | 2268.2   | -                       | 2.99 × 10 <sup>-6</sup> | 0.32             |
| GPE-8<br>post hold<br>(EIS-2) | 612.1                    | 2975.3                   | 2363.1   | 1.90 × 10 <sup>-6</sup> | -                       | 0.32             |



$R_1$ ,  $R_2$  and  $R_3$  are assigned as the previous case and in accordance with the equation (3)  $t_{Li^+}$  is found as 0.32 for GPE-8. This result is fairly lower than GPE-6. In order to validate the result, the same experiment was repeated two more times and the same  $t_{Li^+}$  were obtained. At this point, the lower  $t_{Li^+}$  is explained by a couple of reasons. In the previous section, electrolyte uptake outcomes show that GPE-8 does not swell electrolytes due to its high charge density. So, the added  $30 \mu\text{l}$  1 M  $\text{LiPF}_6$  (EC/DEC 1:1 v%) is not able to be swollen by polymer matrix. Due to the high mobility of  $\text{PF}_6^-$  anions, ionic conductivity is high and  $t_{Li^+}$  is low which is quite close to  $t_{Li^+}$  of 1 M  $\text{LiPF}_6$  (EC/DEC 1:1 v%) ( $\sim 0.40$ ). In addition, high resistance values reveal the structure of GPE-8 and a possible contact issue between GPE and lithium metal may occur despite the presence of liquid electrolyte. Furthermore, decomposition of liquid electrolyte in contact with lithium metal is one of the expected reasons to lead to error in  $t_{Li^+}$  measurements of GPEs. The polarization curve of the measurement seems more stable than the GPE-6 case. After the current, steady state current,  $I_{ss}$ , is stable which might eliminate the decomposition of electrolyte on the lithium surface. At least, it can be said, the effect is not severe. However, investigation of the lithium surface is out of the scope of this work.

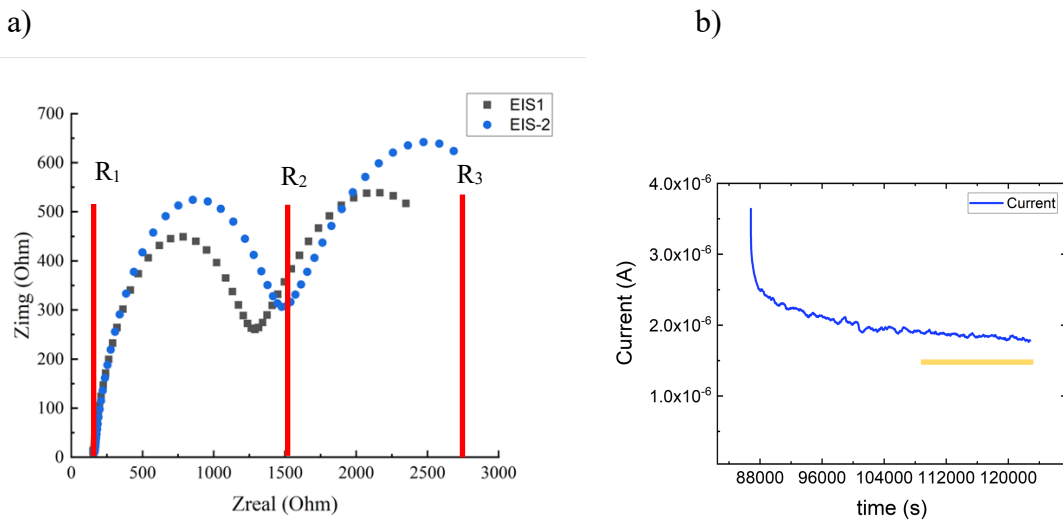


Figure 2.14: a) Impedance response pre- and post-hold of Li symmetric cells with GPE-12 in 1 M  $\text{LiPF}_6$  (EC/DEC 1:1 v%) b) Polarization curve - GPE-12 in 1 M  $\text{LiPF}_6$  (EC/DEC 1:1 v%).

Table 2.8: Extracted resistance and current values from impedance and polarization measurement – in 1 M LiPF<sub>6</sub> (EC/DEC 1:1 v%) swelled GPE-12.

| Sample                         | R <sub>1</sub><br>(ohms) | R <sub>2</sub><br>(ohms) | R <sub>ss</sub> or R <sub>0</sub> (R <sub>2</sub> -<br>R <sub>1</sub> ) (ohms) | I <sub>ss</sub> (A)     | I <sub>o</sub> (A)      | t <sub>Li+</sub> |
|--------------------------------|--------------------------|--------------------------|--|-------------------------|-------------------------|------------------|
| GPE-12 pre<br>hold (EIS-1)     | 153                      | 1288                     | 1135   | -                       | 3.64 × 10 <sup>-6</sup> | 0.37             |
| GPE-12<br>post hold<br>(EIS-2) | 160                      | 1508                     | 1348   | 1.79 × 10 <sup>-6</sup> | -                       | 0.37             |

In accordance with the conductivity measurement, GPE-12 is the most conductive GPE among these results. Due to the trade-off between ionic conductivity and transference number,  $t_{Li+}$  is expected to be low. The measured  $t_{Li+}$  is obtained as 0.37. In comparison to the GPE-8 case, the lower charge density GPE-12 membrane does not show any significant difference. In terms of resistance, the bulk resistance is lower in contrast to the GPE-8 case as well as with the charge transfer resistance. It can be said that the leading parameter for  $t_{Li+}$  in GPE-12 is the liquid electrolyte. Low charge density membranes can decrease the ohmic resistance and increase the contact between GPE and lithium metal due to the structure of the polymer. The noise of the polarization curve shows that side reactions due to PF<sub>6</sub><sup>-</sup> anions on the lithium surface.<sup>109</sup> The steady state current I<sub>ss</sub> is used only at the end of the polarization.

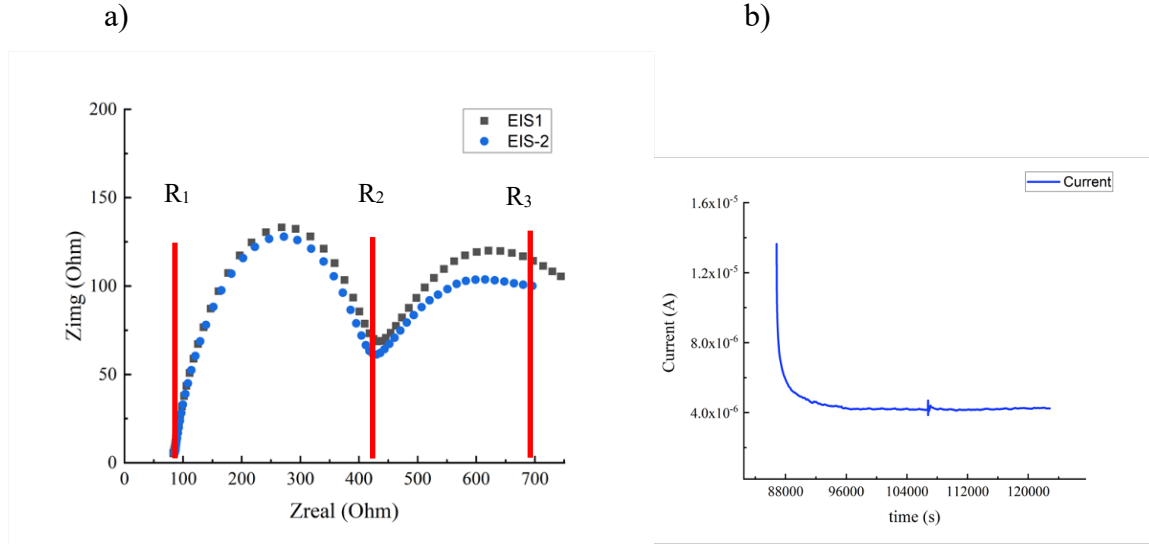


Figure 2.15: a) Impedance response pre- and post-hold of Li symmetric cells with GPE-20 in 1 M LiPF<sub>6</sub> (EC/DEC 1:1 v%) b) Polarization curve - GPE-20 in 1 M LiPF<sub>6</sub> (EC/DEC 1:1 v%).

Table 2.9: Extracted resistance and current values from impedance and polarization measurement – in 1 M LiPF<sub>6</sub> (EC/DEC 1:1 v%) swelled GPE-20.

| Sample                   | R <sub>1</sub><br>(ohms) | R <sub>2</sub><br>(ohms) | R <sub>ss</sub> or R <sub>0</sub><br>(R <sub>2</sub> -R <sub>1</sub> )<br>(ohms) | I <sub>ss</sub> (A)     | I <sub>0</sub> (A)      | t <sub>Li+</sub> |
|--------------------------|--------------------------|--------------------------|--|-------------------------|-------------------------|------------------|
| GPE-20 pre hold (EIS-1)  | 83                       | 438                      | 355  | -                       | 1.37 × 10 <sup>-5</sup> | 0.18             |
| GPE-20 post hold (EIS-2) | 84                       | 440                      | 356  | 4.17 × 10 <sup>-6</sup> | -                       | 0.18             |

The transference number for GPE-20 is the lowest in comparison to previous measurements at 0.18. The estimated lithium transference number is fairly different from the other GPEs. GPE-20 is the lowest charge density membrane with the highest ratio of electrolyte uptake 1 M LiPF<sub>6</sub> (EC/DEC 1:1 v%). Therefore, GPE-20 has the highest lithium concentration (refer to ICP results.). The polarization curve does not show any severe electrolyte decomposition or side reaction with lithium metal. R<sub>1</sub>, the bulk and charge transfer resistances are low which indicate the contact between GPE, and lithium metal has improved. Despite all the positive revision, the observed transference number with GPE-

20 application is not promising for any practical application due to the fact that the estimated  $t_{Li^+}$  is even lower than liquid electrolyte.  $Li^+$  interaction with the PEG chains can slow it down, resulting in lower  $t_{Li^+}$  than compared with the liquid electrolyte.  $Li^+$  interaction with the PEG chains can slow it down, resulting in lower  $t_{Li^+}$  than compared with the liquid electrolyte.

### **2.3.5.1 Transference Number Measurement – EC/DEC (1:1 v%)**

Transference numbers for all the membranes in 1 M  $LiPF_6$  (EC/DEC 1:1 v%) are measured and summarized on the previous section. However, the measured transference numbers are fairly low. In this section, as an example, PEGDA-SS EO=Li 8 (it will refer as SIPE-8) is tried as a single ion conducting polymer electrolyte in EC/DEC 1:1 v% solvent. It is aimed to investigate deeply why the transference numbers are low in 1 M  $LiPF_6$ . The first reason is that the presence of  $PF_6^-$  anions lowers the  $t_+$  due to their high mobility.<sup>110</sup> Secondly, the dissociation fraction of lithium cations from ion pairs or aggregates in the PEGDA-SS polymer matrix may be low. Dissociation rate is reliant upon monomer type, dielectric constant of solvent etc. In order to the effectivity of membrane as SIPE from, GPE-8 was swelled in EC/DEC 1:1 v% and a Li/GPE-8/Li cell was assembled.

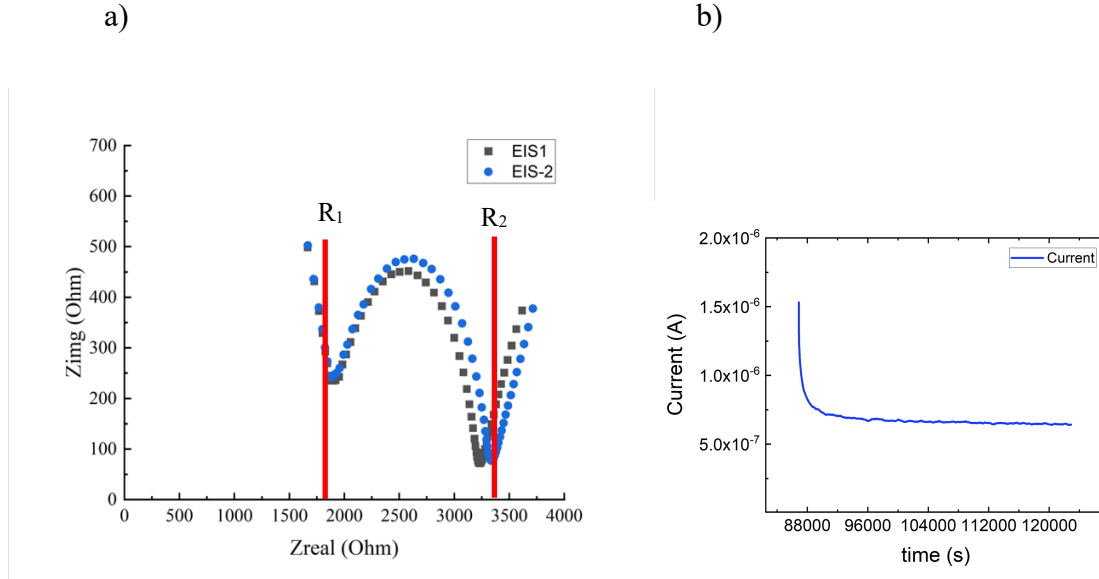


Figure 2.16: a) Impedance response pre and post hold of Li symmetric cells with SIPE-8 in EC/DEC (1:1 v%) b) Polarization curve - SIPE-8 in EC/DEC (1:1 v%).

As it is shown on Figure 2.16, resistance response is slightly different from the binary liquid electrolyte.  $R_1$  represents the bulk solvent resistance which is extremely higher than the 1 M  $\text{LiPF}_6$  due to the lower conductivity of solvent compared to binary electrolyte. Charge transfer resistance is assigned to  $R_2$ . The interfacial resistance is assumed as the difference between the two resistances. SIPE-8 responses are quite different from the GPE -8 in 1 M  $\text{LiPF}_6$  (EC/DEC 1:1 v%). The semi-infinite  $45^\circ$  Warburg element is typically seen in liquid electrolyte impedance data whilst, at lower frequencies, the appearance of Warburg element is clear. The relationship between the length scale (thickness of electrolyte) and the time scale of measurement brings the difference of application of finite element Warburg. However, in this case the occurrence of finite element Warburg might be due to the different SEI thickness. It is commonly known that  $\text{LiPF}_6$  salt is very reactive with lithium metal. Hence, the SEI layer may vary from the GPE case. Additionally, EC is known to help form a stable SEI. Under same conditions, finite element Warburg has occurred. They are different from each other in physical meaning.

The calculated  $t_{\text{Li}^+}$  is 0.37 which is not very different from the previous cases. SIPE are known to have high transference number naturally. The counter ions are immobile and only cations are mobile in the electrolyte systems. At this point, dissociation of ions and the experimental impurities rise to explain the phenomena. It is believed that chemical

and/or electrochemical reactions between the single ion conducting GPEs result in the low calculated  $t_{Li+}$  values, which highlights the difficulty in performing these measurements reliably. Despite the fact that the same experiments are repeated several times, the outcomes do not change. The absolute investigation of the dissociation rate of PEGDA-SS system is beyond this study however it is the subject of ongoing future work.

Table 2.10: Extracted resistance and current values from impedance and polarization measurement – in EC/DEC 1:1 v% swelled PEGDA-SS 8.

| Sample                   | $R_1$<br>(ohms) | $R_2$<br>(ohms) | $R_{ss}$ or $R_0$<br>( $R_2-R_1$ )<br>(ohms) | $I_{ss}$ (A)         | $I_0$ (A)            | $t_+$ |
|--------------------------|-----------------|-----------------|--|----------------------|----------------------|-------|
| SIPE-8 pre hold (EIS-1)  | 1910            | 3228            | 1318   | -                    | $1.5 \times 10^{-6}$ | 0.37  |
| SIPE-8 post hold (EIS-2) | 1928            | 5287            | 3359   | $6.5 \times 10^{-7}$ | -                    | 0.37  |

The polarization takes approximately twenty hours for SIPE-8 application to prevent side reaction and observe the current drop clearly. The  $I_{ss}$  seems more stable in contrast to applications with  $LiPF_6$  because, there is no lithium salt to react with lithium metal and it can be claimed that comparatively stable SEI is formed during the cycling. The current drop is noticeably higher due to the longer time polarization. Some of the GPEs are assembled to be polarized for longer time periods but due to the lithium salt presence, the similar responses cannot be observed.

The other compositions are assembled in EC/DEC (1:1 v%), however, outcomes are not reasonable enough to evaluate further. Investigations of PEGDA-SS gel electrolyte systems and the reasons behind low  $t_{Li+}$  are still going work.

### 2.3.6 Full Cell Cycling Performance– Li metal/LiFePO<sub>4</sub>

The performance and C-rate capabilities of each GPE was tested in Li metal/LiFePO<sub>4</sub> full cell configuration. The batteries were charged to 3.8 V and discharged

at 2 V with various C-rates. Theoretical discharge capacity of  $\text{LiFePO}_4$  is approximately 170 mAh/g, which is lower than more common cathode material  $\text{LiCoO}_2$ . The reason why  $\text{LiFePO}_4$  is chosen is the compatibility to polymer electrolytes. In literature, using Co leads to formation of carbon in the cell and decomposition.<sup>111</sup> As a result, the discharge capacity is extremely low.

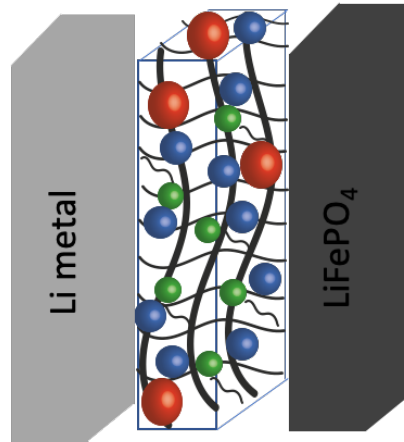


Figure 2.17: Lithium metal/Gel Polymer Electrolyte/Lithium metal full cell configuration.

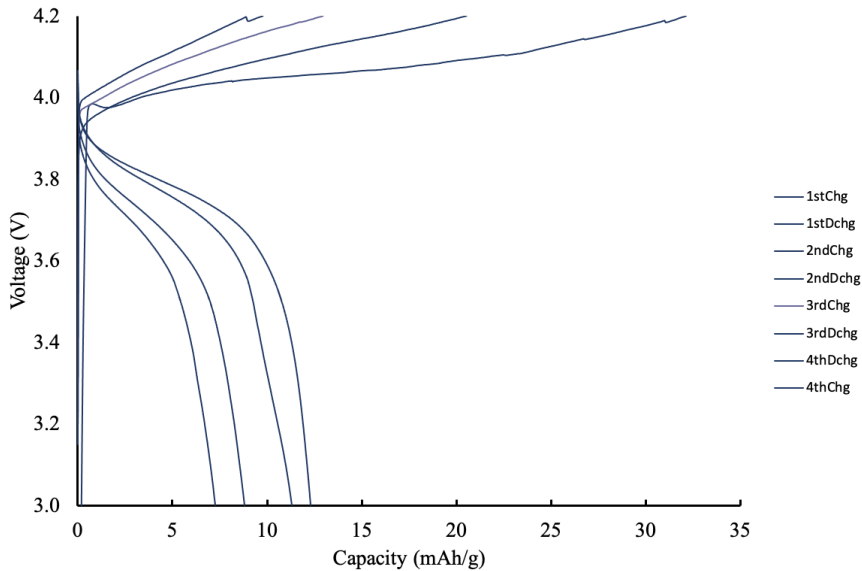
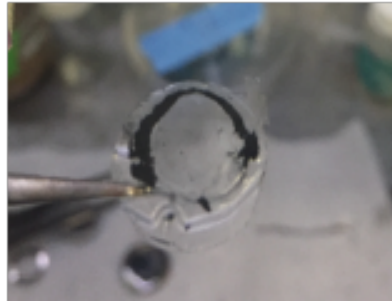


Figure 2.18: Charge and discharge profile of Li/GPE-12/LiCoO<sub>2</sub> at 0.1 C-rate.

As Figure 2.18 shows, the charge and discharge capacity of the cell are extremely low. Due to the incompatibility of the polymer membrane and  $\text{LiCoO}_2$ , this cell is not reversible. In a very simple way, this cell was disassembled, and we tried to see the possible contact problem and carbon decomposition. These side reactions also effect the lithium metal and generate unstable solid electrolyte interface layer on lithium metal. Additionally, polymer membranes are not stable at high potential applications. Figure 2.19 shows the battery components after unsuccessful cycling.

a)



b)

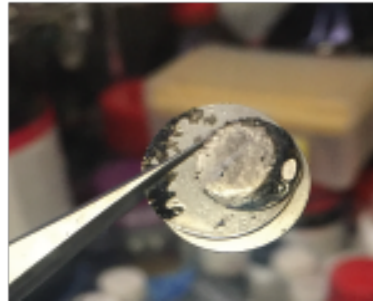


Figure 2.19: a) GPE-12 after failure of the  $\text{Li}/\text{LiCoO}_2$ , the carbon decomposition is seen clearly around the edges of the polymer membrane. b) The darken lithium metal surface which shows the unstable SEI formation. Correspondingly,  $\text{LiFePO}_4$  is chosen for the rest of the study.



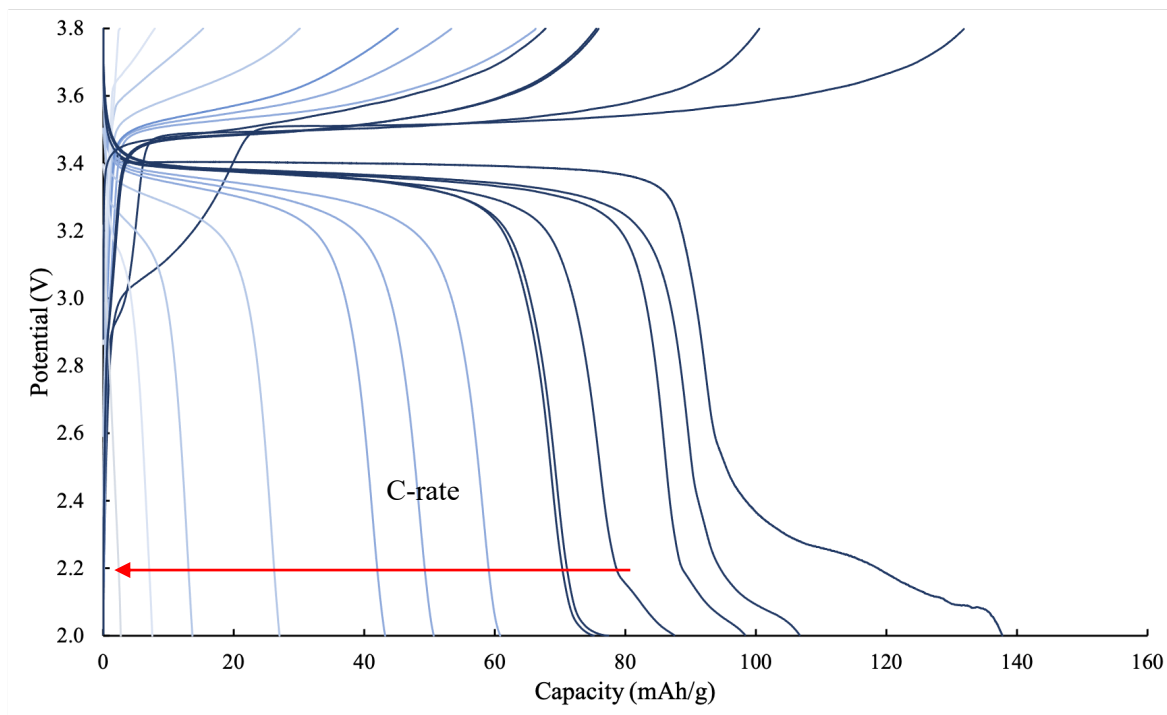


Figure 2.20: Li/GPE-12/LiFePO<sub>4</sub> full cycling performance, including C-rate test from 0.1C – 5 C. 200 cycles are completed with 0.1 C-rate.

GPE-12 was applied with LiFePO<sub>4</sub> cathode under same conditions. The cathode loading for this cell was 1.79 g/cm<sup>2</sup>. For laboratory size applications, the loading is low, but the main purpose is to see the cycling behaviour of the GPEs. The first discharge capacity is around 140 mAh/g which is fairly close to the theoretical capacity. The plateau is very stable at 3.4 V. At the end of the first 5 discharge curves, a small bump is observed which can be related to the stabilization of side reactions and formation of a SEI and cathode electrolyte interface (CEI). In order to see the performance of the cell, the C-rate increased from the 0.1 to 5 C gradually. As Figure 2.20 depicts, discharge capacity is akin to 0 at 5 C-rate. Ionic conductivity of the GPE-12 limits the battery cycling at higher C-rates. However, operating at 0.1 C-rate after % C-rate, the discharge capacity increased to 79 mAh/g and the battery performed 200 cycles with 80% coulombic efficiency. The same cycle configuration is performed several times and the similar results have been obtained. In terms of ionic conductivity and transference number, GPE-12 was selected the optimum for practical applications and the cycle performance has proven it. Despite the relatively low capacity, the ionic conductivity of this membrane is two orders of magnitude lower

than the liquid electrolyte and this membrane is approximately 4 times thicker and the conventional separator which can easily lead to contact issues between the cathode and anode. For the future studies, coating the polymer membrane on the cathode is going to be performed and the outcomes will be compared.

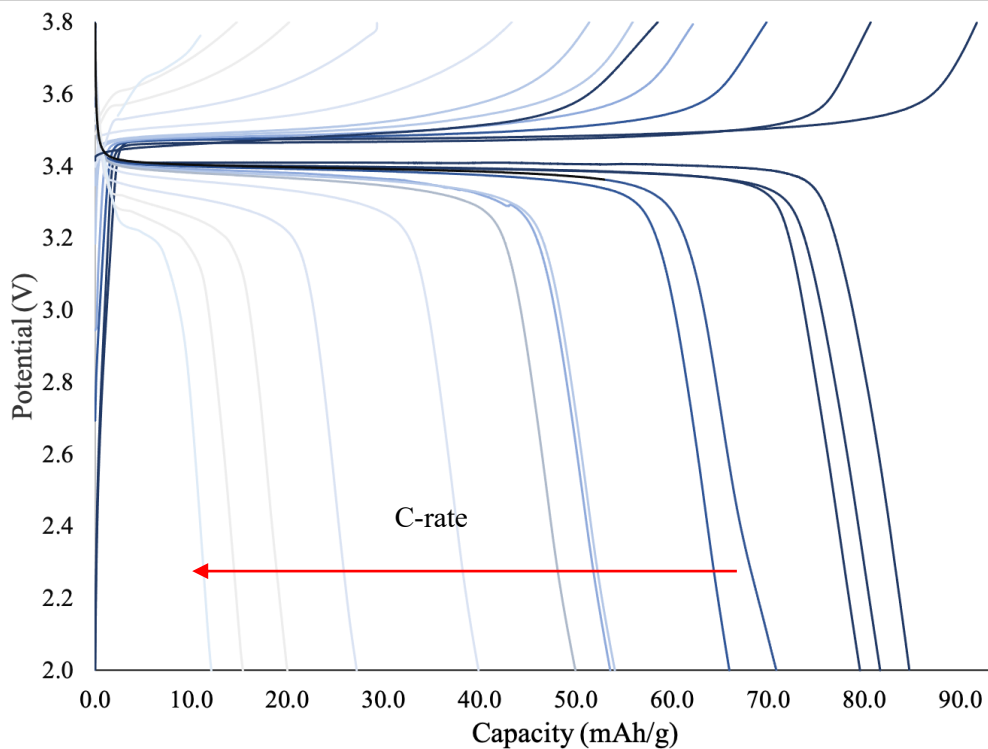


Figure 2.21: Li/GPE-20/LiFePO<sub>4</sub> full cycling performance, including C-rate test from 0.1C – 5 C, 200 cycle is completed at 0.1 C-rate.

The cathode is utilized for GPE-20 under the same conditions. In order to stabilize the cell, the first cycle was done at 0.01 C-rate. Starting cycling at 0.1 C-rate, 85.2 mAh/g discharge capacity was obtained. Until the 30<sup>th</sup> cycle, there is a slight capacity decrease which is expected. The rate is increased from 0.1 C-rate to 5 C-rate (0.1, 0.2, 0.3, 0.4, 0.5, 1, 2, 3, 5 C-rate) starting from the 31<sup>st</sup> cycle. At higher C-rates, the capacity decreases greatly. The reason why is akin to GPE-12. The transport limitation due to ionic conductivity effects the battery performance drastically. However, when the rate was lowered to 0.1 C, the cell started to function at moderate capacity with approximately 70% coulombic efficiency. Identical issues to GPE-12 are reasons to poor capacity outcomes. However, the cell performance is promising with planned modifications beforementioned.

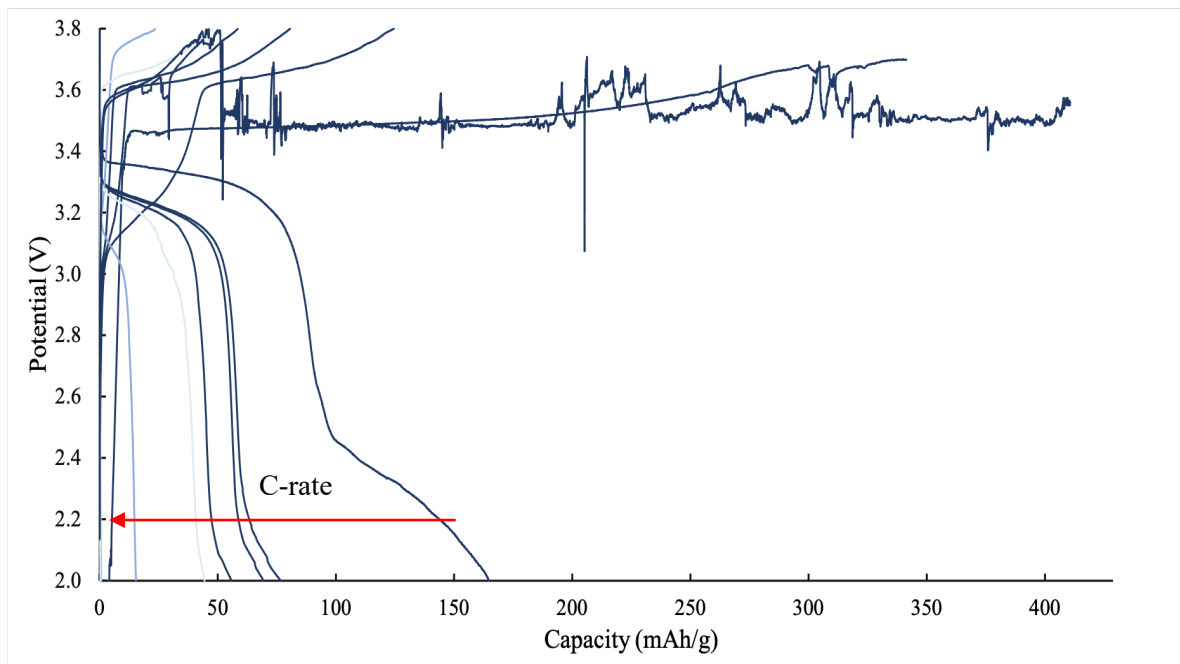


Figure 2.22: Li/GPE-6/LiFePO<sub>4</sub> full cycling performance, including C-rate test from 0.1C – 0.3 C, 95 cycle is completed at 0.1 C-rate.

GPE-6 is applied with lithium metal and the loading LiFePO<sub>4</sub> cathode and run at 0.1 C-rate for 94 cycles. The first charge is referred as conditioning cycle which aims to reduce the possible side reactions. The side reaction can be seen clearly on charge capacity which almost 400 mAh/g. The first discharge capacity is slightly higher than 150 mAh/g that shows the stabilization of the cell. On the 3<sup>rd</sup> cycle, there is a significant capacity drop which continues with the 10<sup>th</sup> cycle. The capacity loss is greater than 50%. This is expected with GPE-6 due to its very rigid nature which creates a very serious contact problem. The bump at the end of the discharge curve is much more evident than the previous GPEs full cell cycling. Therefore, the rate test is only done until 0.3 C-rate, at which point the discharge capacity is almost 0 mAh/g. The cycling rate was turned back to 0.1 C with approximately 40 mAh/g capacity and the cell kept cycling until the 95<sup>th</sup> cycle. Herein, the infinite charge is observed which indicates the battery failure. GPE-6 is not the best future candidate for possible electrolyte applications due to its very stiff nature.

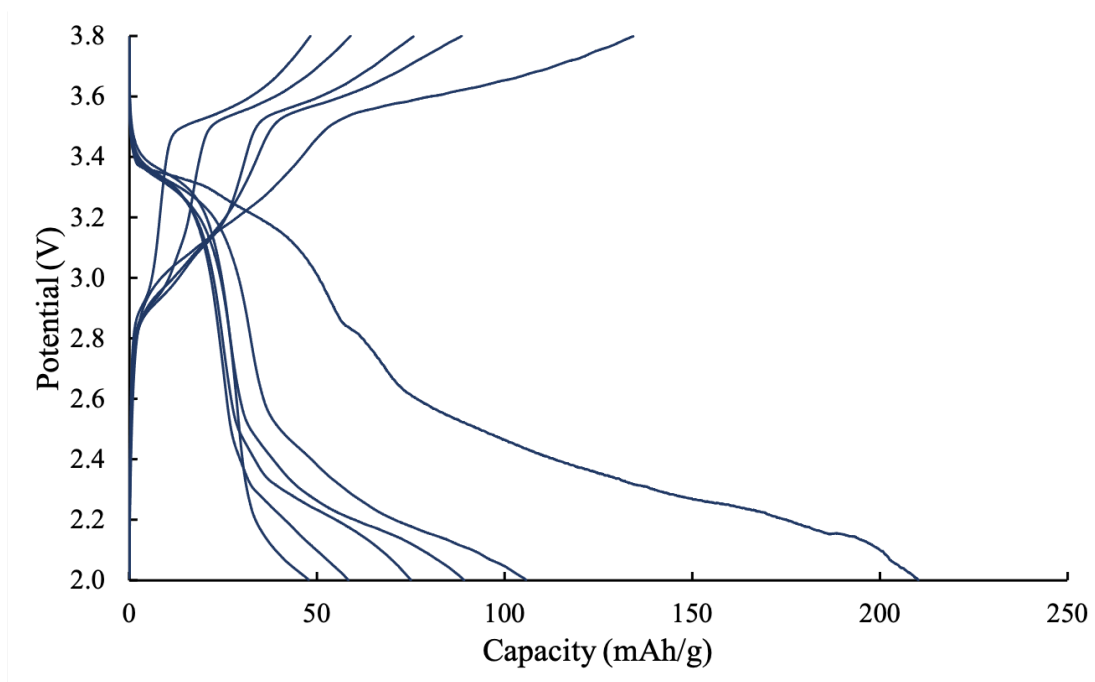


Figure 2.23: Li/GPE-8/LiFePO<sub>4</sub> full cycling performance at C-rate 0.1.

As a last electrolyte, GPE-8 is assembled with LiFePO<sub>4</sub> cathode. The loading of the cathode is slightly lower than previous cathode applications, 1.5 g/cm<sup>2</sup> respectively. Morphologically, GPE-8 is akin to GPE-6, with high charge density that is very mechanically rigid. These features reflect on the charge-discharge curve. After the first discharge, the capacity decreased 50%. Additionally, there is no discharge plateau which indicates the transport limitations. 1 M LiPF<sub>6</sub> (EC-DEC 1:1v%) swelled GPEs' ionic conductivities are not very different from each other at room temperature. Thus, the charge density of the membranes dominates the transport across the cell. As GPE-12 and 20 show promising performance whilst, GPE-6 and GPE-8 can barely cycle with relevant efficiency.

One might point out to the impact of bonded charges during cycling. It is not known the dissociated ion state in these membranes neither dry nor presence of the liquid electrolyte. The effect of the electric field on dissociation and association is still a question. The full performances of each membrane are based on the total number of charges. This is part of the future study of this project. Overall, GPE-8 does not seem very positive candidate for any GPE applications.

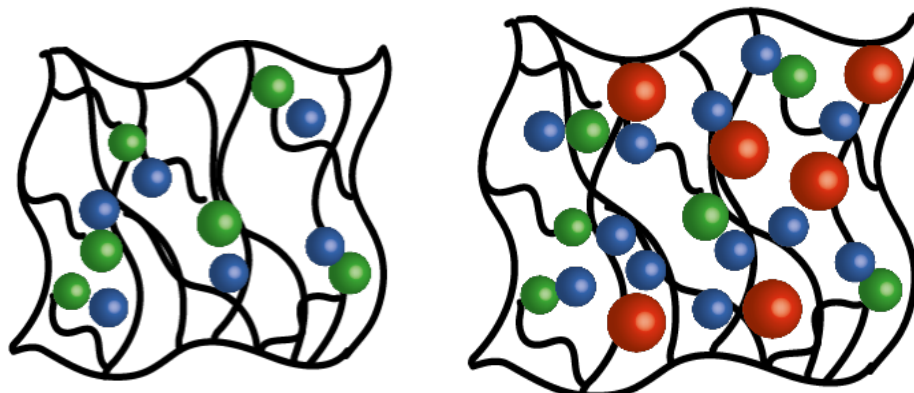
## 2.4 Conclusion

This study has demonstrated the possible applications with GPEs through polymer structure. In order to comprehend the effect of structure, charge density was chosen as the controlled variable. The second point was to understand the salt effect on polymer membranes in terms of transport properties.

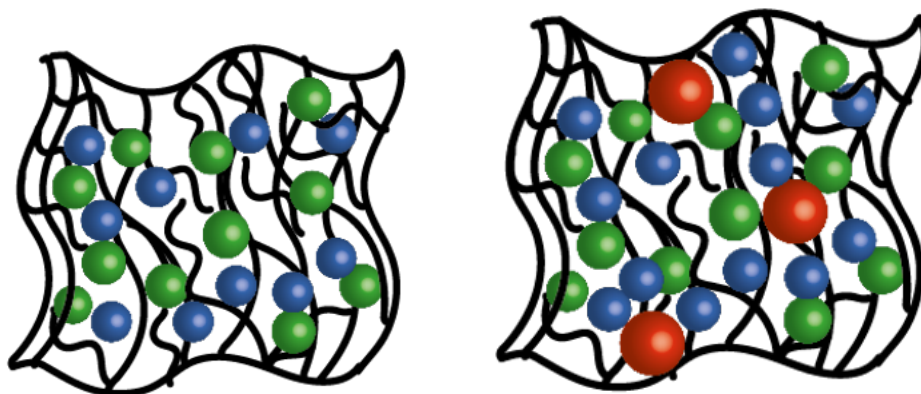
Conduction in polymer electrolyte application is relied on two main factors; segmental motion of the polymer backbone and the concentration of charge carriers. The conduction mechanism is based on the hopping of ions between backbone and solvation sites, in which fast segmental motion is critical. However, fast segmental motion is not enough for high electrolyte conductivity. Concentration of charge carriers is a material property which is dependent on ion dissociation. In terms of the SIPE, low ion dissociation is a critical limitation. Studies suggest that only a small fraction of lithium is in a disassociated state.<sup>112</sup> Dissociation depends on couple factors. In order to dissociate the ion pair, the polymer chains should prefer a stronger affinity for the cation than the anion. The properties of the solvent, such as dielectric constant, should be in favour for this interaction. In this study, we have chosen a different approach to increase the charge carriers, adding conventional liquid electrolyte to the membrane. Without binary salt, it is expected to observe low lithium motion due to the ion association on the backbone. Specifically, in the PEGDA-SS case, ether oxygen ratio dominates the ion dissociation and association. Thus, the effect of charge density was observed clearly for membrane applications. Liquid electrolyte is well-studied and used commercially due to a high ionic conductivity. Adding more mobile ions to the polymer could result in segmental motion reduction because of the high of the electrostatic interactions. However, we observe that total ionic conductivity increases due to the free mobile ions and the addition of solvent.

Figure 2.23A shows GPE-20 before and after swelling electrolyte. Having low charge density results in less crosslinks and less bonded charges. In contrast to B, which shows GPE-6 before and after swelling electrolyte, in the dry state, GPE-6 is very dense and have high bonded charges. Even in this state, ionic aggregates are present due to the electrostatic interaction. After electrolyte swelling, only a few free ions can be present in

the polymer matrix and ionic aggregation has increased. Due to the ion aggregates and high electrostatic interaction, lithium cation motion decreases.



A) Low charge density membrane GPE-20 dry and 1 M LiPF<sub>6</sub> (EC-DEC 1:1 v%) swelled state.



B) High charge density membrane GPE-6 dry and 1 M LiPF<sub>6</sub> (EC-DEC 1:1 v%) swelled state.

Figure 2.24: Sketch of high and low charge density membranes' (GPE-6 and GPE-20) dry and electrolyte (1 M LiPF<sub>6</sub>) swollen states.

Adding 1 M LiPF<sub>6</sub> (EC-DEC 1:1 v%) in high charge density membranes do not increase the total number of charges due its dense nature. We suspected that it may have adverse effects on ion dissociation. On the other hand, GPE-20 has swollen the electrolyte and the total number of charges increases drastically. In this case, the dominate factor for the transport properties is the free charges. In all different EO=Li ratios, the dominating factor for the ionic conductivity is the liquid electrolyte, free charges. However, applying

different polymer backbones or monomer can change it due to ion dissociation and association degree.

For future studies, the chemistry of the polymer backbone should be investigated deeply to fully understand the effect of the free charges. The trade-off between charge carrier concentration and segmental motion must be considered and the possible impacts of liquid electrolyte on ion dissociation and association must also be taken into consideration. In order to comprehend the ion coordination and interactions profoundly, molecular dynamics simulations could be a very useful. In some studies, the effect ion aggregation and polymer segmental motion on  $\text{Li}^+$  transport are studied broadly.<sup>9, 113, 114</sup> PEGDA-SS system is open to be investigated in terms of different behavior of different compositions. Herein, we report the various transport properties of PEGDA-SS membranes both as SIPE and GPE with the current drawbacks. GPE-12 and GPE-20 are possible candidates for GPE applications and future studies.

## 3. Chapter 3- Investigation of Porous Polymer Electrolytes

### 3.1 Introduction

Current electrolytes that are commonly used in lithium-ion batteries are based on a binary salt dissolved in a solvent mixture (i.e.,  $\text{LiPF}_6$  in a liquid organic carbonate mixture).<sup>109</sup> These systems contain both anions and cations, leading to the formation of a significant concentration gradient upon the application of a sustained electric field. This occurrence of concentration gradients results in limited practical charge-discharge rates, as the thickness of the electrode which is accessible to electrochemical reactions is limited and lithium metal batteries may suffer from lithium dendrite formation at the anode. These concentration gradients are based on the mobility of the anions and cations in conjunction with the prevalence of electroneutrality at the continuum level, and they can be prevented via the use of single ion conducting polymer electrolytes (SIPes). For 30 years, polymer electrolytes and SIPes for lithium batteries have been investigated through either fixing the anions to the polymer backbone or using  $\text{Li}^+$  conducting inorganic electrolytes.<sup>115</sup> Polymer electrolytes have more advantages over the inorganic electrolyte applications, particularly an increased compatibility with lithium metal. Therefore, the development of polymer electrolytes is highly favoured in order to obtain a better electrolyte for practical applications. One of the main issues of SIPes is a relatively low conductivity when compared to liquid electrolytes at room temperature, which is reliant on the ion dissociation. In order to achieve higher dissociation, the polymer chain needs to be higher than the appended anion.<sup>116-118</sup> Because polymer behaves like both the solvent and the ion. Thus, increasing the segmental motion of the polymer backbone is critical. However, polymers have strong basic components with very low segmental motion due to their strong inter and intra-chain molecular interactions. Ion dissociation and association are highly essential factors to reach high conductivity. Thus, structure properties and a suitable backbone and ionomer selection are important parameters to reach desirable conductivity. In this chapter, in order to overcome these issues, a gel polymer electrolyte which consists of a single ion conducting polymer electrolyte and the conventional liquid electrolyte was analysed. By using this novel approach, the number of charges provided as counter-charges to tethered anions on the backbone and free charges from the dissolved lithium salt are



going to be evaluated. The impact of the type of polymer backbone and ionomer on transport properties are going to be compared with the Chapter-1. The morphology of the polymer structure and the composition were also examined.

## 3.2 Experimental Section – PEGDMA 750 g/mol-VS

### 3.2.1 Vinyl Sulfonate Salt Preparation

80 ml of ethanol (Sigma Aldrich) was added gradually to 40 g of vinyl sulfonic acid sodium salt solution (25 % wt Sigma Aldrich). The mixture was transferred to the Buchner funnel with flask and connected to the vacuum line in the fume hood and was filtered. The filtration was repeated twice to collect a larger fraction of the salt. The filtrated salt was put in 150 ml flask glassware and placed in vacuum oven. The salt was dried under vacuum for 24 hours at 100 °C. The dried salt was transferred to a vial and dried for 12 hours under vacuum on the schlenk line. This VS salt is referred as ‘dry’ in the next sections.

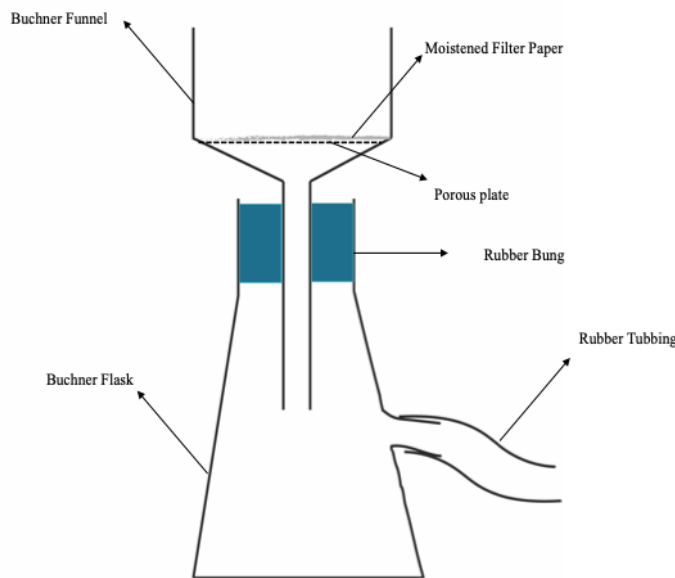


Figure 3.1: Vinyl sulfonate salt preparation set-up.

Vinyl sulfonate salt was prepared using a second method which produced material that was not as dry as the first method. We assume that some amount of trace water

remained in this prepared vinyl sulfonate salt. First, the exact same procedure was applied to have VS in the salt form. Then, the salt was dried under vacuum for 24 hours at 100 °C before use. Drying on the Schlenk line was not performed with this second method. Therefore, membranes made with this salt are going to be referred to as “wet”.

### **3.2.2 Water Content Measurement**

5 g of dry vinyl sulfonate was dissolved in 10 ml DME (1,2-dimethoxyethane, anhydrous, Sigma Aldrich) in an argon filled glovebox. The water content of anhydrous DME's was measured with Karl Fisher titration (KF titration, Mettler Toledo Corp.) and found to be 23.5 ppm. KF titration is a classical titration method in chemical analysis that uses coulometric or volumetric titration to determine trace amount of water in a sample. The main principle behind it is based on Bunsen reaction between iodine and sulfur dioxide in an aqueous medium. The VS-DME mixture was stirred for two days over 3 Å molecular sieves for at least four days to ensure low moisture content.

### **3.2.3 Synthesis of crosslinked PEGDMA Membranes**

#### **3.2.3.1 Transparent PEGDMA-VS-0**

Dried VS was dissolved in anhydrous dimethyl sulfoxide (DMSO, Sigma Aldrich), at the proper amount. The dissolution process was supported by the use of a heat gun (Master Appliance Corp. (Model EC-100)). The proper amount of poly(ethylene glycol) dimethacrylate, (PEGDMA, 750 g/mol, Sigma-Aldrich) was added to the VS-DMSO solution and dissolved. The solution was stirred until fully mixed. After stirring for ten minutes, a small amount of polymer chunks became visible at the bottom of the vial. In order to mix it well, the chunks were smashed with a spatula. To this monomer solution, photoinitiator, 2-hydroxy-4'-(2-hydroxyethoxy)-2-methyl propiophenone (Sigma-Aldrich) was added and dissolved. The monomer solution was sandwiched between two 1/4 in. thick borosilicate glass plates (McMaster Carr) separated by 200 um thick glass microscope slides (VWR). This was then placed in a UVC-515 Ultraviolet Multilinker 254 nm UV oven. The plates were flipped every two minutes to ensure both sides of the solution received equal UV radiation. The monomer solutions were photo-crosslinked for a total of

45 minutes. The resultant polymers were washed with DMSO to remove any unreacted material. The polymers were then placed in a stirred ion exchange solution of 0.5 M lithium chloride to achieve lithiated forms of the polymer. The ion exchange solution was replaced every 12 hours for 48 hours, after which free salt was washed from the films by repeating the same process but with deionized water that did not contain salt. The films were air dried for two days and then brought into an argon filled glovebox ( $< 10$  ppm  $O_2$ ,  $< 0.1$  ppm water) and vacuum dried for 16 hours at  $80$  °C to remove residual solvent. The abbreviation of this membrane for the rest of the study is T-PEGDMA-VS-0.

### **3.2.3.2 Opaque PEGDMA-VS-0**

The appropriate amount of dry VS was dissolved in anhydrous dimethyl sulfoxide (DMSO, Sigma Aldrich). The dissolution process was sped up through the use of a heat gun. The proper amount of PEGDMA (poly(ethylene glycol) dimethacrylate, 750 g/mol) was added to the VS-DMSO mixture and dissolved. After dissolving, the suitable amount of deionized water was added by micropipette to the solution to change the degree of VS dissolving. To this monomer solution, photoinitiator, 2-hydroxy-4'-(2-hydroxyethoxy)-2-methyl propiophenone (Sigma-Aldrich) was added and dissolved. The monomer solution was sandwiched between two 1/4 in. thick borosilicate glass plates (McMaster Carr) separated by 200  $\mu$ m thick glass microscope slides (VWR), which were then placed in a UVC-515 Ultraviolet Multilinker 254 nm UV oven. The plates were flipped every two minutes to ensure both sides of the solution received equal UV radiation. The monomer solutions were photo-crosslinked for a total of 45 minutes. The rest of the process was exactly the same as the T-PEGDMA-VS-0.

Table 3.1: Compositions, formulations and charge density for studied polymer electrolytes.

| <b>Sample Name</b> | <b>Crosslinker</b> | <b>Crosslinker mass (g)</b> | <b>VS (g)</b> | <b>Anhydrous DMSO (g)</b> | <b>Photoinitiator (g)</b> | <b>Water (<math>\mu</math>l)</b> |
|--------------------|--------------------|-----------------------------|---------------|---------------------------|---------------------------|----------------------------------|
| Transparent        | PEGDMA-750 g/mol   | 0.536                       | 0.214         | 0.850                     | 0.0075                    | -                                |
| Opaque             | PEGDMA-750 g/mol   | 0.536                       | 0.214         | 0.799                     | 0.0075                    | 51.45                            |

In order to investigate the effect, the thickness of the opaque membrane had on subsequent measurements, a thicker opaque PEGDMA-VS-0 membrane was prepared. The composition is exactly same as it is written formerly. The prepared monomer solution was sandwich between two 1/4 in. thick borosilicate glass plates (McMaster Carr) separated by two pieces of 200  $\mu$ m thick glass microscope slides (VWR), which were then placed in a UVC-515 Ultraviolet Multilinker 254 nm UV oven and photo-crosslinking was done.

Another crosslinking procedure was applied to see the impact of the crosslinking method. The monomer solution was prepared exactly same as the description of the previous paragraph. Photoinitiator, 2-hydroxy-4'-(2-hydroxyethoxy)-2-methyl propiophenone, was added to the solution and stirred until it was fully dissolved. 1/4 in. thick borosilicate glass plates are capable of absorbing the UV light. Thus, the prepared monomer solution was dropped on the bottom glass plate uniformly and the top plate was not used, in order to increase the degree of crosslinking. The monomer solution on the plate was placed in a UVC-515 Ultraviolet Multilinker 254 nm UV oven for 45 minutes. The other monomer solution which is put without the top glass plate, and it is crosslinked for 1 hour. For both times scales the crosslinking process was done without any breaks. The same procedure was applied for both transparent and opaque PEGDMA-VS-0. The effect of two procedures on the material properties is discussed in the further sections.

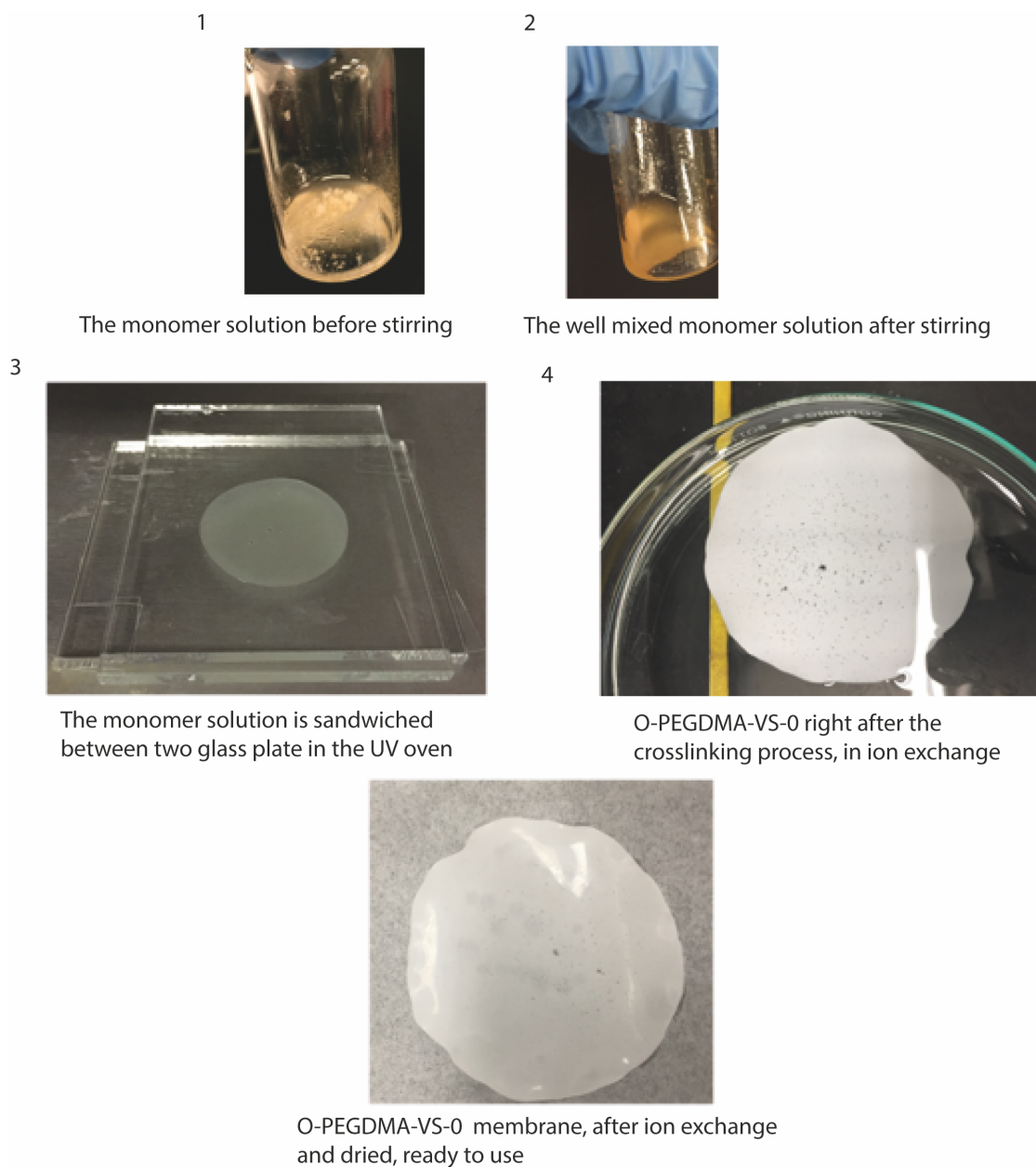


Figure 3.2: O-PEGDMA-VS-0 membrane preparation process in five steps.

### 3.2.3.3 Opaque PEGDMA

In order to make a better comparison with the transparent and opaque PEGDMA-VS-0 and determine the effect of the bound charge while remaining independent of the structure effect, we attempted to make opaque PEGDMA without adding VS monomer. The same procedure is followed as mentioned formerly. The most crucial parameter here is the water content, which causes the phase separation. The amount of water necessary to

add to the monomer solution to produce the desired visual appeared is only determined as a range due to the changing humidity of the environment. This process is very sensitive. Thus, the exact amount of extra water necessary to create the phase separation varies by day. The environmental conditions are highly effective on obtaining the correct porous structure.

Table 3.2: Compositions, formulations and charge density for studied PEGDMA membrane.

| Sample Name   | Crosslinker      | Crosslinker mass (g) | VS (g) | Anhydrous DMSO (g) | Photoinitiator (g) | Water ( $\mu$ l) |
|---------------|------------------|----------------------|--------|--------------------|--------------------|------------------|
| Opaque PEGDMA | PEGDMA-750 g/mol | 0.75                 | -      | 0.85015            | 0.0075             | varies           |

### 3.2.4 Ion Exchange

The lithium form of the sulfonated polymer can be prepared by placing the polymer in a glass petri dish and soaking in 0.5 M lithium chloride (LiCl) in Milli-Q water solution for two days. Every 24 hours, the solution is changed. After two days, the polymer is washed with pure Milli-Q water and soaked in Milli-Q water for another two days. Alternatively, 2 M lithium hydroxide (LiOH) and 1 M LiTFSI (DOL-DME 1:1 v%) are used as ion exchange solutions with the same procedure. Lithium content following ion exchange was measured by Inductively Coupled Plasma – Optical Emission Spectroscopy (ICP-OES) at the Notre Dame Center for Environmental Science and Technology (CEST).

### 3.2.5 Solvent and Salt Drying

Electrolytes salts, solvents 1,3-dioxolane (DOL, anhydrous) and 1,2-dimethoxyethane (DME, anhydrous) solvent mixtures, and ethylene carbonate (EC) and diethyl carbonate (DEC) solvent mixtures used in electrolyte preparation, conductivity, transference number measurement and coin cell applications were obtained from Sigma

Aldrich and were stored over 3 Å molecular sieves for at least four days to ensure low moisture content.

### 3.2.6 Electrolyte Preparation

The first electrolyte, 1 M lithium bis(trifluoromethanesulfonyl)imide (LiTFSI) in DOL (1,3-dioxolane, anhydrous, Sigma-Aldrich) and DME (1,2-dimethoxyethane, anhydrous, Sigma-Aldrich) mixture (1:1 volume) was prepared. In an argon filled glovebox, LiTFSI salt was dried under vacuum at 120 °C for 12 hours. LiTFSI was added to the DOL-DME mixture and dissolved to reach the desired concentration. The electrolyte was kept and used in an argon filled glovebox.

The second electrolyte, 1 M lithium hexafluorophosphate (LiPF<sub>6</sub>) in EC (ethylene carbonate, Sigma Aldrich) and DEC (diethyl carbonate, Sigma Aldrich) solvent mixture (volume 1:1) was prepared in an argon filled glovebox. The solvent mixture of EC-DEC (1:1 volume) was prepared in argon filled glovebox and dried with 3 Å molecular sieves for two days. The water content in EC-DEC (1:1 v%) solvent was measured with the Karlh Fischer (KF) titration method and found to be less than 25 ppm. LiPF<sub>6</sub> salt was added and dissolved in the solvent mixture to reach the desired concentration. For a portion of this study, 1 M LiPF<sub>6</sub> EC-DEC (50:50 volume) (Sigma Aldrich) solution was also used.

### 3.2.7 Solvent and Electrolyte Uptake Test

Uniform 1/2 in. diameter samples of polymer films were prepared in the dry state. The diameter and thickness of each polymer film was measured and weighed in the dry state. It was found previously, for similar polymer samples which swelled in solvents, that equilibrium was reached in four hours.<sup>98</sup> In this study, the polymers were swelled in electrolytes or solvents for twenty-four hours. Before the membranes were swelled in electrolyte, each sample was weighed, and the dimensions (thickness and diameter) were measured with a micrometer (Mitutoyo No. 293-349-30). Each of the samples were placed in a vial and parafilm was used to prevent uptake of moisture. The polymers were submerged in the electrolyte for twenty-four hours. The excess electrolyte was removed from the polymer surface with a Kimwipe tissue and the dimensions (diameter, thickness) and mass uptake were measured.

### **3.3 Characterization**

#### **3.3.1 Elemental Analysis – ICP-OES Inductively Coupled Plasma Atomic Emission Spectroscopy**

##### **3.3.1.1 Sample Preparation**

To be processed efficiently in the plasma, samples must be in either the gas or liquid form. Both dry and swelled state polymers were digested in nitric acid (HNO<sub>3</sub>). In accordance with prepared standards, the desired concentration of lithium in the digested polymer solution was 1 ppm. In the case of 1 M LiTFSI (DOL-DME) or 1 M LiPF<sub>6</sub> (EC-DEC 1:1) electrolyte swelled membranes, before the digestion process, the samples were wiped with a Kimwipe tissue to remove excess solvent and dried under vacuum 80°C for 12 hours. Dry samples were weighed and taken out from the glovebox. The digestion process took place in the fume hood. Before starting, every volumetric flask, single neck round bottom flask, and disposable glass pipets were washed with 5% HNO<sub>3</sub> first and rinsed with deionized water three times to make sure there was no contamination. The polymer samples were put on the single neck round bottom flask and 10 ml of 70 % concentrated HNO<sub>3</sub> was added. The flask was connected to a condenser column. On the hot plates, an oil bath was placed, and the flask containing the sample which was connected to the condenser column was lowered into the oil bath. The sample refluxed in the solution for twelve hours at 250°C. The digested samples were transferred to 100 ml volumetric flasks and diluted with deionized water to 5% HNO<sub>3</sub> and 95% water.

Inductively coupled plasma atomic emission spectroscopy, also referred to as inductively coupled plasma optical emission spectrometry, is an analytical technique used for the detection of chemical elements

##### **3.3.1.2 ICP- OES – Standard Preparation**

Lithium standards for ICP-OES measurements were prepared in the range of 0.16 ppm, 0.4 ppm, 0.8 ppm, 1.6 ppm and 2 ppm. All the volumetric pipets and volumetric flasks were washed with 5% HNO<sub>3</sub> and rinsed with deionized water three times. 1000 ppm lithium standard was obtained from Sigma Aldrich and diluted with deionized water to 100



ml and 250 ml lithium standards in volumetric flasks. From the 100 ml  $\text{Li}^+$  standard, 0.4 ppm and 2 ppm were made via dilution. From the 250 ml  $\text{Li}^+$  standard, 0.16 ppm, 0.8 ppm and 1.6 ppm lithium standards were prepared.

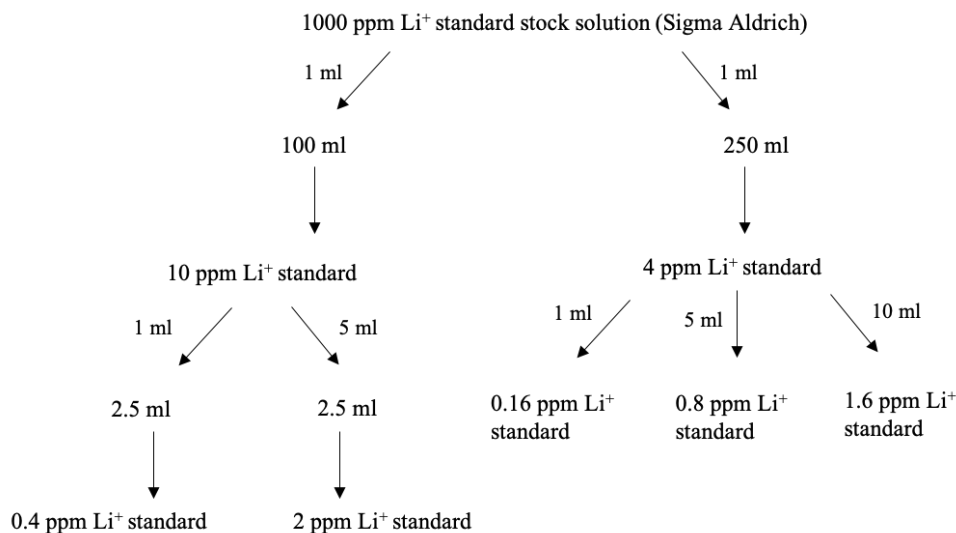


Figure 3.3: ICP-OES standards preparation process for the calibration.

### 3.3.1.3 ICP-OES - Measurement

The prepared polymer and lithium standards were put in 15 ml sample tubes.  $\text{Li}^+$  concentration was measured with a Perkin Elmer Optima 800 ICP-OES. The lithium standard solutions and samples were placed in the sample holder. With regard to standards, first the calibration curve was prepared by the program itself and later on, the samples were measured one by one. Each sample measurement took approximately two minutes. The results were evaluated according to the intensity vs. concentration (ppm).

### 3.3.2 Conductivity Measurement

Each GPE was swelled in 1 M  $\text{LiTFSI}$  (DOL-DME 1:1 v%) or 1 M  $\text{LiFF}_6$  (EC-DEC 1:1 v%) electrolyte or DOL-DME or EC-DEC solvent mixture at least four hours prior to the conductivity measurement. The polymer membrane was taken out from the electrolyte and the excess amount of electrolyte was removed with Kimwipe tissue to measure the thickness. Thickness of the sample is relevant for Novocontrol Turnkey

Broadband Dielectric Spectrometer. After that, the GPEs were rinsed with electrolyte or solvent and sandwiched between brass electrodes within the glovebox, then the Novocontrol Turnkey Broadband Dielectric Spectrometer was used to measure conductivity over the temperature range of -20 °C to 85 °C from cold to hot. The  $\sigma_{DC}$  was extracted as the region over which a plateau in the  $\sigma_{AC}$  vs frequency is observed.

### **3.3.3 Fourier-Transform Infrared Spectroscopy (FTIR)**

Dry opaque and transparent PEGDMA-VS-0 membranes were cut to approximately 6 mm in diameter disks and put into the vials within the glovebox. The vials were sealed with parafilm to prevent contamination during transport and were removed from the glovebox. A Jasco 6300 Fourier Transform Infrared (FTIR) spectrometer was used for analysis. Each membrane sample was scanned 25 times per measurement over a range of wavenumbers from 650  $\text{cm}^{-1}$  to 4000  $\text{cm}^{-1}$ .

### **3.3.4 Scanning Electron Microscope (SEM)**

Transparent and opaque PEGDMA-VS-0 membranes were cut approximately 6 mm diameter disks and put into vials within the glovebox. The vials were sealed with parafilm to prevent contamination during transport and were removed from the glovebox. A Magellen 400 Scanning Electron Microscope (SEM) was used for surface characterization of the membranes. SEM micrographs were obtained using a current of 13 pA and an accelerating voltage of 5 kV.

### **3.3.5 Lithium Symmetric Cells – Transference Number Measurement**

In the glovebox, lithium metal (Alfa Aesar, 0.75 mm thick, 99.9 %) was polished to remove the oxide layer. Two 3/8 in. diameter lithium pieces were punched from the polished lithium metal. Beforehand, 1/2 in. diameter size GPEs were swelled in 1M LiTFSI (DOL-DME 1:1) electrolyte until reaching equilibrium. Within 2032 type coin cells (MTI Corp), lithium metal was wetted with 20 microliters of electrolyte to increase the contact between the metal and the GPE. The swelled GPE was placed between two lithium metal, in contact with both polished sides. Two stainless steel spacers (15.5 mm diameter x 0.2 mm thick) and one wave spring were used, and the coin cell was sealed with an electronic

crimper. An Ametek Princeton Applied Research Parstat MC was used for the impedance spectroscopy and transference number ( $t_+$ ) measurements.

### **3.3.6 Cathode Preparation – LiFePO<sub>4</sub>**

LiFePO<sub>4</sub> powder (MTI Corporation) was mixed with Carbon Black (MTI Batch No. 0011512) and polyethylene oxide (PEO, 100k g/mol) with the mass ratio of 60:20:20. Then, 300 microliters of acetonitrile (CH<sub>3</sub>CN) was added to the mixture and stirred overnight. The cathode slurry was spread on aluminum foil with a doctor blade to a thickness of 200 micrometers. The cathode sheet was transferred to the glovebox and was dried at 90 °C, under high vacuum for 12 hours to remove any residual CH<sub>3</sub>CN and water. After the drying process, the prepared cathode sheet was punched with 3/8 in. hole punch into circular pieces to be used for coin cell applications.

### **3.3.7 Li/LiFePO<sub>4</sub> Cells - Galvanostatic Cycling**

In the glovebox, lithium metal (Alfa Aesar, 0.75 mm thick, 99.9 %) was polished to remove the oxide layer. One 3/8 in. diameter lithium piece was punched from the polished lithium metal. With the same diameter punch, one piece of LiFePO<sub>4</sub> (thickness 50 – 60 micrometer) was punched from the dried cathode sheet. A 1/2 in. diameter size of polymer membrane was swelled in 1M LiTFSI (DOL-DME 1:1) electrolyte until it reached equilibrium. Inside 2032 type coin cells (MTI Corp), the LiFePO<sub>4</sub> cathode was wetted with 20 microliters of electrolyte to increase the contact with the GPE. Before placing the lithium metal, an additional 10 microliter electrolyte was added on the GPE. Two stainless steel spacers (15.5 mm diameter x 0.2 mm thick) and one wave spring were used, and the coin cell was sealed with an electronic crimper. A Neware Battery Systems Battery Tester was used for galvanostatic cycling.

In some experiments, a commercial LiCoO<sub>2</sub> cathode (MTI Corporation) sheet was used. These are indicated specifically within the results section.

## 3.4 Results and Discussion

### 3.4.1 Polymer synthesis and composition (PEGDMA 750 mol/g-VS)

As a starting point, we define our membranes in accordance with their appearances; transparent and opaque PEGDMA-VS-0. One of the fundamental reasons to make PEGDMA-VS GPEs is to understand their transport and electrochemical behaviours and potential application for LiBs. In Chapter 1, we studied PEGDA 700 mol/g with NaSS with varied EO=Li ratios. In this section, we choose to study PEGDMA 750 mol/g as the backbone with vinyl sulfonate. In terms of backbone chemistry, PEGDA 700 mol/g and PEGDMA 750 g/mol are fairly akin to each other. The only difference is the additional acrylate groups in PEGDMA which gives the ability to covalently link up to four other PEGDMA chains through radical polymerization. By introducing vinyl sulfonate groups to the polymer network, the desired effect is to increase the ion dissociation and mobility of bonded charges. The similar system was developed and used by the Archer's group for Li-S systems with 1 M LiTFSI (DOL-DME 1:1 v%) successfully. Hence, we study the similar polymer chemistry for Li-ion battery systems with both 1 M LiTFSI (DOL-DME 1:1 v%) and 1 M LiPF<sub>6</sub> (EC-DEC 1:1 v%).

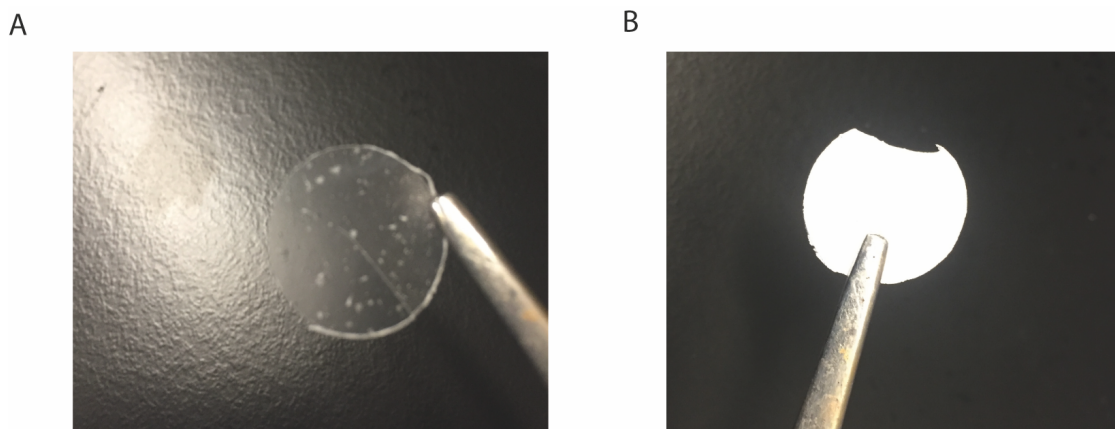


Figure 3.4: A) T-PEGDMA-VS-0 membrane B) O-PEGDMA-VS-0 membrane.

### 3.4.2 Electrolyte Uptake Measurement

Electrolyte uptake measurements were conducted to quantify the extent of swelling. This experiment was done with 1 M LiPF<sub>6</sub> (EC-DEC 1:1 v%) electrolyte. In accordance with Table 3.3, both the membranes are capable of swelling the electrolyte. The opaque membranes swell more than the transparent membranes due to their porous structure which is confirmed through later SEM analysis. After measuring the electrolyte uptake ratio, these membranes were dried in vacuum oven at 120°C for 24 hours to evaporate the EC-DEC solvent in the membranes. Through swelling, the membranes' mass doubled. After drying the solvent off from the membranes, the salt in the polymer network is obtained. The increments of the mass after swelling and drying process indicates the amount of lithium salt in the polymer network. Hence, opaque membranes are able to swell more due to the porous structure but after the drying, dissolved lithium salt does not tend to stay in the network. Elemental analysis was conducted to evaluate the lithium concentration in the membranes.

Table 3.3: 1 M LiPF<sub>6</sub> (EC-DEC 1:1 %) uptake data, by mass and volume, after four hours of swelling for studied SIPEs.

\*Calculated by measuring change in thickness and diameter. \*\* calculated by measuring change in thickness and assuming isotropic expansion.

| Sample        | Mass Increase %* | Standard Deviation | Volume Increase %** | Standard Deviation |
|---------------|------------------|--------------------|---------------------|--------------------|
| O-PEGDMA-VS-0 | 329              | ±33                | 166                 | ±8                 |
| T-PEGDMA-VS-0 | 245              | ±21                | 155                 | ±9                 |

### 3.4.3 ICP-OES Elemental Analysis

Similar to the PEGDA-SS case, lithium content is determined by elemental analysis. After synthesising the crosslinked polymer, the elemental analysis confirms the ionic exchange between Na<sup>+</sup> and Li<sup>+</sup>. After swelling the membranes in electrolyte, the excess amount of lithium, which was dissolved in the binary solvent mixture, in the

polymer matrix is acquired. Hence, the total lithium in the gel polymer electrolyte system is obtained. We will be able distinguish the effect of lithium salt and bonded charges on the transport properties.

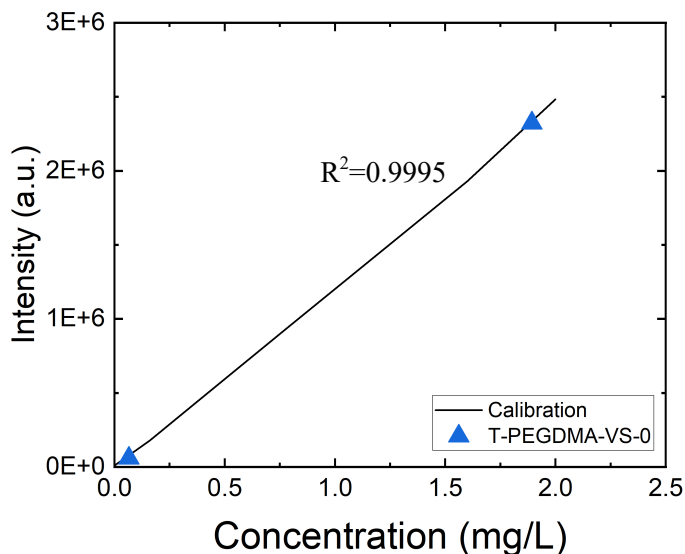


Figure 3.5: Dry (0.5 M LiCl ionic exchange solution) and 1 M LiPF<sub>6</sub> (EC-DEC 1:1 v%) swelled T-PEGDMA-VS-0 crosslinked membranes.

Figure 3.5 shows the outcomes of ICP-OES analysis for dry and in 1 M LiPF<sub>6</sub> (EC-DEC 1:1 v%) T-PEGDMA-VS-0 membranes. The comparison between the calculated value and the obtained value ratio should be 90-95% to confirm the ionic exchange. The experiment was repeated twice, and the same results are collected. In accordance with the results, the ionic exchange does not happen in both membranes. The measured Li<sup>+</sup> concentration in both O-PEGDMA-VS-0 and T-PEGDMA-VS-0 are extremely low which indicates there are no tethered anions in the polymer matrix. However, 1 M LiPF<sub>6</sub> swelled membranes after solvent drying show  $4.1 \times 10^{-3}$  mol/cm<sup>3</sup> and  $4.3 \times 10^{-3}$  mol/cm<sup>3</sup> lithium concentrations. The same experiment was tried with 1 M LiTFSI (DOL-DME 1:1 v%) and there was no lithium in the membrane. Interestingly, 1 M LiPF<sub>6</sub> (EC-DEC 1:1 v%) swelled membranes have high lithium concentration. Therefore, it shows that the polymer and ionomer interaction with cations and anions are different in this case. SEM images show the porous structure for opaque membrane in the upcoming section. We can speculate that the pores are small enough to keep Li<sup>+</sup> ions with PF<sub>6</sub><sup>-</sup> anions. So, Li<sup>+</sup> ions

are able to stay in the polymer network. The reason why the same results cannot be obtained with 1 M LiTFSI is because the TFSI<sup>-</sup> anion is bigger than PF<sub>6</sub><sup>-</sup> anion, 3.9 × 8.0 Å and 3.5 × 3.5 Å respectively.<sup>119</sup> Hypothetically, we assume that the pores shrink in the presence of carbonate solvent. Considering the size of the ions, with Li<sup>+</sup>, only PF<sub>6</sub><sup>-</sup> is able to stay in the pores. A high lithium concentration is obtained in this case.

Table 3.4: Elemental Analysis Results for O-PEGDMA-VS-0 and T-PEGDMA-VS-0 as dry (ionic exchange in 1 M LiCl).

| Sample Name   | Targeted Li <sup>+</sup> Concentration (mol/cm <sup>3</sup> ) | Measured Li <sup>+</sup> Concentration (Only ionic exchange) (mol/cm <sup>3</sup> ) | $\frac{C_{Li^+}^{measured}}{C_{Li^+}^{estimated}}$ |
|---------------|---|---|--|
| T-PEGDMA-VS-0 | $2.3 \times 10^{-3}$  | $9.1 \times 10^{-7}$  | 4%   |
| O-PEGDMA-VS-0 | $2.7 \times 10^{-3}$  | $6.6 \times 10^{-5}$  | 3%   |

Table 3.5: Elemental Analysis Results for T-PEGDMA-VS-0 and O-PEGDMA-VS-0 in 1 M LiPF<sub>6</sub> (EC-DEC 1:1 v%).

| Sample Name   | Targeted Li <sup>+</sup> Concentration (mol/cm <sup>3</sup> ) | Measured Li <sup>+</sup> Concentration in 1 M LiPF <sub>6</sub> (EC-DEC 1:1 v%) (mol/cm <sup>3</sup> ) | $\frac{C_{Li^+}^{measured}}{C_{Li^+}^{estimated}}$ | In 1 M LiTFSI (DOL-DME 1:1 v%) (mol/cm <sup>3</sup> ) |
|---------------|---|--|--|---|
| T-PEGDMA-VS-0 | $2.3 \times 10^{-3}$  | $4.1 \times 10^{-3}$   | 178%   | $1.6 \times 10^{-5}$                                  |
| O-PEGDMA-VS-0 | $2.4 \times 10^{-3}$  | $4.5 \times 10^{-3}$   | 187%   | $1.8 \times 10^{-4}$                                  |

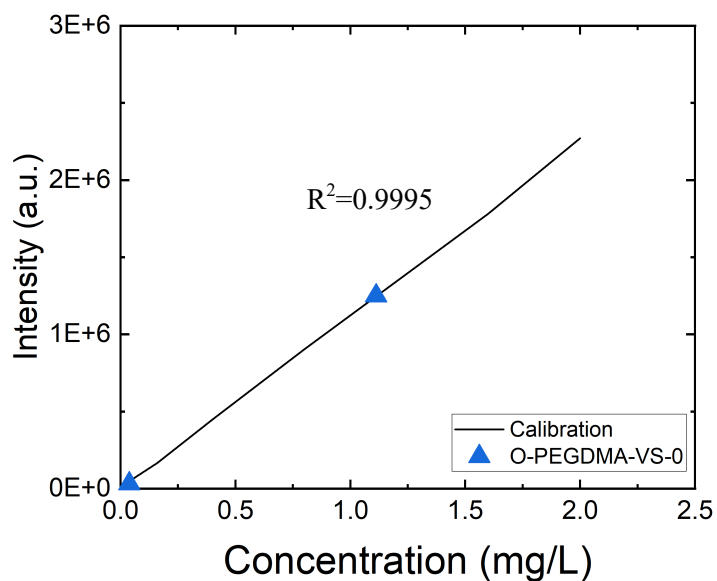


Figure 3.6: 1 M LiPF<sub>6</sub> (EC-DEC 1:1 v%) electrolyte swelled and dry O-PEGDMA-VS-0 crosslinked membranes.

The dry case results could be due to unsuccessful ion exchange, if the ionic exchange solution is not strong enough, thus 2 M LiOH and 1 M LiTFSI (DOL-DME 1:1 v%) were also tried as new ionic exchange solutions. The experiment was conducted with only for O-PEGDMA-VS-0.



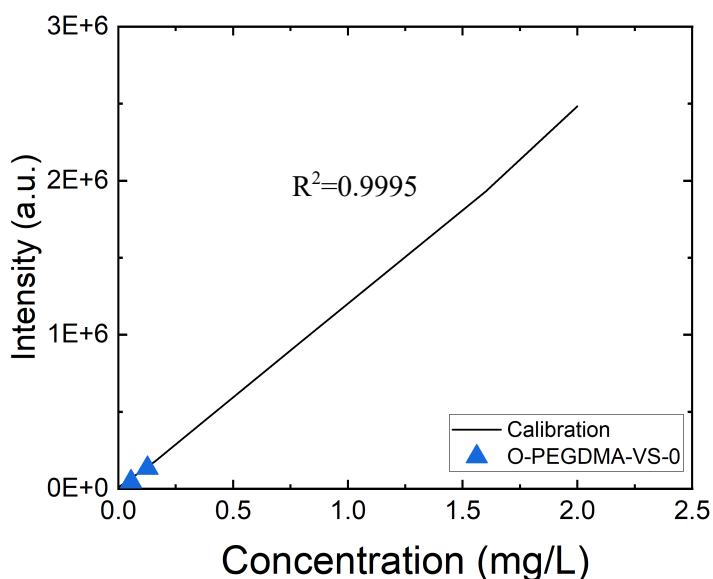


Figure 3.6: Dry (2 M LiOH and 1 M LiTFSI (DOL-DME 1:1 v%) ionic exchange solution) O-PEGDMA-VS-0 crosslinked membranes.

Table 3.6: Elemental Analysis Results for O-PEGDMA-VS-0 in 1 M LiTFSI (DOL-DME 1:1 v%) and 2 M LiOH.

| Sample Name   | Targeted Li <sup>+</sup> Concentration (mol/cm <sup>3</sup> ) | In 1 M LiTFSI (DOL-DME 1:1 v%) (mol/cm <sup>3</sup> ) | $\frac{C_{Li^+}^{measured}}{C_{Li^+}^{estimated}}$ | In 2 M LiOH (mol/cm <sup>3</sup> ) | $\frac{C_{Li^+}^{measured}}{C_{Li^+}^{estimated}}$ |
|---------------|---|---|--|------------------------------------|--|
| O-PEGDMA-VS-0 | $2.3 \times 10^{-3}$  | $1.8 \times 10^{-4}$                                  | 8%   | $8.1 \times 10^{-5}$               | 4%   |

Despite changing the ionic exchange solutions, the outcomes do not change. Therefore, it is stated that somehow, VS does not dissociate, and cations cannot be present in the polymer matrix. In order to confirm this, FTIR measurement was done for the membranes to see if the sulfonate peak exists. In the following section, FTIR results are going to be discussed.

As an additional elemental analysis, the wet opaque PEGDMA-VS was tested in the dry state. Since the sulfonate peak is observed within the FTIR spectrum, we expected to see bonded charges. However, there is no lithium cation detected. Table 3.7 shows the results in comparison to T-PEGDMA-VS-0 case.

Table 3.7: Elemental Analysis Results for T-PEGDMA-VS-0 and wet Opaque PEGDMA-VS as dry case.

| <b>Sample Name</b> | <b>Targeted Li<sup>+</sup> Concentration (mol/cm<sup>3</sup>)</b> | <b>Measured Li<sup>+</sup> Concentration (Only ionic exchange) (mol/cm<sup>3</sup>)</b> | $\frac{C_{Li^+}^{measured}}{C_{Li^+}^{estimated}}$ |
|--------------------|---|---|--|
| T-PEGDMA-VS-0      | $2.3 \times 10^{-3}$  | $9.1 \times 10^{-7}$  | 4%   |
| Wet-O-PEGDMA-VS-0  | $1.8 \times 10^{-3}$  | $8.8 \times 10^{-5}$  | 4%   |

It is evident that vinyl sulfonate does not polymerize with the PEGDMA backbone. After washing and digesting the sample for ICP-OES, the VS is washed away.

### 3.4.4 Scanning Electron Microscopy Images (SEM)

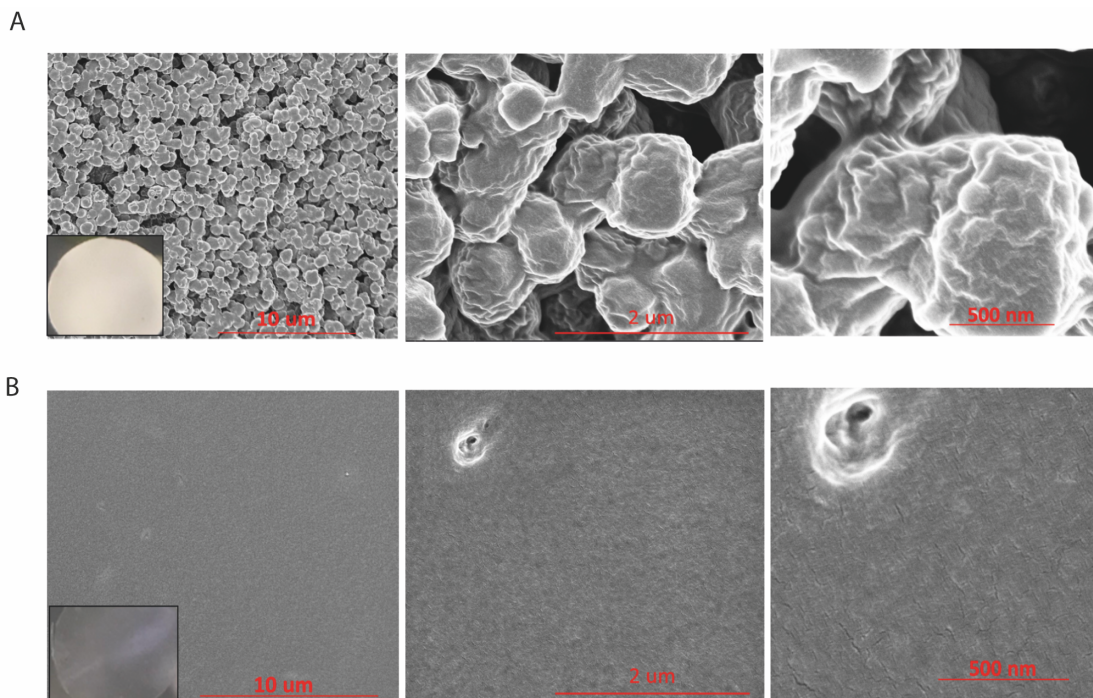


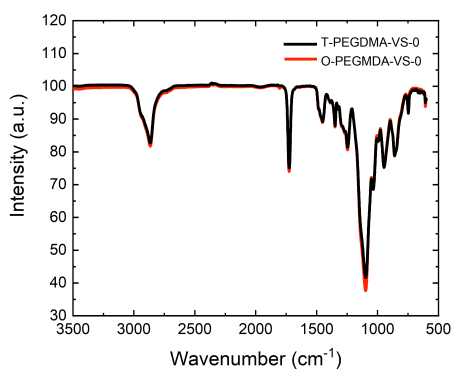
Figure 3.7: a) SEM images of O-PEGDMA-VS-0. b) SEM images of T-PEGDMA-VS-0.

SEM imaging was utilized to see the structure of the opaque and transparent PEGDMA-VS-0 membranes. At three different magnification scales, the membranes were investigated. The opaque membrane uniformly has a nanoporous structure, as depicted in Figure 3.7 A. This structure forms due to phase separation during the membrane preparation. Obtaining the actual size of the pores in the membrane in the swelled state is beyond our laboratory facilities and scope of this study. The main interest is to comprehend transport behaviours in the presence of liquid electrolyte. The same monomer is used for T-PEGDMA-VS-0 membrane preparation without any phase separation and there is no porous structure. In following sections, the impact of the structure difference on transport properties is going to be evaluated in terms of ionic conductivity, cation transference number, and cycling properties.

### 3.4.5 Analysis Fourier-Transform Infrared Spectroscopy (FTIR)

FTIR analysis was performed on opaque and transparent samples to detect the crosslinking and incorporation of sulfonate groups, achieved by linking VS into the polymer network. In accordance with ICP-OES, any bound charges were not detected. Figure 3.8 shows the FTIR spectra of opaque and transparent PEGDMA-VS-0 and pure PEGDMA membranes. The sulfonate stretch S=O (anhydrous) peak is expected in the range of 1195-1168  $\text{cm}^{-1}$ . As it is depicted in Figure 3.8, neither opaque or transparent membranes have the peak. With regard to Archer's and coworkers' study, the S=O stretch was detected at 1175  $\text{cm}^{-1}$ .<sup>74</sup> The opaque and transparent membranes are perfectly crosslinked regarding to the C=O bond. However, it is evident that VS does not cooperate in PEGDMA matrix.

A



B

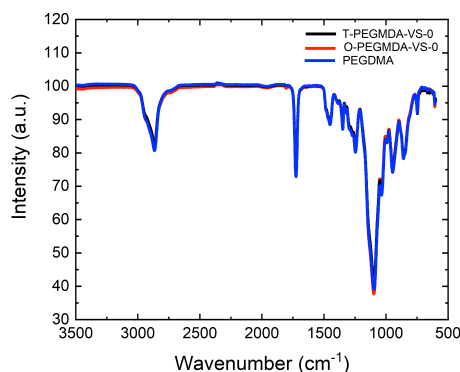


Figure 3.8: Fourier transform infrared spectra of control PEGDMA and ionomer membranes created using our UV-cross-linking approach. A illustrates the opaque and transparent PEGDMA-VS-0 crosslinked membranes. B compares the pure PEGDMA membrane to transparent and opaque PEGDMA-VS-0.

As it was mentioned on the membrane synthesis section, the monomer solution is sandwiched between two glass plates for UV crosslinking. Based on the laboratory experience, it is found that the glass plates absorb UV light. Thus, the monomer solution is casted on the glass plate and crosslinked under  $\text{N}_2$  with open surface.

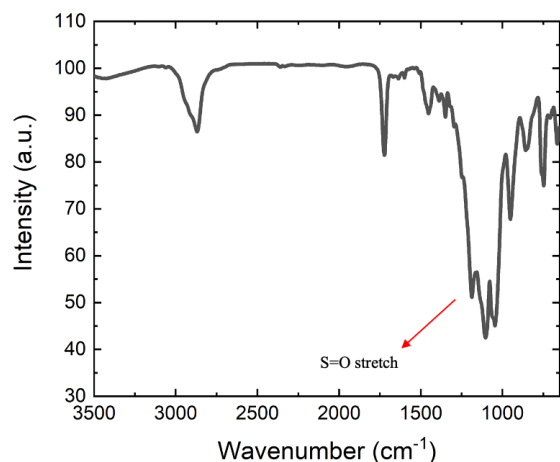


Figure 3.9: Fourier transform infrared spectra (FTIR) of wet Opaque-PEGDMA-VS UV crosslinked membrane with open surface.

Figure 3.9 illustrates membranes which were prepared by the second method (without drying in Schenk line). The sulfonate stretch is detected in wet opaque-PEGDMA-VS membrane. S=O stretch is expected to be observed between 1230-1120  $\text{cm}^{-1}$ . In comparison to Figure 3.8, the presence of sulfonate is group is clear. Further characterizations, elemental analysis and transport property measurements were conducted.

### 3.4.6 Conductivity Measurement

Conductivity measurements were conducted with two commonly used electrolytes; 1 M LiTFSI (DOL-DME 1:1 v%) and 1 M LiPF<sub>6</sub> (EC-DEC 1:1 v%) and in their solvent mixtures. Similar to the PEGDA-SS case, we would like to compare SIPE and GPE behavior and the effect of only bonded charges and lithium salt. The SIPE case only depends on the bound charges on VS and dissociation of the PEGDMA-VS. The ionic conductivity relies on the interaction between lithium cations, solvent molecular, and polymer chains. Hence, we would like to compare different polymer chemistries (PEGDA-SS and PEGDMA-VS) to discern transport properties.

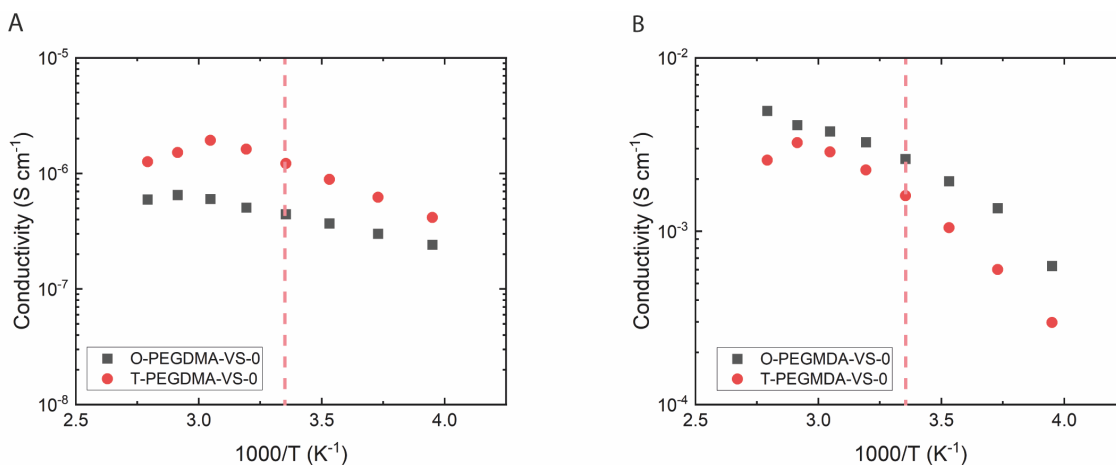


Figure 3.10: a) Conductivity of opaque and transparent PEGDMA-VS-0 swelled to equilibrium in DOL-DME (1:1 v%) b) Conductivity of opaque and transparent PEGDMA-VS-0 swelled to equilibrium in 1 M LiTFSI (DOL-DME 1:1 v %).

The first conductivity measurement was done with swelled transparent and opaque PEGDMA-VS-0 in DOL-DME (1:1 v%) solvent mixture. As it is found with ICP-OES and proven by FTIR spectroscopy, VS does not dissociate in the membrane. Therefore, there is no Li<sup>+</sup> in the PEGDMA-VS-0 without the addition of lithium salt. The ionic conductivity shows the conductivity of DOL-DME mixture which matches with the literature.<sup>120</sup> As expected, ionic conductivity increases with the elevated temperature. At 25°C, the ionic conductivities of the transparent and opaque membranes are akin to each other. The opaque membrane was measured at  $4.43 \times 10^{-7}$  S/cm, and the transparent membrane was measured at  $1.22 \times 10^{-6}$  S/cm. The small difference does not indicate any difference between two membranes. It might be due to measurement error. Thus, the same experiment is performed with 1 M LiTFSI (DOL-DME 1:1 v%) swelled opaque and transparent PEGDMA-VS-0 to investigate the lithium salt effect.

Ionic conductivity of 1 M LiTFSI (DOL-DME 1:1 v%) swelled PEGDMA-VS-0 is shown in Figure 3.10-B. At 25°C, the ionic conductivity for both membranes is remarkably higher than the DOL-DME case. The addition of the lithium salt is very clear in terms of equation  $\sum_i \eta_i q_i \mu_i$ . Firstly, the number of charges has increased because of the free Li<sup>+</sup> from the LiTFSI salt. Second, the free TFSI<sup>-</sup> anions also contributes to the total ionic conductivity. The total number of charges in the polymer could have been calculated by ICP-OES analysis but because of the VS issue, we cannot obtain the dry state and compare with the electrolyte swelled case. At 25°C, the highest ionic conductivity of

$2.61 \times 10^{-3}$  S/cm was obtained with opaque PEGDMA-VS-0, with the transparent obtaining  $1.60 \times 10^{-3}$  S/cm. When we compare the results with the DOL-DME (1:1 v%) case, it can be seen that the ionic conductivity of opaque membrane increases more than the transparent case. Theoretically, it might be due to the structure difference. SEM images shows the nanoporous structure of opaque membrane. Despite the fact that VS does not dissociate in the polymer matrix, different dissolved degrees changes the polymer vastly. Hypothetically, a porous structure without any tethered anions in the system increases in favor of  $\text{Li}^+$  cation transfer due the size of the  $\text{Li}^+$ . In order to investigate and try proving our theory, the same experiment is proceeded with 1 M  $\text{LiPF}_6$  (EC/DEC 1:1 v%) and only in EC-DEC solvent mixture.

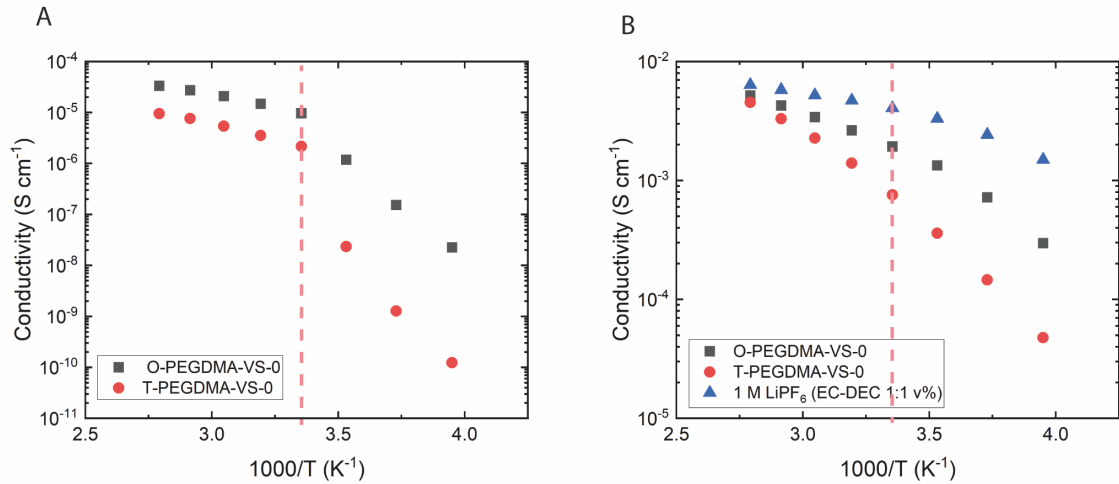


Figure 3.11: A) Conductivity of opaque and transparent PEGDMA-VS-0 swelled to equilibrium in EC-DEC solvent mixture (1:1 v %) B) Conductivity of opaque and transparent PEGDMA-VS-0 swelled to equilibrium in 1 M  $\text{LiPF}_6$  (EC-DEC 1:1 v %) and 1 M  $\text{LiPF}_6$  (EC-DEC 1:1 v%).

Ionic conductivity with respect to temperature was measured for the transparent and opaque PEGDMA-VS-0 in an EC-DEC (1:1 v%) solvent mixture and 1 M  $\text{LiPF}_6$  (EC-DEC 1:1v%). These results are shown in Figure 3.11. As stated previously, solvent polymer interactions cannot be disregarded in terms of determining the transport properties. Here, EC-DEC solvent's high dielectric constant effect can be observed clearly. Most of the time, high dielectric constant solvents induce a higher conductivity for high charge density membranes. In this particular case, we cannot relate charge density of the polymer to high conductivity because, simply the bounded charge density of both transparent and opaque

membranes is zero. Herein, the impurity ions from the solvents should be taken into consideration. It is known that these membranes do not contain bound charges. The measured ionic conductivity solely in solvents possibly indicate the impurity ions in the solvents. Additionally, the interactions between the polymer chains and the different solvents may have an impact too.

Before 20°C, the ionic conductivity values are remarkably low with regard to the melting degree of EC. (Melting degree of EC is approximately 20°C). After this, at 25°C, opaque membrane and transparent PEGDMA-VS-0 exhibit  $9.68 \times 10^{-6}$  S/cm and  $2.17 \times 10^{-6}$  S/cm respectively. In comparison to DOL-DME instance, the ionic conductivities results are reversed. The opaque membrane has a lower ionic conductivity in DOL-DME, which has lower dielectric constant than EC-DEC. A higher polarity promotes better cation dissociation and rapid transport. This suggests the opaque membrane interacts with EC-DEC differently than with DOL-DME due to its chemical structure. Ion transport and mobility in the polymer matrix change by polymer segmental motion.<sup>121, 122</sup> Consequently, without the lithium salt, conductivity depends on the characteristic of the solvent type and its impurity, along with the interactions between polymer and the solvent molecules.

As a last conductivity measurement, opaque and transparent PEGDMA-VS-0 membranes were swelled in 1 M LiPF<sub>6</sub> (EC-DEC 1:1 v%) electrolyte until they reached equilibrium. Ionic conductivity at 25°C for both transparent and opaque case is remarkably higher than all the previous cases including the PEGDA-SS case from the previous chapter. The opaque membrane exhibited  $1.93 \times 10^{-3}$  S/cm ionic conductivity at 25°C which is one of the highest ionic conductivity that has been reported in the literature for GPE applications. On the contrary, T-PEGDMA-VS-0 resulted in a conductivity of  $7.56 \times 10^{-4}$  S/cm. It is evident that different polymer structures impact the transport of ions. The ionic conductivity improvement with 1 M LiPF<sub>6</sub> (EC-DEC 1:1 v%) is also a function of high dielectric constant of the EC-DEC solvent mixture. Due to the high dielectric constant of EC ( $\epsilon = 90$ ), it can attribute the dissociation of lithium salt. Ionic conductivity at 25°C of both membranes in solvents and electrolyte summarized in Table 3.8.



Table 3.8: Ionic Conductivity of O-PEGDMA-VS-0 and T-PEGDMA-VS-0 at 25°C in solvent mixtures and electrolytes.

| Sample Name   | DOL-DME<br>(1:1 v%)<br>(S/cm) | 1 M LiTFSI<br>(DOL-DME 1:1<br>v%)<br>(S/cm) | EC-DEC (1:1<br>v%)<br>(S/cm) | 1 M LiPF <sub>6</sub> (EC-<br>DEC 1:1 v%)<br>(S/cm) |
|---------------|-------------------------------|---|------------------------------|---|
| O-PEGDMA-VS-0 | $4.43 \times 10^{-7}$         | $2.61 \times 10^{-3}$                       | $9.68 \times 10^{-6}$        | $1.93 \times 10^{-3}$                               |
| T-PEGDMA-VS-0 | $1.22 \times 10^{-6}$         | $1.60 \times 10^{-3}$                       | $2.17 \times 10^{-6}$        | $7.56 \times 10^{-4}$                               |

### 3.4.7 Lithium Symmetric Cell- Impedance Measurement (Lithium Transference Number)

As it was mentioned in the previous chapter, the transference number is a crucial property to explain Li<sup>+</sup> transport in the electrolyte. As was done in chapter 1 for the PEGDA-SS samples, the Bruce Vincent method, which is based on potentiostatic polarization of the cell and impedance measurements, was used to interrogate the transference number of opaque and T-PEGDMA-VS-0 system in 1 M LiTFSI (DOL-DME) and 1 M LiPF<sub>6</sub> (EC-DEC) electrolytes. The impedance results are presented in Nyquist plot form. All the measurements were done from the 100000 Hz to 0.1 Hz frequency range, and the applied voltage was less than or equal to 10mV. Each semicircle was fit with a simple binomial to obtain the  $Z_{re}$  values when  $Z_{im} = 0$ . Transference measurements were not performed on opaque and transparent PEGDA-VS-0 in EC/DEC or DOL/DME.

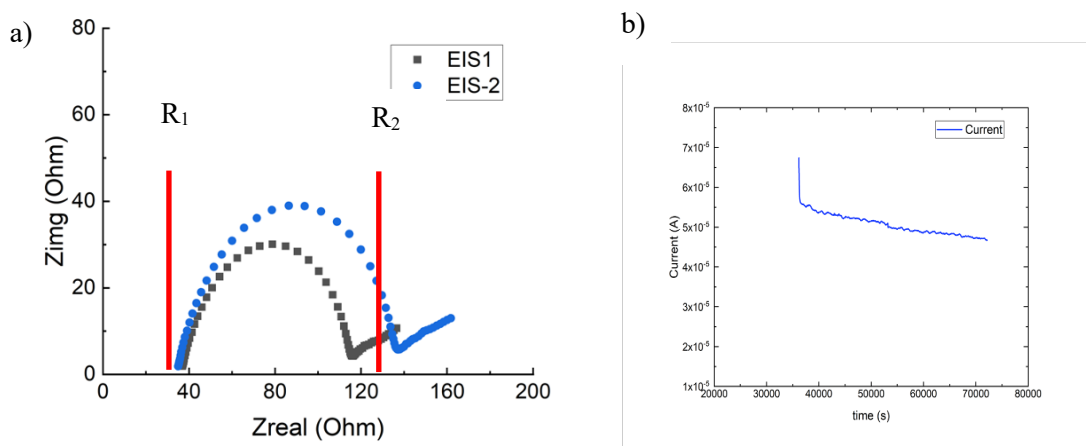


Figure 3.12: a) Impedance response pre- and post-potentiostatic hold of Li symmetric cells with O-PEGDMA-VS-0 in 1 M LiTFSI (DOL-DME 1:1 v%) b) Polarization curve – O-PEGDMA-VS-0 in 1 M LiTFSI (DOL-DME 1:1 v%).

The first measurement was conducted with the opaque membrane swelled in 1 M LiTFSI (DOL-DME 1:1 v%).  $R_1$  is assigned to the bulk electrolyte resistance and  $R_2$  represents the charge transfer resistance which increases after polarization due to decomposition on the lithium metal anode surface. On the contrary in the PEGDA-SS impedance measurement, at high frequency region, there is only one semi-circle which forms in this experiment. In literature, the first semi-circle represents the solid electrolyte interface (SEI). Medium frequency regions generally are attributed to charge transfer. The cell resistance after the polarization is not extremely high due to the porous structure. In related studies,<sup>123</sup> porous structure is claimed to improve the ion transport through the electrolyte.

Under these conditions, the transference number is calculated as 0.63. For a gel polymer electrolyte application, it is a high transference number especially in the presence of anions. We hypothesize that  $\text{Li}^+$  cations can transport through the pores whereas the TFSI<sup>-</sup> anions cannot due to their size. Therefore, a high transference number is achieved. When we look at the polarization curve, there is a small drop after the polarization starts.  $I_{ss}$  keeps slightly decreasing but the last  $I_{ss}$  value that is obtained is the same order of magnitude. The average is taken for  $I_{ss}$  and used for the calculation.

Table 3.9: Extracted resistance and current values from impedance and longer polarization measurement – 1 M LiTFSI (DOL-DME 1:1v%) swelled O-PEGDMA-VS-0.

| Sample Name                     | $R_1$<br>(ohms) | $R_2$<br>(ohms) | $R_{ss}$ or $R_0$<br>$(R_2-R_1)$<br>(ohms) | $I_{ss}$ (A)          | $I_o$ (A)             | $t_{Li+}$ |
|---------------------------------|-----------------|-----------------|--|-----------------------|-----------------------|-----------|
| O-PEGDMA-VS-0 pre hold (EIS-1)  | 37              | 116             | 79   | -                     | $6.74 \times 10^{-5}$ | 0.63      |
| O-PEGDMA-VS-0 post hold (EIS-2) | 34              | 137             | 103  | $4.67 \times 10^{-6}$ | -                     | 0.63      |

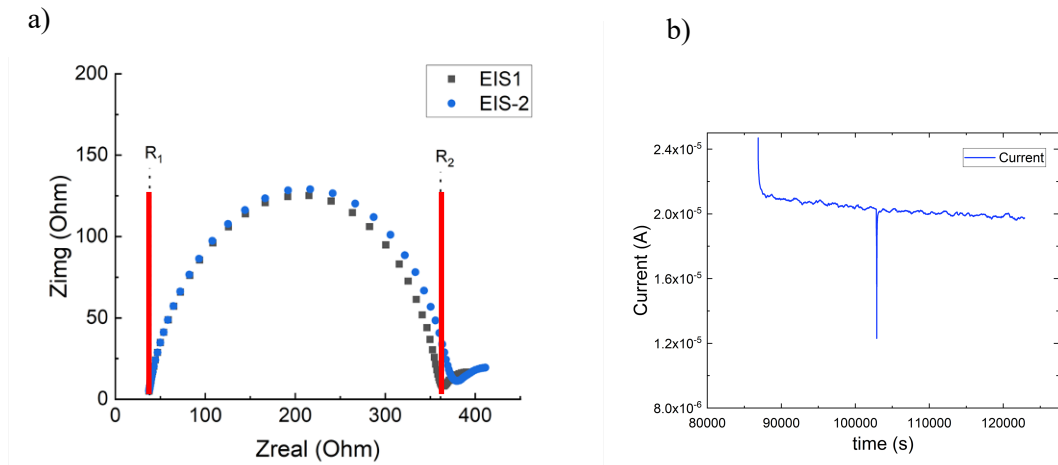


Figure 3.13: a) Impedance response pre and post hold of Li symmetric cells with T-PEGDMA-VS-0 in 1 M LiTFSI (DOL-DME 1:1 v%) b) Polarization curve – T-PEGDMA-VS-0 in 1 M LiTFSI (DOL-DME 1:1 v%).

Table 3.10: Extracted resistance and current values from impedance and polarization measurement – 1 M LiTFSI (DOL-DME 1:1v%) swelled transparent PEGDMA-VS-0.

| Sample Name                        | $R_1$<br>(ohms) | $R_2$<br>(ohms) | $R_{ss}$ or $R_0$<br>( $R_2-R_1$ )<br>(ohms) | $I_{ss}$ (A)          | $I_o$ (A)             | $t_{Li+}$ |
|------------------------------------|-----------------|-----------------|--|-----------------------|-----------------------|-----------|
| T-PEGDMA-VS-0 pre hold<br>(EIS-1)  | 36.90           | 363.61          | 326.71                                       | -                     | $2.47 \times 10^{-5}$ | 0.46      |
| T-PEGDMA-VS-0 post hold<br>(EIS-2) | 36.95           | 376.93          | 339.98                                       | $1.99 \times 10^{-5}$ | -                     | 0.46      |

A Li/T-PEGDMA-VS-0/Li cell was assembled for impedance measurement to obtain the transference number. Interestingly, pre-hold and post hold charge transfer resistance are not very different from each other. However, there is a remarkable difference in comparison to the opaque case. According to the Bruce Vincent, the calculated transference number is 0.46. This value is higher than all of PEGDA-SS case which are similar in terms of their dense structure.

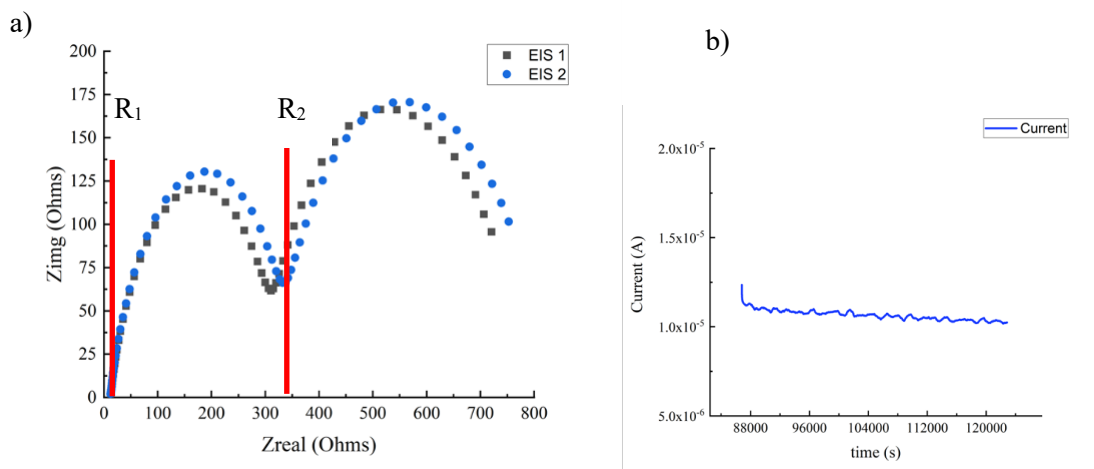


Figure 3.14: a) Impedance response pre and post hold of Li symmetric cells with O-PEGDMA-VS-0 in 1 M LiPF<sub>6</sub> (EC-DEC 1:1 v%) b) Polarization curve – O-PEGDMA-VS-0 in 1 M LiPF<sub>6</sub> (EC-DEC 1:1 v%).

O-PEGDMA-VS-0 was swelled in 1 M LiPF<sub>6</sub> (EC-DEC 1:1 v%) electrolyte before assembling for impedance measurement. The first semi-circle represents the SEI formation on the lithium metal, which is higher than the previous case. There are two reasons that could be the possible explanation for this. Firstly, it is known that LiPF<sub>6</sub> is very reactive with lithium metal.<sup>124</sup> Thus, the resistance is higher in this case. The polarization curve shows inappreciable noise which is related to reactivity of LiPF<sub>6</sub> on lithium metal surface.

In accordance with the equation (-), the transference number of O-PEGDMA-VS-0 is found as 0.79. It is a remarkable result in terms of all GPE applications with 1 M LiPF<sub>6</sub> (EC-DEC 1:1 v%) which have been shown in the literature. Archer's group study presented an impressive  $t_+$  particularly same materials with different electrolyte (0.5 M LiPS (DOL-DME 1:1 v%) and 1 M LiTFSI (DOL-DME 1:1v%)) respectively 0.98 and 0.96.<sup>74</sup> This study is slightly different from the current study. In Archer's group study, the sulfonate groups were successfully incorporated in the network and confirmed by FTIR. Therefore, the extremely high transference numbers were based on the presence of SO<sub>3</sub><sup>-</sup> groups which helped to increase the permeability of the membrane that resulted in higher electrolyte uptake. Also, SO<sub>3</sub><sup>-</sup> groups lead to a higher dielectric constant in which dissociation of Li<sup>+</sup> increased. Lastly, PS anions could not diffuse through the membrane and an impressive  $t_+$  were obtained. In our case, it is confirmed that there are no sulfonate groups tethered in the polymer matrix. Our hypothesis relies on the structure of the O-PEGDMA-VS-0. Due to

the different size of the  $\text{Li}^+$  and  $\text{PF}_6^-$  anions,  $\text{Li}^+$  is able to diffuse through the porous structure whilst,  $\text{PF}_6^-$  transport is limited with regard to segmental motion of the PEGDMA backbone. Thus,  $\text{Li}^+$  can diffuse faster and this leads to an impressive transference number. When we see the polarization curve, there is no severe drop on current despite the increment on the impedance. However, there is still a decreasing trend on the current for 10 hours of polarization. Therefore, the polarization time was increased twice, but the rest of the conditions were kept constant and the same experiment were conducted.

Due to complexity of measurement, the same experiments were repeated several times. The results are fairly akin to each other and consistent. The outcomes are shown in Table 3.12.

Table 3.11: Extracted resistance and current values from impedance and polarization measurement – 1 M  $\text{LiPF}_6$  (EC-DEC 1:1v%) swelled O-PEGDMA-VS-0.

| Sample Name                     | $R_1$<br>(ohms) | $R_2$<br>(ohms) | $R_{ss}$ or $R_0$<br>( $R_2-R_1$ )<br>(ohms) | $I_{ss}$ (A)          | $I_0$ (A)             | $t_{Li^+}$ |
|---------------------------------|-----------------|-----------------|--|-----------------------|-----------------------|------------|
| O-PEGDMA-VS-0 pre hold (EIS-1)  | 14              | 312             | 298  | -                     | $1.24 \times 10^{-5}$ | 0.79       |
| O-PEGDMA-VS-0 post hold (EIS-2) | 14              | 336             | 322  | $1.04 \times 10^{-5}$ | -                     | 0.79       |

Table 3.12: O-PEGDMA-VS-0  $t_{Li+}$  measurement results under the same conditions.

| Sample Name      | $t_{Li+}$ |
|------------------|-----------|
| O-PEGDMA-VS-0 -1 | 0.79      |
| O-PEGDMA-VS-0 -2 | 0.71      |
| O-PEGDMA-VS-0 -3 | 0.78      |

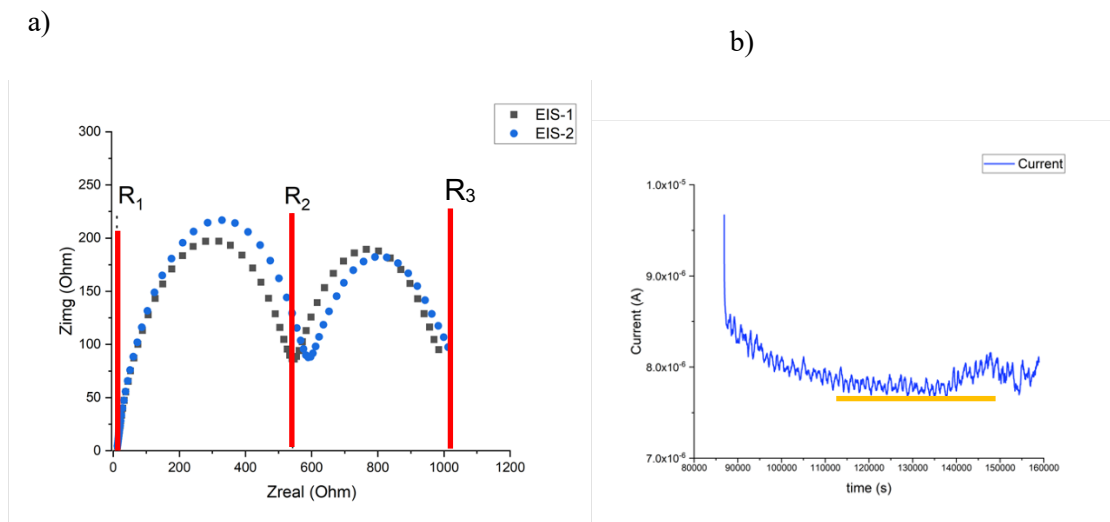


Figure 3.15: a) Impedance response pre and post hold of Li symmetric cells with O-PEGDMA-VS-0 in 1 M LiPF<sub>6</sub> (EC-DEC 1:1 v%)- longer polarization b) Longer polarization curve – O-PEGDMA-VS-0 in 1 M LiPF<sub>6</sub> (EC-DEC 1:1 v%).

As stated in the previous paragraph, the experiment was repeated with a 20 hour polarization period under the same conditions. Swelled O-PEGDMA-VS-0 membrane was assembled with two lithium metal plates for transference number measurement. On pre hold, the bulk electrolyte resistance  $R_1$  is obtained at 13 ohms after the fitting process, which is quite identical to previous opaque membrane result whereas, the charge transfer resistance is higher, 558 ohms respectively. After 20 hours of polarization,  $R_1$  and  $R_2$  do not change abruptly in comparison to the pre-hold resistances. In accordance with fitted resistance and  $I_0$  and  $I_{ss}$ , the calculated  $t_+$  is 0.71. The outcome is still very high for GPE electrolyte applications. However, it is marginally lower than the preceding experiments.

Table 3.13: Extracted resistance and current values from impedance and longer polarization measurement – 1 M LiPF<sub>6</sub> (EC-DEC 1:1v%) swelled O-PEGDMA-VS-0.

| Sample Name                     | R <sub>1</sub><br>(ohms) | R <sub>2</sub><br>(ohms) | R <sub>ss</sub> or R <sub>0</sub><br>(R <sub>2</sub> -R <sub>1</sub> )<br>(ohms) | I <sub>ss</sub> (A)     | I <sub>o</sub> (A)      | t <sub>Li+</sub> |
|---------------------------------|--------------------------|--------------------------|--|-------------------------|-------------------------|------------------|
| O-PEGDMA-VS-0 pre hold (EIS-1)  | 13                       | 558                      | 545  | -                       | 9.67 × 10 <sup>-6</sup> | 0.71             |
| O-PEGDMA-VS-0 post hold (EIS-2) | 13                       | 606                      | 593  | 7.87 × 10 <sup>-6</sup> | -                       | 0.71             |

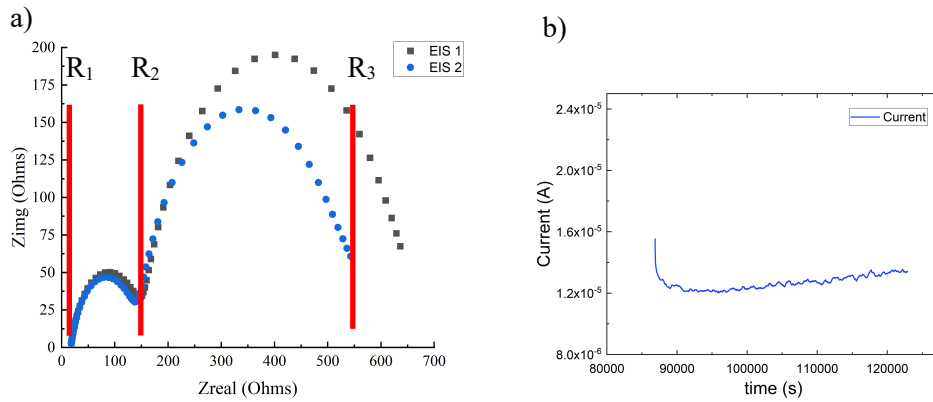


Figure 3.16 : a) Impedance response pre and post hold of Li symmetric cells with thick O-PEGDMA-VS-0 in 1 M LiPF<sub>6</sub> (EC-DEC 1:1 v%) b) Polarization curve –thick O-PEGDMA-VS-0 in 1 M LiPF<sub>6</sub> (EC-DEC 1:1 v%).



Table 3.14: Extracted resistance and current values from impedance and polarization measurement – 1 M LiPF<sub>6</sub> (EC-DEC 1:1v%) swelled thick O-PEGDMA-VS-0.

| <b>Sample Name</b>                    | <b>R<sub>1</sub><br/>(ohms)</b> | <b>R<sub>2</sub><br/>(ohms)</b> | <b>R<sub>ss</sub> or R<sub>0</sub><br/>(R<sub>3</sub>-R<sub>1</sub>)<br/>(ohms)</b> | <b>I<sub>ss</sub> (A)</b> | <b>I<sub>0</sub> (A)</b> | <b>t<sub>Li+</sub></b> |
|---------------------------------------|---------------------------------|---------------------------------|---|---------------------------|--------------------------|------------------------|
| Thick O-PEGDMA-VS-0 pre hold (EIS-1)  | 17                              | 150                             | 133   | -                         | 1.55 × 10 <sup>-5</sup>  | 0.81                   |
| Thick O-PEGDMA-VS-0 post hold (EIS-2) | 18                              | 142                             | 124   | 1.34 × 10 <sup>-5</sup>   | -                        | 0.81                   |

| <b>Sample Name</b>                    | <b>R<sub>1</sub><br/>(ohms)</b> | <b>R<sub>3</sub><br/>(ohms)</b> | <b>R<sub>ss</sub> or R<sub>0</sub><br/>(R<sub>3</sub>-R<sub>1</sub>)<br/>(ohms)</b> | <b>I<sub>ss</sub> (A)</b> | <b>I<sub>0</sub> (A)</b> | <b>t<sub>Li+</sub></b> |
|---------------------------------------|---------------------------------|---------------------------------|---|---------------------------|--------------------------|------------------------|
| Thick O-PEGDMA-VS-0 pre hold (EIS-1)  | 17                              | 605                             | 588   | -                         | 1.55 × 10 <sup>-5</sup>  | 0.31                   |
| Thick O-PEGDMA-VS-0 post hold (EIS-2) | 18                              | 535                             | 517   | 1.34 × 10 <sup>-5</sup>   | -                        | 0.31                   |

As mentioned earlier, a thick O-PEGDMA-VS-0 membrane was prepared to investigate the impact of the thickness of the membrane. Under normal conditions, the opaque membrane's thickness varies between 100-140  $\mu\text{m}$ . In this analysis, the thickness

was doubled (please the PEGDMA-VS synthesising section (3.2.3)). Figure 3.17 depicts the  $R_1$  and  $R_2$  and  $R_3$  resistances on the Nyquist plot. The  $t_+$  was calculated by taking into consideration the first semi-circle. The extracted resistance,  $I_o$  and  $I_{ss}$  values are shown on Table 3.14. In accordance with these values, the calculated  $t_+$  is 0.81. Additionally, if the SEM images of thick opaque membrane is seen, the porous structure is noticeably larger than the standard opaque membrane. The pores are extremely large which resembles the conventional separator's pores. Herein, we recalculate the  $t_+$  by taking into consideration  $R_3$  resistance. In this case, the  $R_3$  plays a crucial role for obtaining the RI of the electrolyte. Therefore,  $t_+$  is calculated as 0.31 (Please see the chapter about  $R_3$  resistance explanation.).

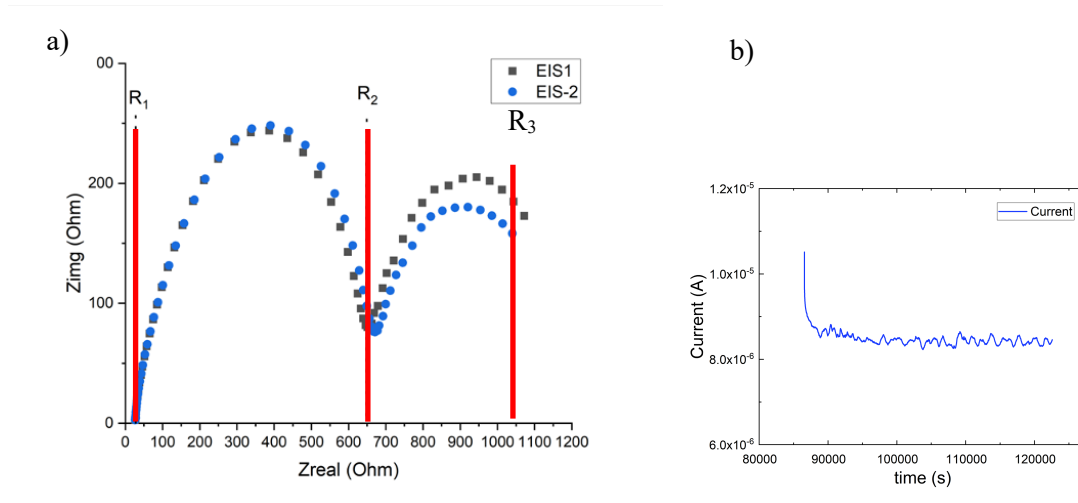


Figure 3.17: a) Impedance response pre and post hold of Li symmetric cells with T-PEGDMA-VS-0 in 1 M  $\text{LiPF}_6$  (EC-DEC 1:1 v%) b) Polarization curve – T-PEGDMA-VS-0 in 1 M  $\text{LiPF}_6$  (EC-DEC 1:1 v%).

In order to make a relevant comparison between two membranes, T-PEGDMA-VS-0 was swelled in 1 M  $\text{LiPF}_6$  (EC-DEC 1:1 v%) electrolyte and assembled with two lithium metal for impedance measurement. The bulk electrolyte resistance was marginally higher than opaque case. Since two semi circles have occurred in this case too, we consider first the charge resistance  $R_2$  for  $t_+$  calculation.  $R_2$  is twice as large as the opaque value, which is expected due its morphology.  $t_+$  was calculated as 0.65 which was surprisingly higher than expected. The same experiment was repeated, and the similar results were obtained with small variations. Morphologically, T-PEGDMA-VS was similar to PEGDA-SS (please see the SEM images). There was no nanoporous structure that makes  $\text{Li}^+$  transport

in a faster way. However, relatively high transference number suggests that methyl acrylate groups improves the ion transport through the polymer matrix. Since there are no delocalized sulfonate groups in the membrane that neither improves the polarity or dissociation.

The polarization curve shows more stable behavior in the transparent case. The current drop is noticeably higher than previous cases.

Table 3.15: Extracted resistance and current values from impedance and polarization measurement – 1 M LiPF<sub>6</sub> (EC-DEC 1:1v%) swelled T-PEGDMA-VS-0.

| Sample Name                        | R <sub>1</sub><br>(ohms) | R <sub>2</sub><br>(ohms) | R <sub>ss</sub> or R <sub>0</sub><br>(R <sub>2</sub> -R <sub>1</sub> )<br>(ohms) | I <sub>ss</sub> (A)     | I <sub>0</sub> (A)      | t <sub>Li+</sub> |
|------------------------------------|--------------------------|--------------------------|--|-------------------------|-------------------------|------------------|
| T-PEGDMA-VS-0 pre hold<br>(EIS-1)  | 29                       | 671                      | 642  | -                       | 1.05 × 10 <sup>-5</sup> | 0.65             |
| T-PEGDMA-VS-0 post hold<br>(EIS-2) | 29                       | 691                      | 662  | 8.44 × 10 <sup>-6</sup> | -                       | 0.65             |

### 3.4.8 Opaque and Transparent PEGDMA-VS with SO<sub>3</sub><sup>-</sup>

Due to the sulfonate dissociation issue, a different crosslinking procedure is tried to make the SO<sub>3</sub><sup>-</sup> groups incorporate into the polymer network. According to FTIR results, the sulfinate stretch is observable. Hence, regarding the new crosslinking procedure, opaque and transparent PEGDMA-VS membranes were prepared, and the characterization was done in the same way with only 1 M LiPF<sub>6</sub> (EC-DEC 1:1 v%).

### 3.4.8.1 Ionic Conductivity Measurements

The wet opaque and transparent PEGDMA-VS were swelled in 1 M LiPF<sub>6</sub> (EC-DEC 1:1 v%) and solvent mixture EC-DEC for at least 4 hours in order to reach equilibrium.

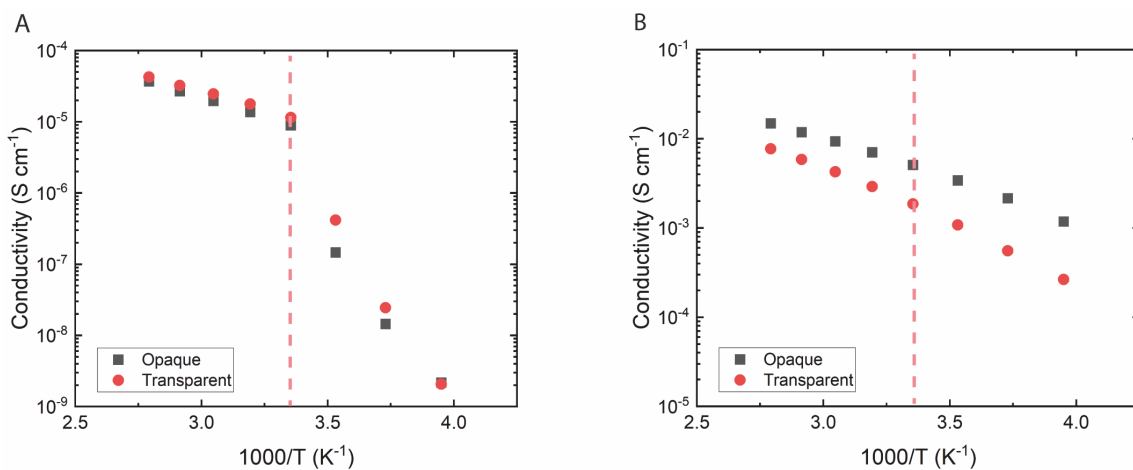


Figure 3.18: A) Conductivity of opaque (wet) and transparent PEGDMA-VS swelled to equilibrium in EC-DEC (1:1 v%) B) Conductivity of opaque (wet) and transparent PEGDMA-VS swelled to equilibrium in 1 M LiPF<sub>6</sub> (EC-DEC 1:1 v%).

Despite the SO<sub>3</sub><sup>-</sup> group confirmation from the FTIR results, the impact cannot be observed with an ionic conductivity measurement. The ionic conductivity of wet opaque membrane at 25°C was measured  $8.88 \times 10^{-6}$  S/cm, indicating that there are no charges on the polymer network. The transparent membrane results are depicted, in which the same results are shown here due to the fact that the wet vinyl sulfonate salt was not used to make this membrane. Figure 3.18 shows the ionic conductivity in 1 M LiPF<sub>6</sub> (EC-DEC 1:1 v%) and EC-DEC (1:1 v%). The ionic conductivity of wet opaque membrane is  $5.08 \times 10^{-3}$  S/cm swelled in 1 M LiPF<sub>6</sub>. This outcome matches with the previous results and SEM images. The wet opaque membrane has the nanoporous structure which was confirmed by the SEM images.

### 3.4.8.2 Impedance Measurement – Li<sup>+</sup> Transference Number

The impedance measurement was done under the same conditions with all the previous cases. Again, the thickness of this membrane was 300  $\mu\text{m}$ . The bulk electrolyte resistance is as akin to former cases for both pre hold and post hold. The charge transfer resistance is very low despite the thickness of the membrane which also confirms the thicker membrane experiments. According to the fitted values, the calculated transference number is 0.63. In comparison to former case,  $t_+$  is lower. As it was stated previously, it is highly possible that the ions move through the channels. These channels were observed in this material too but are not well structured. Also, we are seeing that having negatively charged ions in the polymer network does not impact the outcome effectively. However, with respect to Archer's group study, the positive impact of the sulfonate group was reported.<sup>74</sup> In accordance with the FTIR outcome, the existence of  $\text{SO}_3^-$  in the network is observable after the crosslinking process whereas ICP-OES results shows that there are no bonded charges to the polymer network. Thus, we assume that the  $\text{SO}_3^-$  does not dissociate in the PEGDMA network but is just present after the crosslinking. The nanoporous structure remains. We can conclude that, the structure plays the crucial role for determining the transport properties. Transparent PEGDMA-VS cannot be prepared with the same VS salt because of the water content. For transparent membrane, dry VS salt is used. Hence, this section only includes the opaque wet PEGDMA-VS.

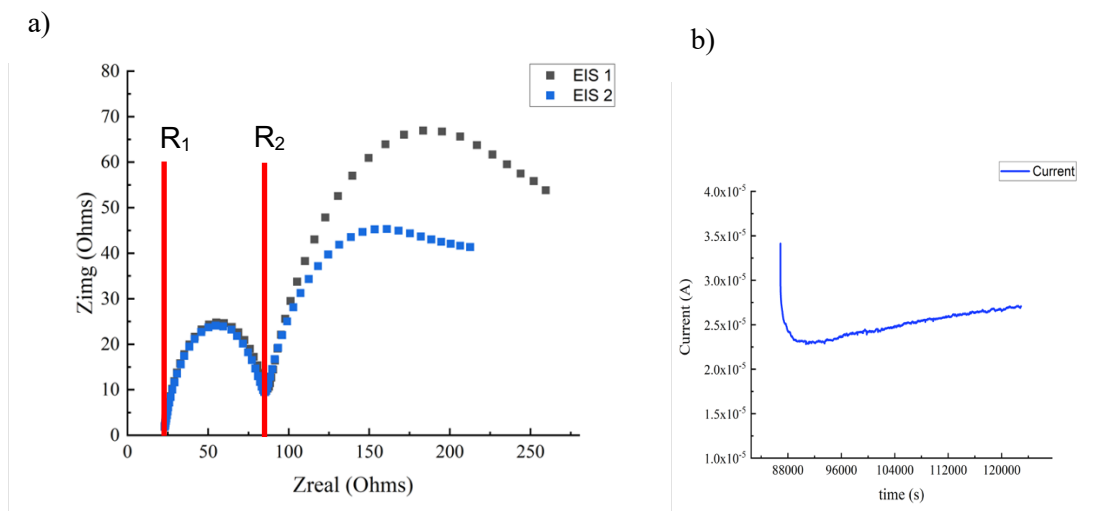


Figure 3.19: a) Impedance response pre and post hold of Li symmetric cells with wet opaque PEGDMA-VS in 1 M LiPF<sub>6</sub> (EC-DEC 1:1 v%) b) Polarization curve – Wet opaque PEGDMA-VS in 1 M LiPF<sub>6</sub> (EC-DEC 1:1 v%).

Table 3.16: Extracted resistance and current values from impedance and polarization measurement – 1 M LiPF<sub>6</sub> (EC-DEC 1:1v%) swelled wet opaque PEGDMA-VS.

| Sample Name                        | R <sub>1</sub><br>(ohms) | R <sub>2</sub><br>(ohms) | R <sub>ss</sub> or R <sub>0</sub><br>(R <sub>2</sub> -R <sub>1</sub> )<br>(ohms) | I <sub>ss</sub> (A)     | I <sub>0</sub> (A)      | t <sub>Li+</sub> |
|------------------------------------|--------------------------|--------------------------|--|-------------------------|-------------------------|------------------|
| Wet PEGDMA-VS pre hold<br>(EIS-1)  | 23                       | 85                       | 62   | -                       | 3.41 × 10 <sup>-5</sup> | 0.63             |
| Wet PEGDMA-VS post hold<br>(EIS-2) | 23                       | 83                       | 60   | 2.37 × 10 <sup>-5</sup> | -                       | 0.63             |

### 3.4.9 Full Cell Cycling Performance

After the characterization of the membranes, in order to study their applicability, a Li/cathode configuration is employed, and full cell cycling was performed. Two different cathode materials were used namely, LiCoO<sub>2</sub> and LiFePO<sub>4</sub>. Figure 3.20 shows the performance of the Li/O-PEGDMA-VS-0/LiCoO<sub>2</sub>. Commercial 1 M LiPF<sub>6</sub> (EC-DEC 1:1 v%) electrolyte was used for swelling the GPEs for all these battery studies.

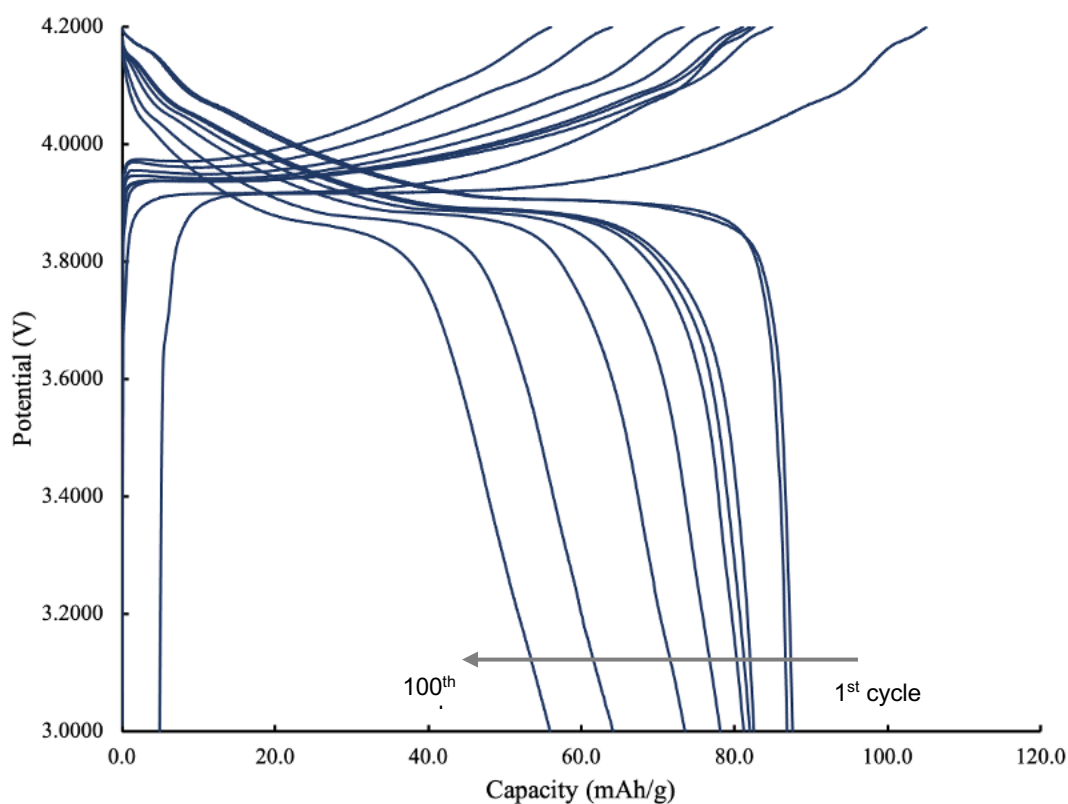


Figure 3.20: Li/O-PEGDMA-VS-0-separator/LiCoO<sub>2</sub> full cycling performance, at 0.1 C-rate.

O-PEGDMA-VS-0 was assembled with Li metal and LiCoO<sub>2</sub> for full cell cycling experiment. In the previous chapter, the issues related to LiCoO<sub>2</sub> were mentioned in detail. However, a couple of opaque membranes are assembled to see the effects. The cells generally failed after 20-50 cycles due to the incompatibility between the polymer electrolyte and LiCoO<sub>2</sub> cathode. Since, the transport properties of membranes are highly promising, in order to prevent side reaction between opaque membrane and LiCoO<sub>2</sub>

cathode, an inert separator was placed between them. Thus, the thickness of the electrolyte was increased 25  $\mu\text{m}$ . The discharge capacity after the first cycle is 93.4 mAh/g. The capacity is low in comparison to theoretical capacity of  $\text{LiCoO}_2$  ( $\sim 274$  mAh/g).<sup>125</sup> One of the reasons is the thickness of the membrane and contact issue. Even though the separator prevents the carbon decomposition of the cathode, ion diffusion is limited by the increased thickness. This can be seen also through the gradual capacity decrease. At the 100<sup>th</sup> cycle, the discharge capacity is less than 60 mAh/g. This cycling performance was compared with conventional liquid electrolyte with a separator. The rest of the study proceeded with a  $\text{LiFePO}_4$  cathode.

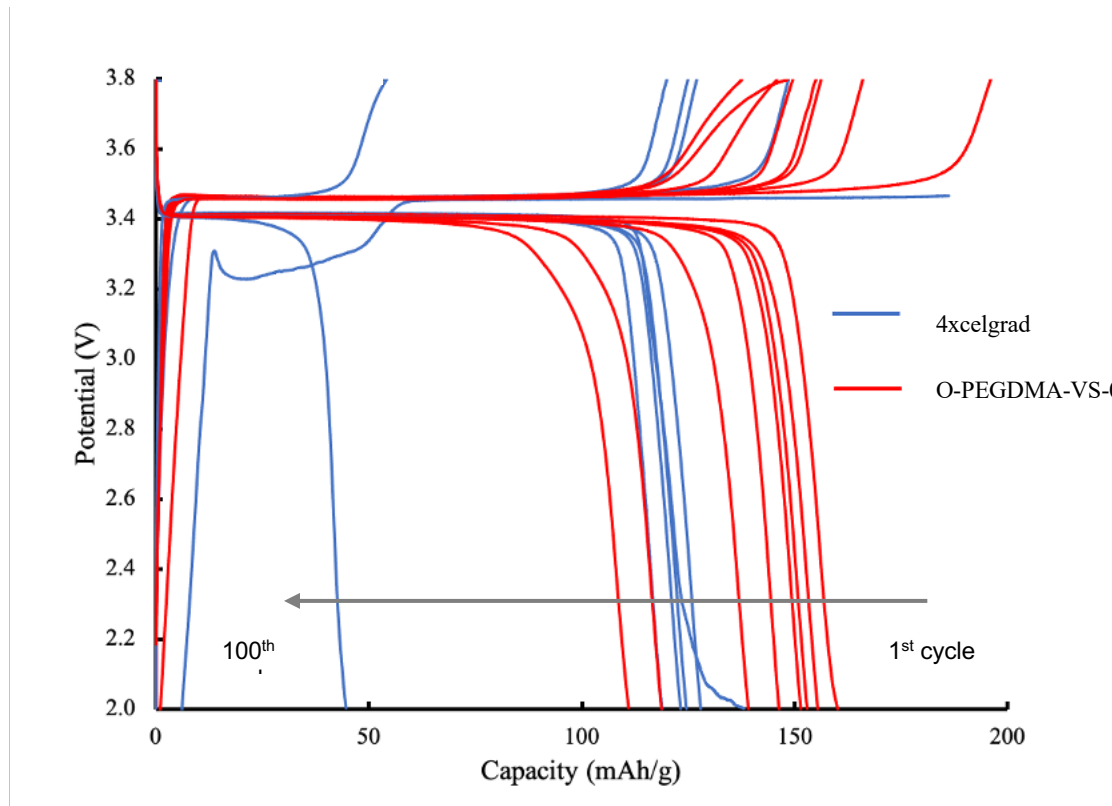


Figure 3.21: Li/O-PEGDMA-VS-0-separator/ $\text{LiFePO}_4$  comparison Li/4xcelgrad/ $\text{LiFePO}_4$  full cycling performance, at 0.1 C-rate.

To comprehend the better performance of O-PEGDMA-VS-0, a comparison was done with a conventional battery configuration. However, due to the thickness difference between celgard and opaque membrane, 4 celgard films were assembled in the cell (100  $\mu\text{m}$  thickness). Figure 3.21 depicts charge and discharge profiles of O-PEGDMA-VS-0 and celgard under the same conditions. The first discharge capacity of opaque membrane is



154.1 mAh/g whereas, celgrad results in around 130 mAh/g. At the 10<sup>th</sup> cycle, both the cells have a slight loss of capacity due to the SEI layer formation and side reactions. These cells completed 300 full cycles at 0.1 C-rate including the C-rate test. At the 300<sup>th</sup> cycle, the opaque membrane has an extraordinary capacity of 111.1 mAh/g. The conventional cell's capacity was 47.1 mAh/g. In terms of GPE applications, the opaque membrane is one of most impressive membrane for LiBs. Despite the thickness, this outcome proves that structure of the polymer electrolyte dominates the transport across the cell.

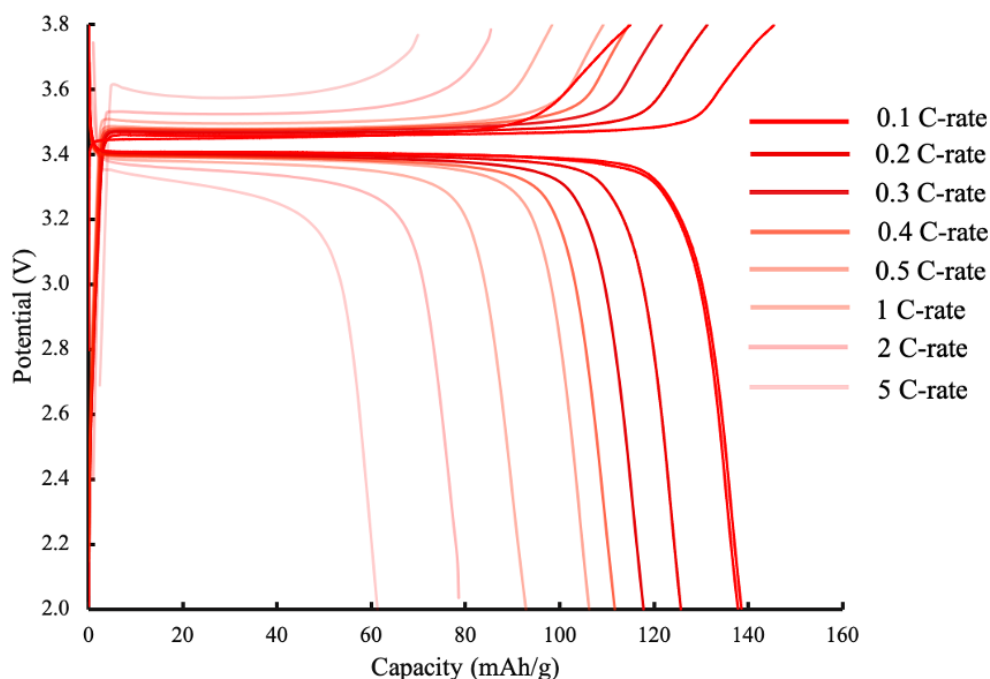


Figure 3.22: C-rate test performance of O-PEGDMA-VS-0.

A C-rate test was applied from 0.1 C-rate to 5 C-rate gradually on the opaque membrane coin cell. Within the increment of the C-rate, the decrease on the capacity can be seen clearly. Until 1 C-rate, the battery cycles approximately 100 mAh/g capacity which is noticeably better than the previous PEGDA-SS applications. At 5 C-rate, the discharge capacity is 61.3 mAh/g. With regard to polymer electrolyte applications, at higher C-rate, the battery tends to fail because of the transport limitations. Thus, opaque membrane's full cell cycling performance is outstanding.

In full cycling experiments, any of the transparent PEGDMA-VS-0 membrane were not utilised in full cycle cell configurations. Every attempt resulted in a short circuit. Therefore, the opaque membrane's performance is compared with celgard.

### 3.5 Summary and Outcomes

In this work, the transport properties of PEGDMA-VS-0 in 1 M LiTFSI (DOL-DME 1:1 v%) and 1 M LiPF<sub>6</sub> (EC-DEC 1:1 %) have been investigated. It is seen that the structure of membrane has a great impact on the transport properties. O-PEGDMA-VS-0 has a unique porous structure due to the phase separation in polymer matrix. In the presence of free anions, the cation transference number cannot exceed 0.5. However, within the porous structure, O-PEGDMA-VS-0 showed an extraordinary  $t_+$ , 0.71-0.78 (from different experiments). We hypothesised based on the experimental outcomes, Li<sup>+</sup> is transported through the channels produced by unique pores. Figure 3.23 represents the Li<sup>+</sup> transport in O-PEGDMA-VS-0.

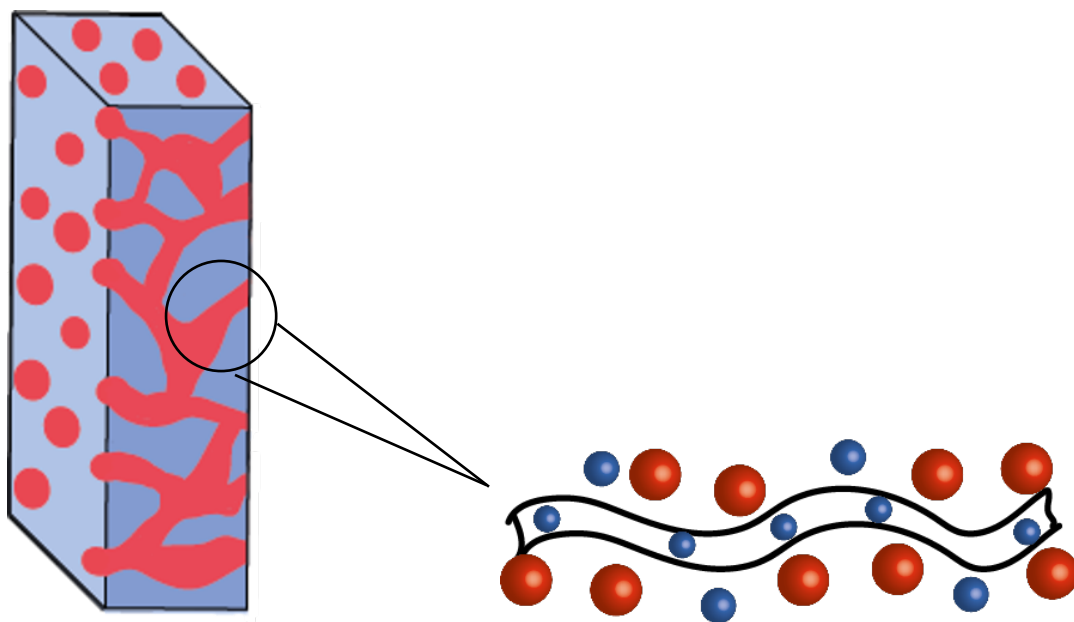


Figure 3.23: A sketch macroscopic and microscopic of O-PEGDMA-VS-0 membrane, swelled in 1 M LiPF<sub>6</sub> (EC-DEC 1:1 v%).

The behaviour of O-PEGDMA-VS-0 is quite different in electrolyte solution. In porous channels, attached anions are not present. The shrinkage of these channels in the presence of 1 M LiPF<sub>6</sub> (it is due to the EC), only Li<sup>+</sup> can transport through the channels.

Not having  $\text{SO}_3^-$  in the PEGDMA backbone is still a question and the investigation is still continued. Despite that, the opaque PEGDMA-VS-0 seems very promising candidate as GPE for LiBs. Both high ionic conductivity and transference number have been achieved. The further investigation is going to be reported.

## **4. Chapter 4- Continuum Modelling of Single Ion Conducting Polymer Electrolytes**

### **4.1 Introduction**

The first two chapters consist of detailed experimental studies on gel polymer electrolytes with varying transport properties, chemistry and structure. Modelling studies play a crucial role in the research of lithium-ion battery systems (LiBs) in order to predict outcomes under certain conditions. Lithium-ion batteries have been extensively researched throughout the academic and industrial fields across the world during the past 50+ years.<sup>126</sup> The development of portable electronic devices and electric vehicles have resulted in high demand of lithium-ion batteries.<sup>127</sup> Since the invention of batteries, the improvements of rechargeable batteries have often relied on trial-and-error experimental tests. In our modern days, regarding the high cost of experiments and the value of time associated with performing them, the importance of deep theoretical understandings of the fundamentals of LiBs has risen. To speed up the development process, physical theories guide the design of better, more efficient and more sustainable experimental set-ups.<sup>128</sup> Experimental observations are explained by physical theories. Thus, the battery field has been grown by contribution of both theoretical and experimental studies.

A mathematical model usually consists of a set of equations. These models help researchers comprehend the fundamentals of existing systems and predict properties and the performance of new designs. Computational simulations, based on rigorous theoretical modelling and coupled to validation and quantification of the uncertainties, have the potential to enhance batteries' performances, tailor architectural configurations toward optimal functioning of energy storage devices, and shape new materials for greater capacity and power release.<sup>42</sup> Additionally, experiments depend on some uncertain conditions that cannot be controlled all the time. Modelling gives the user power to simulate extreme conditions and be prepared for unexpected circumstances. On the other hand, theoretical models need verification and should be based on realistic conditions. Comparing modelling results with experimental outcomes and observing reasonable results show the accuracy of the model. In terms of modelling studies, verification of the model is highly important. The one crucial advantage of mathematical modelling is the cost effectiveness in

comparison to certain physical experiments. Hence, modelling can accelerate the innovations and technology promptly and reduce the time to the market of new designs. Battery modelling can be defined with respect to the different approaches. Each model has its own methodology to investigate specific targets. Some models are designed to describe the system in its own systematic characteristics such as the rate of discharge and the capacity.<sup>129</sup>Equivalent circuit models simulate the battery with combination of variable voltage sources, resistors, and capacitors.<sup>130, 131</sup>

Over the last 40 years, computational modelling of LiBs has improved remarkably in terms of both describing material properties as well as the operating principles of the battery. There are several methods to describe these, each according to the desired phenomena; i) atomistic models such as molecular dynamics (MD) are applied for structural characterization of electrolyte and active materials, kinetic Monte Carlo (kMC) method is used for explaining interface reactions,<sup>132, 133</sup> ii) electronic models are utilized for simulating the atomistic structure and explaining the local energy density in the electrolyte. As iii) continuum models have been used to explore porous electrode behavior, charge and discharge capacity predicting.<sup>28</sup> A set of partial differential equations are used in the form concentration of species, thermal effects or stress evaluation during the battery operations. Multi-scale and multi-physics approach on continuum level modelling give us the ability to comprehend the processes that take place during charge/discharge, from the atomistic scale up to the cell size.<sup>134, 135</sup> Thus, optimum battery design and lifetime prediction can be achieved by this approach. Understanding the physical processes and theoretical explanation for each of them during operation of a cell is crucial. Figure 4.1 illustrates the list of processes and required models for a conventional lithium ion battery.

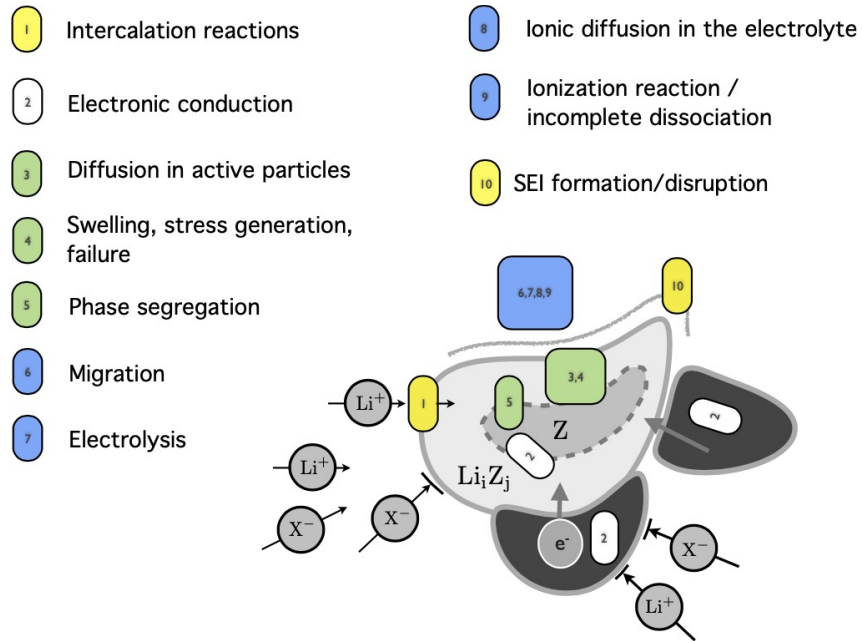


Figure 4.1: A list of processes that take place in a battery during normal operation. The light grey represents the active particle in cathode. The dark grey areas are the conductive particle.  $\text{Li}^+$  and  $\text{X}^-$  are the mobile ions which are dissolved from the  $\text{LiX}$  electrolyte.

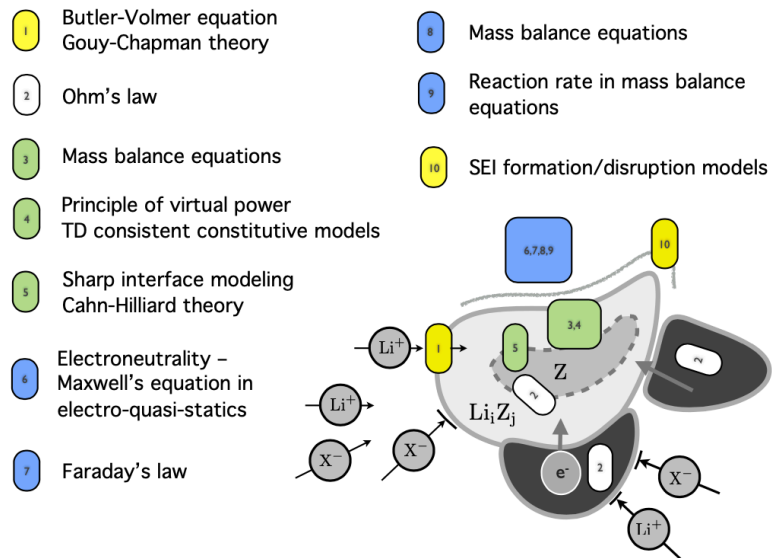


Figure 4.2: A list of models for the processes that take place in a battery during normal operation.

Any rigorous model of physical phenomena stems from a few pillars. They are, in order: the balance (or continuity) equations; the thermodynamic analysis, in terms of energy and entropy balance; the constitutive theory and specifications; and objectivity, which in the presence of large deformations shall also be properly investigated. Governing equations result from this fundamental sequence of tasks. Scientific rigor claims that this sequence shall be respected, but this is unfortunately not always the case in the literature on battery modelling. From the second law of thermodynamics restrictions arise that constitutive modelling should account for.<sup>136-138</sup>

In Figure 4.1 and 4.2 illustrates the processes and relevant models to describe these processes during a normal battery operation. For instance, intercalation of  $\text{Li}^+$  into the active material is indicated by process 1. Butler Volmer equation Gouy-Chapman theory is used to model the process. Mass transfer entails a description of the movement of mobile ionic species. In the absence of convection, as usually assumed under operation conditions, movement of species is governed by diffusion, driven by gradients of concentration, or by migration, driven by an electric field.<sup>139, 140</sup>

In this study, we focus on the continuum model to investigate the impact that the transport properties of an electrolyte have on cycling behavior. Since the first commercialized lithium ion battery was on the market, both the electrode materials have been developed. The usage of  $\text{LiCoO}_2$  then  $\text{LiFePO}_4$  is proposed as olivine structure.<sup>141, 142</sup> Recently, lithium nickel manganese cobalt oxide (LNMC) has been investigated deeply as a better cathode material.<sup>143, 144</sup> On the other hand, since 1991, the same binary liquid electrolyte in a carbonate-based solvent has been used in commercial LiBs.<sup>126</sup> In conjunction with this fact, the conventional liquid electrolyte has caused many issues in battery operation, such as flammability, toxicity, and electrolyte decomposition.<sup>145-148</sup> Thus, replacing the binary liquid electrolyte to a more environmentally friendly, less toxic alternative, while achieving high transport property features, specifically, high ionic conductivity, is ideal.

In this chapter, we have modeled gel polymer electrolyte systems based on experimental results with respect to a single ion conducting and a gel polymer electrolyte. Single ion conducting polymer electrolyte (SIPE) consists of a polymer and solvent

mixture whereas, gel polymer electrolyte (GPE) includes conventional liquid electrolyte in the polymer. For the sake of the modelling, the SIPE system will be discussed first.

#### **4.1.1 Single Ion Conducting Polymer Electrolyte Modeling**

Developing a highly conductive electrolyte to compete with conventional liquid electrolyte is one of the challenges in lithium ion battery research. Since development of the first commercial electrolyte, the same material has been used in all practical LiBs. The main effort in the electrolyte field is to replace the liquid electrolyte to a more stable, less toxic and conductive electrolyte, such as solid state polymer electrolytes, SIPEs or GPEs.<sup>149, 150</sup> The crucial point in the application of polymer electrolyte is the transport of charge mechanism in the polymer matrix. Both experimental and molecular dynamics studies have provided beneficial information, especially on ion states. In polymer electrolyte applications, poly (ethylene oxide) is of the most applied materials due to its high segmental motion and solvating power. It is agreed that cations are generally present as ion complexes with several ether oxygen atoms (4 or 6 EO and  $\text{Li}^+$ ). If anions are present in the polymer (binary salt dissolved in polymer or additional liquid electrolyte) they often prevent this segmental motion. High cation mobility (can be also referred as transference number) is desirable for maximizing the efficiency of the process, whereas high anion mobility decreases the performance of the system. Therefore, SIPEs are appealing for electrolyte research field.

Despite the large body of experimental studies on SIPEs for LiBs, there are limited number of modelling studies. The first study on polymer electrolyte modelling by considering transport properties, especially lithium transference number was published by Newman's group in 1994.<sup>11</sup> This is the milestone of the polymer electrolytes with high transport properties. In 2018, Krewer's group published a study based on SIPEs. Pseudo-two-dimensional (P2D) model was used to compare the outcomes of SIPE and conventional binary electrolyte.<sup>37</sup> The applied model was based Newman's work with some modifications. At higher rates, it was reported that the potential losses in electrolyte region fairly less in SIPE case which led to higher energy than the liquid electrolyte case. In addition, the effect of the electrode thickness was investigated and resulted that SIPE are found to be suitable for thicker electrode designs. McMeeking and his colleagues



studied SIPE in solid state form. 1 dimensional model was developed with lithium metal anode and a porous cathode in the view of electrochemical kinetics and ion transport.<sup>151</sup> It was reported that when the conductivity of the electrolyte is high, there is significant drop on the redox reactions and vice versa which indicates the importance of transport properties.

In polymer electrolyte systems, ion dissociation and association are very important for conductivity. Ions form aggregates and pairs in the polymer matrix and the conductivity of the system is reliant on the number of mobile charges and their mobility.<sup>152</sup> In PEO based electrolytes, ether oxygen provides certain dissociation, in which a significant amount of ion pairing is expected due to the low polarity of PEO. Colby and coworkers studied extensively ion states in PEO and sulfonate-based polymer systems which reveals this ion aggregation and pairing.<sup>102</sup>

Both experimentally and theoretically, obtaining this type of dissociation and association is very challenging. Furthermore, the definition of mobile or bonded charges is complex and very hard to acquire. In 2006, Colby and coworkers published an experimental study on SIPE based on PEO.<sup>153</sup> The  $\text{Li}^+$  mobility and conduction were evaluated with regard to segmental motion and conductivity. The outcomes revealed that most of  $\text{Li}^+$  were present in ion pair states due to the low dielectric constant of PEO. Even though the literature presents this with only a few examples, it is evident that dissociation in equilibrium is limited.

SIPE electrolytes are fairly promising in terms of achieving a high cation transference number under suitable circumstances. In this chapter, we investigate SIPE electrolyte with varying transport properties and dissociation reaction kinetics on a 1D continuum model scheme. A sketch of an SIPE is demonstrated in Figure 4.3.

## 4.2 1 Dimensional Ionic Transport Continuum Model of Single Ion Conducting Polymer Electrolyte

Herein we report a novel 1D continuum approach for a SIPE system. Most of the studies reported in literature are based on Newman and coworkers' model. In this study, we follow another approach which was developed by our group previously.<sup>41, 154, 155</sup> Hence, balance equations and boundary conditions are written differently. All the relevant constants (diffusion coefficient, thickness of the electrolyte) are taken from experimental outcomes.

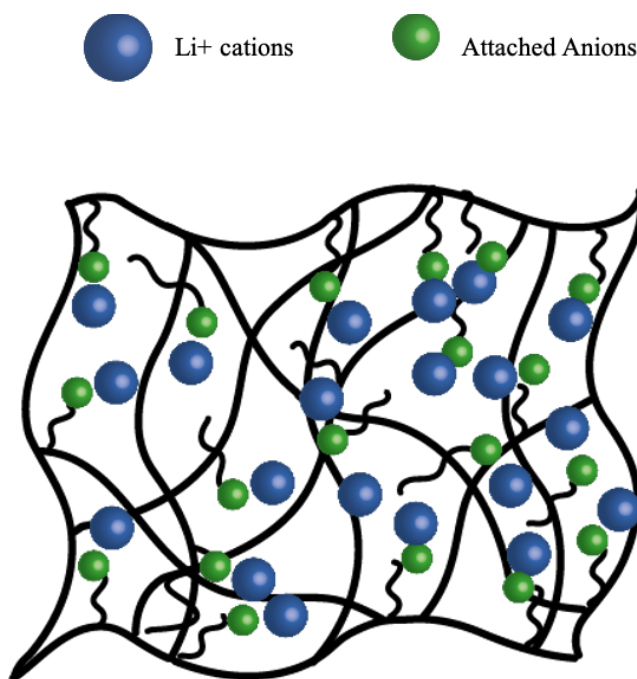


Figure 4.3: A sketch of single ion conducting polymer electrolyte (SIPE). Blue spheres represent lithium cations. Green spheres are representative of anions which are attached to the polymer backbone and chains.

In SIPE systems, only the cation is considered as moving via diffusion and migration due to the applied electric field. In the system, there is no concentration gradient because of the immobile anions. Therefore, only the transport of the cation is present in the model. The second crucial aspect of this study is to investigate the impact of the dissociation reaction kinetics to the battery response. The design of SIPE has relied on two essential parameters; i) high backbone segmental motion, which is related to mobility of  $\text{Li}^+$ , and ii) high ion dissociation which shows the mobile number of charges. In order to

investigate the first issue, we are going to use different ranges of diffusion coefficients based on ionic conductivity experiments. The dissociation rate is going to be discussed with respect to reaction kinetics. It is, to our best knowledge, the first-time single ion conducting polymer electrolyte modelling with varying reactions rates and transport properties are modelled. The modelling is demonstrated in Figure 4.4.

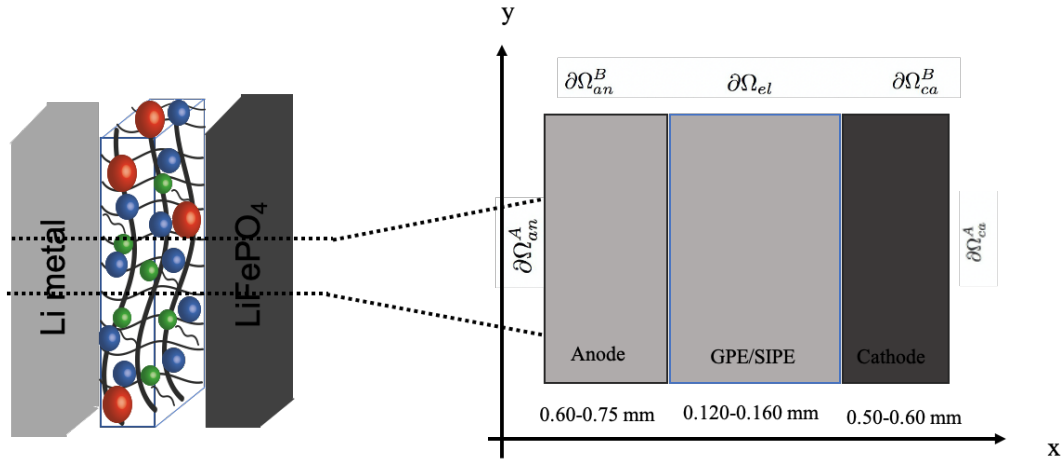


Figure 4.4: Schematic representation of the planar Li/SIPE or GPE/LiFePO<sub>4</sub> the thickness and the domains. Blue spheres are the lithium cations; green spheres are the tethered anions. The red spheres are mobile PF<sub>6</sub><sup>-</sup> anions.

#### 4.2.1 Single Ion Conducting Polymer Electrolyte Model Description

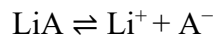
Figure 4.3 illustrates the SIPE, with fixed anions in the polymer backbone and mobile lithium ions. Thus, there is no concentration evaluation on the system with respect to time due to immobile anions. Theoretically, in the presence of covalently anchored anions, all the long-range ion transport observed within such electrolytes can be attributed to the active cationic species, meaning the transference number,  $t_+$ , approaches unity. As it was mentioned previously,  $t_+$  is an important transport property for advanced electrolytes.

As it was stated beforehand, polymer segmental motion is important for high Li<sup>+</sup> mobility. The chemical characteristics of polymers are modelled with atomistic scale methods, molecular dynamics simulations.<sup>7</sup> However, based on the ionic conductivity of each membrane, the diffusion coefficient can be controlled and the impact of the mobility of the cations can be captured.

$$\sigma_{tot} = \sum_j n_j \mu_j q_j \quad (1)$$

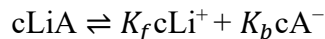
In accordance with the total ionic conductivity equation, the mobility of ions ( $\mu$ ) depends on the ionic conductivity ( $\sigma$ ) and vice versa. In this study, various diffusion coefficients are employed to observe the impact in a continuum level. add references based on mobility and dissociation

The second important parameter is the ion dissociation rate. Dissociation in polymer membranes is very challenging. Achieving modest dissociation is critical for SIPEs to make electrolytes perform as good  $\text{Li}^+$  conductors. Most studies suggest that only a small fraction of lithium is mobile in the polymer matrix. With a high degree of dissociation, the number of charge carriers in the polymer is increased. Thus, we expect to observe better cell performance. Regarding modelling of chemical reactions, the reaction kinetics are required to be identified comprehensively. Hence, the dissociation of  $\text{Li}^+$  from the polymer backbone is one of the important aspects of this study. The polymer matrix is considered as  $\text{LiA}$ , and the dissociation reaction is expressed as:



$\text{A}^-$  represents the tethered anions in the polymer backbone. Dissociation reaction kinetics can be modeled with two different approaches. The most common approach is infinitely fast kinetics. For instance, the kinetics of transformation of high-affinity to low affinity integrins and vice versa in focal adhesions is much faster than the diffusion of the low-affinity integrin itself across the lipid bilayer membrane. In similar cases, it can be assumed that the time required to reach chemical equilibrium is orders of magnitudes smaller than the timescale of other processes. However, the dissociation reaction cannot satisfy this condition. Thus, the diffusion of  $\text{Li}^+$  is required to use the mass action law to capture the impact of reaction kinetics.

The dissociation reaction is a reversible reaction, namely association. In the view of mass action law, the reaction is written as follows:



$K_f$  and  $K_b$  express the forward and backward reaction constant, respectively. For ideal systems, in which the solvent (if any) does not take part in reactions and the chemical potentials have entropy and energy contributions only, the chemical reaction kinetics are

often modeled via the law of mass action. The ratio of the reaction constants generates the equilibrium constant of the reaction,  $K_{eq}$ .

$$K_{eq} = \frac{K_f}{K_b} \quad (2)$$

Obtaining the reaction constants experimentally is highly challenging. Although, the ion state can be determined by FTIR or Raman spectroscopy, it is dependent on the type of the ionomer. Colby and coworkers extensively studied PEG membranes and cation states based on the backbone chemistry and dissociation. Colby paper references. Therefore, the limited dissociation of 1% is determined based on literature. The required experiments are going to be conducted and reported in another publication.

### 4.3 Balance Laws

#### 4.3.1 Mass Balance

The general mass balance is written as follows,

$$\frac{\partial c_\alpha}{\partial t} + \vec{h}_\alpha = 0 \quad (3)$$

In this equation,  $c_\alpha$  is the molarity (i.e. the number of moles per unit volume) of a generic species  $\alpha$ ;  $h_\alpha$  is the mass flux in terms of moles, i.e. the number of moles of species  $\alpha$  measured per unit area per unit time. In our model, there only  $\text{Li}^+$  in the polymer,

$$\frac{\partial c_{\text{Li}^+}^p}{\partial t} + \vec{h}_{\text{Li}^+}^p = w \quad (4)$$

$w$  represents the reaction rate which is defined by the reaction constants. The mass balance is written for the bonded anions and polymer (LiA) as follows,

$$\begin{aligned} \frac{\partial c_{\text{A}^-}}{\partial t} &= w \\ \frac{\partial c_{\text{LiA}}}{\partial t} &= -w \end{aligned} \quad (5)$$

### 4.3.2 Faraday's Law

Charges in the electrolyte solution are transported by dissociated ions. Therefore, the charge density  $\zeta$  is related to the concentration of ions, by the following identity,

$$\zeta = F \sum_{\alpha} z_{\alpha} c_{\alpha} \quad (6)$$

$F$  is Faraday's constant (96485.3383 C/mol) and  $z_{\alpha}$  is the number of electrons transferred per ion  $\alpha$ , typically +1 for  $\text{Li}^+$  cations and -1 for anions. The flux of mass in balance of each species contributes to a current density  $\vec{i}$  in view of Faraday's law of electrolysis.

$$\vec{i} = F \sum_{\alpha} z_{\alpha} \vec{h}_{\alpha} = F(\vec{h}_{\text{Li}^+} - \vec{h}_{\text{A}^-}) \quad (7)$$

Please note that,  $X^-$  is hold in the existence of mobile anions.

### 4.4 Balance Equations of SIPE - Strong Forms

The content of moving species inside a body is characterized by its molar concentration. In this case, only  $\text{Li}^+$  is considered as a moving species. We assume that time variation of the species content inside an arbitrary subregion is due to a flux across the boundary of the region and to a mass sink/supply due to chemical reactions. Therefore, lithium concentration with respect to time can be written as follows as the first balance equation.

$$-\frac{d}{dt} c_{\text{Li}}(x, t) = K_{\text{f}} c_{\text{Li}}(x, t) + K_{\text{b}} (c_{\text{Li}}(x, t))^2 - K_{\text{f}} c_{\text{LiA}}^k \quad (8)$$

The second balance equation is,

$$\nabla \cdot \vec{h}_{\text{Li}^+} = 0 \quad (9)$$

As a condition but not a balance law, we can write,

$$c_{\text{LiA}}(\vec{x}, t) = c_{\text{LiA}}(\vec{x}, 0) - c_{\text{Li}^+}(\vec{x}, t) \quad (10)$$

In addition to the set of equations, an electroneutrality condition is imposed to make the charge neutrality. Electroneutrality is not a fundamental law whereas, an approximation towards the solution. In this regard, the electrochemical double layer formation at the electrode/electrolyte material interface is neglected in this model.

$$\sum_{n=i} z_i c_i = 0 \quad (11)$$

where  $z_i$  is the charge number of species  $i$ , the net charge is always zero and the total current density satisfies the charge balance equation both in electrolyte and porous electrode,

$$\text{div} [\vec{i}] = 0 \quad (12)$$

Constitutive assumptions relate the mass fluxes  $\vec{h}_i$  the current densities  $i_e$  and  $i_s$  and the bulk terms  $R_i$  (resistance) to the molar concentrations  $c_i$  and the electric potentials electrode and electrolyte, which are the thermodynamic variables and the unknown fields of the model. Faraday's law relates the electrolytic current density to the ionic mass fluxes in the electrolyte, whereas Ohm's law is assumed to govern the movement of electrons in the matrix phase. Either dilute, moderately dilute, or concentrated solution theories may be adopted, leading to thermodynamic scenarios characterized by an increasing degree of mathematical complexity. As the constitutive law, the Fickian-diffusion relation is imposed to calculate electrostatic potential. The electrostatic potential,  $\phi$ , is the result of idealized electric charges moving from one electrode to the other, modelled by Fickian-diffusion.

#### 4.4.1 Weak Forms of the Balance Equations

The weak formulation results from multiplying the strong form of governing equations by a suitable set of tests functions and performing an integration upon the domain, thereby exploiting the integration by parts formula with the aim of reducing the order of differentiation in space.<sup>156</sup> Galerkin approach emanates when unknown fields are discretised with shape functions that coincide with test functions. For the timed discretization, 'Backward Euler Method' is applied.

The unknown fields are lithium concentration  $c_{Li^+}$  and electric potential,  $\phi$ .

We can discretize the  $Li^+$  concentration by test function  $\psi_i$ ,

$$c_{Li}(x, t) = \varphi_j(x)c_{Li}^j(t) \quad (13)$$

Hence, the first equation is formed as,

$$-\frac{d}{dt}\varphi_j(x_k)c_{Li}^j = K_f\varphi_j(x_k)c_{Li}^j + K_b(\varphi_j(x_k)c_{Li}^j)^2 - K_f c_{LiA}^k \quad (14)$$

With the first equation, we will be able to acquire the  $c_{Li}$  over time. Importantly, the polymer concentration  $c_{LiA}$  is known by the experimental outcomes, since it is the LiA concentration at initial time. Backward Euler method is applied to discretise the equation with respect to time.

$$-\varphi_j(x_k)\frac{c_{Li}^j(t_{n+1}) - c_{Li}^j(t_n)}{\Delta t} = K_f\varphi_j(x_k)c_{Li}^j(t_{n+1}) + K_b(\varphi_j(x_k)c_{Li}^j(t_{n+1}))^2 - K_f c_{LiA}^k \quad (15)$$

For the sake of the implementation, the residual is written as follows,

$R(c_{Li}^j(t_{n+1})) = 0$  and the equation is formed as,

$$R(c_{Li}^j(t_{n+1})) = -\varphi_j(x_k)\frac{c_{Li}^j(t_{n+1})}{\Delta t} - K_f\varphi_j(x_k)c_{Li}^j(t_{n+1}) - K_b(\varphi_j(x_k)c_{Li}^j(t_{n+1}))^2 + K_f c_{LiA}^k + \varphi_j(x_k)\frac{c_{Li}^j(t_n)}{\Delta t} \quad (16)$$

In order to approximate the solution of the non-linear equation, a Newton-Raphson iterative algorithm has been implemented on MATLAB.

Using the notation of Gateaux derivative, the iterative Newton-Raphson scheme is applied in terms of the increment  $\delta c_{Li}^j$  as,

$$-\varphi_j(x_k)\frac{\delta c_{Li}^j}{\Delta t} - K_f\varphi_j(x_k)\delta c_{Li}^j - 2K_b(\varphi_j(x_k)c_{Li}^j)(\varphi_j(x_k)\delta c_{Li}^j) = -R \quad (17)$$

The final form of the Newton Raphson scheme of the first equation is obtained,



$$\begin{aligned}
& [-\varphi_j(x_k) \frac{1}{\Delta t} - K_f \varphi_j(x_k) - 2K_b(\varphi_z(x_k) c_{Li}^z)(\varphi_j(x_k))](\delta c_{Li}^j) = \\
& = \varphi_j(x_k) \frac{c_{Li}^j(t_{n+1})}{\Delta t} + K_f \varphi_j(x_k) c_{Li}^j(t_{n+1}) + K_b(\varphi_j(x_k) c_{Li}^j(t_{n+1}))^2 - K_f c_{LiA}^k - \varphi_j(x_k) \frac{c_{Li}^j(t_n)}{\Delta t}
\end{aligned} \tag{18}$$

The weak form of the governing equation in equation (9) is written by multiplying with the test function ‘ $\omega$ ’ and applying divergence theorem.

$$\int_{\Gamma} w \vec{h} \cdot \vec{n} d\Gamma + D_{Li} \int_{\Omega} \nabla w \nabla c_{Li+}^j d\Omega + \frac{FD_{Li+}}{RT} \int_{\Omega} \nabla w c \nabla \phi d\Omega = 0 \tag{19}$$

Recalling that

$$\vec{h} = -D \nabla c_{Li+} - \frac{FD_{Li+}}{RT} c_{Li+} \nabla \phi \tag{20}$$

The discretized fields of unknowns as follows,

$$\begin{cases} w = \varphi_i(x) \\ c = \varphi_j(x) c^j(t) \\ \phi = \varphi_j(x) \phi^j(t) \end{cases} \tag{21}$$

Therefore, the equation is reformed,

$$\int_{\Gamma} \varphi_i \vec{h}_n d\Gamma + D_{Li} \int_{\Omega} \nabla \varphi_i \nabla \varphi_j d\Omega c^j(t_{n+1}) + \frac{FD_{Li+}}{RT} \int_{\Omega} \nabla \varphi_i \varphi_k c^k(t) \nabla \varphi_j \phi_j(t) d\Omega = 0 \tag{22}$$

The final form is,

$$\left[ \frac{FD_{Li+}}{RT} \int_{\Omega} \nabla \varphi_i \nabla \varphi_j \varphi_k d\Omega c^k(t) \right] \phi_j(t) = - \int_{\Gamma} \varphi_i \vec{h}_n d\Gamma - D_{Li} \int_{\Omega} \nabla \varphi_i \nabla \varphi_j d\Omega c^j(t_n) \tag{23}$$

The governing equations of the model is completed by,

$$c_{LiA}(\vec{x}, t_{(n+1)}) = c_{LiA}(\vec{x}, 0) - c_{Li+}(\vec{x}, t_{(n+1)}) \tag{24}$$

## 4.5 Boundary and Initial Conditions, Modeling Assumption and Material Parameters

Firstly, as SIPE electrolyte, PEGDA-SS membranes in solvent are chosen to be modelled based on the experimental outcome which were explained in detail in Chapter 1. Poly(ethylene glycol) diacrylate is widely investigated polymer in terms of gel polymer electrolyte applications. More specifically, Colby and coworkers' two fundamental publications on dissociation of PEG systems and ion states in PEG membranes are the driving studies for our model.<sup>102</sup> Based on experiments carried out and explained Chapter 1, two samples were chosen to be modelled due to their charge densities. GPE-6 has the highest charge density membrane whereas, GPE-20 has the lowest charge density. These two cases are enough to interpret the behaviour of PEGDA-SS membranes as a SIPE.

Table 4.1: Diffusion coefficients of GPE-6 and GPE-20 in EC-DEC (1:1 v%) solvent mixture.

| Sample Name | Solvent Mixture | Diffusion Coefficient (m <sup>2</sup> /s) |
|-------------|-----------------|---|
| GPE-6       | EC-DEC (1:1 v%) | $1.06 \times 10^{-11}$                    |
| GPE-20      | EC-DEC (1:1 v%) | $2.17 \times 10^{-12}$                    |

The polymer at the initial state is assumed to be dissociated 1% and the initial concentration of Li<sup>+</sup> is calculated based on this assumption. As boundary conditions, Dirichlet and Neumann are imposed. The conditions are as follows,

$$\begin{cases} \phi(0, t) = 0 \\ \vec{h}_{Li^+} \cdot \vec{n}(0, t) = \vec{h}_n = -\frac{I(t)}{FA} \\ \vec{h}_{Li^+} \cdot \vec{n}(L, t) = \vec{h}_n = +\frac{I(t)}{FA} \end{cases} \quad (25)$$

The net area of the electrode is assumed to be ( $A=2 \times 10^{-2}$  m<sup>2</sup>) which is related to the current density I(t) through the battery. The full battery modelling is going to be discussed after the electrolyte modelling. Thus, the interface conditions are given in the following section. The electrolyte thickness (l) is 120  $\mu$ m which was measured

experimentally. The concentration of ions across the electrolyte is uniform at  $t=0$  and 1% of the dissociated lithium of the total number of charges in the membrane. The total number of charges is obtained experimentally which refers to the initial concentration,  $2.622 \times 10^{-3} \text{ mol/cm}^3$ . The charge and discharge process are assumed to be isothermal at  $25^\circ\text{C}$ . The C-rate is set to 0.1 C based on the experimental evidence.

As it was mentioned previously, the impact of the reaction kinetics of dissociation is one of the key points of the 1D SIPE modelling. In this regard, the equilibrium constant of 1% dissociation is kept constant and reaction constant of backward and forward  $K_f$  and  $K_b$  are changed to observe the effect. Table 4.2 and 4.3 summarizes the tested  $K_f$  and  $K_b$ .  
Table 4.2: Reaction kinetics of GPE-6.

| Reaction Type            | $K_{eq}$ | $K_f$                  | $K_b$                  |
|--------------------------|----------|------------------------|------------------------|
| Infinitely Fast Kinetics | 0.2648   | $13240 \times 10^{-6}$ | $50000 \times 10^{-6}$ |
| Slower Kinetics          | 0.2648   | $264.8 \times 10^{-6}$ | $1000 \times 10^{-6}$  |

Table 4.3: Reaction kinetics of GPE-20.

| Reaction Type            | $K_{eq}$ | $K_f$                  | $K_b$                  |
|--------------------------|----------|------------------------|------------------------|
| Infinitely Fast Kinetics | 0.1291   | $6456 \times 10^{-6}$  | $50000 \times 10^{-6}$ |
| Slower Kinetics          | 0.2648   | $129.2 \times 10^{-6}$ | $1000 \times 10^{-6}$  |

In this, decomposition of electrolyte, such that contact issues between electrolyte and the electrodes, which result in SEI and lithium dendrite formations, are not taken into consideration to reduce the complexity. The governing equations have been solved numerically through the Finite Element Method in MATLAB. The electrolyte geometry has been discretised into 150 elements. The time evolution is resolved with a time increment  $\Delta t = 0.1\text{s}$  through the simulation.

## 4.6 Results and Discussion

The diffusion coefficient is the primary electrolyte property when designing single ion conducting polymer electrolyte. Table 4.1 shows different calculated diffusion coefficients of PEGDA-SS membranes based on the ionic conductivity experiments. Since, the ionic conductivities are akin to each other due to the similar features, the GPE-6 was chosen to conduct the simulations. Afterwards, different diffusion coefficients are model to compare the GPE-6 system.

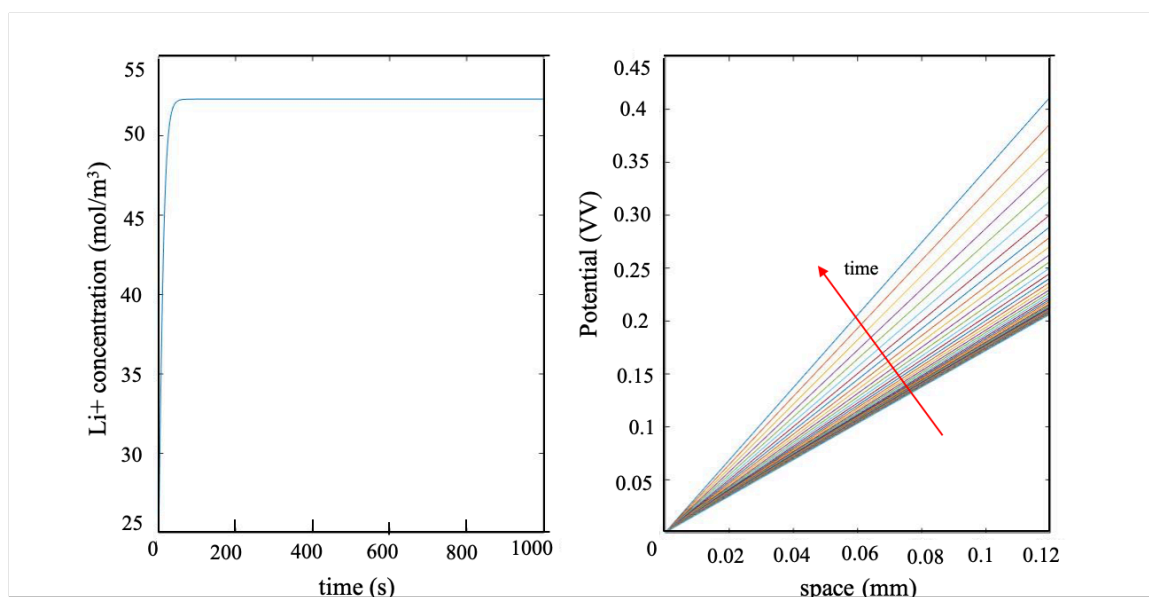


Figure 4.5: Lithium concentration and potential profile of GPE-6 with slow kinetics.

Figure 4.5 illustrates the lithium concentration with respect to space. Since there is only  $\text{Li}^+$  mobile in the polymer matrix, a concentration gradient does not occur across the cell. In comparison to a conventional liquid electrolyte, 1 M  $\text{LiPF}_6$ , under the same conditions, a serious concentration gradient is observed due to the presence of mobile  $\text{PF}_6^-$  anions. The full cell configurations for conventional liquid electrolyte and SIPE are in progress and the comparison will be reported in a future publication. The comparison of reaction kinetics is shown in Figure 4.6. With infinitely fast kinetics, the concentration equilibrium,  $53 \text{ mol/m}^3$ , has been reached in only few time steps. In contrast, the same equilibrium concentration takes more time for slower kinetics, as it is expected. We expect to see a difference in behaviour during full cell cycling while the intercalation reaction happens. The reaction kinetics clearly effects the present effective number of charges in

the membrane which directly influences the number of lithium ions which can diffuse to the cathode with respect to discharge process.

The voltage profile is shown in Figure 3.5. Evidently, due to the low conductivity, the equilibrium potential is obtained as 0.4 V which is a fairly high response. Regarding the conductivity equation, the low mobility of  $\text{Li}^+$  increases the resistance of the electrolyte which can be seen as potential. Besides, due to high charge density structure of GPE-6, the mobile number of charges is low as well. The reaction kinetics only has influence on the time required to reaching equilibrium. With infinitely fast kinetics, 0.4 V is obtained in couple time steps, whereas the evolution of potential is clearly seen with slower kinetics. This is also detected on the  $\text{Li}^+$  concentration profile. Instead of having a jump, there is a small bump that represents the effects of slower kinetics.

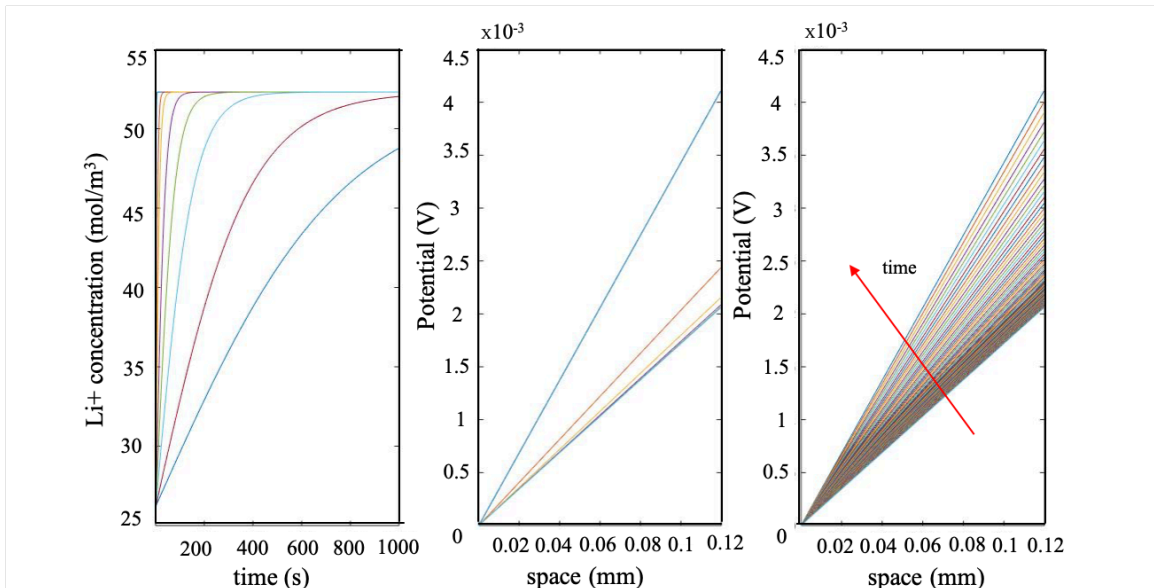


Figure 4.6: Lithium concentration and potential profile of GPE-6 with  $1.06 \times 10^{-9} \text{ m}^2/\text{s}$  with fast and slow reaction kinetics.

Based on the experimental outcomes, the ionic conductivity is one of the limiting factors for SIPE system. In order to investigate the impact of the diffusion coefficient has on the SIPE performance, two extreme coefficients are used as the constant property. Under the dissociation rate (1%), the same  $K_f$  and  $K_b$  are used while the diffusion coefficient is increased and decreased two orders of magnitude,  $1.06 \times 10^{-9} \text{ m}^2/\text{s}$  and  $1.06 \times 10^{-13} \text{ m}^2/\text{s}$ . The outcomes are shown in Figure 4.6. Applying higher diffusion coefficient,

$1.06 \times 10^{-9} \text{ m}^2/\text{s}$ , resulted with relatively low potential response across the electrolyte. The potential can be related to the resistance of the electrolyte. With high diffusion, the mobility of the cations increases with respect to the total ionic conductivity relation, thus the electric potential decreases, i.e., resistance. Taking into consideration the strong form of equation (9), the electric potential is solely dependent on the diffusion coefficient of the electrolyte. In comparison to dual ion electrolyte systems, in which the ion mobility is higher, the potential response of SIPE indicates the importance of ion mobility. Similar conditions can be reached by increasing the ion mobility of polymer electrolyte with only one mobile species. The concentration profile demonstrates the influence of reaction kinetics. The blue line depicts the infinitely fast kinetics in Figure 4.6.

Hence, it takes only few steps to reach the equilibrium concentration. When slowing down the kinetics, the evaluation of lithium concentration is much clearer. With respect to time, the equilibrium concentration is reached slowly. With the slowest reaction kinetics, in 1000 second, lithium cannot reach the equilibrium concentration even though the assumed dissociation is 1% of the total concentration. This reaction kinetics response is observed in the potential evaluation as well. With slower kinetics, there is no jump in the potential, whereas, due to the fast kinetics, the potential does not evolve smoothly, instead jumping from  $2.5 \times 10^{-3} \text{ V}$  to  $4 \times 10^{-3} \text{ V}$  in few time steps.

Considering the conductivity equation, the performance increases with high ion mobility. Based on the modelling power, 50% dissociation is computed under the same conditions. With experimental studies, there is not any studies on polymer electrolyte that can reach to 50% dissociation of the ions. The diffusion coefficient is taken as  $1.06 \times 10^{-11}$  and the dissociation is assumed as 50% which is an extreme situation. The fundamental reason is to examine the behaviour of high number of free or mobile charges in the polymer network. The results are shown only with slow reactions kinetics. Since the equilibrium concentration and potential values do not change with respect to reaction kinetics. As it is expected, the lithium concentration increases with time and reaches equilibrium which is,  $2100 \text{ mol}/\text{m}^3$ . On the other hand, the most striking feature is the potential. The potential is in the same order of magnitude of the  $1.06 \times 10^{-9}$  diffusion coefficient application latter  $9 \times 10^{-3} \text{ V}$ , former  $4.5 \times 10^{-3} \text{ V}$ . The reason why is dependent on equation (1). By keeping the diffusion coefficient constant, the mobility of

the  $\text{Li}^+$  is kept constant as well. However, the number of mobile charges increases due to the high dissociation degree. Thus, there are 50% more mobile lithium cations on the electrolyte. (number of charges ' $\eta$ '). Having a high number of mobile charges improves the performance of the electrolyte similar to increasing the mobility. The same effect is observed on the potential values. In both cases, the potential is in the same order of magnitude. Consequently, it approves the theory behind our model.

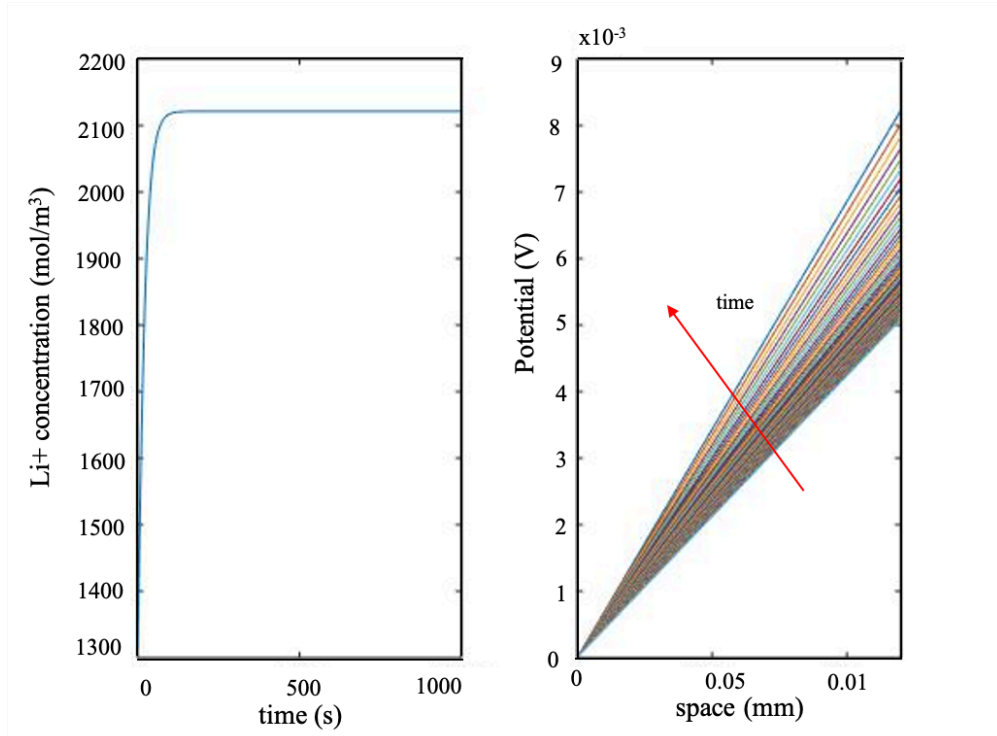


Figure 4.7: Lithium concentration and potential profiles of GPE-6 with 50 % dissociation.

The outcome suggests that the SIPE's performance can be improved by either with high mobility or a high number of free charges.

The simulation is run with a diffusion coefficient of  $1.06 \times 10^{-13}$ , under the same conditions to see the potential response at low mobility. The concentration profile is the same as the previous case. This is because the concentration of lithium in the polymer is only dependent on the dissociation and the reaction kinetics. Since the number of mobile charges is kept constant, there is no difference on the concentration profile. On the contrary, the electric potential is driven by the mobility of  $\text{Li}^+$ , i.e., the diffusion coefficient. Since the diffusivity is very low, the potential is tremendous. Within the only two order of

magnitude difference on diffusion coefficient, the equilibrium potential is increased from 0.4 V to 40 V. Under these circumstances, this SIPE is not applicable for battery applications. Overall, we can say that in SIPE systems, mobility of cations and the dissociation reaction are the driven factors.

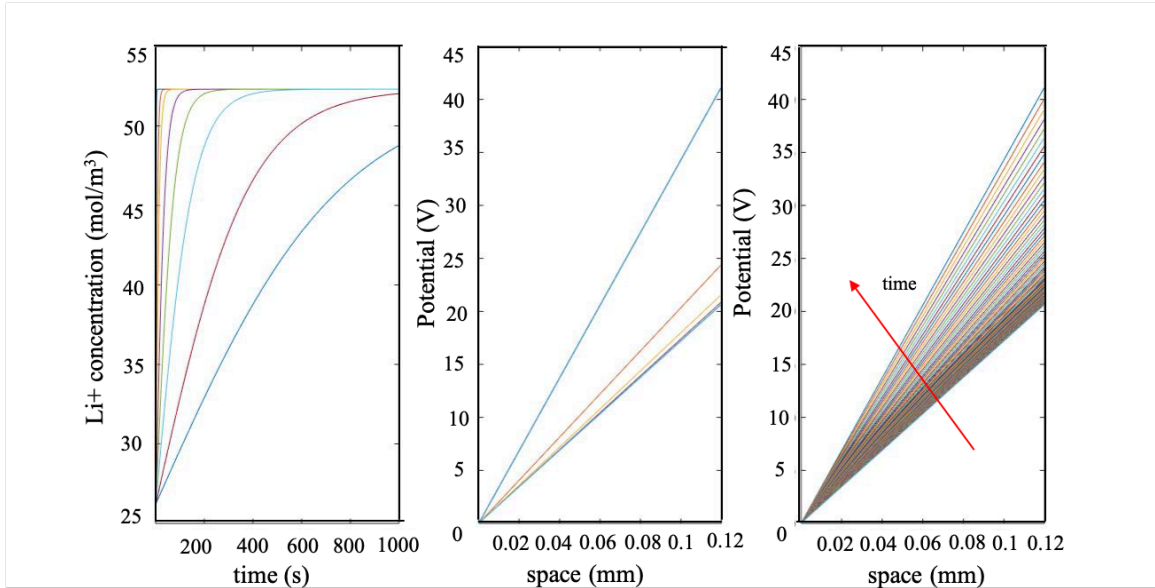


Figure 4.8: Lithium concentration and potential profiles of GPE-6 with  $1.06 \times 10^{-13} \text{ m}^2/\text{s}$  with fast and slow kinetics.

The similar materials with different charge density membranes are modelled in accordance with the experimental results. These membranes are also made of PEGDA-SS. The only difference between them is the charge density. The detailed synthesis is given in Chapter-1. Since, ionic conductivity of each membranes is akin to each other, GPE-20 is chosen to be compared with GPE-6 due to the low charge density.



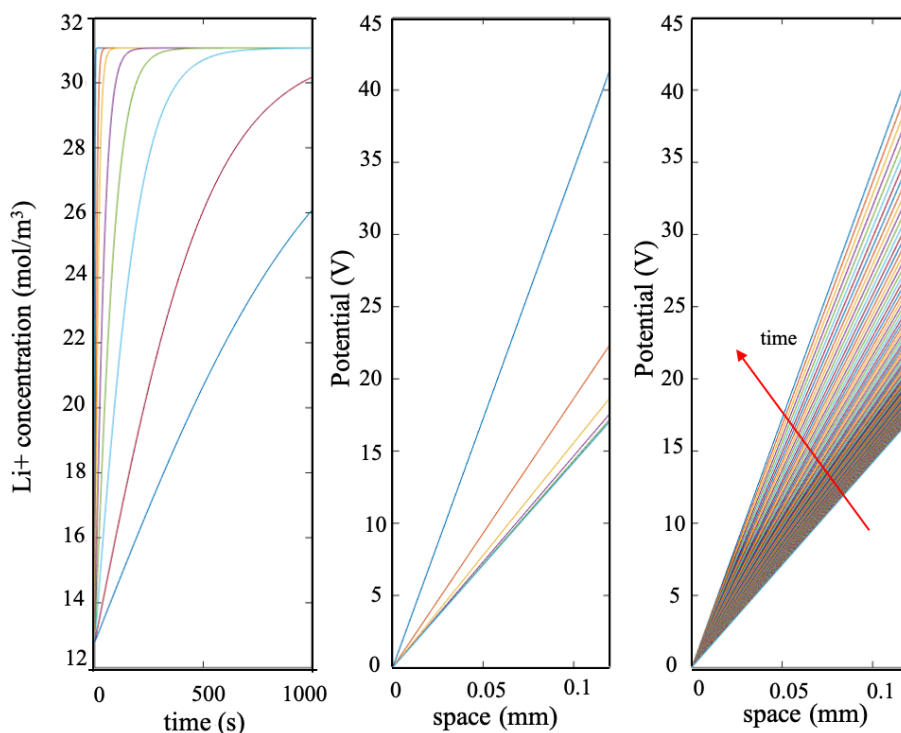


Figure 4.9: Lithium concentration and potential profiles of GPE-20 with infinitely fast and slow kinetics.

The ether oxygen ratio is the only difference between the two PEGDA-SS SIPE membranes. Figure 4.9 represents the lithium concentration profile and potential evaluation across the electrolyte with GPE-20. The initial lithium concentration of the membrane is lower than the GPE-6 with regard to charge density. Therefore, the equilibrium lithium concentration is lower as expected. Due to the low diffusion coefficient the potential response is 40 V which proves the previous comparing calculation of diffusion coefficients. The slower and fast kinetics only change the required time to reach the equilibrium potential. However, the impact is going to be clearer on full cell cycling.

#### 4.7 Summary and Outcomes

In this study, a single ion conducting polymer electrolyte is modelled based on experimental results. The lithium concentration profile and electric potential are examined with the given conditions. As it was mentioned in literature, the performance of an SIPE is reliant on the dissociation and mobility of the ions. Herein, these two parameters' impact

are investigated with regard to literature and experimental evidence. The ionic conductivity of each GPE (PEGDA-SS) membranes are akin to each other. Thus, the calculated diffusion coefficients do not vary. However, due to the charge densities, the number of charges varies, and the concentration profile of each membrane is different from each other. The potential is decreased with the escalated number of mobile charges in the polymer. If the number of charges in the membrane is constant, the only way to improve the performance of the electrolyte is to increase the diffusion coefficient of the SIPE.

These two methods are also demonstrated in certain experimental studies. Hence, our theoretical approach meets the realistic scheme of an SIPE. Additionally, the reaction kinetics of dissociation of ions is modelled. In most of the modelling studies, infinitely fast kinetics are taken into consideration for simplification. Most of the chemical reactions can be modelled with this approach. However, this is not enough to capture reaction dynamics in SIPEs. The impact of the reaction kinetics is still under investigation especially, the full cell battery response. The outcomes will be published in another study.

# **5. Chapter 5- The Influence of Electrode Morphology in the Electro-Chemo-Mechanical Response of Conventional Lithium-ion Batteries**

## **5.1 Introduction**

Over the last decade, the importance of lithium-ion batteries has risen due to the power supply of mobile devices. Because of the high working voltage and large power density, they are preferable for electric vehicles and hybrid electric vehicles (HEVs).<sup>1</sup> Numerical and experimental studies have continued in order to grasp a much more clear understanding of the processes during charge and discharge. However, the high cost and time requirements of experimental studies mean numerical studies have become crucial in this analysis. Computational simulations, based on rigorous theoretical modeling and coupled to validation and quantification of the uncertainties, have the potential to enhance batteries' performance, tailor architectural configurations toward optimal functioning of energy storage devices, and shape new materials for greater capacity and power release. In terms of macroscale modelling, the impact of thick electrodes was studied broadly.<sup>157</sup> The effect of electrode thickness on cycling performance is one of the crucial point to reach high performance lithium ion battery systems.

As depicted in Figure 5.1, an electrochemical cell generally consists of two electrodes (anode and cathode) that are internally separated by an electrolyte, which can be solid or liquid. The electrodes are electrically connected through current collectors and a conductive lead, which ensure the flow of current during battery operations. During battery discharging, the electrochemical affinity of the electrodes triggers the migration of Li ions from the anode to the cathode across the electrolyte, as well as the flow of electrons, with the same direction, through the external lead. The opposite happens during battery discharging, induced by an external current.

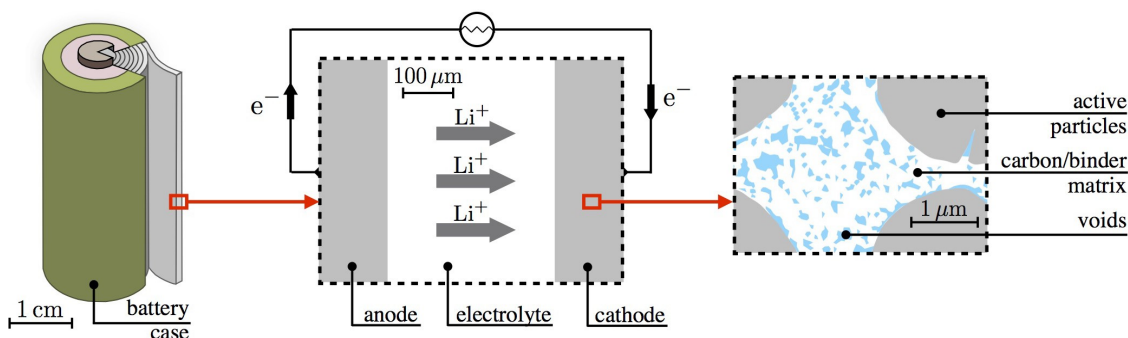


Figure 5.1: Schematic representation of a typical electrochemical cell and the characteristic microstructure of a porous electrode.

Although the scenario depicted in Fig. 5.1 is quite simple, modeling of Li-ion batteries is rather challenging as their behavior is intrinsically multi-physics and multi-scale.<sup>158</sup> Modeling of batteries involves the description of different (coupled) processes as transport of mass, charged species, electrochemical reactions, as well as the accompanying mechanical effects. On the other hand, such relevant phenomena take place at the characteristic length scale of the electrode compound, which can be several orders of magnitude smaller than the battery size, as for example in porous electrodes, i.e., those generally implemented in commercial batteries.

Any porous electrode is a complex media made of different phases as showed in Fig. 5.1. It consists of particles of micrometric size (as  $\text{LiCoO}_2$ ,  $\text{LiFePO}_4$ , and  $\text{LiMn}_2\text{O}_4$  as cathode materials,  $\text{LiC}_6$ , as anode material) embedded in a porous matrix formed by the mixture of carbon nanoparticles and (polymeric) binder. The porosity of the carbon/binder matrix is filled with liquid electrolyte which penetrates from the separator up to the particle surface. Such particles are generally called active or storage particles since Li ions are inserted/extracted from them through an electrochemical charge transfer reaction. On the other hand, the carbon/binder matrix, which is electrochemically inert, increases the overall electrical conductivity of the electrode and provides structural integrity. The reason that electrodes are made porous materials is to increase the surface over which the electrochemical charge transfer reaction can occur, thus increasing the efficiency of batteries.<sup>159</sup>

The function of a battery arises from the electrochemical reaction that occurs at the boundary between active materials and electrolyte. Such a reaction refers to an electrochemical charge transfer coupled with insertion (or extraction) of Li ions from the

electrolyte into the structure of the active materials. The kinetics of this process, and then the response of the battery, is not only related to the electrochemical affinity of the reactants and products, but also on their transport in solid and liquid phases, which is related to the geometry of the battery cell. Therefore, theoretical and numerical studies might have a crucial role to propose new material shapes and architectures in a complementary way to the experiments.

The modelling of lithium batteries has a wide spectrum, such as, microscopic or macroscopic scale. Despite the progresses, modeling the complex microstructure of a battery still represents an open challenge. The different nature of the phenomena involved (mechanical, electrical, electrochemical, and thermal) and the interactions among them lead to complex mathematics with a very high number of unknown fields (displacements, electric potential, concentrations, temperature).<sup>160</sup> Thus, the reasons for power loss with electro-chemical cycling have been one of the significant research branches of LIBs.<sup>161, 162</sup> The main mechanisms of aging can be categorized in four groups, namely: surface film formation (solid electrolyte interphase (SEI), lithium plating), bulk changes (phase segregation), mechanical effects due to lithiation (fracturing, dissipation, grinding), and parasitic reactions (corrosion, binder degradation).<sup>163, 164</sup> However, it is out of the scope of this study.

In this chapter the influence of electrodes morphology on the response of the battery is evaluated through a series of numerical analysis. The first aim of this study to comprehend the impact of electrode morphology in conventional LiBs. As following, the best performance electrode morphology is going to be applied with gel polymer electrolytes which were investigated profoundly on the previous chapters. To this end, we first consider a fictitious 2D planar battery made up of homogeneous electrodes and the conventional liquid electrolyte. The operating voltage of the battery is simulated accounting for electro-chemo-mechanical interactions in a thermodynamic consistent framework. The impact of electrodes geometry is then evaluated by simulating the battery response with different electrodes configurations.

## 5.2 Mathematical Model

### 5.2.1 Electrolyte Model

The battery cell is supposed to have a liquid electrolyte which is a solution of a binary salt, say LiX, in a solvent and a separator. The electrolyte is then characterized by the presence of ionic species  $\text{Li}^+$  and  $\text{X}^-$  after the complete decomposition of the binary salt LiX. The electrolyte is modeled following the approach based on Salvadori and colleagues<sup>41</sup>, which assume the transport of dissolved ions driven by diffusion and migration in a non convecting medium. Different from widespread models of electrolytes (see work of Newman's and coworkers<sup>165</sup> for example), the kinetics of positive and negative ions is modeled independently, without neglecting charge separations and the related electro- magnetic interactions. As pursued in the aforementioned work of Salvadori and colleagues<sup>41</sup>, the latter is considered in the framework of the electro-quasi- statics' approximation - i.e. by neglecting the time derivative of the magnetic field in Maxwell's equations. Without going into the details for the sake of brevity, the balance laws in the electrolyte domain  $V_e$  include. The charge conservation of the mobile species is written as,

$$\frac{\partial c_{\text{Li}^+}}{\partial t} + \vec{h}_{\text{Li}^+} = 0, \quad (1a)$$

$$\frac{\partial c_{\text{X}^-}}{\partial t} + \vec{h}_{\text{X}^-} = 0, \quad (1b)$$

where  $c_\alpha$  is the molarity (i.e., the number of moles per unit volume) of the specie  $\alpha = \text{Li}^+$ ,  $\text{X}^-$ ;  $h_\alpha$  is the mass flux in terms of moles, i.e. the number of moles of species  $\alpha$  measured per unit area per unit time. Maxwell's equations in electro-quasi static form,

$$\text{div} \left[ \frac{\partial \vec{D}_e}{\partial t} + \vec{i}_e \right] = 0, \quad (2a)$$

$$\vec{E}_e = -\nabla [\phi_e], \quad (2b)$$

where  $D_e$ ,  $i_e$ ,  $E_e$ , and  $\phi_e$  refer to the electric displacement, current density, electric field, and electric potential in the electrolyte respectively. Then balance of linear and angular momentum is written:

$$\text{div} [\boldsymbol{\sigma}_e] + \vec{b} = \vec{0}, \quad (3a)$$

$$\boldsymbol{\sigma}_e = \boldsymbol{\sigma}_e^T, \quad (3b)$$

where  $\boldsymbol{\sigma}$  is the Cauchy stress tensor, and  $\boldsymbol{b}$  is the vector of body forces, i.e. force per unit volume. Inertial effects are neglected in equation (3a). In this chapter  $\boldsymbol{\sigma}$  is used to define ‘Cauchy stress tensor’. The connection among balance equations (1) - (2) - (3) is provided by the constitutive definition of  $h_\alpha$ ,  $D_e$ ,  $i_e$ , and  $\boldsymbol{\sigma}_e$  in terms of the independent variables  $c_\alpha$ ,  $\phi_e$ , and displacement vector  $u_e$ . The flux of ionic species yields,

$$\vec{h}_{Li^+} = -D_{Li^+} \nabla [c_{Li^+}] - \frac{D_{Li^+} F}{RT} c_{Li^+} \left(1 - 2 \frac{c_{Li^+}}{c^{max}}\right) \nabla [\phi_e], \quad (4a)$$

$$\vec{h}_{X^-} = -D_{X^-} \nabla [c_{X^-}] + \frac{D_{X^-} F}{RT} c_{X^-} \left(1 - 2 \frac{c_{X^-}}{c^{max}}\right) \nabla [\phi_e], \quad (4b)$$

which is the extension of Nernst-Planck equation to saturable solution, see the study<sup>155</sup> for details. In equations (4)  $D|\alpha$  is the diffusion coefficient of species  $\alpha$ ;  $c^{max}$  is the ionic saturation limit; symbols  $F$ ,  $R$ , and  $T$  refer to Faraday constant, universal gas constant, and absolute temperature respectively. The current density is merely defined by exploiting Faraday’s law as,

$$\vec{i}_e = F \left( \vec{h}_{Li^+} - \vec{h}_{X^-} \right), \quad (5)$$

Assuming the electrolyte as an isotropic, linear, homogeneous dielectric, the constitutive definition of the electric displacement reads,

$$\vec{D} = \epsilon \vec{E}, \quad (6)$$

where  $\epsilon = \epsilon |r| \epsilon |r|$  is electrolyte permittivity, which is given, as usual, relative to that of vacuum (denoted with  $\epsilon|0$ ) as a relative permittivity  $\epsilon|r$ . From the mechanical point of view, the electrolyte is assumed as an isotropic-linear-elastic medium, accordingly the stress tensor is related to the elastic strain tensor  $\boldsymbol{\epsilon}_e$  through the following relationship,

$$\boldsymbol{\sigma}_e = K_e \text{tr} [\boldsymbol{\epsilon}_e] \mathbf{1} + 2 G_e \text{dev} [\boldsymbol{\epsilon}_e], \quad (7)$$

where  $K_e$  is the bulk modulus and  $G_e$  is the shear modulus. The elastic strain tensor is function of  $\vec{u}_e$  through formula,

$$\boldsymbol{\epsilon}_e = \frac{1}{2} \left( \nabla [u_e] + \nabla [u_e]^T \right). \quad (8)$$

As customary in small-strain theories.

## 5.2.2 Intercalating Electrodes

Electrodes are here assumed as homogeneous media, characterized by the presence of intercalated Li ions and moving electrons. According to Danilov's group's study<sup>22</sup>, Li ions in active materials are screened by the mobile electrons, which accompany lithium when moves from one interstitial site to the other. Therefore, the charge of Li cation after intercalation into active particles is instantaneously wiped out by the transport of electrons over the current collectors towards the particle surface. The active particles in the composite electrode are thus idealized as interstitial solid solution containing dissolved lithium Li and electrons which are free to move.

Because active materials have much higher conductivity than the electrolyte, the electromagnetic problem will be considered in the electro-static approximation. According to the framework developed in<sup>154</sup>, the governing equations for the electrodes can be summarized as follow; conservation of dissolved lithium,

$$\frac{\partial c_{Li}}{\partial t} + \text{div} \left[ \vec{h}_{Li} \right] = 0 \quad (9)$$

where  $c_{Li}$  is the molarity of dissolved Li, and  $\vec{h}_{Li}$  the flux vector is. The charge conservation,

$$\text{div} \left[ \vec{i}_a \right] = 0, \quad (10)$$

where  $\vec{i}_a$  refers to the current density in the electrodes.

Balance of linear and angular momentum,

$$\text{div} \left[ \boldsymbol{\sigma}_a \right] + \vec{b} = \vec{0}, \quad (11a)$$

$$\boldsymbol{\sigma}_a = \boldsymbol{\sigma}_a^T, \quad (11b)$$

Constitutive equations are derived from thermodynamic principles, as for examples carried out in study of Salvadori's group<sup>166</sup>[8], and are given in terms of lithium concentration  $c_{Li}$ , electric potential  $\phi_a$ , and displacement vector  $\vec{u}_a$ . To account for the effects of lithiation, the strain tensor  $\boldsymbol{\varepsilon}_q = \frac{1}{2} (\nabla [u_a] + \nabla [u_a]^T)$  is additively decomposed two contributions as follow,



$$\boldsymbol{\varepsilon}_a = \boldsymbol{\varepsilon}^{el} + \boldsymbol{\varepsilon}^{ch}, \quad (12)$$

where  $\boldsymbol{\varepsilon}^{el}$  is the elastic part of the deformation, while the chemical strain  $\boldsymbol{\varepsilon}^{ch}$  represent the volumetric deformation of the electrode lattice associated with lithium intercalation as,

$$\boldsymbol{\varepsilon}^{ch} = \omega_{Li} (c_{Li} - c_{Li}^0) \mathbb{1}, \quad (13)$$

With obvious meaning of constants  $K_a$  and  $G_a$ .

In a thermodynamic consistent theory, the definition of the Li flux in Eq. (9) is derived by applying the generalized Fick's law. For the sake of simplicity, the effect of complicate phenomena, such as phase- segregation, are not considered in this study. In accordance with the chemical potential of dissolved lithium has the usual expression for single-phase intercalating electrodes,

$$\mu_{Li} = \mu_{Li}^0 + RT \ln \left( \frac{c_{Li}}{c_{Li}^{max} - c_{Li}} \right) - \omega_{Li} \text{tr}[\boldsymbol{\sigma}_a], \quad (14)$$

with  $\mu_{Li}^0$  denoting the reference chemical potential. Therefore, the flux of dissolved lithium in the electrodes yields,

$$\vec{h}_{Li} = -D_{Li} \nabla [c_{Li}] + \frac{D_{Li} \omega_{Li}}{RT} c_{Li} \left( \frac{c_{Li}^{max} - c_{Li}}{c_{Li}^{max}} \right) \nabla [\text{tr}[\boldsymbol{\sigma}_a]] \quad (15)$$

where  $D_{Li}$  is the diffusivity of Li ions in the hosting lattice. Note that the transport of dissolved lithium is driven by chemo-mechanical effects, since the lithium flux is proportional to the gradient of Li concentration and to the gradient of hydrostatic pressure. Guided by Joule effect, a linear law is set as usual for the electrons flow. Accordingly, the current is made proportional to the gradient of the electric potential through the electrical conductivity  $\kappa_a > 0$

$$\vec{i}_a = \kappa_a \nabla [\phi_a]. \quad (16)$$

### 5.2.3 Interface Conditions

We introduce the boundary values and the jump of a generic function  $f(\vec{x}, t)$  at the interface between electrodes and electrolyte  $I = \partial V_a \cap \partial V_e$  as,

$$f|_I^a = \lim_{\vec{x} \in V_a \rightarrow I} f(\vec{x}, t), \quad f|_I^e = \lim_{\vec{x} \in V_e \rightarrow I} f(\vec{x}, t), \quad (17)$$

And

$$[[f]] = f|_I^a - f|_I^e . \quad (18)$$

The electrochemical reaction occurring at electrodes surface is here modeled through the standard Butler- Volmer equation. Therefore, instead of resolving explicitly the boundary layers between electrodes and electrolyte, the involved phenomena are incorporated in a zero-thickness interface. Accordingly, the electric potential can be discontinuous at the interface (see studies of Dreyer and coworkers.<sup>167, 168</sup>) for a comprehensive treatment of the argument). The Butler-Volmer equation defines the kinetics of the surface electrochemical reaction in term of current density  $i_{BV}$  as follows,

$$i_{BV} = i_0 \left\{ \exp \left[ \frac{\alpha_A F \eta_S}{RT} \right] - \exp \left[ -\frac{\alpha_C F \eta_S}{RT} \right] \right\} , \quad (19)$$

where  $i_0$  is the exchange current density,  $\alpha_A$  and  $\alpha_B$  positive kinetic constants, and  $\eta_S$  is the surface overpotential. The exchange current density is function of the concentration of lithium at the interface as follow<sup>169</sup>

$$i_0 = K_S F (c_{Li^+}|_I^e)^{\alpha_A} (c_{Li}^{max} - c_{Li}|_I^a)^{\alpha_A} (c_{Li}|_I^a)^{\alpha_C} , \quad (20)$$

while the surface overpotential is defined as

$$\eta_S = [[\phi]] - U_S , \quad (21)$$

with  $U_S$  denoting the surface open circuit potential, and  $[[\phi]]$  the jump to the electric potential at the interface. According to Purkayasta's study<sup>170</sup>, the surface open circuit potential  $U_S$  (also referred as surface OCP) is related to the ideal chemical potential,  $\mu_{Li}$ , of lithium at the active particle surface through the following equation,

$$F U_S(t) = \widetilde{\mu}_{Li} - \mu_{Li}(t)|_I^a \quad (22)$$

Where  $\widetilde{\mu}_{Li}$  the chemical potential of lithium of a reference electrode. Positive surface overpotential drives anodic currents, i.e.,  $i_{BV} > 0$ , while negative  $\eta_S$  causes cathodic currents, i.e.,  $i_{BV} < 0$ . The surface mass flux at particles surface in normal direction will be denoted with  $h_B$ . It is related through Faraday's law to the surface current density in the same direction at the same location.

$$i_{BV} = F h_{BV} . \quad (23)$$

On the other hand there is no intercalation of  $X^-$  ions into the active particles, while the interface condition for the current density follows the approach developed previously.<sup>41</sup> From the mechanical point of view, compatibility and traction continuity are imposed across the interface I. In conclusion, the electrochemical interface conditions can be summarized as follow,

$$\vec{h}_{Li} \cdot \vec{n}_a = -\vec{h}_{Li^+} \cdot \vec{n}_e = h_{BV}, \quad (25a)$$

$$\vec{h}_{X^-} \cdot \vec{n}_a = 0,$$

$$\vec{i}_a \cdot \vec{n}_a = - \left( \frac{\partial \vec{D}_e}{\partial t} + \vec{i}_e \right) \cdot \vec{n}_e = -i_{BV} \quad (25b)$$

$$[[\phi]] = U_S - \eta_S \quad (25c)$$

$$[[\vec{u}]] = \vec{0}, \quad (25d)$$

$$[[\sigma]] \cdot \vec{n} = \vec{0}. \quad (25e)$$

where  $\vec{n} = \vec{n}_a = -\vec{n}_e$  denotes the outward normal vector to a surface.

#### 5.2.4 Material Parameters

We start by considering the fictitious planar battery represented in Fig. 5.2. The electrodes consist of 10  $\mu\text{m}$  thick graphite as anode and 10  $\mu\text{m}$   $\text{LiCoO}_2$  cathode separated by 30  $\mu\text{m}$  separator with 1 M  $\text{LiPF}_6$  liquid electrolyte. For the simplicity, the binder and carbon particles in the cathode material are not taken into consideration. The cross sectional area is assumed 200  $\text{cm}^2$  as representative of a commercial cylindrical battery.<sup>171</sup>

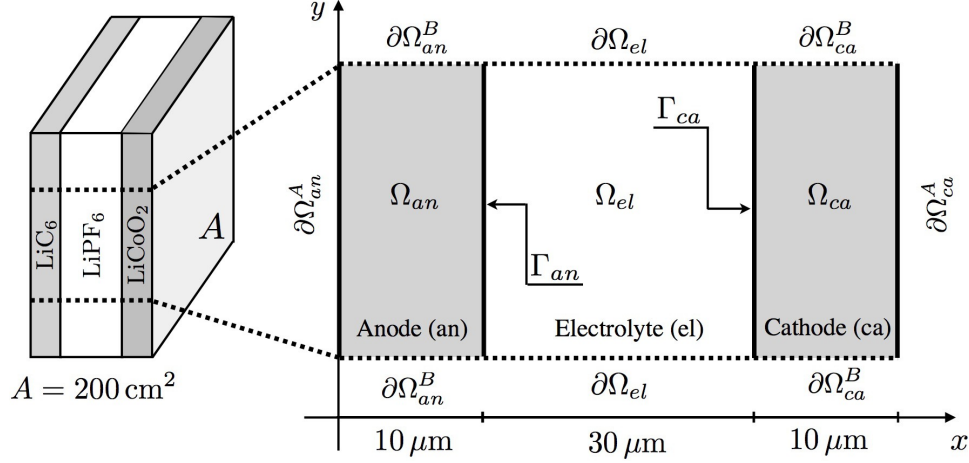


Figure 5.2: Schematic representation of the planar Li-ion batteries that is taken for full cell battery simulations.

The subscripts an and ca will identify LiC<sub>6</sub> anode and LiCoO<sub>2</sub> cathode from now to on. The electrodes are both modeled by means of governing equations for intercalating electrodes discussed in Section 5.2.2. The relevant material parameters, taken from the literature, are listed in Table 1. In the same way, governing equations for the electrolytic solution are given in Section 5.2.1 and the pertinent material parameters are reported in Table 5.1. Denoting with  $x$  the amount of lithium ions of positive Li <sub>$x$</sub> CoO<sub>2</sub> electrode, in battery operations  $x$  ranges approximatively between  $x = 0.5$  and  $x = 1.0$ . Therefore, the theoretical capacity of the battery can be estimated based on the amount of lithium that can be extracted from the positive electrode as follow,

$$V_{\text{LiCoO}_2} \frac{c_{\text{Li}}^{\text{max}}}{2} F = 64 \text{ mAh}, \quad (26)$$

where  $V_{\text{LiCoO}_2}$  is the volume of the positive electrode, while  $F$  refers to the Faraday's constant.

The electro-chemo-mechanical behavior of anode/electrolyte  $\Gamma_a$  and cathode/electrolyte  $\Gamma_{ca}$  interfaces is described in Section 5.2.3. The intercalation reaction of lithium in positive and negative electrodes are written as,



The Butler-Volmer kinetic equation, is given in terms of the ideal chemical potential of lithium as,

$$U_S = -\frac{\mu_{Li}}{F} = -\frac{\mu_{Li}^0}{F} - \frac{RT}{F} \ln \left( \frac{c_{Li}}{c_{Li}^{max} - c_{Li}} \right) + \frac{\omega_{Li}}{F} \text{tr} [\boldsymbol{\sigma}_a] , \quad (29)$$

having taken  $\mu_{Li}^0 = 0$  J/mol as usual. In this way the theoretical OPC defined in formula (29) depends on concentration of dissolved lithium and hydrostatic pressure at electrode surface. Note that the reference chemical potential  $\mu^0$  does not influence the profile of  $U_S$ . Its value has been taken as,

$$\left. \frac{\mu_{Li}^0}{F} \right|_{LiC_6} = -0.1 \text{ V} , \quad \left. \frac{\mu_{Li}^0}{F} \right|_{LiCoO_2} = -4.2 \text{ V} \quad (30)$$

In order to match the measured OCP of graphite and lithium cobalt oxide for  $Li_{10.5}CoO_2$  and  $Li_{10.5}C_6$  assuming a stress-free electrode, for  $c_{Li} = c_{max}/2$  and  $\text{tr} [\boldsymbol{\sigma}_a] = 0$ . The other material parameters appearing in equations (20)-(21) are taken from [14] and are listed in Table 5.1.

Table 5.1: Material parameters of anode, cathode and the interfaces of anode/electrolyte and cathode/electrolyte

| Material Parameters  | Anode/Electrolyte                                 | Cathode/Electrolyte                                 |
|--|---|---|
|  | <i>LiC<sub>6</sub></i>                            | <i>LiCoO<sub>2</sub></i>                            |
| $c_{\text{Li}}^{\text{max}}$ (mol/m <sup>3</sup> )                 | $2.64 \times 10^4$ <sup>172</sup>                 | $2.39 \times 10^4$ <sup>169</sup>                   |
| D <sub>Li</sub> (m <sup>2</sup> /s)                                | $3.90 \times 10^{-14}$ <sup>172</sup>             | $5.387 \times 10^{-15}$ <sup>169</sup>              |
| $\omega_{\text{Li}}$ (m <sup>3</sup> /mol)                         | $1.642 \times 10^{-6}$ <sup>172</sup>             | $-5.300 \times 10^{-7}$ <sup>173</sup>              |
| E (Gpa)  | 15 <sup>172</sup>                                 | 370 <sup>169</sup>                                  |
| $\nu$ (-)  | 0.3 <sup>172</sup>                                | 0.2 <sup>169</sup>                                  |
| $\kappa$ (S/m)   | 100 <sup>174</sup>                                | 10 <sup>174</sup>                                   |
|  | <i>LiPF<sub>6</sub> Electrolyte</i>               |   |
| $c_{\text{Li}}^{\text{max}}$ (mol/m <sup>3</sup> )                 | $1.0 \times 10^4$ <sup>155</sup>                  |   |
| $D_{\text{Li}}^+$ (m <sup>2</sup> /s)                              | $2.0 \times 10^{-11}$ <sup>155</sup>              |   |
| $D_{\text{X}}^-$ (m <sup>2</sup> /s)                               | $3.00 \times 10^{-11}$ <sup>155</sup>             |   |
| E (MPa)  | 450 <sup>175</sup>                                |   |
| $\nu$ (-)  | 0.499 This study                                  |   |
| $\epsilon_r$ (-)   | 95 <sup>155</sup>                                 |   |
|  | <i>LiC<sub>6</sub>/LiPF<sub>6</sub> interface</i> | <i>LiCoO<sub>2</sub>/LiPF<sub>6</sub> interface</i> |
| $\alpha_A$ (-)   | 0.5 <sup>176</sup>                                | 0.5 <sup>176</sup>                                  |
| $\alpha_B$ (-)   | 0.5 <sup>176</sup>                                | 0.5 <sup>176</sup>                                  |
| $\kappa_S$ (m <sup>2.5</sup> mol <sup>-0.5</sup> s <sup>-1</sup> ) | $1.764 \times 10^{-11}$ <sup>176</sup>            | $6.667 \times 10^{-11}$ <sup>176</sup>              |

## 5.2.5 Geometry and Boundary Conditions

In order to assess the impact of electrode morphology on battery performance, either one or both of the electrodes are designed as comb-like profile as depicted in Figure 5.3. The morphology is constrained to fixed area of the electrode; hence the capacity of the battery does not change with the variation of the electrode design. The length and the height of the comb are varied in accordance with the number of comb as well as the porosity

changes with the added number of the combs. The height of each comb is proportional to height of the electrode and the number of combs is applied. Meanwhile, the length varies with the function of comb numbers and the initial value of the electrode.  $\alpha$  is defined as the function of comb number. Therefore, the essential height and width of the modified electrodes are calculated as follows.  $n$  is defined as the number of comb and  $H$  is the height of the electrode. the details are depicted in figure 5.3.

$$\begin{aligned}
 A_{\text{gross}} &= hb^0 + (\Delta b) \\
 A_{\text{void}} &= (\alpha(n)b^0 + \Delta b)\alpha(n)h \\
 h(n) &= \frac{H}{n+1} \\
 \Delta b &= \frac{b^0 \cdot \alpha^2 n}{(1 - \alpha n)} \\
 t^n &= h \cdot (1 - \alpha n)
 \end{aligned} \tag{31}$$

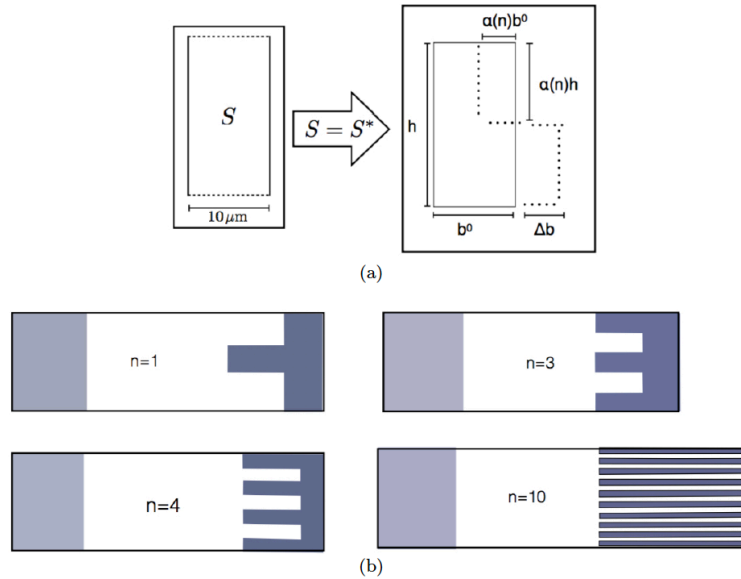


Figure 5.3: The schematic representation of modified electrode.

*Boundary conditions* - The boundary conditions are imposed on the boundary of both the electrodes,  $\partial\Omega_{an}$  and  $\partial\Omega_{ca}$ , and electrolyte  $\partial\Omega_e$ . For the sake of clarity, the electrodes boundary is split in two parts as follow,

$$\partial\Omega_{an} = \partial\Omega_{an}^A \cup \partial\Omega_{an}^B, \quad \text{and} \quad \partial\Omega_{ca} = \partial\Omega_{ca}^A \cup \partial\Omega_{ca}^B. \tag{32}$$

The battery response will be evaluated upon constant current discharging for different C-rates, as customary for experimental tests. To this end a uniform discharging current is prescribed on both sides of the battery as follow,

$$\vec{i}_{an} \cdot \vec{n}_{an} = -\frac{I(t)}{A} \quad \text{on } \partial\Omega_{an}^A, \quad \vec{i}_{ca} \cdot \vec{n}_{ca} = \frac{I(t)}{A} \quad \text{on } \partial\Omega_{ca}^A, \quad (33)$$

where A is the battery cross-sectional area and I(t) reefers to the current flowing through the battery. In order to make initial and boundary conditions compatible with thermodynamic equilibrium at t = 0, I is tuned in time as,

$$I(t) = (1 - e^{-t}) I_{1.0} C_r, \quad (34)$$

where  $I_{1.0} = 3.2 \text{ A/m}^2$  is the electric current corresponding to 1 C-rate discharging, while  $C_r$  is the discharge rate. On the other hand, the flux of current is zero on the remaining part of the boundary for reasons of symmetry, thus the following conditions arise.

$$\vec{i}_{an} \cdot \vec{n}_{an} = 0 \quad \text{on } \partial\Omega_{an}^B, \quad \vec{i}_{ca} \cdot \vec{n}_{ca} = 0 \quad \text{on } \partial\Omega_{ca}^B, \quad \vec{i}_{el} \cdot \vec{n}_{el} = 0 \quad \text{on } \partial\Omega_{el}, \quad (35)$$

In line with battery morphology and processes, neither neutral lithium nor ionic species  $\text{Li}^+$  and  $\text{X}^-$  can flow through the external boundary so that,

$$\vec{h}_{\text{Li}} \cdot \vec{n}_{an} = 0 \quad \text{on } \partial\Omega_{an}, \quad \vec{h}_{\text{Li}} \cdot \vec{n}_{ca} = 0 \quad \text{on } \partial\Omega_{ca},$$

$$\vec{h}_{\text{Li}^+} \cdot \vec{n}_{el} = \vec{h}_{\text{X}^-} \cdot \vec{n}_{el} = 0 \quad \text{on } \partial\Omega_{el}.$$

Assuming the battery case as infinitely rigid, the cell expansion/contraction is prevented during battery operations. Thus, the following mechanical boundary conditions can be formed as,

$$u_x = 0 \quad \text{on } \{\partial\Omega_{an}^A \cup \partial\Omega_{ca}^A\}, \quad u_y = 0 \quad \text{on } \{\partial\Omega_{el} \cup \partial\Omega_{an}^B \cup \partial\Omega_{ca}^B\}.$$

*Initial conditions* - Initial conditions at t = 0 are imposed for species concentration in both cathode and electrolyte. When the battery is first assembled, the Li ions are completely stored in the positive electrode while the anode is free of lithium, i.e., the battery is fully discharged. In order to evaluate the battery response upon discharging, the battery has to be charged first, so that Li ions can be transferred from the positive to the negative electrode. We thus assume the initial concentration of lithium in the electrodes as that of the battery with theoretical full state of charge. Due to the electrochemical properties



of LiCoO<sub>2</sub>, only half of its theoretical capacity can be used practically, thus the initial concentration of Li ions in the electrodes are taken as

$$c_{\text{Li}} \Big|_{t=0} = 1.2 \times 10^4 \text{ mol/m}^3 \quad \text{in } \Omega_{an} \cup \Omega_{ca},$$

since the electrodes have the same volume. The initial concentration of ionic species in the electrolyte are taken from Salvadori's study<sup>155</sup>, yielding

$$c_{\text{Li}^+} \Big|_{t=0} = c_{\text{X}^+} \Big|_{t=0} = 1.5 \times 10^3 \text{ mol/m}^3 \quad \text{in } \Omega_{el}.$$

## 5.2.6 Finite Element Implementation

The system of equations discussed in previous sections has been solved numerically through the Finite Elements Method. Firstly, a non-dimensional weak form has been derived for the overall battery after rewriting the governing equations of each battery component in dimensionless form. Then, the weak form has been discretized in space with the Finite Elements Method, while the evolution in time has been resolved with the Backward Euler Scheme. Finally, the resulting nonlinear algebraic problem has been implemented in the commercial FE software ABAQUS by writing a User Element Subroutine.

## 5.2.7 Non-Dimensional Governing Equations and Weak Forms

Intercalating electrodes - Equations (9) - (10) - (11) have been rephrased in term a dimensional variable

$$x_i^* = \frac{x_i}{l}, \quad t^* = \frac{t}{t}, \quad c_{\text{Li}}^* = \frac{c_{\text{Li}}}{c}, \quad \phi^* = \frac{\phi F}{RT}, \quad u_i^* = \frac{u_i}{l}, \quad \sigma_{ij}^* = \frac{\sigma_{ij}}{\sigma},$$

by introducing  $l$ ,  $t$ ,  $c$ ,  $\sigma$  as reference length, time, concentration, and stress respectively. In this way, the governing equations of intercalating electrodes are equivalent to the following non-dimensional ones

$$\frac{\partial c_{\text{Li}}^*}{\partial t^*} + \text{div}^* [\vec{h}_{\text{Li}}^*] = 0,$$

$$\text{div}^* [\vec{i}_a^*] = 0,$$

$$\operatorname{div}^*[\boldsymbol{\sigma}_a^*] = \vec{0},$$

$$\operatorname{div}^*[\vec{h}_{\text{Li}}^*] = \sum_{i=1}^2 \frac{h_{\text{Li}}^*}{\partial x_i^*}, \quad \operatorname{div}^*[\boldsymbol{\sigma}_a^*] = \sum_{i=1}^2 \sum_{j=1}^2 \frac{\sigma_{ij}^*}{\partial x_j^*} \vec{e}_i, \quad \vec{h}_{\text{Li}}^* = \frac{\vec{h}_{\text{Li}} \bar{t}}{\bar{c}}, \quad \vec{i}_a^* = \frac{\vec{i}_a \bar{t}}{\bar{c} \bar{l} F}.$$

Note that equations (37) have the same expression of (9) - (10) - (11) but are formulated in terms of non-dimensional variables and operators. Similarly, a non-dimensional counterpart of the constitutive laws (14) - (16) - (17) can be easily obtained as follow

$$\boldsymbol{\sigma}_a^* = K_a^* \operatorname{tr}[\boldsymbol{\varepsilon}_a - \boldsymbol{\varepsilon}^{ch}] \mathbf{1} + 2 G_a^* \operatorname{dev}[\boldsymbol{\varepsilon}_a],$$

$$\vec{h}_{\text{Li}}^* = -\mathbb{D}_{\text{Li}}^* \nabla^* [c_{\text{Li}}^*] + \frac{\mathbb{D}_{\text{Li}}^* \omega_{\text{Li}}^*}{(RT)^*} c_{\text{Li}}^* \left( \frac{(c_{\text{Li}}^{max})^* - c_{\text{Li}}^*}{(c_{\text{Li}}^{max})^*} \right) \nabla [\operatorname{tr}[\boldsymbol{\sigma}_a^*]]$$

$$\vec{i}_a^* = \kappa_a^* \nabla^* [\phi_a^*].$$

with non-dimensional material parameters defined as

$$\mathbb{D}_{\text{Li}}^* = \frac{\mathbb{D}_{\text{Li}} \bar{t}}{\bar{l}^2}, \quad \omega_{\text{Li}}^* = \omega_{\text{Li}} \bar{c}, \quad (RT)^* = RT \frac{\bar{c}}{\bar{\sigma}}, \quad (c_{\text{Li}}^{max})^* = \frac{c_{\text{Li}}^{max}}{\bar{c}},$$

$$\kappa_a^* = \frac{\kappa_a \bar{t} RT}{\bar{c} \bar{l}^2 F^2}, \quad K_a^* = \frac{K_a}{\bar{\sigma}}, \quad G_a^* = \frac{G_a}{\bar{\sigma}}.$$

To include the effect of stress gradient in equation (16) we define an additional dimensionless variable  $\Sigma^*$  as,

$$\Sigma^* - \operatorname{tr}[\boldsymbol{\sigma}^*] = 0,$$

which will be approximate as an explicit degree of freedom. Eq. (40) is then added to the set of governing equations (37) for the numerical resolution of the problem. Electrolyte - Following the same procedure adopted for electrodes, governing equations (1) - (2) - (3) are first made dimensionless by introducing the following non dimensional variables

$$x_i^* = \frac{x_i}{\bar{l}}, \quad t^* = \frac{t}{\bar{t}}, \quad c_{\text{Li}^+}^* = \frac{c_{\text{Li}^+}}{\bar{c}}, \quad c_{\text{X}^-}^* = \frac{c_{\text{X}^-}}{\bar{c}},$$

$$\phi^* = \frac{\phi F}{RT}, \quad u_i^* = \frac{u_i}{\bar{l}}, \quad \sigma_{ij}^* = \frac{\sigma_{ij}}{\bar{\sigma}},$$

with  $l$ ,  $t$ ,  $c^-$ ,  $\sigma^-$  representing reference length, time, concentration, and stress respectively. Taking advantage of the definitions (4.1), the balance laws of electrolyte are equivalent to the following non-dimensional ones

$$\frac{\partial c_{\text{Li}^+}^*}{\partial t^*} + \text{div}^*[\vec{h}_{\text{Li}^+}^*] = 0, \quad (42a)$$

$$\frac{\partial c_{\text{X}^-}^*}{\partial t^*} + \text{div}^*[\vec{h}_{\text{X}^-}^*] = 0, \quad (42b)$$

$$\text{div}^* \left[ \frac{\partial \vec{D}_e^*}{\partial t^*} + (\vec{h}_{\text{Li}^+}^* - \vec{h}_{\text{X}^-}^*) \right] = 0, \quad (42c)$$

$$\text{div}^*[\sigma_e^*] = \vec{0}, \quad (42d)$$

Where,

$$\text{div}^*[\vec{h}_\beta^*] = \sum_{i=1}^2 \frac{h_\beta^*}{\partial x_i^*}, \quad \text{div}^*[\sigma_e^*] = \sum_{i=1}^2 \sum_{j=1}^2 \frac{\sigma_{ij}^*}{\partial x_j^*} \vec{e}_i, \quad \vec{h}_\beta^* = \frac{\vec{h}_\beta \bar{t}}{\bar{c} \bar{l}}, \quad \vec{D}_e^* = \frac{\vec{D}_e}{\bar{c} \bar{l} F},$$

And

$$\beta = \text{Li}^+, \text{X}^-.$$

In this way the dimensionless form of the constitutive laws (4) - (6) - (3) result as follow

$$\vec{h}_{\text{Li}^+}^* = -\mathbb{D}_{\text{Li}^+}^* \nabla [c_{\text{Li}^+}^*] - \mathbb{D}_{\text{Li}^+}^* c_{\text{Li}^+}^* \left( 1 - 2 \frac{c_{\text{Li}^+}^*}{(c^{\text{max}})^*} \right) \nabla^* [\phi_e^*],$$

$$\vec{h}_{\text{X}^-}^* = -\mathbb{D}_{\text{X}^-}^* \nabla^* [c_{\text{X}^-}^*] + \mathbb{D}_{\text{X}^-}^* c_{\text{X}^-}^* \left( 1 - 2 \frac{c_{\text{X}^-}^*}{(c^{\text{max}})^*} \right) \nabla^* [\phi_e^*],$$

$$\vec{D}^* = -\mathbb{F}^* \nabla^* [\phi_e^*],$$

$$\sigma_e^* = K_e^* \text{tr}[\epsilon_e] \mathbb{1} + 2 G_e^* \text{dev}[\epsilon_e].$$

Where,

$$\mathbb{D}_{\text{Li}^+}^* = \frac{\mathbb{D}_{\text{Li}^+} \bar{t}}{\bar{l}^2}, \quad \mathbb{D}_{\text{X}^-}^* = \frac{\mathbb{D}_{\text{X}^-} \bar{t}}{\bar{l}^2}, \quad \left( \frac{F}{RT} \right)^* = 1, \quad (c^{max})^* = \frac{c^{max}}{\bar{c}},$$

$$\hat{\kappa}_e^* = \frac{\hat{\kappa}_e RT}{\bar{c} \bar{l}^2 F^2}, \quad K_e^* = \frac{K_e}{\bar{\sigma}}, \quad G_e^* = \frac{G_e}{\bar{\sigma}}.$$

### 5.2.7.1 Weak form

The weak formulation results from multiplying the strong form of governing equations by a suitable set of tests functions and performing an integration upon the domain, exploiting the integration by parts formula with the aim of reducing the order of differentiation in space. The asterisk is omitted for the sake of readability. In conclusion, the overall weak form of battery governing equations can be written in the time interval  $[0, \text{tf}]$  as

Find  $y(\vec{x}, t) \in V[0, \text{tf}]$  such that

$$\frac{\partial}{\partial t} b(\hat{y}(\vec{x}), c_L(\vec{x}, t)) + a(\hat{y}(\vec{x}), y(\vec{x}, t)) = f(\hat{y}(\vec{x})) \quad \forall \hat{y}(\vec{x}) \in \mathcal{V} \quad (45)$$

$$b(\hat{y}(\vec{x}), c_L(\vec{x}, t)) = \int_{\Omega_a} \hat{c}_L c_L \, dA + \int_{\Omega_e} \hat{c}_{\text{Li}^+} c_{\text{Li}^+} \, dA + \int_{\Omega_e} \hat{c}_{\text{X}^-} c_{\text{X}^-} \, dA + \int_{\Omega_e} \hat{\kappa}_e \nabla[\hat{\phi}_e] \cdot \nabla[\phi_e] \, dA,$$

$$\begin{aligned} a(\hat{y}(\vec{x}), y(\vec{x}, t)) &= \int_{\Omega_a} \nabla[\hat{c}_L] \cdot \left\{ \mathbb{D}_L \nabla[c_L] - \mathbb{D}_\Sigma(c_L) \nabla[\Sigma] \right\} dA + \int_{\Omega_a} \kappa_a \nabla[\hat{\phi}_a] \cdot \nabla[\phi_a] \, dA + \\ &+ \int_{\Omega_a} \nabla_S[\hat{\vec{u}}_a] : \boldsymbol{\sigma}_a(c_L, \Sigma, \vec{u}_a) \, dA + \int_{\Omega_a} \hat{\Sigma} \left\{ \Sigma - \text{tr}[\boldsymbol{\sigma}_a(c_L, \Sigma, \vec{u}_a)] \right\} dA + \\ &+ \int_{\Omega_e} \nabla[\hat{c}_{\text{Li}^+}] \cdot \left\{ \mathbb{D}_{\text{Li}^+} \nabla[c_{\text{Li}^+}] + \mathbb{D}_\phi^+(c_{\text{Li}^+}) \nabla[\phi_e] \right\} dA + \\ &+ \int_{\Omega_e} \nabla[\hat{c}_{\text{X}^-}] \cdot \left\{ \mathbb{D}_{\text{X}^-} \nabla[c_{\text{X}^-}] - \mathbb{D}_\phi^-(c_{\text{X}^-}) \nabla[\phi_e] \right\} dA + \end{aligned}$$

$$\begin{aligned}
& + \int_{\Omega_e} \nabla [\hat{\phi}_e] \cdot \left\{ \mathbb{D}_{\text{Li}^+} \nabla [c_{\text{Li}^+}] + \mathbb{D}_{\phi}^+ (c_{\text{Li}^+}) \nabla [\phi_e] - \mathbb{D}_{\text{X}^-} \nabla [c_{\text{X}^-}] + \mathbb{D}_{\phi}^- (c_{\text{X}^-}) \nabla [\phi_e] \right\} dA + \\
& + \int_{\Omega_e} \nabla_S [\vec{u}_e] : \boldsymbol{\sigma}_e(\vec{u}_e) dA + \\
& + \int_{\Gamma_{an}} \hat{\Delta} c_{\text{Li}} h_{BV}(\Delta\phi) ds + \int_{\Gamma_{an}} \hat{\Delta} \phi i_{BV}(\Delta\phi) ds - \int_{\Gamma_{an}} \hat{\Delta} \vec{u} \cdot \vec{T}_{\Gamma}(\Delta\vec{u}) ds + \\
& + \int_{\Gamma_{ca}} \hat{\Delta} c_{\text{Li}} h_{BV}(\Delta\phi) ds + \int_{\Gamma_{ca}} \hat{\Delta} \phi i_{BV}(\Delta\phi) ds - \int_{\Gamma_{ca}} \hat{\Delta} \vec{u} \cdot \vec{T}_{\Gamma}(\Delta\vec{u}) ds, \\
\\
f(\hat{y}(\vec{x})) = & - \int_{\partial^N \Omega_{an}} \hat{c}_L \{ \vec{h}_L \cdot \vec{n}_{an} \} ds - \int_{\partial^N \Omega_{ca}} \hat{c}_L \{ \vec{h}_L \cdot \vec{n}_{ca} \} ds + \\
& - \int_{\partial^N \Omega_{an}} \hat{\phi}_{an} \{ \vec{i} \cdot \vec{n}_{an} \} ds - \int_{\partial^N \Omega_{ca}} \hat{\phi}_{ca} \{ \vec{i} \cdot \vec{n}_{ca} \} ds + \\
& + \int_{\partial^N \Omega_{an}} \vec{u}_{an} \cdot (\boldsymbol{\sigma}_{an} \vec{n}_{an}) ds + \int_{\partial^N \Omega_{ca}} \vec{u}_{ca} \cdot (\boldsymbol{\sigma}_{ca} \vec{n}_{ca}) ds.
\end{aligned}$$

where  $\mathbb{D}|\Sigma$ ,  $\mathbb{D}|+\phi$ ,  $\mathbb{D}|-\phi$  stands for

$$\mathbb{D}_{\Sigma} = \frac{\mathbb{D}_L \omega_L}{RT} c_L \left( \frac{c_L^{max} - c_L}{c_L^{max}} \right), \quad \mathbb{D}_{\phi}^+ = \frac{\mathbb{D}_{\text{Li}^+} F}{RT} c_{\text{Li}^+} \left( 1 - 2 \frac{c_{\text{Li}^+}}{c^{max}} \right), \quad \mathbb{D}_{\phi}^- = \frac{\mathbb{D}_{\text{X}^-} F}{RT} c_{\text{X}^-} \left( 1 - 2 \frac{c_{\text{X}^-}}{c^{max}} \right),$$

and  $\Omega_a = \Omega_{an} \cup \Omega_{ca}$  is the domain occupied by the electrodes. Symbol  $\Delta$  defines the jump of a certain variable at the interfaces (a stands for an or ca depending on the interface  $\Gamma$  where integrals are computed)

$$\Delta c_{\text{Li}} = c_L - c_{\text{Li}^+}, \quad \Delta \phi = \phi_a - \phi_e, \quad \Delta \vec{u} = \vec{u}_a - \vec{u}_e,$$

while  $\vec{T}_{\Gamma}$  is the traction normal to the interface

$$\vec{T}_{\Gamma} = \boldsymbol{\sigma}_a \vec{n}_a = -\boldsymbol{\sigma}_e \vec{n}_e.$$

$y = \{c_L, \phi_a, u_a, \Sigma, c_{\text{Li}^+}, c_{\text{X}^-}, \phi_e, u_e\}$  collecting the time-dependent unknown fields. Column  $y^{\wedge}$  collects the steady state test functions that correspond to the unknown fields in  $y$ , i.e.  $y^{\wedge} = \{\hat{c}_L, \hat{\phi}_a, \hat{u}_a, \hat{\Sigma}, \hat{c}_{\text{Li}^+}, \hat{c}_{\text{X}^-}, \hat{\phi}_e, \hat{u}_e\}$ . The identification of the functional space  $V$  falls beyond the scope of this work.

## 5.2.8 Numerical Resolution

As discussed earlier, in the framework of the Finite Element Method, the weak form (47) is discretized in space and time prior to the implementation in the commercial software ABAQUS. In this way, the resulting non-linear problem is solved through the Newton-Raphson algorithm in a monolithic scheme.

The numerical implementation of the interface conditions between active materials and electrolyte are of particular interest in these electro-chemo-mechanical systems. In this work we have chosen to implement the interface conditions by using zero-thickness interface elements between electrodes and electrolyte. For this sake, we have extended the numerical approach used for cohesive mechanics to the electro-chemo-mechanical interfaces at hand. Accordingly, zero-thickness interface elements, generated using the open-source program mesh-generator, have been placed between electrodes and electrolyte. Such an approach requires that the FE mesh of active materials and electrolyte must be conformal, i.e., the nodes at interface must superpose (see Fig. 5.4).

The computational domain, which can be reduced to the one reported in Fig. 5.4 for reasons of symmetry, has been discretized using 4-node bilinear elements. Due to the regular morphology of the battery components, a structured FE grid has been generated with the mesh-generator Gmsh.

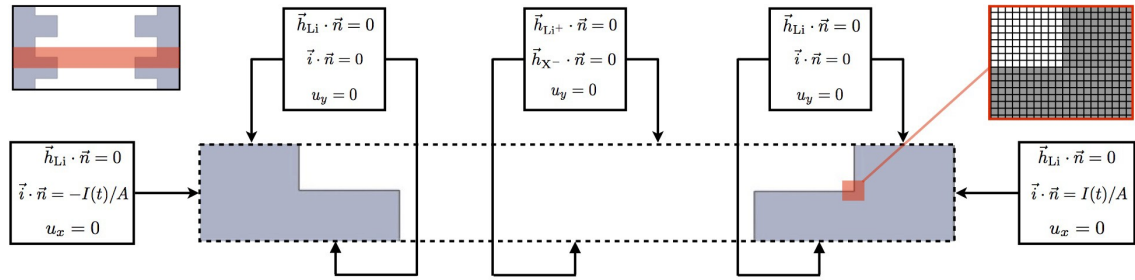


Figure 5.4: Computational domain adopted for the numerical simulations along with a schematic representation of the boundary conditions used.

Three distinct User Elements have been developed for the implementation in ABAQUS: one for the active materials, one for the electrolyte, and one for the interfaces. All these elements have five degrees of freedom as depicted in Figure 5.5. In particular, the nodal unknowns are  $\{cLi^+, cX^-, \varphi_e, u_x, u_y\}$  in the electrolyte and  $c_{Li}, \Sigma, \varphi_e, u_x, u_y$  in the electrodes. Since the nodes of the interface elements belong either to the electrolyte or to the electrodes, the nodal unknowns in the interface elements follow from the ones implemented in the bulk elements.

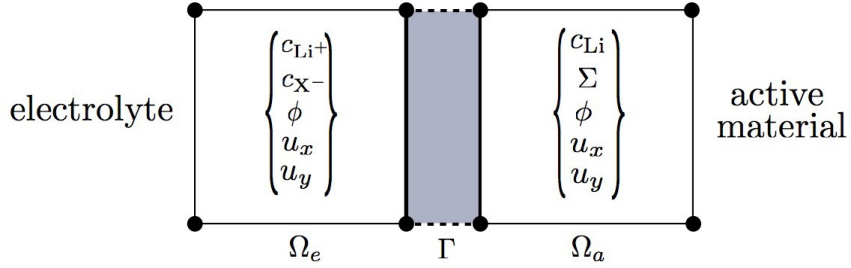


Figure 5.5: Computational domain adopted for the numerical simulations along with a schematic representation of the boundary conditions used.

## 5.3 Results and Discussion

### 5.3.1 Electro-Chemo-Mechanical Response of the Planar Battery

The battery voltage - The response of the battery with planar electrodes (see Fig. 5.2) is first discussed in order to evaluate the model capability in a simple one-dimensional case. Such a battery has been simulated assuming a constant-current-discharge regime for 1.0, 2.0, 4.0, and 8.0 C-rates. Figure 6a shows the predicted voltage profiles as a function of time, while in Fig. 6b the battery voltage is plotted against the extracted charge, the integral in time of the current that flows across the battery.

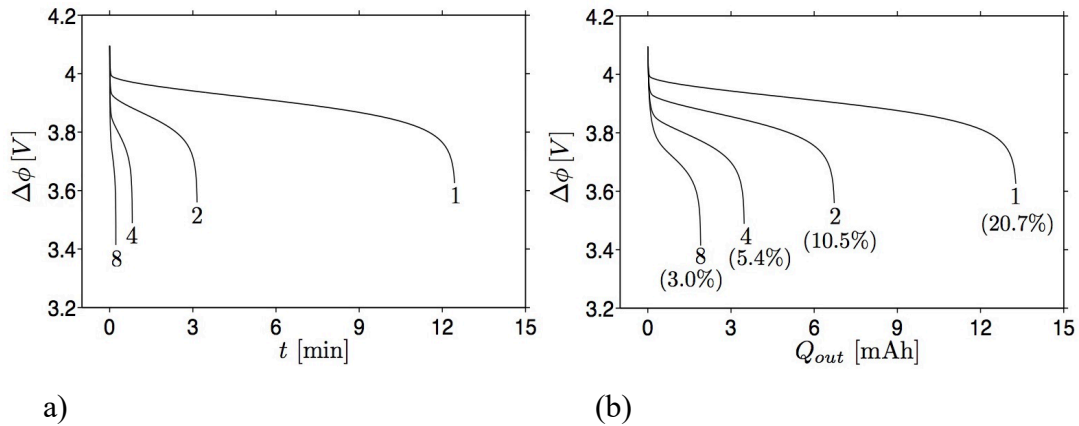


Figure 5.6: a) Simulated voltage profiles of the planar battery during constant-current-discharging at C-rates=1.0, 2.0, 4.0, and 8.0. In (b) is reported the ratio of extracted charge at the end of the extraction process over the theoretical capacity of the battery 64 mAh.

Independently on the discharging rate, the voltage profiles show three distinct phases: at first the voltage drops sharply, then the discharge proceeds showing a gently

sloped voltage, finally the discharging ends after another sudden voltage drop. It is worth nothing that here we do not make use of experimental OCP as carried out in many numerical works, instead the surface OCP appearing in the Butler-Volmer equation is related to the ideal chemical potential of Li ions dissolved in the electrodes as showed in Eq. (23). Therefore, we would rather discuss the numerical outcomes in view of the model assumptions, focusing on the role played by the morphology of the electrodes, than aim to experimental measurements. As expected, the battery voltage is highly dependent on the discharging rate. Indeed, the operating voltage attains lower values for higher discharging rate as a result of higher battery overpotentials. The amount of extracted charge is dependent on the discharge rate as well (see. Fig. 6b): the higher the discharge rate, the less the extracted charge. For quantitative comparisons, the ratio between the simulated extracted charge and the theoretical one is reported in Fig. 6b. This percentage can be regarded as a measure of the efficiency of the battery. For the planar geometry, the battery performance at 8.0 C-rate is very bad, since only 3% of the theoretical capacity is used. Note that even for 1 C-rate the amount of extracted charge is only about 20% of the theoretical availability. The chemo-mechanical response - Figure 7a plots the evolution in time of Li ions the battery at 1.0 C-rate discharging. During discharging, the lithium ions intercalate into the positive electrode ( $\text{LiCoO}_2$ ) and de-intercalate from the anode ( $\text{LiC}_6$ ). In this way the concentration of lithium progressively increases in the cathode, accumulating near the electrolyte, while the contrary happens in the negative electrode. The simulation ends after 12.5 minutes, when lithium in the cathode reaches its saturation limit in correspondence of cathode ( $c_{max}^{Li} = 2.39 \times 10^4 \text{ mol/m}^3$ ). Indeed, further current, in the prescribed regime, is prevented by saturation of lithium in the positive electrode. The latter is thus the limiting factor for the performance of this Li-ion battery.



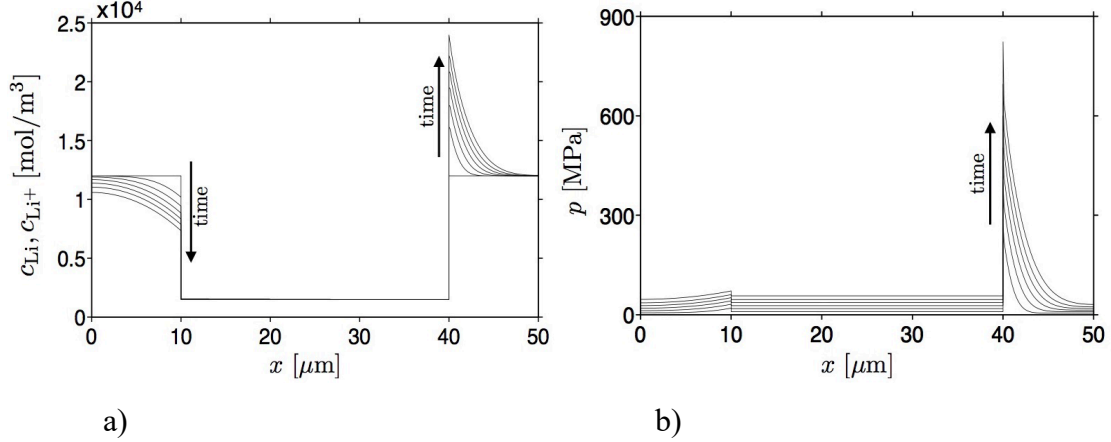


Figure 5.7: Lithium concentration (a) and hydrostatic pressure (b) in the planar battery as a function of  $x$  coordinate at time  $t=0, 2, 4, 6, 8, 12$  minutes, and at the end of the process for 1.0 C-rate discharging.

Owing to the much higher diffusivity of lithium ions in liquid electrolytes, the profile of Li ions is essentially flat in the separator. The overall amount of Li ions dissolved in the electrolyte is conserved since lithium is consumed at  $\Gamma_{ca}$  with the same velocity as it is generated at  $\Gamma_{an}$ , and charge remains balanced. Figure 5.7b depicts the simulated mechanical response in terms of hydrostatic pressure, i.e.,  $p = \frac{1}{3} \text{tr} [\sigma]$ . Since no external forces are prescribed on the battery case, the stress evolution is triggered by the volumetric strain induced by lithium intercalation and de-intercalation in the electrodes. The electrolyte acts passively by contrasting the volume change in the electrodes with its mechanical stiffness. As shown in Fig. 5.7b, the pressure, zero at initial time, increases with time in each component of the battery. On one hand,  $p$  is essentially uniform in the separator with magnitude smaller than 100 Mpa. On the other, the stress distribution is not uniform in the electrodes and attains its maximum value at interface  $\Gamma_{ca}$ . The pressure is positive, i.e., tensile, in both positive and negative electrodes because of the value of parameters  $\omega_{Li}$ . In fact, from experimental evidence, both  $\text{LiC}_6$  and  $\text{LiCoO}_2$  shrink upon de-lithiation and lithiation respectively. The numerical results show that the chemo-mechanical coupling influences the duration of the discharging process, and consequently, the amount of extracted charge at the end of the process. This relies on the definition of the chemical potential in Eq. (14), from which the stress state influences the transport of lithium and the surface OCP in the Butler-Volmer equation (see Equations (15)-(29)).

Therefore, based on these outcomes, the mechanics of intercalating electrodes highly impact the operating voltage of Li-ion batteries, and cannot be considered to be negligible.

### 5.3.2 The Impact of Cathode Morphology

In this section, electro-chemo-mechanical response of the battery is evaluated. The positive electrode  $\text{LiCoO}_2$  is assumed to have a comb-like morphology which was explained in detail on the previous section. This morphological change impact on the amount of surface of the cathode in contact with the electrolyte, accordingly the electrochemical charge transfer reaction takes place on a greater surface than the one of the planar batteries simulated in Section 5.1. However, as it is mentioned in Section 3.2, this morphological change does not affect the overall area of active material, so that the theoretical capacity of the battery is independent on the shape of the cathode.

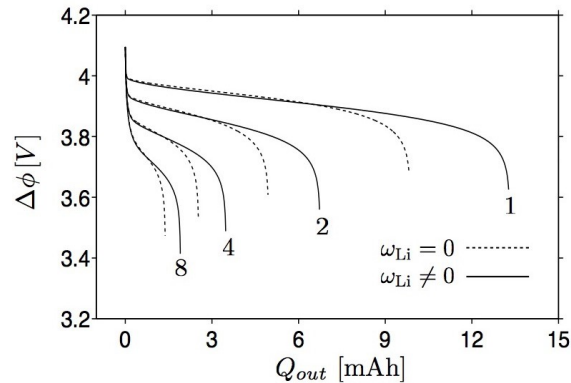


Figure 5.8: Comparison between the simulated voltages in the planar battery obtained through fully coupled chemo-mechanical analysis ( $\omega_{\text{Li}} \neq 0$ ), and by neglecting the mechanical effects ( $\omega_{\text{Li}} = 0$ ). The battery has been simulated upon constant-current-discharging at 1.0, 2.0, 4.0, 8.0 C-rates.

*The battery voltage* - Figure 5.9 depicts the simulated voltage of the battery for different cathode morphology, e.g.,  $n =$  from 1 to 15. A constant current discharge process is considered for each analysis. For both C-rates 1 and 8, the higher number of combs results with higher operating voltage of the battery. Hence, the available surface for lithium intercalation on the positive electrode affects the battery overpotential i.e., the energetic dissipation associated with battery functioning. Accordingly, the amount of extracted charge is impacted by the number of additional combs. For instance, the increment of the

battery efficiency can be seen clearly with number of combs is equal to 2 with respect to planar battery ( $n=0$ , as a reference). With regard to C-rate 1, the efficiency of battery retains increasing gradually up to comb number 9 in terms of extracted charged. While  $n=10,12,15$  respectively, the capacity of the battery remains steady 76.56%. The similar outcomes are observed for C-rate8 under the same conditions. Even though, the performance of battery increases within the number of combs, in comparison to C-rate1, the extracted charged of the theoretical capacity is fairly below.

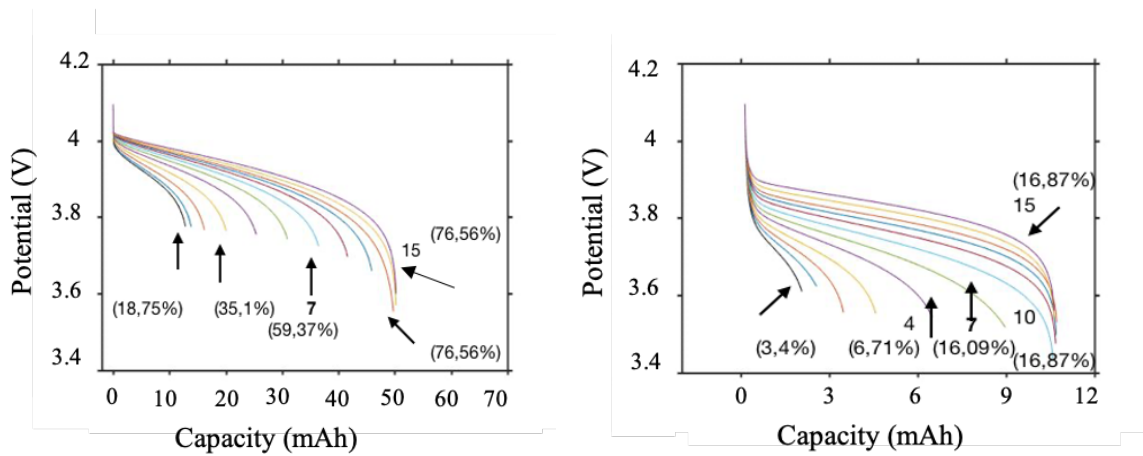


Figure 5.9: Impact of cathode morphology on the simulated voltage for 1.0 (a) and 8.0 (b) C-rate discharging. Each voltage profile is labelled by the integer  $n$ , i.e., the constant that identifies the shape of cathode. The battery efficiency, reported in parenthesis, is computed as the ratio between the extracted charge at the end of the discharging and the theoretical capacity.

*The chemo-mechanical response* -The effect of the cathode morphology on lithium concentration is evaluated at C-rate1 for combs numbers 1 and 10. As expected, the higher available surface area for the electrochemical reaction, the more uniform lithium distribution on the positive electrode. For  $n=1$ , the lithium dissolved in the cathode is concentrated near the surface between electrolyte. The lithium profile on the anode follows the same profile as the reference battery ( $n=0$ ). The battery discharging ends due to the saturation limit on the cathode interface  $\Gamma_{ca}$ . Hence, similar to the planar battery configuration for one comb, cathode is still the limiting factor for performance of the battery. The almost identical results are obtained with  $n=2,3,4$ : the voltage cut-off is caused by the saturation of lithium on the positive electrode.

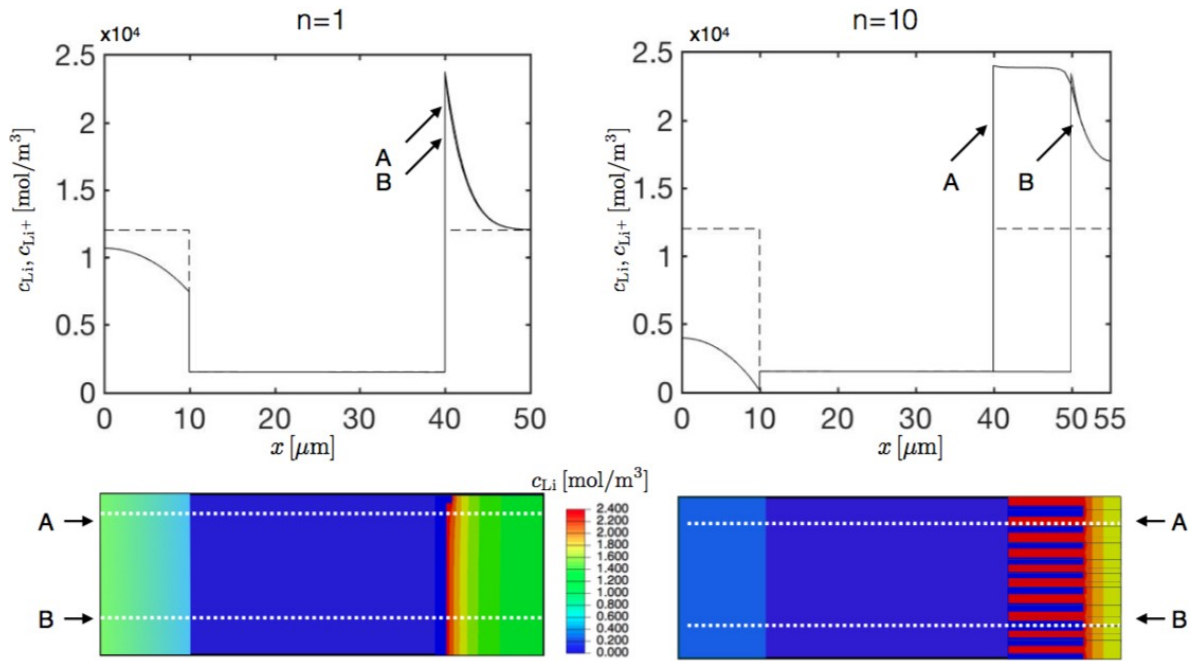


Figure 5.10: Comparison between the lithium distribution in the battery at the end of 1.0 C-rate discharging for cathode morphologies  $n = 1$  and  $n = 10$ .

In the cases of  $n > 4$ , the situation has been changing as it is showed on Figure 10, while the number of combs is equal to 10. Differently from the case with  $n = 1$ , lithium does not saturate in any point of the positive electrode at the end of the discharging thus, cathode does not affect the end of the discharge process. Accordingly, the  $\text{LiC}_6$  is the limiting factor for the battery  $n=10$  at C-rate1. The discharging is induced by the depletion of lithium on the anode at  $\Gamma_{\text{an}}$ . Thus, the further current flow of current is prevented in the Li-ion battery.

### 5.3.3 Changing the morphology of both electrodes

In this section, the battery response is simulated by comb-like geometry for both anode and cathode. A schematic representation of the simulated battery geometries is reported in Figure xx. Note that in each battery configuration, the electrode morphology is the same for both electrodes. Akin to previous example, the battery geometry is defined by the number of combs with respect to  $n$  which is depicted on 3.

*The battery voltage* - Battery response- 12 demonstrates the simulated battery voltage for different number of combs under constant current regimes for 1.0 and 8.0 C-rates. As resulted in former section, the operating battery voltage increases with the number of combs. The battery morphology impacts on the amount of the extracted charge in a similar way: the higher comb number, the higher the efficiency of the battery. At 1.0 C-rate, while the comb number is higher than 6, the efficiency of the battery exceeds 50%. Furthermore, over 90% efficiency has been obtained with 15 combs.

With regard to comparison between 1.0 and 8.0 C-rate discharging, the simulated voltage highly depends on the applied discharge rate at the certain number of combs on the electrodes. For instance, the impact is clear while only one comb is applied, the efficiency is 18.75% and 4.68% respectively. This dissimilarity diminishes within the increment on the comb number thus, the extracted charge does not vary remarkably. In accordance with the results on Figure xx, the efficiency of battery cannot be evaluated solely by either the number of combs. The striking impact of the morphology on discharge rate seen clearly while,  $n = 6$ . The usable capacity of the battery is around 50% at 1.0 C-rate, whereas at 8.0 C-rate only 15% can be achieved.

*The chemo-mechanical response* - The impact of the battery geometry on lithium concentration is depicted on Figure 5.12. Similar to previous example, increment on the surface area of the electrodes results much more uniform lithium concentration on cathode. Due to high number of on the cathode, the discharge is ruled by the depletion of the lithium on the anode at  $\Gamma_{an}$  at 1.0 C-rate. Thus, the presentation of the comb on the anode restrains this phenomenon. While the number of combs is equal to 10 at two different c-rates, the impact of the geometry is seen utterly. At 1.0 C-rate, on the cathode, the lithium concentration remains uniform on point A, whereas, on point B there is a sharp decrease after the saturation point. At the high C-rate, the main difference is the slight concentration decrease after the saturation point on the cathode. Therefore, lithium concentration on  $\Gamma_{an}$  is the primary parameter for the cut-off of the battery. The importance of the geometry raises with the high C-rates. The optimal conditions can be reached by 19 number of combs in terms of the lithium concentration with respect to time. Due to the reaction kinetics, on  $\Gamma_{ca}$  the saturation limit has reached, and, on the cathode, the lithium concentration is flat as desirable. Within the escalation of the comb number, the concentration of the lithium on

$\Gamma_{an}$  is greatly low but not zero, on the  $\Gamma_{ca}$  after the saturation limit, the lithium diffusion is enhanced gradually and at 19, it reaches the optimal state. Theoretically, the increment on comb number leads to the smooth lithium concentration over the discharge and the intercalation reaction on the boundary. With regard to the very thin and long combs on the electrodes, convergence issues occur, and the realism cannot be captured. Hence, the comparison has done with the 15 combs.

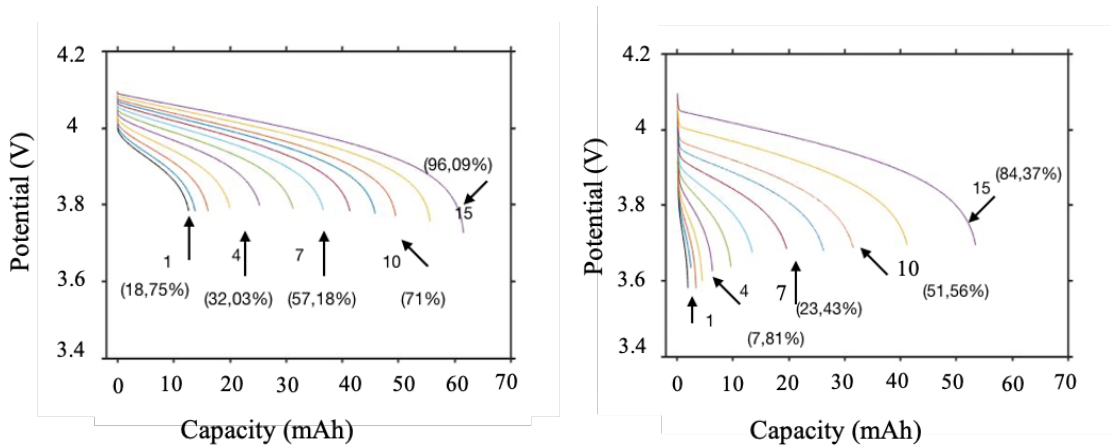


Figure 5.11: Impact of battery morphology on the simulated voltage for 1.0 (a) and 8.0 (b) C-rate discharging. Each voltage profile is labelled by the integer  $n$ , i.e. the constant that identifies the shape of the electrodes. The battery efficiency, reported in parenthesis, is computed as the ratio between the extracted charge at the end of the discharging and the theoretical capacity.

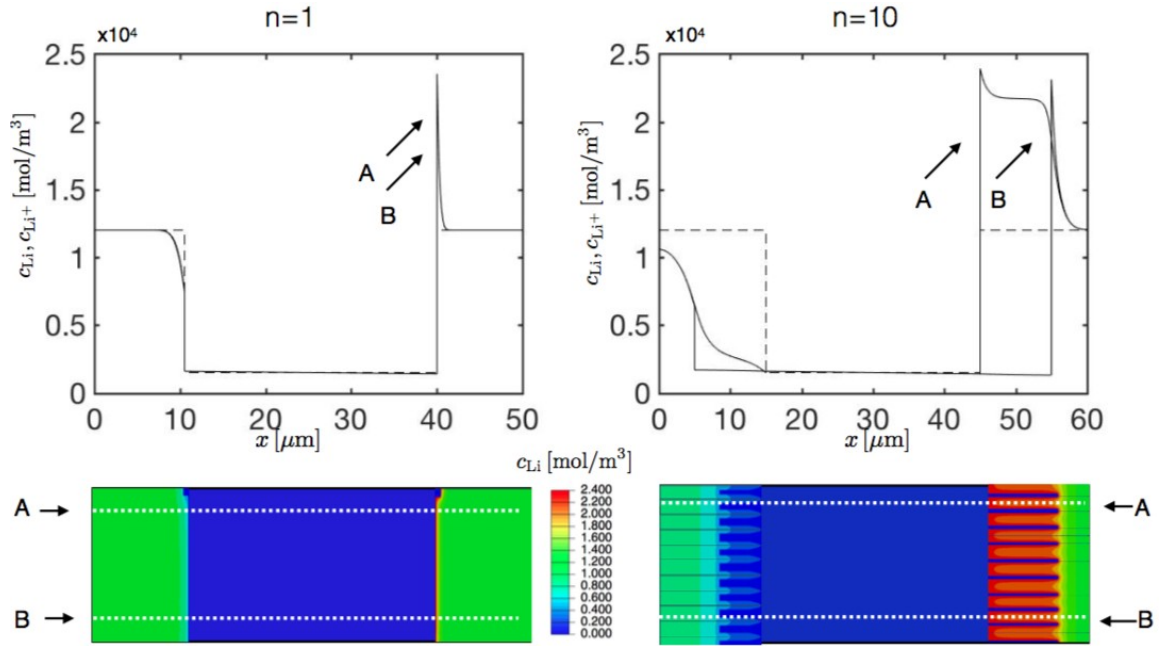


Figure 5.12: Comparison between the lithium distribution in the battery at the end of 8.0 C-rate discharging process for battery morphologies  $n = 1$  and  $n = 10$ .

## 5.4 Conclusion

In this study, the effect of electrode structure has been investigated lithium-ion battery via thermo-chemo-mechanical coupled conventional lithium-ion battery. With the modification of the  $\text{LiCoO}_2$  cathode, the discharge capacity of the battery has improved by the time escalating the number of combs. Using high number of combs resulted a change in the limiting factor on lithium concentration. The depletion on anode has become the limiting factor interestingly. In order to prevent this, the modifying the anode side is crucial. Therefore, using modified electrodes has improved the battery exceedingly. The battery performance is increased up to 80% at high C-rates, 60 mAh respectively. Despite the fact that it is a numerical study, we show that improving the surface area of the electrode could influence the battery performance significantly. This unique model is going to be expanded with different electrolyte applications.

## 6. Summary and Outlook

This work discussed an investigation of transport properties of gel polymer electrolytes with free and bonded ions, beginning with an experimental investigation of ionic conductivity and transference number and later the modelling of these systems. Chapter 2 focused on electrolyte which are made of poly(ethylene glycol)diacrylate backbone with sodium styrene sulfonate ionomer. A series of cross-linked PEGDA-SS films were synthesized with varying EO=Ch ratios. By changing the EO=Ch ratio, we aimed to investigate the differences in transport properties due to varying anion content/dissociability. Furthermore, with the addition of liquid electrolyte, how the transport properties change in different EO=Ch ratio were studied. These membranes were further characterized in terms of conductivity, transference number, and electrolyte uptake ability. It is known that the total ionic conductivity relies on the number of charges and the mobility. High charge density PEGDA membranes resulted in low ionic conductivity in solvents which was due to high degrees of ionic aggregates. Thus, it was determined that ion dissociability is highly related to ionic aggregates. The loose  $\text{Li}^+$  coordination is an essential factor in the case of only bonded charges. In the presence of liquid electrolyte, the ionic conductivity of low charge density membranes increased due to both high number of charges and anion mobility. However, high charge density membranes did not show any improvement in terms of ionic conductivity. From the elemental analysis, due to the stiff characteristic of the membranes, liquid electrolyte could not diffuse in the polymer matrix. Consequently, it is understood that the charge density of the membranes is a crucial parameter for transport properties. Further investigations are going on to comprehend the ion states of each EO=Ch ratio in the presence of 1 M LiTFSI (DOL-DME 1:1 v%) and 1 M  $\text{LiPF}_6$  (EC-DEC 1:1 v%).

As a following of the first chapter outcome, another set of crosslinked membranes were synthesized with a slightly different polymer backbone poly(ethylene glycol) dimethacrylate with vinyl sulfonate ionomer. The crosslinked membranes were characterized in the same way with the PEGDA-SS membranes. The transport properties of opaque PEGDMA-VS membrane which had no bonded charges (O-PEGDMA-VS-0) were found highly promising with the addition of liquid electrolyte. The main difference of these from the PEGDA-SS membranes was that there were no bonded charges. The



reason why the high transport properties is related to the nanoporous structure. In Li/LiFePO<sub>4</sub> half cell configuration, the cell showed an exceptional performance in comparison to conventional cell. The further investigations are ongoing to discern the structure properties and the ion transport mechanism.

The rest of the dissertation is devoted to theoretical and simulation studies of polymer electrolytes and investigation of the impact of cathode shape. In chapter 4, a detailed model of single ion conducting polymer electrolyte was discussed. This model was developed based on the experimental evidence from the Chapter 2. A novel set of equations were written to describe the behavior of a PEGDA-SS SIPE membrane with regard to slower and infinitely fast kinetics. In terms of lithium concentration profile, both membranes showed similar behavior with a slight difference on the equilibrium concentration due to the number of charges. On the other hand, the potential profile was found different. The GPE-6 had one order magnitude lower potential than the GPE-20 which was explained with high diffusion coefficient. Following this, the diffusion coefficient was increased to  $1.06 \times 10^{-9} \text{m}^2/\text{s}$  and the equilibrium potential decreased from 0.4 V to  $4 \times 10^{-3} \text{V}$ . Thus, keeping the number charges but increasing the mobility of the membrane resulted with an improvement. Consequently, this model shows that in order to improve the performance of SIPE, either the number of charges should be increased by increasing the dissociability or the mobility of the ion.

Chapter 5 focused on the improving the performance of conventional Li-ion battery by modifying the shape of the electrodes. As it was discussed on the previous chapters, polymer electrolytes with advanced transport properties seem a promising alternative to liquid electrolyte. However, there are still certain challenges to be overcome. In this chapter, the impact of electrodes geometry is then evaluated by simulating the battery response with different electrodes configurations in a fictitious 2D planar conventional lithium-ion battery scheme. A fully thermo-chemo-mechanical coupled model was developed to study the battery response under different electrode shapes and C-rates. It was found that changing only the cathode morphology by adding combs leads to lithium depletion which is the limiting factor for the battery performance. Therefore, at higher C-rate, there was tremendous capacity loss. Modifying the structure of the anode prevented

the depletion of  $\text{Li}^+$  and the battery showed an excellent performance even at very high C-rates.

In addition to completed studies discussed herein, an advanced model for polymer electrolyte (SIPE) with liquid electrolyte is an ongoing project. This model is being developed based on O-PEGDMA-VS-0 membrane and its unique porous structure. A novel set of balance equations were written to describe the transport of ion in these membrane in continuum level. The outcome will be presented in future publications.

## 7. References

1. Harper, G.; Sommerville, R.; Kendrick, E.; Driscoll, L.; Slater, P.; Stolkin, R.; Walton, A.; Christensen, P.; Heidrich, O.; Lambert, S.; Abbott, A.; Ryder, K.; Gaines, L.; Anderson, P., Recycling lithium-ion batteries from electric vehicles. *Nature* **2019**, *575* (7781), 75.
2. Whittingham, M. S., Lithium batteries and cathode materials. *Chemical reviews* **2004**, *104* (10), 4271.
3. Jiangfeng, Q.; Wesley, A. H.; Wu, X.; Priyanka, B.; Mark, E.; Oleg, B.; Ji-Guang, Z., High rate and stable cycling of lithium metal anode. *Nature Communications* **2015**, *6* (1).
4. Obrovac, M. N.; Chevrier, V. L., Alloy negative electrodes for Li-ion batteries. *Chemical reviews* **2014**, *114* (23), 11444.
5. Goodenough, J. B.; Kim, Y., Challenges for Rechargeable Li Batteries †. *Chemistry of Materials* **2010**, *22* (3), 587-603.
6. Li, G.; Monroe, C. W., Multiscale Lithium-Battery Modeling from Materials to Cells. *Annual review of chemical and biomolecular engineering* **2020**.
7. Mogurampelly, S.; Borodin, O.; Ganesan, V., Computer Simulations of Ion Transport in Polymer Electrolyte Membranes. *Annu. Rev. Chem. Biomol. Eng.* **2016**, *7* (1), 349-371.
8. Borodin, O.; Smith, G. D.; Douglas, R., Force field development and MD simulations of poly(ethylene oxide)/LiBF<sub>4</sub> polymer electrolytes. *Journal of Physical Chemistry B* **2003**, *107* (28), 6824-6837.
9. Diddens, D.; Heuer, A.; Borodin, O., Understanding the Lithium Transport within a Rouse-Based Model for a PEO/LiTFSI Polymer Electrolyte. *Macromolecules* **2010**, *43* (4), 2028-2036.
10. Newman, J. S.; Thomas-Alyea, K. E., Electrochemical systems. In *Electrochemical systems*, Hoboken, N.J: Wiley-Interscience: 2004.
11. Doyle, M.; Fuller, T. F.; Newman, J., The importance of the lithium ion transference number in lithium/polymer cells. *Electrochimica Acta* **1994**, *39* (13), 2073-2081.
12. Doyle, M.; Fuller, T. F.; Newman, J., Modeling of Galvanostatic Charge and Discharge of the Lithium/Polymer/Insertion Cell. *Journal of The Electrochemical Society* **1993**, *140* (6), 1526.
13. Fuller, T. F.; Doyle, M.; Newman, J., Simulation and optimization of the dual lithium ion insertion cell. *Journal of the Electrochemical Society* **1994**, *141* (1).
14. Hofmann, T.; Westhoff, D.; Feinauer, J.; Andrä, H.; Zausch, J.; Schmidt, V.; Müller, R., Electro-chemo-mechanical simulation for lithium ion batteries across the scales. *International Journal of Solids and Structures* **2020**, *184*, 24-39.
15. Newman, J.; Chapman, T. W., Restricted diffusion in binary solutions. *AIChE Journal* **1973**, *19* (2), 343-348.
16. Hage, D. S.; Reference Module in Chemistry, Molecular Sciences and Chemical Engineering. *Choice Reviews Online* **2014**, *51* (12), 51-6506-51-6506.
17. Diederichsen, K. M.; McShane, E. J.; McCloskey, B. D., Promising Routes to a High Li<sup>+</sup> Transference Number Electrolyte for Lithium Ion Batteries. *ACS Energy Letters* **2017**, *2* (11), 2563-2575.

18. Valoén, L. O.; Reimers, J. N., Transport Properties of LiPF<sub>6</sub>-Based Li-Ion Battery Electrolytes. *Journal of The Electrochemical Society* **2005**, *152* (5), A882.
19. Ehrl, A.; Landesfeind, J.; Wall, W. A.; Gasteiger, H. A., Determination of Transport Parameters in Liquid Binary Lithium Ion Battery Electrolytes. *Journal of The Electrochemical Society* **2017**, *164* (4), A826.
20. Richardson, G. W.; Foster, J. M.; Ranom, R.; Please, C. P.; Ramos, A. M., Charge transport modelling of lithium ion batteries. **2020**.
21. Georén, P.; Lindbergh, G., Characterisation and modelling of the transport properties in lithium battery polymer electrolytes. *Electrochimica Acta* **2001**, *47* (4), 577-587.
22. Eurandom; Energy Materials and, D.; Electromechanics and Power, E.; Danilov, D.; Niessen, R. A. H.; Notten, P. H. L., Modeling all-solid-state Li-ion batteries. *Journal of the Electrochemical Society* **2011**, *158* (3), A215-A222.
23. Rajmakers, L. H. J.; Danilov, D. L.; Eichel, R. A.; Notten, P. H. L., An advanced all-solid-state Li-ion battery model. *Electrochimica acta* **2020**, 330.
24. Fabre, S. D.; Guy-Bouyssou, D.; Bouillon, P.; Le Cras, F.; Delacourt, C., Charge/Discharge Simulation of an All-Solid-State Thin-Film Battery Using a One-Dimensional Model. *Journal of The Electrochemical Society* **2011**, *159* (2), A104-A115.
25. Bates, A.; Mukherjee, S.; Schuppert, N.; Son, B.; Kim, J. G.; Park, S., Modeling and simulation of 2D lithium-ion solid state battery. *International Journal of Energy Research* **2015**, *39* (11), 1505-1518.
26. Teichert, K.; Oldham, K., Modeling Cyclic Capacitive Loading of Thin-Film Batteries. *Journal of The Electrochemical Society* **2017**, *164* (2), A360-A369.
27. Grazioli, D.; Verners, O.; Zadin, V.; Brandell, D.; Simone, A., Electrochemical-mechanical modeling of solid polymer electrolytes: Impact of mechanical stresses on Li-ion battery performance. *Electrochimica Acta* **2019**, *296*, 1122-1141.
28. Haftbaradaran, H.; Song, J.; Curtin, W. A.; Gao, H., Continuum and atomistic models of strongly coupled diffusion, stress, and solute concentration. *Journal of power sources* **2011**, *196* (1), 361-370.
29. Bishop, S., Electro-chemo-mechanics of solids. *Cham : Springer*: **2017**.
30. Zhao, Y.; Stein, P.; Bai, Y.; Al-Siraj, M.; Yang, Y.; Xu, B.-X., A review on modeling of electro-chemo-mechanics in lithium-ion batteries. *Journal of power sources* **2019**, *413*, 259-283.
31. Faliya, K.; Kliem, H., Charge distributions in poly(ethylene oxide)-based electrolytes for lithium-ion batteries. *Electrochimica Acta* **2018**, *290*, 211-219.
32. Svanberg, C.; Adebahr, J.; Ericson, H.; Börjesson, L.; Torell, L. M.; Scrosati, B., Diffusive and segmental dynamics in polymer gel electrolytes. *The Journal of Chemical Physics* **1999**, *111* (24), 11216-11221.
33. Andersson, D.; Svanberg, C.; Swenson, J.; Howells, W. S.; Börjesson, L., Diffusive dynamics in polymer gel electrolytes investigated by quasi-elastic neutron scattering. *Physica B: Physics of Condensed Matter* **2001**, *301* (1-2), 44-48.
34. Wu, S.-L.; Javier, A. E.; Devaux, D.; Balsara, N. P.; Srinivasan, V., Discharge Characteristics of Lithium Battery Electrodes with a Semiconducting Polymer Studied by Continuum Modeling and Experiment. *Journal of The Electrochemical Society* **2014**, *161* (12), A1836-A1843.

35. Gouverneur, M.; Schmidt, F.; Schnhoff, M., Negative effective Li transference numbers in Li salt/ionic liquid mixtures: does Li drift in the Wrong direction? *Phys. Chem. Chem. Phys.* **2018**, *20* (11), 7470-7478.
36. Kim, H. K.; Balsara, N. P.; Srinivasan, V., Continuum Description of the Role of Negative Transference Numbers on Ion Motion in Polymer Electrolytes. *Journal of the Electrochemical Society* **2020**, *167* (11).
37. Wolff, N.; Röder, F.; Krewer, U., Model Based Assessment of Performance of Lithium-Ion Batteries Using Single Ion Conducting Electrolytes. *Electrochimica Acta* **2018**, *284*, 639-646.
38. Legrand, N.; Raël, S.; Knosp, B.; Hinaje, M.; Desprez, P.; Lopicque, F., Including double-layer capacitance in lithium-ion battery mathematical models. *Journal of Power Sources* **2014**, *251*, 370-378.
39. Finsterbusch, M.; Danner, T.; Tsai, C.-L.; Uhlenbruck, S.; Latz, A.; Guillon, O., High Capacity Garnet-Based All-Solid-State Lithium Batteries: Fabrication and 3D-Microstructure Resolved Modeling. *ACS applied materials & interfaces* **2018**, *10* (26), 22329.
40. Jokar, A.; Rajabloo, B.; Désilets, M.; Lacroix, M., Review of simplified Pseudo-two-Dimensional models of lithium-ion batteries. *Journal of Power Sources* **2016**, *327*, 44-55.
41. Salvadori, A.; Grazioli, D.; Geers, M. G. D.; Danilov, D.; Notten, P. H. L., A multiscale-compatible approach in modeling ionic transport in the electrolyte of (Lithium ion) batteries. *Journal of Power Sources* **2015**, *293* (C), 892-911.
42. Franco, A. A., Multiscale modelling and numerical simulation of rechargeable lithium ion batteries: concepts, methods and challenges. *RSC Adv.* **2013**, *3* (32), 13027-13058.
43. Franco, A. A.; Rucci, A.; Brandell, D.; Frayret, C.; Gaberscek, M.; Jankowski, P.; Johansson, P., Boosting Rechargeable Batteries R&D by Multiscale Modeling: Myth or Reality? *Chem Rev.* **2019**; Vol. 119, p 4569.
44. Arunachalam, H.; Korneev, S.; Battiato, I.; Onori, S., Multiscale modeling approach to determine effective lithium-ion transport properties. *American Control Conference (ACC)*, Seattle, WA **2017**; pp 92-97.
45. Inceoglu, S.; Rojas, A. A.; Devaux, D.; Chen, X. C.; Stone, G. M.; Balsara, N. P., Morphology–Conductivity Relationship of Single-Ion-Conducting Block Copolymer Electrolytes for Lithium Batteries. *ACS Macro Letters* **2014**, *3* (6), 510-514.
46. Zhang, H.; Li, C.; Piszcz, M.; Coxa, E.; Rojo, T.; Rodriguez-Martinez, L. M.; Armand, M.; Zhou, Z., Single lithium-ion conducting solid polymer electrolytes: advances and perspectives. *Chem. Soc. Rev.* **2017**, *46* (3), 797-815.
47. Bouchet, R.; Maria, S.; Meziane, R.; Aboulaich, A.; Lienafa, L.; Bonnet, J.-P.; Phan, T. N. T.; Bertin, D.; Gignes, D.; Devaux, D.; Denoyel, R.; Armand, M., Single-ion BAB triblock copolymers as highly efficient electrolytes for lithium-metal batteries. *Nature Materials* **2013**, *12* (5), 452-457.
48. Ma, Q.; Zhang, H.; Zhou, C.; Zheng, L.; Cheng, P.; Nie, J.; Feng, W.; Hu, Y. S.; Li, H.; Huang, X.; Chen, L.; Armand, M.; Zhou, Z., Single Lithium-Ion Conducting Polymer Electrolytes Based on a Super-Delocalized Polyanion. *Angewandte Chemie International Edition* **2016**, *55* (7), 2521-2525.

49. Piszcz, M.; Garcia-Calvo, O.; Oteo, U.; Lopez Del Amo, J. M.; Li, C.; Rodriguez-Martinez, L. M.; Youcef, H. B.; Lago, N.; Thielen, J.; Armand, M., New Single Ion Conducting Blend Based on PEO and PA-LiTFSI. *Electrochimica Acta* **2017**, *255*, 48-54.
50. Zugmann, S.; Fleischmann, M.; Amereller, M.; Gschwind, R. M.; Wiemhöfer, H. D.; Gores, H. J., Measurement of transference numbers for lithium ion electrolytes via four different methods, a comparative study. *Electrochimica Acta* **2011**, *56* (11), 3926-3933.
51. Yuan, H.; Luan, J.; Yang, Z.; Zhang, J.; Wu, Y.; Lu, Z.; Liu, H., Single Lithium-Ion Conducting Solid Polymer Electrolyte with Superior Electrochemical Stability and Interfacial Compatibility for Solid-State Lithium Metal Batteries. *ACS applied materials & interfaces* **2020**, *12* (6).
52. Tang, S.; Guo, W.; Fu, Y. Z., Advances in Composite Polymer Electrolytes for Lithium Batteries and Beyond. *Advanced Energy Materials*.
53. Zhao, S.; Wu, Q.; Ma, W.; Yang, L., Polyethylene Oxide-Based Composites as Solid-State Polymer Electrolytes for Lithium Metal Batteries: A Mini Review. *Frontiers in Chemistry* **2020**, *8*.
54. Li, S.; Zhang, S. Q.; Shen, L.; Liu, Q.; Ma, J. B.; Lv, W.; He, Y. B.; Yang, Q. H., Progress and Perspective of Ceramic/Polymer Composite Solid Electrolytes for Lithium Batteries. *Advanced Science* **2020**, *7* (5), n/a-n/a.
55. Falco, M.; Castro, L.; Nair, J. R.; Bella, F.; Bardé, F.; Meligrana, G.; Gerbaldi, C., UV-Cross-Linked Composite Polymer Electrolyte for High-Rate, Ambient Temperature Lithium Batteries. *ACS Applied Energy Materials* **2019**, *2* (3), 1600-1607.
56. Zhou, D.; Zhang, M.; Sun, F.; Arlt, T.; Frerichs, J. E.; Dong, K.; Wang, J.; Hilger, A.; Wilde, F.; Kolek, M.; Hansen, M. R.; Bieker, P.; Manke, I.; Stan, M. C.; Winter, M., Performance and behavior of LLZO-based composite polymer electrolyte for lithium metal electrode with high capacity utilization. *Nano energy* **2020**, *77*.
57. Murugan, R.; Thangadurai, V.; Weppner, W., Fast Lithium Ion Conduction in Garnet-Type  $\text{Li}_7\text{La}_3\text{Zr}_2\text{O}_{12}$ . *Angewandte Chemie International Edition* **2007**, *46* (41), 7778-7781.
58. Li, Y.; Zhang, W.; Dou, Q.; Wong, K. W.; Ng, K. M., Correction:  $\text{Li}_7\text{La}_3\text{Zr}_2\text{O}_{12}$  ceramic nanofiber-incorporated composite polymer electrolytes for lithium metal batteries. *Journal of Materials Chemistry A* **2019**, *7* (8), 4190-4190.
59. Bruce, P. G., The A-C Conductivity of Polycrystalline LISICON,  $\text{Li}_{2+2x}\text{Zn}_{1-x}\text{GeO}_4$ , and a Model for Intergranular Constriction Resistances. *Journal of The Electrochemical Society* **1983**, *130* (3), 662.
60. Zhang, Z.; Huang, Y.; Gao, H.; Huang, J.; Li, C.; Liu, P., An all-solid-state lithium battery using the  $\text{Li}_7\text{La}_3\text{Zr}_2\text{O}_{12}$  and  $\text{Li}_{6.7}\text{La}_3\text{Zr}_{1.7}\text{Ta}_{0.3}\text{O}_{12}$  ceramic enhanced polyethylene oxide electrolytes with superior electrochemical performance. *Ceramics international* **2020**, *46* (8), 11397-11405.
61. Peng, X.; Huang, K.; Song, S.; Wu, F.; Xiang, Y.; Zhang, X., Garnet-Polymer Composite Electrolytes with High  $\text{Li}^+$  Conductivity and Transference Number via Well-Fused Grain Boundaries in Microporous Frameworks. *ChemElectroChem* **2020**, *7* (11), 2389-2394.
62. Xie, Z.; Wu, Z.; An, X.; Yue, X.; Xiaokaiti, P.; Yoshida, A.; Abudula, A.; Guan, G., A sandwich-type composite polymer electrolyte for all-solid-state lithium metal

batteries with high areal capacity and cycling stability. *Journal of membrane science* **2020**, 596.

63. Cai, D.; Wang, D.; Chen, Y.; Zhang, S.; Wang, X.; Xia, X.; Tu, J., A highly ion-conductive three-dimensional LLZAO-PEO/LiTFSI solid electrolyte for high-performance solid-state batteries. *Chemical Engineering Journal* **2020**, 394.

64. Subramani, R.; Tseng, Y.-H.; Lee, Y.-L.; Chiu, C.-C.; Hou, S.-S.; Teng, H., High Li<sup>+</sup> transference gel interface between solid-oxide electrolyte and cathode for quasi-solid lithium-ion batteries. *J. Mater. Chem. A* **2019**, 7 (19), 12244-12252.

65. Yang, C.; Liu, B.; Jiang, F.; Zhang, Y.; Xie, H.; Hitz, E.; Hu, L., Garnet/polymer hybrid ion-conducting protective layer for stable lithium metal anode. *Nano Research* **2017**, 10 (12), 4256-4265.

66. Ford, H. O.; Park, B.; Jiang, J. Z.; Seidler, M. E.; Schaefer, J. L., Enhanced Li<sup>+</sup> Conduction within Single-Ion Conducting Polymer Gel Electrolytes via Reduced Cation-Polymer Interaction. *Acs Materials Letters* **2020**, 2 (3), 272-279.

67. Shen, X.; Hua, H.; Li, H.; Li, R.; Hu, T.; Wu, D.; Zhang, P.; Zhao, J., Synthesis and molecular dynamic simulation of a novel single ion conducting gel polymer electrolyte for lithium-ion batteries. *Polymer (Guilford)* **2020**, 201.

68. Deng, K.; Wang, S.; Ren, S.; Han, D.; Xiao, M.; Meng, Y., Network type sp<sup>3</sup> boron-based single-ion conducting polymer electrolytes for lithium ion batteries. *Journal of Power Sources* **2017**, 360, 98-105.

69. Chen, G.; Niu, C.; Liao, X.; Chen, Y.; Shang, W.; Du, J.; Chen, Y., Boron-containing single-ion conducting polymer electrolyte for dendrite-free lithium metal batteries. *Solid State Ionics* **2020**, 349.

70. Chen, Z.; Steinle, D.; Nguyen, H.-D.; Kim, J.-K.; Mayer, A.; Shi, J.; Paillard, E.; Iojoiu, C.; Passerini, S.; Bresser, D., High-energy lithium batteries based on single-ion conducting polymer electrolytes and Li[Ni<sub>0.8</sub>Co<sub>0.1</sub>Mn<sub>0.1</sub>]O<sub>2</sub> cathodes. *Nano energy* **2020**, 77.

71. Zhang, J.; Wang, S.; Han, D.; Xiao, M.; Sun, L.; Meng, Y., Lithium (4-Styrenesulfonyl) (Trifluoromethanesulfonyl) Imide Based Single-ion Polymer Electrolyte with Superior Battery Performance. *Energy Storage Materials* **2019**, 24.

72. Roth, E. P.; Orendorff, C. J., How Electrolytes Influence Battery Safety. *Interface magazine* **2012**, 21 (2), 45-49.

73. Li, L.; Wang, M.; Wang, J.; Ye, F.; Wang, S.; Xu, Y.; Liu, J.; Xu, G.; Zhang, Y.; Zhang, Y.; Yan, C.; Medhekar, N. V.; Liu, M.; Zhang, Y., Asymmetric gel polymer electrolyte with high lithium ion conductivity for dendrite-free lithium metal batteries. *J. Mater. Chem. A* **2020**, 8 (16), 8033-8040.

74. Ma, L.; Nath, P.; Tu, Z.; Tikekar, M.; Archer, L. A., Highly Conductive, Sulfonated, UV-Cross-Linked Separators for Li-S Batteries. *Chemistry of Materials* **2016**, 28 (14), 5147-5154.

75. Ma, L.; Fu, C.; Li, L.; Mayilvahanan, K. S.; Watkins, T.; Perdue, B. R.; Zavadil, K. R.; Helms, B. A., Nanoporous Polymer Films with a High Cation Transference Number Stabilize Lithium Metal Anodes in Light-Weight Batteries for Electrified Transportation. *Nano Letters* **2019**, 19 (2).

76. Wang, Y.; Fu, L.; Shi, L.; Wang, Z.; Zhu, J.; Zhao, Y.; Yuan, S., Gel Polymer Electrolyte with High Li<sup>+</sup> Transference Number Enhancing the Cycling Stability of Lithium Anodes. *ACS applied materials & interfaces* **2019**, 11 (5), 5168.

77. Zhou, J.; Ji, H.; Liu, J.; Qian, T.; Yan, C., A new high ionic conductive gel polymer electrolyte enables highly stable quasi-solid-state lithium sulfur battery. *Energy Storage Materials* **2019**, *22*, 256-264.
78. He, Y.; Wang, J.; Zhang, Y.; Huo, S.; Zeng, D.; Lu, Y.; Liu, Z.; Wang, D.; Cheng, H., Effectively suppressing lithium dendrite growth via an es-LiSPCE single-ion conducting nano fiber membrane. *J. Mater. Chem. A* **2020**, *8* (5), 2518-2528.
79. Du, Z.; Su, Y.; Qu, Y.; Zhao, L.; Jia, X.; Mo, Y.; Yu, F.; Du, J.; Chen, Y., A mechanically robust, biodegradable and high performance cellulose gel membrane as gel polymer electrolyte of lithium-ion battery. *Electrochimica Acta* **2019**, *299*, 19-26.
80. Kou, Z. Y.; Liu, C. J.; Miao, C.; Mei, P.; Yan, X. M.; Xiao, W., High-performance gel polymer electrolytes using P(VDF-HFP) doped with appropriate porous carbon powders as the matrix for lithium-ion batteries. *Ionics* **2020**, *26* (4), 1729-1737.
81. Jie, J.; Liu, Y.; Cong, L.; Zhang, B.; Lu, W.; Zhang, X.; Liu, J.; Xie, H.; Sun, L., High-performance PVDF-HFP based gel polymer electrolyte with a safe solvent in Li metal polymer battery. *Journal of energy chemistry* **2020**, *49*, 80-88.
82. Hao, X.; Wenren, H.; Wang, X.; Xia, X.; Tu, J., A gel polymer electrolyte based on PVDF-HFP modified double polymer matrices via ultraviolet polymerization for lithium-sulfur batteries. *Journal of colloid and interface science* **2020**, *558*, 145-154.
83. Zhao, L.; Fu, J.; Du, Z.; Jia, X.; Qu, Y.; Yu, F.; Du, J.; Chen, Y., High-strength and flexible cellulose/PEG based gel polymer electrolyte with high performance for lithium ion batteries. *Journal of Membrane Science* **2020**, *593*.
84. Kim, D.; Liu, X.; Yu, B.; Mateti, S.; O' Dell, L. A.; Rong, Q.; Chen, Y., Amine-Functionalized Boron Nitride Nanosheets: A New Functional Additive for Robust, Flexible Ion Gel Electrolyte with High Lithium-Ion Transference Number. *Advanced Functional Materials* **2020**, *30* (15), n/a-n/a.
85. Xu, W.; Wang, J.; Ding, F.; Chen, X.; Nasybulin, E.; Zhang, Y.; Zhang, J.-G., Lithium metal anodes for rechargeable batteries. *Energy Environ. Sci.* **2014**, *7* (2), 513-537.
86. Chazalviel, J. N., Electrochemical aspects of the generation of ramified metallic electrodeposits. *Physical Review A* **1990**, *42* (12), 7355-7367.
87. Monroe, C.; Newman, J., Dendrite growth in lithium/polymer systems. A propagation model for liquid electrolytes under galvanostatic conditions. *Journal of the Electrochemical Society* **2002**, *150* (10).
88. Tikekar, M. D.; Archer, L. A.; Koch, D. L., Stabilizing electrodeposition in elastic solid electrolytes containing immobilized anions. *Science Advances* **2016**, *2* (7).
89. Li, L.; Li, S.; Lu, Y., Suppression of dendritic lithium growth in lithium metal-based batteries. *Chem. Commun.* **2018**, *54* (50), 6648-6661.
90. Cheng, X.-B.; Zhang, R.; Zhao, C.-Z.; Zhang, Q., Toward Safe Lithium Metal Anode in Rechargeable Batteries: A Review. *Chemical reviews* **2017**, *117* (15), 10403.
91. Xu, R.; Cheng, X.-B.; Yan, C.; Zhang, X.-Q.; Xiao, Y.; Zhao, C.-Z.; Huang, J.-Q.; Zhang, Q., Artificial Interphases for Highly Stable Lithium Metal Anode. *Matter* **2019**, *1* (2), 317-344.
92. Mukul, D. T.; Snehashis, C.; Zhengyuan, T.; Lynden, A. A., Design principles for electrolytes and interfaces for stable lithium-metal batteries. *Nature Energy* **2016**, *1* (9).



93. Tu, Z.; Choudhury, S.; Zachman, M. J.; Wei, S.; Zhang, K.; Kourkoutis, L. F.; Archer, L. A., Designing Artificial Solid-Electrolyte Interphases for Single-Ion and High-Efficiency Transport in Batteries. *Joule* **2017**, *1* (2), 394-406.
94. Kato, Y.; Hori, S.; Saito, T.; Suzuki, K.; Hirayama, M.; Mitsui, A.; Yonemura, M.; Iba, H.; Kanno, R., High-power all-solid-state batteries using sulfide superionic conductors. *Nature Energy* **2016**, *1* (4).
95. Kreuer, K. D.; Wohlfarth, A.; De Araujo, C. C.; Fuchs, A.; Maier, J., Single Alkaline-Ion (Li<sup>+</sup>, Na<sup>+</sup>) Conductors by Ion Exchange of Proton-Conducting Ionomers and Polyelectrolytes. *ChemPhysChem* **2011**, *12* (14), 2558-2560.
96. Liumin, S.; Yong-Sheng, H.; Hong, L.; Michel, A.; Liquan, C., A new class of Solvent-in-Salt electrolyte for high-energy rechargeable metallic lithium batteries. *Nature Communications* **2013**, *4* (1), 1481.
97. Shah, D. B.; Kim, H. K.; Nguyen, H. Q.; Srinivasan, V.; Balsara, N. P., Comparing Measurements of Limiting Current of Electrolytes with Theoretical Predictions up to the Solubility Limit. *The Journal of Physical Chemistry C* **2019**, *123* (39), 23872-23881.
98. Merrill, L.; Ford, H.; Schaefer, L., Application of Single-Ion Conducting Gel Polymer Electrolytes in Magnesium Batteries. *ACS Appl. Energy Mater.* **2019**, *2*, 9, 6355–6363.
99. Rajput, N. N.; Murugesan, V.; Shin, Y.; Han, K. S.; Lau, K. C.; Chen, J.; Liu, J.; Curtiss, L. A.; Mueller, K. T.; Persson, K. A., Elucidating the Solvation Structure and Dynamics of Lithium Polysulfides Resulting from Competitive Salt and Solvent Interactions. *Chemistry of Materials* **2017**, *29* (8).
100. Wang, F.; Varenne, F.; Ortiz, D.; Pinzio, V.; Mostafavi, M.; Le Caër, S., Degradation of an Ethylene Carbonate/Diethyl Carbonate Mixture by Using Ionizing Radiation. *ChemPhysChem* **2017**, *18* (19), 2799-2806.
101. Fiates, J.; Zhang, Y.; Franco, L. F. M.; Maginn, E. J.; Doubek, G., Impact of anion shape on Li<sup>+</sup> solvation and on transport properties for lithium-air batteries: a molecular dynamics study. *Phys. Chem. Chem. Phys.* **2020**, *22* (28), 15842-15852.
102. Wang, J.-H. H.; Yang, C. H.-C.; Masser, H.; Shiau, H.-S.; O'reilly, M. V.; Winey, K. I.; Runt, J.; Painter, P. C.; Colby, R. H., Ion States and Transport in Styrenesulfonate Methacrylic PEO 9 Random Copolymer Ionomers. *Macromolecules* **2015**, *48* (19), 7273-7285.
103. Cao, C.; Wang, H.; Liu, W.; Liao, X.; Li, L., Nafion membranes as electrolyte and separator for sodium-ion battery. *International journal of hydrogen energy* **2014**, *39* (28), 16110-16115.
104. Yee, R. S. L.; Rozendal, R. A.; Zhang, K.; Ladewig, B. P., Cost effective cation exchange membranes: A review. *Chemical engineering research & design* **2012**, *90* (7), 950-959.
105. Bruce, P. G.; Vincent, C. A., Steady state current flow in solid binary electrolyte cells. *Journal of Electroanalytical Chemistry* **1987**, *225* (1), 1-17.
106. Evans, J.; Vincent, C. A.; Bruce, P. G., Electrochemical measurement of transference numbers in polymer electrolytes. *Polymer (Guilford)* **1987**, *28* (13), 2324-2328.
107. Nguyen, T. Q.; Breitkopf, C., Determination of Diffusion Coefficients Using Impedance Spectroscopy Data. *Journal of The Electrochemical Society* **2018**, *165* (14), E826-E831.

108. Guan, X.; Wu, Q.; Zhang, X.; Guo, X.; Li, C.; Xu, J., In-situ crosslinked single ion gel polymer electrolyte with superior performances for lithium metal batteries. *Chemical Engineering Journal* **2020**, 382.
109. Kawamura, T.; Okada, S.; Yamaki, J.-I., Decomposition reaction of LiPF<sub>6</sub>-based electrolytes for lithium ion cells. *Journal of power sources* **2006**, 156 (2), 547-554.
110. Zhang, Z., Anion Solvation in Carbonate Electrolytes. *Journal of Physical Chemistry. C* **2015**, 119 (49).
111. Lepage, D.; Michot, C.; Liang, G.; Gauthier, M.; Schougaard, S. B., A Soft Chemistry Approach to Coating of LiFePO<sub>4</sub> with a Conducting Polymer. *Angewandte Chemie International Edition* **2011**, 50 (30), 6884-6887.
112. Schaefer, J. L.; Yanga, D. A.; Archer, L. A., High Lithium Transference Number Electrolytes via Creation of 3-Dimensional, Charged, Nanoporous Networks from Dense Functionalized Nanoparticle Composites. *Chemistry of Materials* **2013**, 25 (6), 834-839.
113. Wheatle, B. K.; Lynd, N. A.; Ganesan, V., Effect of Polymer Polarity on Ion Transport: A Competition between Ion Aggregation and Polymer Segmental Dynamics. *ACS Macro Letters* **2018**, 7 (10), 1149-1154.
114. Pignanelli, F.; Romero, M.; Faccio, R.; Mombro, A. W., Experimental and Theoretical Study of Ionic Pair Dissociation in a Lithium Ion-Linear Polyethylenimine-Polyacrylonitrile Blend for Solid Polymer Electrolytes.(Report). *Journal of Physical Chemistry B* **2017**, 121 (27), 6759-6765.
115. Savoie, B. M.; Webb, M. A.; Miller, T. F., Enhancing Cation Diffusion and Suppressing Anion Diffusion via Lewis-Acidic Polymer Electrolytes. *The journal of physical chemistry letters* **2017**, 8 (3), 641.
116. Porcarelli, L.; Shaplov, A. S.; Bella, F.; Nair, J. R.; Mecerreyes, D.; Gerbaldi, C., Single-Ion Conducting Polymer Electrolytes for Lithium Metal Polymer Batteries that Operate at Ambient Temperature. *ACS Energy Letters* **2016**, 1 (4), 678-682.
117. Oh, H.; Xu, K.; Yoo, H. D.; Kim, D. S.; Chanthad, C.; Yang, G.; Jin, J.; Ayhan, I. A.; Oh, S. M.; Wang, Q., Poly(arylene ether)-Based Single-Ion Conductors for Lithium-Ion Batteries. *Chemistry of Materials* **2016**, 28 (1), 188-196.
118. Doyle, M.; Lewittes, M. E.; Roelofs, M. G.; Perush, S. A., Ionic conductivity of nonaqueous solvent-swollen ionomer membranes based on fluorosulfonate, fluorocarboxylate, and sulfonate fixed ion groups. *Journal of Physical Chemistry B* **2001**, 105 (39), 9387-9394.
119. Qi, X.; Blizanac, B.; Dupasquier, A.; Meister, P.; Placke, T.; Oljaca, M.; Li, J.; Winter, M., Investigation of PF<sub>6</sub> and TFSI anion intercalation into graphitized carbon blacks and its influence on high voltage lithium ion batteries. *Phys. Chem. Chem. Phys.* **2014**, 16 (46), 25306-25313.
120. Matsuda, Y.; Morita, M.; Yamashita, T., Conductivity of the LiBF<sub>4</sub>/mixed ether electrolytes for secondary lithium cells. *J. Electrochem. Soc.; (United States)* **1984**, 131 (12).
121. Every, H. A.; Zhou, F.; Forsyth, M.; Macfarlane, D. R., Lithium ion mobility in poly(vinyl alcohol) based polymer electrolytes as determined by <sup>7</sup>Li NMR spectroscopy. *Electrochimica acta* **1998**, 43 (10-11), 1465-1469.
122. Austen Angell, C., Concepts and conflicts in polymer electrolytes: The search for ion mobility. *Electrochimica acta* **2019**, 313 (C), 205-210.

123. Christian, H.; Dipan, K., Development of Hierarchically Porous Ionomer Membranes for Versatile and Fast Metal Ion Conduction. *ACS Omega* **2019**, *4* (2), 2684-2692.
124. Jang, E. K.; Ahn, J.; Yoon, S.; Cho, K. Y., High Dielectric, Robust Composite Protective Layer for Dendrite-Free and LiPF<sub>6</sub> Degradation-Free Lithium Metal Anode. *Advanced Functional Materials* **2019**, *29* (48), n/a-n/a.
125. Needham, S. A.; Wang, G. X.; Liu, H. K.; Drozd, V. A.; Liu, R. S., Synthesis and electrochemical performance of doped LiCoO<sub>2</sub> materials. *Journal of power sources* **2007**, *174* (2), 828-831.
126. Tarascon, J. M.; Armand, M., Issues and challenges facing rechargeable lithium batteries. *Nature* **2001**, *414* (6861), 359.
127. Scrosati, B.; Garche, J., Lithium batteries: Status, prospects and future. *Journal of power sources* **2010**, *195* (9), 2419-2430.
128. Salvadori, A.; Grazioli, D., Computer simulation for battery design and lifetime prediction. *Advances in Battery Technologies for Electric Vehicles* **2015**, (80), 417-442.
129. Doerffel, D.; Abu Sharkh, S., A critical review of using the Peukert equation for determining the remaining capacity of lead-acid and lithium-ion batteries. *Journal of Power Sources* **2006**, *155* (2), 395-400.
130. Von Srbik, M.-T.; Marinescu, M.; Martinez-Botas, R. F.; Offer, G. J., A physically meaningful equivalent circuit network model of a lithium-ion battery accounting for local electrochemical and thermal behaviour, variable double layer capacitance and degradation. *Journal of power sources* **2016**, *325*, 171-184.
131. Widanage, W. D.; Barai, A.; Chouchelamane, G. H.; Uddin, K.; McGordon, A.; Marco, J.; Jennings, P., Design and use of multisine signals for Li-ion battery equivalent circuit modelling. Part 2: Model estimation. *Journal of power sources* **2016**, *324* (C), 61-69.
132. Ramadesigan, V.; Northrop, P. W. C.; De, S.; Santhanagopalan, S.; Braatz, R. D.; Subramanian, V. R., Modeling and Simulation of Lithium-Ion Batteries from a Systems Engineering Perspective. *Journal of the Electrochemical Society* **2012**, *159* (3).
133. Xing, L.; Vatamanu, J.; Borodin, O.; Smith, G. D.; Bedrov, D., Electrode/Electrolyte Interface in Sulfolane-Based Electrolytes for Li Ion Batteries: A Molecular Dynamics Simulation Study. *The Journal of Physical Chemistry C* **2012**, *116* (45), 23871-23881.
134. Ngandjong, A. C.; Rucci, A.; Maiza, M.; Shukla, G.; Vazquez-Arenas, J.; Franco, A. A., Multiscale Simulation Platform Linking Lithium Ion Battery Electrode Fabrication Process with Performance at the Cell Level. *The journal of physical chemistry letters* **2017**, *8* (23), 5966.
135. Röder, F.; Braatz, R. D.; Krewer, U., Multi-Scale Simulation of Heterogeneous Surface Film Growth Mechanisms in Lithium-Ion Batteries. *Journal of The Electrochemical Society* **2017**, *164* (11), E3335-E3344.
136. Mazur, P.; Groot, S. R. d., *Non-equilibrium thermodynamics*. Dover ed. ed.; New York : Dover Publications: **1984**.
137. Fried, E.; Anand, L.; Gurtin, M. E., *The mechanics and thermodynamics of continua*. New York : Cambridge University Press: **2010**.

138. Miller, R. E.; Elliott, R. S.; Tadmor, E. B., *Continuum mechanics and thermodynamics : from fundamental concepts to governing equations*. Cambridge, UK ; New York : Cambridge University Press: **2012**.
139. Aikens, D. A., Electrochemical methods, fundamentals and applications. *Journal of Chemical Education* **1983**, *60* (1), A25.
140. Bower, A. F.; Guduru, P. R.; Sethuraman, V. A., A finite strain model of stress, diffusion, plastic flow, and electrochemical reactions in a lithium-ion half-cell. *Journal of the mechanics and physics of solids* **2011**, *59* (4), 804-828.
141. Bower, A. F.; Guduru, P. R.; Chason, E., Analytical solutions for composition and stress in spherical elastic-plastic lithium-ion electrode particles containing a propagating phase boundary. *International journal of solids and structures* **2015**, *69-70* (C), 328-342.
142. Hutzenlaub, T.; Asthana, A.; Becker, J.; Wheeler, D. R.; Zengerle, R.; Thiele, S., FIB/SEM-based calculation of tortuosity in a porous LiCoO<sub>2</sub> cathode for a Li-ion battery. *Electrochemistry Communications* **2013**, *27*, 77-80.
143. Jiang, K.-c.; Xin, S.; Lee, J.-s.; Kim, J.; Xiao, X.-l.; Guo, Y.-g., Improved kinetics of LiNi<sup>1/3</sup>Mn<sup>1/3</sup>Co<sup>1/3</sup>O<sub>2</sub> cathode material through reduced graphene oxide networks. *Phys. Chem. Chem. Phys.* **2012**, *14* (8), 2934-2939.
144. Paulus, A.; Hendrickx, M.; Bercx, M.; Karakulina, O. M.; Kirsanova, M. A.; Lamoen, D.; Hadermann, J.; Abakumov, A. M.; Van Bael, M. K.; Hardy, A., An in-depth study of Sn substitution in Li-rich/Mn-rich NMC as a cathode material for Li-ion batteries. *Dalton Trans.* **2020**, *49* (30), 10486-10497.
145. Zeng, Z.; Liang, W.-I.; Liao, H.-G.; Xin, H. L.; Chu, Y.-H.; Zheng, H., Visualization of electrode-electrolyte interfaces in LiPF<sub>6</sub>/EC/DEC electrolyte for lithium ion batteries via in situ TEM. *Nano letters* **2014**, *14* (4), 1745.
146. Flamme, B.; Rodriguez Garcia, G.; Weil, M.; Haddad, M.; Phansavath, P.; Ratovelomanana-Vidal, V.; Chagnes, A., Guidelines to design organic electrolytes for lithium-ion batteries: environmental impact, physicochemical and electrochemical properties. *Green Chem.* **2017**, *19* (8), 1828-1849.
147. Xu, K., Nonaqueous liquid electrolytes for lithium-based rechargeable batteries. *Chemical reviews* **2004**, *104* (10), 4303.
148. Zhang, S. S., A review on electrolyte additives for lithium-ion batteries. *Journal of power sources* **2006**, *162* (2), 1379-1394.
149. Wang, Q.; Jiang, L.; Yu, Y.; Sun, J., Progress of enhancing the safety of lithium ion battery from the electrolyte aspect. *Nano energy* **2019**, *55*, 93-114.
150. Liu, K.; Liu, Y.; Lin, D.; Pei, A.; Cui, Y., Materials for lithium-ion battery safety. *Science Advances* **2018**, *4* (6).
151. Mykhaylov, M.; Ganser, M.; Klinsmann, M.; Hildebrand, F. E.; Guz, I.; McMeeking, R. M., An elementary 1-dimensional model for a solid state lithium-ion battery with a single ion conductor electrolyte and a lithium metal negative electrode. *Journal of the mechanics and physics of solids* **2019**, *123*, 207-221.
152. Richardson, G.; Foster, J. M.; Sethurajan, A. K.; Krachkovskiy, S. A.; Halalay, I. C.; Goward, G. R.; Protas, B., The Effect of Ionic Aggregates on the Transport of Charged Species in Lithium Electrolyte Solutions. *Journal of The Electrochemical Society* **2018**, *165* (9), H561-H567.

153. Dou, S.; Zhang, S.; Klein, R. J.; Runt, J.; Colby, R. H., Synthesis and Characterization of Poly(Ethylene Glycol)-Based Single-Ion Conductors. *Chemistry of Materials* **2006**, *18* (18), 4288-4295.
154. Salvadori, A.; Grazioli, D.; Geers, M. G. D., Governing equations for a two-scale analysis of Li-ion battery cells. *International journal of solids and structures* **2015**, *59* (11), 90-109.
155. Salvadori, A.; Grazioli, D.; Magri, M.; Geers, M. G. D.; Danilov, D.; Notten, P. H. L., On the role of saturation in modeling ionic transport in the electrolyte of (Lithium ion) batteries. *Journal of power sources* **2015**, *294*, 696-710.
156. Alonso, A.; Valli, A., A domain decomposition approach for heterogeneous time-harmonic Maxwell equations. *Computer methods in applied mechanics and engineering* **1997**, *143* (1-2), 97-112.
157. Nishikawa, K.; Fukunaka, Y.; Sakka, T.; Ogata, Y. H.; Selman, J. R., Measurement of LiClO<sub>4</sub> Diffusion Coefficient in Propylene Carbonate by Moiré Pattern. *Journal of The Electrochemical Society* **2006**, *153* (5), A830.
158. Grazioli, D.; Magri, M.; Salvadori, A., Computational modeling of Li-ion batteries. *Solids, Fluids, Structures, Fluid-Structure Interactions, Biomechanics, Micromechanics, Multiscale Mechanics, Materials, Constitutive Modeling, Nonlinear Mechanics, Aerodynamics* **2016**, *58* (6), 889-909.
159. Scrosati, B., High Energy Density Lithium Batteries. Materials, Engineering, Applications. Herausgegeben von Katerina E. Aifantis, Stephen A. Hackney und R. Vasant Kumar. *Angewandte Chemie* **2011**, *123* (23), 5362-5363.
160. Bangerth, W.; Hartmann, R.; Kanschat, G., deal.II-A general-purpose object-oriented finite element library. *ACM Transactions on Mathematical Software (TOMS)* **2007**, *33* (4), 24-es.
161. Arora, P., Capacity Fade Mechanisms and Side Reactions in Lithium-Ion Batteries. *Journal of The Electrochemical Society* **1998**, *145* (10), 3647.
162. Ning, G.; Haran, B.; Popov, B. N., Capacity fade study of lithium-ion batteries cycled at high discharge rates. *Journal of power sources* **2003**, *117* (1-2), 160-169.
163. Vetter, J.; Novák, P.; Wagner, M. R.; Veit, C.; Möller, K. C.; Besenhard, J. O.; Winter, M.; Wohlfahrt-Mehrens, M.; Vogler, C.; Hammouche, A., Ageing mechanisms in lithium-ion batteries. *Journal of power sources* **2005**, *147* (1), 269-281.
164. An, S. J.; Li, J.; Daniel, C.; Mohanty, D.; Nagpure, S.; Wood, D. L., The state of understanding of the lithium-ion-battery graphite solid electrolyte interphase (SEI) and its relationship to formation cycling. *Carbon (New York)* **2016**, *105*, 52-76.
165. Newman, J.; Thomas, K. E.; Hafezi, H.; Wheeler, D. R., Modeling of lithium-ion batteries. *Journal of power sources* **2003**, *119-121*, 838-843.
166. Salvadori, A.; McMeeking, R.; Grazioli, D.; Magri, M., A coupled model of transport-reaction-mechanics with trapping. Part I – Small strain analysis. *Journal of the Mechanics and Physics of Solids* **2018**, *114*, urn:issn:0022-5096.
167. Dreyer, W.; Guhlke, C.; Miller, R., Modeling of electrochemical double layers in thermodynamic non-equilibrium. *Phys. Chem. Chem. Phys.* **2015**, *17* (40), 27176-27194.
168. Dreyer, W.; Guhlke, C.; Müller, R., A new perspective on the electron transfer: recovering the Butler–Volmer equation in non-equilibrium thermodynamics. *Physical Chemistry Chemical Physics* **2016**, *18* (36), 24966-24983.

169. Malavé, V.; Berger, J. R.; Zhu, H.; Kee, R. J., A Computational Model of the Mechanical Behavior within Reconstructed  $\text{Li}_x\text{CoO}_2$  Li-ion Battery Cathode Particles. *Electrochimica acta* **2014**, *130*, 707-717.
170. Purkayastha, R.; McMeeking, R., An integrated 2-D model of a lithium ion battery: the effect of material parameters and morphology on storage particle stress. *Solids, Fluids, Structures, Fluid-Structure Interactions, Biomechanics, Micromechanics, Multiscale Mechanics, Materials, Constitutive Modeling, Nonlinear Mechanics, Aerodynamics* **2012**, *50* (2), 209-227.
171. Danilov, D.; Notten, P. H. L., Mathematical modelling of ionic transport in the electrolyte of Li-ion batteries. *Electrochimica acta* **2008**, *53* (17), 5569-5578.
172. Bohn, E.; Eckl, T.; Kamlah, M.; McMeeking, R., A Model for Lithium Diffusion and Stress Generation in an Intercalation Storage Particle with Phase Change. *Journal of The Electrochemical Society* **2013**, *160* (10), A1638-A1652.
173. Mukhopadhyay, A.; Sheldon, B. W., Deformation and stress in electrode materials for Li-ion batteries. *Progress in Materials Science* **2014**, *63*, 58-116.
174. Renganathan, S.; Sikha, G.; Santhanagopalan, S.; White, R. E., Theoretical Analysis of Stresses in a Lithium Ion Cell. *Journal of The Electrochemical Society* **2010**, *157* (2), A155.
175. Chen, J.; Hu, H.; Li, S.; He, Y., Evolution of mechanical properties of polypropylene separator in liquid electrolytes for lithium-ion batteries. *Journal of Applied Polymer Science* **2018**, *135* (27), n/a-n/a.
176. Guo, M.; White, R. E., Thermal Model for Lithium Ion Battery Pack with Mixed Parallel and Series Configuration. *Journal of The Electrochemical Society* **2011**, *158* (10), A1166.
177. Lasia, A., *Electrochemical impedance spectroscopy and its applications*. New York : Springer: 2014.

## 8. Appendices

### 8.1 Chapter-3

Impedance experiments results are fitted according to the Randles circuit model. A Randles circuit is defined as an equivalent electrical circuit that consists of an active electrolyte resistance  $R_S$  in series with the parallel combination of the double-layer capacitance  $C_{dl}$  and an impedance of a faradaic reaction. It is broadly used in EIS for interpretation of impedance spectra, often with a constant phase element (CPE) replacing the double layer capacity ( $C_{dl}$ ). The Randles equivalent circuit is one of the simplest possible models describing processes at the electrochemical interface. In real electrochemical systems, impedance spectra are usually more complicated and, thus, the Randles circuit may not give appropriate results.<sup>177</sup>

#### 8.1.1 The Principles of Electrochemical Impedance Spectroscopy

Considering Ohm's law which describes the relationship between voltage to a direct current passing through a resistor,

$$E = IR \quad (1)$$

Impedance, very simply, extends the concept of resistance to an alternating current circuit, and generally represented as  $Z$ , we can simply write,

$$E = IZ \quad (2)$$

As it was mentioned earlier, EIS experiment is simply applying an oscillating voltage, and measuring the (oscillating) current response. Thus, the equation is formed as,

$$E(t) = |E| \sin(\omega t) \quad (3)$$

Where  $|E|$  is the amplitude of the voltage signal, and  $\omega=2\pi f$  (the angular frequency). The response will be a current with an amplitude  $|I|$ , which is also shifted in phase from the applied signal,

$$I(t) = |I|\sin(\omega t + \theta) \quad (4)$$

The current is shifted in phase because of reactance (e.g., a capacitance or inductance) in addition to the resistance (which changes the amplitude). The impedance can therefore be expressed like this,

$$Z = \frac{E(t)}{I(t)} = \frac{|E|\sin(\omega t)}{|I|\sin(\omega t + \theta)} = |Z| \frac{\sin(\omega t)}{\sin(\omega t + \theta)} \quad (5)$$

EIS basics are explained in a simple way. For complex systems, the definition of current and voltage is written in the view of Euler's formula,

$$e^{jx} = \cos(x) + j\sin(x) \quad (6)$$

The resistance can be written in this form,

$$Z = |Z|e^{j\theta} = \frac{|E|e^{j\omega t}}{|I|e^{j\omega t + \theta}} \quad (7)$$

$$E = IZ = I|Z|e^{j\theta} \quad (8)$$

The ratio of an oscillating voltage to an oscillating current is the impedance, which has a magnitude  $|Z|$  and a phase angle  $\theta$ . More commonly for impedance spectroscopy, however, the Cartesian complex plane representation is used, dividing the complex impedance into the real and imaginary parts,

$$Z = Z' + jZ'' \quad (9)$$

$Z'$  and  $Z''$  are the resistive and reactive parts of the impedance respectively. This scheme is the basics of Nyquist plot which is used to show the real and imaginary parts of the impedance measurement. (please see Results and Discussion-Impedance Measurement section.)

### 8.1.1.1 The Basic Electrical Circuit Components

The Randles circuit consists of resistors and capacitors. The physical meaning and how to model EIS data and Nyquist plot are explained briefly in this section.



The first one is the resistors, which obey Ohm's law, so the current is always proportional to the voltage. There is no reactive part (i.e., phase shift) which results in no dependence on frequency. We can write,

$$Z_R = R \quad (10)$$

R is the resistance.

Capacitors have a purely reactive impedance. An ideal capacitor has zero resistance. When an alternating voltage is applied across a capacitor, the current leads the voltage (the phase is  $-90^\circ$ ), and the impedance is inversely proportional to the frequency. The impedance increases with decreasing frequency. Consider applying a DC voltage across a capacitor – after a long enough time, the capacitor is fully charged and no more current flows. The impedance is effectively infinity. The equation describing a capacitor is,

$$Z_C = \frac{1}{j\omega C} \quad (11)$$

where j is the imaginary unit,  $\omega=2\pi f$  and C is the capacitance. The Nyquist plot for a capacitor therefore looks like a vertical line, where  $Z' = 0$  for all frequencies. Capacitances arise all over the place in electrochemical systems, pretty much anywhere you have an interface – most often from the capacitance of the double layer, but also dielectric capacitance, or at grain boundaries in solids.

In series, the summation of additives,

$$Z = \sum_n Z_n \quad (12)$$

The impedance of the series RC circuit is therefore just the addition of the individual impedances of the resistor and the capacitor together,

$$Z = Z_R + Z_C = R + \frac{1}{j\omega C} \quad (13)$$

The series RC circuit can be considered as a simple model for things like a blocking interface. For instance, an inert electrode immersed in a conducting electrolyte, where R represents the ionic resistance of the electrolyte, and C represents the capacitance of the double layer on the electrode surface.

If the parallel configuration is considered, the RC circuit is written as,

$$\frac{1}{Z} = \frac{1}{R} + j\omega C \text{ and } Z = \frac{R}{1+j\omega RC} \quad (14)$$

From this equation, at high frequency, i.e.,  $\omega \rightarrow \infty$ , the lower term on the fraction goes to infinity, so the impedance tends towards zero; the ideal circuit behaves like the capacitor at infinite frequency such that it has zero impedance. At low frequency, i.e.,  $\omega \rightarrow 0$ , however, the bottom term becomes 1, so the total impedance of the circuit equals R, i.e., with a direct current, the circuit behaves like a resistor. Eventually with a direct current, the capacitor becomes fully charged and the current only goes through the resistor. The Nyquist plot for this circuit, then, is a semicircle, intercepting the real ( $Z'$ ) axis at 0 and R: Semicircles in the Nyquist plot are very common in electrochemical impedance and are usually associated with processes such as charge transfer, because at an electrode surface the transfer of charge happens in parallel with the charging of the double layer capacitance, hence the semicircle.

### 8.1.2 Fitted Impedance Data

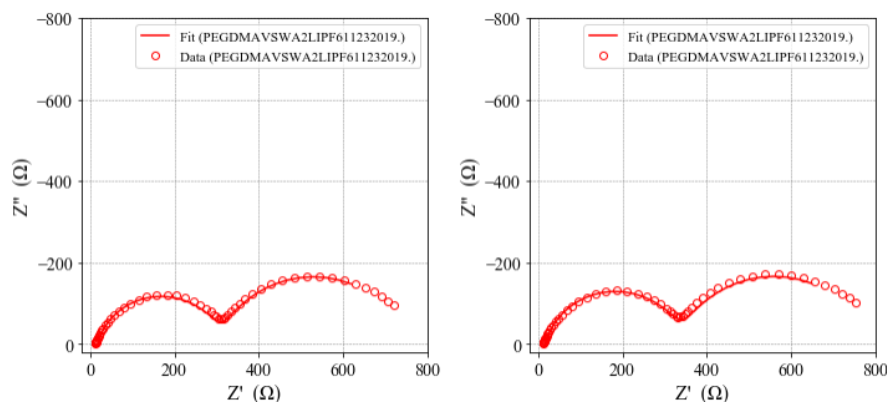


Figure S 7.1: Fitted impedance results pre and post polarization of 1 M LiPF<sub>6</sub> (EC-DEC) swelled O-PEGDMA-VS-0.

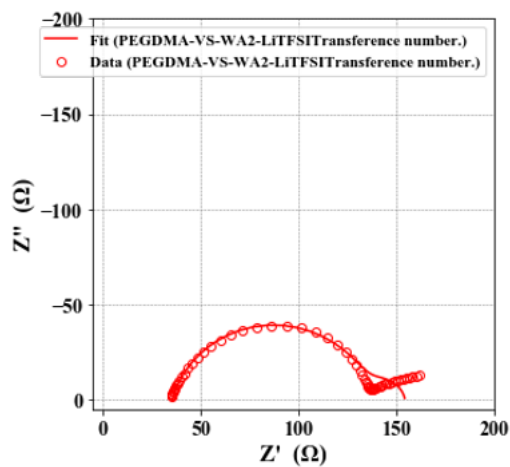


Figure S 7.2: Fitted impedance results pre and post polarization of 1 M LiTFSI (DOL-DME) swelled O-PEGDMA-VS-0.

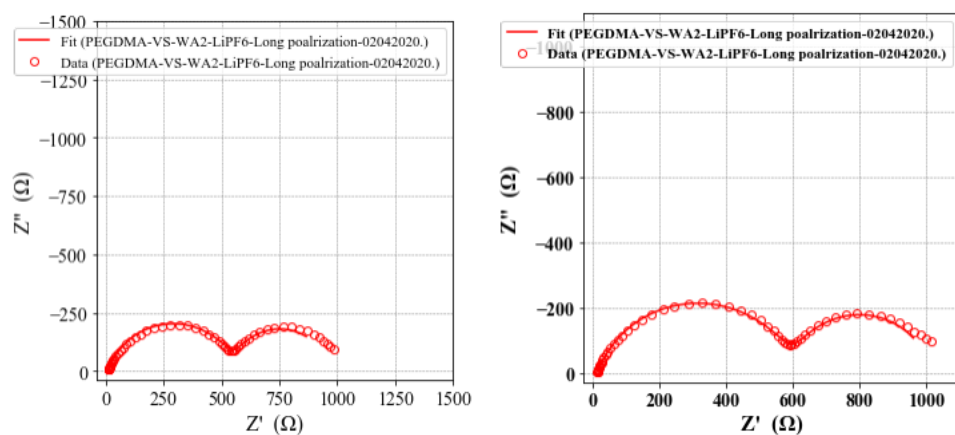


Figure S 7.3: Fitted impedance results pre and post polarization of 1 M LiPF6 (EC-DEC) swelled O-PEGDMA-VS-0 (longer polarization).

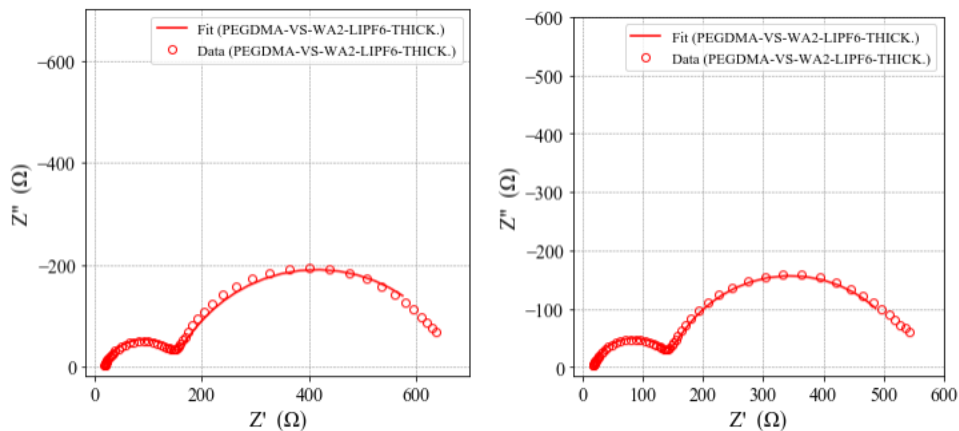


Figure S 7.4: Fitted impedance results pre and post polarization of 1 M LiPF<sub>6</sub> (EC-DEC) swelled thick Opaque PEGDMA-VS-0.

### 8.1.3 Liquid Electrolyte Characterization

Two widely known and used liquid electrolytes 1 M LiTFSI (DOL-DME 1:1 v%) and 1 M LiPF<sub>6</sub> (EC-DEC 1:1 v%) are characterized with regard to ionic conductivity and transference number.

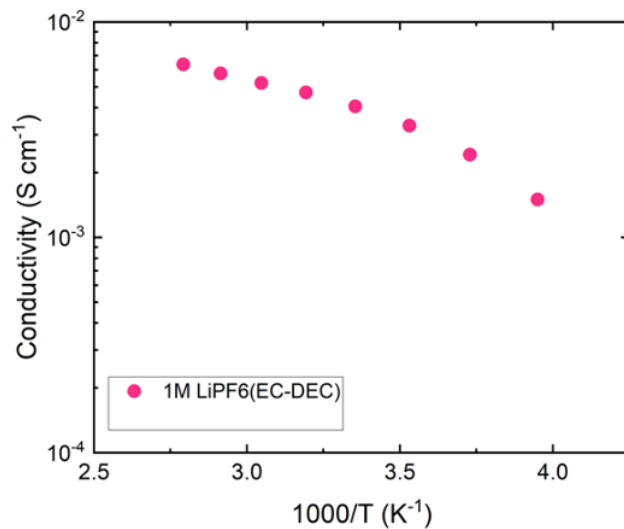


Figure S 7.5: Conductivity of 1 M LiPF<sub>6</sub> (EC-DEC 1:1 v%) between -20°C to 85°C.

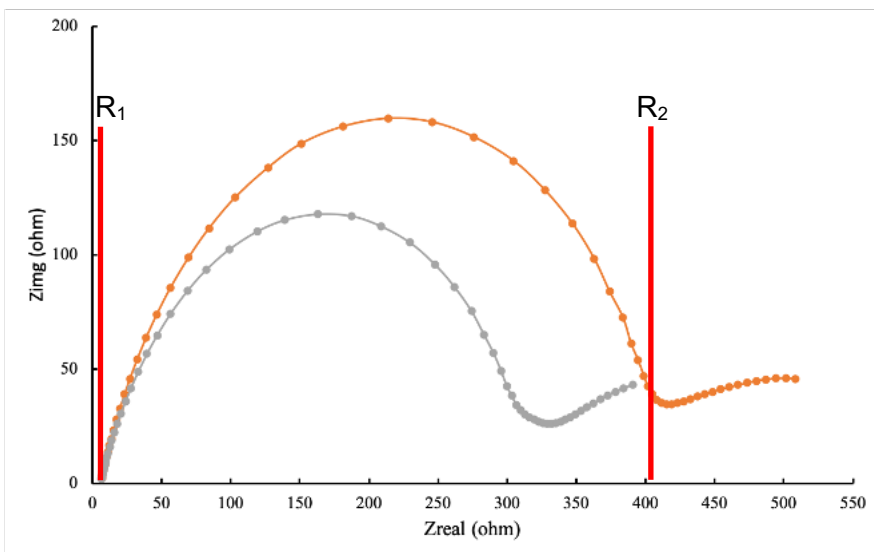


Figure S 7.6: Impedance data pre and post hold 1 M LiPF<sub>6</sub> (EC-DEC 1:1 v%).  $t_{Li^+}$  is obtained as 0.37.

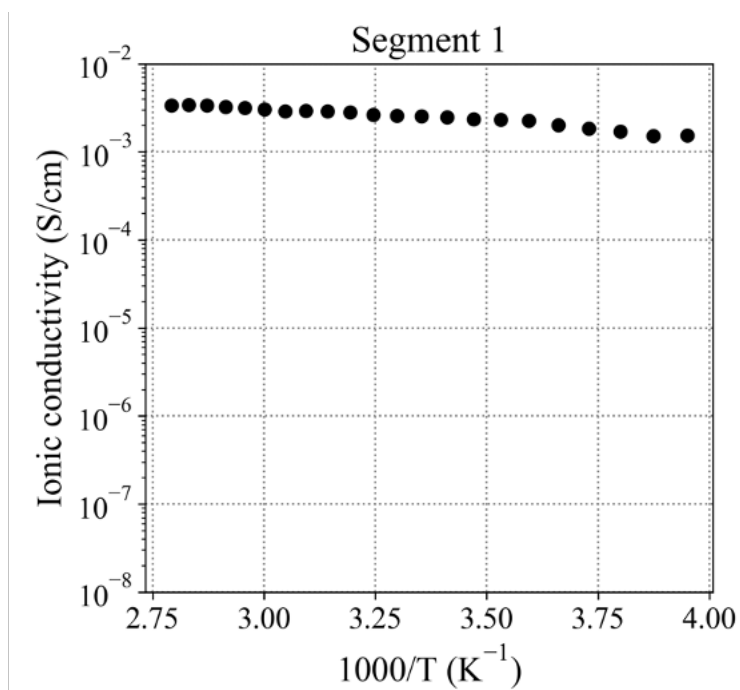


Figure S 7.7: Conductivity of 1 M LiTFSI (DOL-DME 1:1 v%).

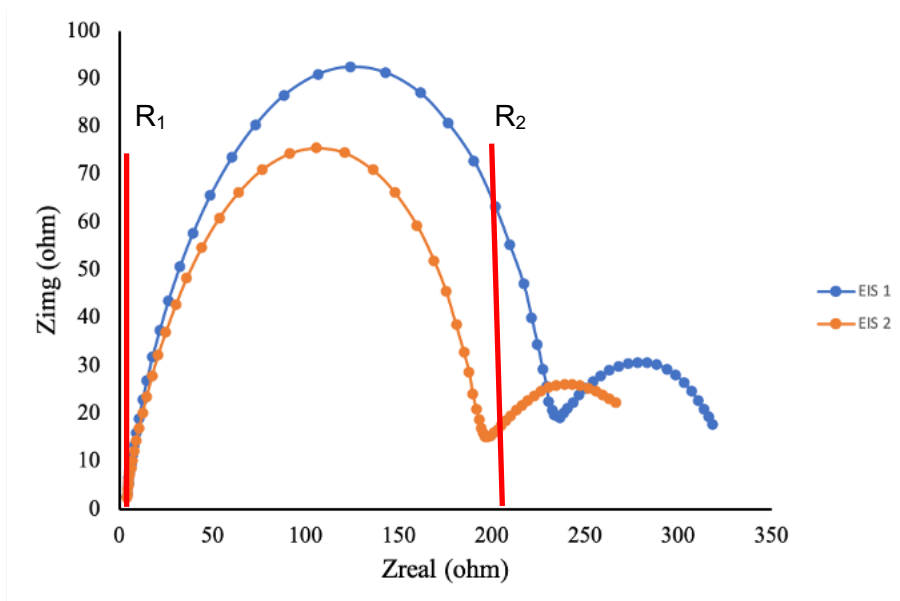


Figure S 7.8: Impedance data pre and post hold 1 M LiTFSI (DOL-DME 1:1 v%).  $t_{Li^+}$  is obtained as 0.57.

**MODULO DI EMBARGO DELLA TESI**  
**(da compilare solo se si richiede un periodo di segretazione della tesi)**

Il/La sottoscritto/a.....Buket Boz..... Nato/a il...02/08/1990 Konak.....  
a (indicare anche l'eventuale paese estero).....Turkey.....  
provincia di (ovvero sigla del paese estero).....TR.....  
dottorato di ricerca in ..... Ingegneria Meccanica e Industriale  
.....

DICHIARA

- che il contenuto della tesi **non può essere immediatamente consultabile per il seguente motivo**

-----Brevetto e motivi di priorità nella ricerca-----  
-----

La motivazione deve essere dettagliata e controfirmata obbligatoriamente dal Tutor e/o Coordinatore  
(Brevetto, segreto industriale, motivi di priorità nella ricerca, motivi editoriali, altro)


- che il testo completo della tesi potrà essere reso consultabile dopo:

- 12 mesi dalla data di conseguimento titolo
- 24 mesi dalla data di conseguimento titolo
- altro periodo 6 mesi


- che sarà comunque consultabile immediatamente l'abstract della tesi, che viene consegnato alla U.O.C. Dottorati e Scuole di Specializzazione

Luogo e Data

Firma del Dichiarante

  
\_\_\_\_\_

Controfirma del Tutor e/o Relatore e/o Coordinatore del  
Dottorato per la motivazione di embargo e il periodo.

  
\_\_\_\_\_